Aus dem Experimental and Clinical Research Center (ECRC),
eine gemeinsame Einrichtung des Max-Delbrück-Centrums für Molekulare Medizin und der Charité-Universitätsmedizin Berlin.
Direktor: Prof. Dr. Friedemann Paul

Habilitationsschrift

Pathology and Treatment of Neuroinflammation: Implications of Ultrahigh Field Magnetic Resonance Methods

zur Erlangung der Lehrbefähigung
für das Fach Experimentelle Neuroimmunologie

vorgelegt dem Fakultätsrat der Medizinischen Fakultät
Charité - Universitätsmedizin Berlin

von

Dr. rer. medic. Sonia Waiczies
geboren in Attard (Malta)

Eingereicht: Juli 2021
Dekan: Prof. Dr. med. Axel R. Pries
1. Gutachter/in: Prof. Dr. Imke Metz, Göttingen
2. Gutachter/in: Prof. Dr. Carsten Lukas, Bochum

Inhaltsverzeichnis

Abkürzungen

^{19}F	fluorine
BBB	blood-brain barrier
BV	brain volume
CEL	contrast-enhancing lesion
CNS	central nervous system
CRP	cryogenically cooled RF probe
CSF	cerebrospinal fluid
CVS	central vein sign
DC	dendritic cell
DHODH	dihydroorotate dehydrogenase
DMT	disease modifying treatment
EAE	experimental autoimmune encephalomyelitis
Erk1	extracellular signal-regulated kinase 1
FA	flip angle
GBCA	gadolinium-based contrast agents
HPLC/MS	high-performance liquid chromatography / mass spectrometry
MAPK	mitogen-activated protein kinase
MS	multiple sclerosis
MRI	magnetic resonance imaging
MRS	magnetic resonance spectroscopy
RRMS	relapsing remitting multiple sclerosis
RF	radio frequency
RT	room temperature
SJL/J	Swiss Jim Lambert / Jackson Laboratory
SNR	signal-to-noise ratio
SPIO	superparamagnetic iron oxide
T_2	spin-spin relaxation time
T_1	spin-lattice relaxation time
TF	teriflunomide
USPIO	ultrasmall superparamagnetic iron oxide
UHF	ultrahigh field
VV	ventricle volume

1 Einleitung

1.1 Introduction to multiple sclerosis

Multiple sclerosis (MS) is a chronic, inflammatory, and demyelinating condition of the central nervous system (CNS) that has a higher prevalence in women (Harbo et al., 2013). It typically affects young adults in their twenties although some patients experience their initial event during childhood or adolescence (Dendrou et al., 2015; Baecher-Allan et al., 2018). The disease course is highly variable and involves a wide range of neurological symptoms that can span between slight tingling in the periphery to complete paralysis during the late stages of disease (Reich et al., 2018). Lesions can occur in both white matter and grey matter and typically affect autonomic, motor, sensory and visual functions. Most patients (approximately 85%) show a relapsing and remitting (RRMS) disease phase, which ultimately transitions (usually within 15-20 years) to a progressive course - secondary progressive MS or SPMS (Krieger et al., 2016; Baecher-Allan et al., 2018). Disability and disease progression is driven by several aspects such as accumulation of inflammatory lesions, oxidative stress following mitochondrial damage, as well as a reduced neuronal reserve leading to failure in axonal loss compensatory mechanisms (Mahad et al., 2015). Already in the nineteenth century axonopathies were observed in MS tissue by Jean-Martin Charcot (1825-1893) who was the first to give a comprehensive description of MS as a neurological disease (Charcot, 1868).

The pathology of MS is characterized by demyelinated focal lesions in the CNS infiltrated by immune cell populations (Lassmann, 2018). Under physiological conditions, immune cells seek out unwanted pathogen or tumour-associated molecular patterns, which cause them to orchestrate complex effector mechanisms and to recruit with other cells towards the affected region (Nourshargh and Alon, 2014). The result of such mechanisms could cause damage if persisting for too long and could drive chronic inflammation or autoimmunity when the effector mechanisms are directed against self (Stephenson et al., 2018).

The pathogenesis of MS involves an immune-mediate response against antigens of the CNS with inflammatory bouts involving immune cells infiltrating the blood-brain barrier (BBB), ultimately leading to neurodegeneration and tissue destruction (Lassmann, 2019). During all courses of disease, active demyelination and neurodegeneration are associated with immune cell infiltration and activated microglia

(Stephenson et al., 2018). Activated microglia are more pronounced in PPMS than RRMS; they engulf myelin degradation products and typically surround the rim of slow expanding (smoldering) lesions (Magliozzi et al., 2013; Frischer et al., 2015).

T cells are the key immune cells that orchestrate pathogenesis and disease progression (Kaskow and Baecher-Allan, 2018) and most disease modifying treatments (DMTs) typically target these cells, whether investigational (Lunemann et al., 2002; Aktas et al., 2003; Waiczies et al., 2005; Waiczies et al., 2007; Paul et al., 2008)[1] or already approved treatments (Rommer et al., 2019). An acute inflammation involves trafficking of T cells from the periphery into the CNS and is accompanied by disruption of the BBB, a hallmark of the RRMS pathology (Filippi et al., 2018).

However, T cells are not the only cells involved in the pathology of MS. Other inflammatory cells including dendritic cells, macrophages and activated microglia also play an important role in the pathogenesis and are also targets of existing DMTs (Mishra and Yong, 2016). Furthermore, B cells have long been recognized to be important in the MS pathology; they secrete proinflammatory cytokines as well as antibodies in the CNS (Sabatino et al., 2019). More than half a century ago, unique IgG antibodies from clonal B cells were identified in cerebrospinal fluid (CSF) of MS patients (Yahr et al., 1954). These oligoclonal bands are identified on electrophoretic techniques and are a hallmark of MS (Deisenhammer et al., 2019). They are detected in more than 90% of MS patients and are still a useful diagnostic biomarker (Thompson et al., 2018b).

During the progression from an RRMS course to SPMS disease, the inflammatory process subsides and the neurodegenerative component gains momentum (Mahad et al., 2015). During secondary and primary progressive stages of MS, treatment with neuroprotective or regenerative therapies would have a more determining impact in treatment than anti-inflammatory DMTs; however such treatment options for SPMS and PPMS remain limited (Faissner et al., 2019). Despite their immense success, most anti-inflammatory MS therapies can only delay the conversion to progressive disease by preventing further neurodegeneration but cannot reverse neurodegenerative progression (Bergamaschi et al., 2016). Although neurodegeneration is considered to be more extensive during progressive stages of disease, it is already present during early, even preclinical stages of MS. Axonal

[1] Eigene Arbeiten

transections and degeneration are detectable in early MS (Trapp et al., 1998) but become more prominent during progressive disease (Frischer et al., 2015). On the other hand, inflammatory processes remain an important component of active tissue injury, even during progressive disease, and may occur behind an intact blood brain barrier (Lassmann et al., 2012). Although less pronounced than in active lesions, inflammation is also present in nonactive lesions and in normal-appearing white matter (Frischer et al. 2009).

Although fewer breaches in the BBB exist during PPMS, diffuse immune cell infiltrates are still prevalent within the parenchyma (Hochmeister et al., 2006). A neuropathological assessment of PPMS spinal cord tissue showed a strong association between meningeal inflammation and severity of pathology (Androdias et al., 2010). B cell accumulation may contribute to the deteriorating clinical course (Cencioni et al., 2021). Studies on postmortem brain tissue of SPMS patients shows tightly packed B cells and some T cells in ectopic lymphoid follicles that resemble secondary lymphoid organs within intracortical perivascular cuffs (Magliozzi et al., 2007; Magliozzi et al., 2013). More recently, lymphoid follicles in postmortem SPMS and PPMS brain and spinal cords were shown to be devoid of follicular regulatory T cells (Bell et al., 2020). These regulatory cells are key suppressors of germinal center-derived autoreactive B cell responses and could indicate a reduced regulated control of the humoral immune responses in these follicles that might contribute to the resulting cortical pathology of progressive MS (Negron et al., 2020).

T cells are key to the MS pathogenesis and most DMTs typically exert their action by modifying the proliferative or migratory behaviour of these cells. However DMTs target other immune cell populations, including B cells that also play an important role in the MS pathogenesis particularly during progressive disease (Sabatino et al., 2019). B cell depletion therapies that specifically target the B cell antigen marker CD20 — such as the monoclonal antibodies rituximab, ocrelizumab and ofatumumab — have shown therapeutic efficacy in MS (Lee et al., 2021). The significance of targeting B cells during progressive disease was hailed a few years ago (Mullard, 2015). Ocrelizumab was shown to reduce the progression of upper limb disability in patients with advanced PPMS (Giovannoni et al., 2019). This underscores that targeting the inflammatory process — even during progressive disease — remains an area of intense investigation in MS research.

1.2 The animal model of multiple sclerosis

The experimental autoimmune encephalomyelitis (EAE) is an animal model that resembles several aspects of MS. It has proven invaluable for understanding inflammatory and neurodegenerative processes and for identifying new MS treatment strategies (Glatigny and Bettelli, 2018). EAE can be induced in several species — from rodents to primates. Typically, susceptible animal strains are immunized with encephalitogenic myelin antigen components after emulsification in complete Freund's adjuvant (Aktas et al., 2003). EAE can also be induced by transferring encephalitogenic T cells from immunized donors to susceptible recipients (Jager et al., 2009).

EAE has been a vital tool for identifying novel therapeutic strategies and investigating their potential value for MS patients. Some of the therapies discovered in the EAE model are established treatments for MS (Glatigny and Bettelli, 2018). The discovery that antibodies against α4βI integrin (natalizumab) prevent traffic of mononuclear leukocytes across the vascular endothelium of the CNS in EAE (Yednock et al., 1992) resulted in studies showing a rapid and sustained reduction in disease activity in MS patients (Kappos et al., 2013). Several other examples exist. In the EAE animal model, the dihydroorotate dehydrogenase (DHODH) inhibitor teriflunomide (TF) reduced disease severity and progression in different animal strains (Merrill et al., 2009; Merrill, 2009; Ringheim et al., 2013). In later clinical studies in RRMS patients, TF reduced relapse rate, disability progression, as well as lesion volume and brain volume loss (Wiese et al., 2013; Xu et al., 2016; Radue et al., 2017). Further examples include the sphingosine-1-phosphate receptor modulators fingolimod and siponimod. The latter improves cortical network functionality in EAE mice (Gentile et al., 2016), while it later was shown to reduce the risk of further disability progression in SPMS patients (Kappos et al., 2018).

Nonetheless, EAE is a simple model of MS and does not completely reflect the intricate inflammatory and neurodegenerative processes that occur during CNS immunopathology and autoimmunity in MS (Baxter, 2007). Just as findings that are observed in culture need to be confirmed in animal models such as the EAE due to the complexity of biological processes during inflammation, it is equally crucial to ascertain that changes and observations in the EAE are also clinically relevant in MS patients.

1.3 Magnetic resonance imaging crucial for identifying MS pathology

To gain a comprehensive and longitudinal view of brain inflammation in patients, non-invasive methods that employ high resolution brain imaging would be advantageous. The development of several imaging modalities has provided the possibility to study physiological or pathological processes in intact organisms. Magnetic resonance imaging (MRI) is an imaging modality the application of which can be easily translated to the clinic. MRI has been indispensable for the diagnosis and monitoring of MS (Filippi et al., 2016a; Rovira and de Stefano, 2016; Filippi et al., 2019a). The advent of ultrahigh field (UHF) magnetic field strengths (see next chapter) has increased the signal sensitivity of this imaging modality (Niendorf et al., 2016d) and further increased its capability of uncovering more discreet morphological changes during the pathological processes especially during MS (**Figure 1**).

MR protocols for the diagnosis, prognosis and monitoring of MS patients follow specific guidelines of the Magnetic Resonance Imaging in MS group (MAGNIMS) in Europe (Rovira et al., 2015; Wattjes et al., 2015) or the Consortium of Multiple Sclerosis Centers (CMSC) in North America (Traboulsee et al., 2016). Standardized MRI protocols from harmonized initiatives are essential to facilitate swift clinical translation and comparison of data across different clinical environments around the world (Arevalo et al., 2019; Schmierer et al., 2019; Pereira et al., 2020).

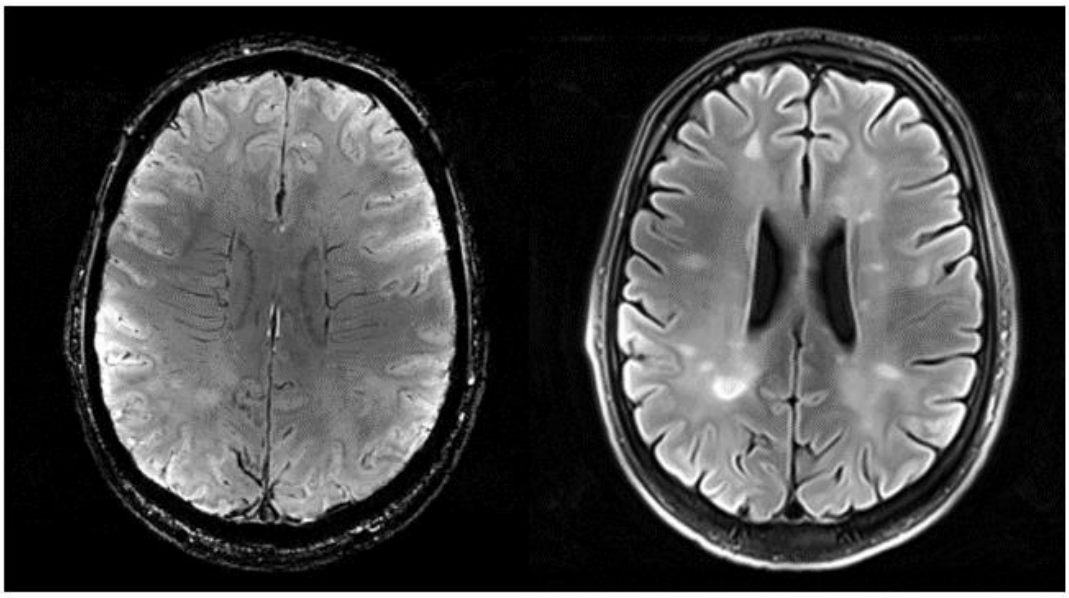

Figure 1. MS lesions are easier to detect at 7-Tesla MRI

MRI protocols for MS comprise multiple MRI contrasts. These contrasts are governed by the spin-lattice (longitudinal) relaxation time T_1, the spin-spin (transversal) relaxation time T_2, the effective spin-spin relaxation time T_2*, and diffusion weighted imaging (DWI) (Maranzano et al., 2019).

T_2-weighted (T_2w) MRI is well established in clinical practice and is used to identify white matter (WM) lesions that are characterized by hyperintense appearance (Zivadinov and Bakshi, 2004; Hemond and Bakshi, 2018). Detection of hyperintense lesions on T_2w MRI is an important criterion for MS diagnosis (Thompson et al., 2018a). However, the lesion load alone correlates weakly with clinical disability, since it does not specify lesion severity or describe underlying pathophysiology (Zivadinov and Bakshi, 2004; Neema et al., 2007; Hemond and Bakshi, 2018), unless parametric mapping of the transverse relaxation time T_2 is implemented (Shepherd et al., 2017). T_2* is sensitive to iron content which correlates with disease duration, activity and severity (Walsh et al., 2013; Ropele et al., 2014; Walsh et al., 2014; Bozin et al., 2015; Bagnato et al., 2018) and is already detected in early MS (Bonnier et al., 2014; Blazejewska et al., 2015). Therefore T_2*w MRI may become a tool to assess the development of MS already at an early stage. T_2*w MRI has also gained popularity to detect the central vein sign that is considered a specific imaging marker for MS lesions (Tallantyre et al., 2009a; Geraldes et al., 2018a; Hemond and Bakshi, 2018; Sinnecker et al., 2019). By expanding the MR protocol with further MR techniques, the time required per patient examination will naturally increase considerably. Therefore, dual contrast techniques would be desirable to reduce scan time to promote clinical application. Recently our group reported on a simultaneous T_2 and T_2* mapping method that reduced acquisition time and could delineate MS lesions just as clearly as separate T_2 and T_2* maps acquired with standard techniques (Herrmann et al., 2021).

Contrast-enhanced MRI has been an integral part of the MR protocol to diagnose MS patients and monitor their treatment, it is used to investigate acute inflammation due to a recent infiltration of inflammatory cells into the CNS. When the BBB is disrupted, contrast agents leak through the BBB into the inflamed tissue, resulting in the appearance of contrast-enhancing lesions (CEL) that are detected with MRI (Thompson et al., 2018b).

Detection of CELs with gadolinium-based contrast agents (GBCA) is currently the gold standard to detect episodes of BBB disruptions and to differentiate new, active

lesions from older ones (Thompson et al., 2018c). A continuous neurological decline in the absence of new CELs implies disease progression and is indicative of RRMS conversion to SPMS. Parametric mapping of the T_1 relaxation time of CELs and the surrounding CNS tissue provides a quantitative MRI approach for measuring disease activity as well as further diagnostic information to better discriminate lesion subtypes and enable faster staging of disease activity (Kober et al., 2012). However, concerns regarding potential long-term deposition of GBCA in the brain and other organs and tissue restricts the frequent application of this important diagnostic tool (McDonald et al., 2015; McDonald et al., 2017; Schlemm et al., 2017; El-Khatib et al., 2019).

Neurodegeneration and brain atrophy is another feature of MS that can be measured by volumetric MRI and occurs already early during the disease (Azevedo et al., 2015; Solomon et al., 2017). Brain atrophy is accompanied by a gradual enlargement of the cerebrospinal fluid (CSF)-filled brain ventricles. Atrophy also occurs during normal ageing, although shrinkage of the cortex and expansion of the ventricles proceeds more rapidly in MS patients (Turner et al., 2003; De Stefano et al., 2016), especially during the secondary-progressive phase, when neurodegenerative processes dominate. Alongside the appearance of new lesion activity, brain and spinal cord atrophy are sometimes used to predict the impact of MS therapies on neurological disability and which MS patients will be therapy responders. A meta-analysis of randomized trials evaluating a broad range of DMTs showed that treatment effect on brain atrophy is closely correlated with the treatment effect size on 2-year disability progression in RRMS patients (Sormani et al., 2014). When atrophy is used as neuroprotective measure to determine treatment response, brain volume (BV) changes should be assessed at least 6 to 12 months following treatment start and not earlier (Barkhof et al., 2009).

Measurements of atrophy are not implemented in clinical practice. Global brain atrophy measurements lack pathological specificity. Changes in the volumes of brain compartments may be the result of changes in the parenchymal tissue (myelin, axon, glial content) but also physiological fluctuations such as water content changes (Duning et al., 2005), hydration status (Dieleman et al., 2017) or circadian rhythm (Trefler et al., 2016). Additionally, non-tissue related reductions in BV, referred to as pseudoatrophy, may also occur, for instance following anti-inflammatory therapies, as a result of accelerated water losses and fluid shifts (Zivadinov et al., 2008). Thus, the cross-sectional predictive value of BV is suitable at group level, especially for

outcomes like cognition, but the predictive value in individual patients might be more questionable (Barkhof, 2016). Furthermore, there are issues regarding inconsistencies when measuring whole BV amongst different automated and semi-automated methods that still needs to be thoroughly investigated, especially in MS patients (Wang et al., 2016). Therefore improvements in MRI technologies should not only include standardization of MR data acquisitions and reconstructions but also a harmonization of post-processing pipelines to identify reliable changes in the CNS of MS patients and to provide clinicians with a better guide to enhance the accuracy and speed of an MS diagnosis (Filippi et al., 2019b). In addition further quantitative MRI biomarkers are required to better understanding the pathology are needed to promote a more accurate diagnosis of MS (Filippi et al., 2019a).

1.4 Ultrahigh Field MRI to study neuroinflammatoy pathology

Ultrahigh field (UHF) MRI refers to MRI measurements carried out on scanners with a main magnetic field strength $B_0 \geq 7.0$ Tesla. UHF MRI opens new opportunities that mainly revolve around the improved sensitivity and specificity associated with increasing B_0. The benefits from an increase in signal sensitivity and signal-to-noise ratio (SNR) can be invested in enhanced spatial or temporal resolutions, both key to superior imaging for more accurate and definitive diagnoses (Sinnecker et al., 2015; Niendorf et al., 2016b). Furthermore structural imaging at the mesoscopic scale (Dumoulin et al., 2018) and hemodynamic responses (Uludağ and Blinder, 2018) benefit from UHF MRI.

When studying MS pathology, the increased sensitivity and specificity bestowed by UHF has given us new insights into leptomeningeal enhancement and the properties of lesions at different stages of the disease, including detection of the central vein sign (CVS), as well as an improved understanding of the pathology when using metabolic imaging (Bruschi et al., 2020). MS lesions have long been shown from histopathological studies to show a perivenous distribution i.e. they form around veins and venules (Sati et al., 2016). The CVS can be identified on T_2* weighted MRI (Tan et al., 2000; Maggi et al., 2014; Sati et al., 2016) at lower magnetic field strengths (1.5-3.0 T), but more CVS are detected at 7.0 T (Tallantyre et al., 2009b; Sinnecker et al., 2013; Muller et al., 2014; Filippi et al., 2019a). Other MRI features that have been uncovered by 7.0 T MRI in MS patients include hypointense rim structures as well as a differentiation of MS grey matter lesions (Sinnecker et al., 2012a; Sinnecker

et al., 2012b; Wuerfel et al., 2012; Kuchling et al., 2014). One of the greatest challenges is to differentiate MS lesions from those occurring in other neuroinflammatory conditions such as Neuromyelitis Optica Spectrum Disorder (NMOSD) and Susac syndrome (Geraldes et al., 2018b). New findings revealed by UHF MRI have proven to be indispensable to make a definitive diagnosis (Filippi et al., 2019a). UHF MRI gives a better delineation of features such as the CVS and hypointense rim; this has helped differentiate MS lesions from other neuroinflammatory disorders such as Susac syndrome (Wuerfel et al., 2012) and neuromyelitis optica (NMO) (Sinnecker et al., 2012a). On the other hand UHF MRI has also exposed common pathological findings with other MS variants such as Baló's concentric sclerosis (Blaabjerg et al., 2016; Behrens et al., 2018).

Apart from the many opportunities associated with UHF MRI for the detection and differentiation of MS lesions, some challenges exist. One of these challenges concerns the radio-frequency (RF) coils that are used at UHF to transmit and receive the RF signal that is required to acquire the MR image (Vaughan et al., 2001). The higher the magnetic field, the higher the resonance frequencies required and therefore the shorter the wavelengths that are used. Apart from the higher energy required by the radio pulses, constructive and destructive interferences occur due to the shortening of the waves in the tissue (from c. 50 cm at 1.5 T to c. 13 cm at 7.0 T). These will cause strong inhomogeneities of the transmission field (B_1^+) causing signal losses over some parts of the image. In this case, multichannel transmission using parallel transmit (pTx) RF coils and RF pulse design approaches would benefit from enhanced B_1^+ homogeneity and thus facilitate uniform coverage of the brain (Padormo et al., 2016).

1.5 Fluorine (^{19}F) MRI to study neuroinflammatory pathology

One approach to study neuroinflammation is to detect and quantify inflammatory cells in vivo. MRI methods are highly suited for tracking cells in vivo since they provide simultaneous anatomical and physiological information. UHF MRI provides an added advantage since it offers a higher spatial resolution. In general, all MRI methods, including the experimental ones, would benefit from UHF MRI due to the gain in sensitivity and signal-to-noise ratio (SNR) that enables higher spatial resolution (detail) and better signal detection (sensitivity).

The initial cell labeling strategies for MRI made use of contrast agents that modulate the MR relaxation times (T_1, T_2, T_2*) of labeled inflammatory cells. The shortening of T_1 or T_2/T_2* results in an increase or decrease in signal, respectively. T_1 agents include manganese (Mn) chelates or gadolinium (Gd) chelates such as Gd-DTPA (diethylene-triamine pentaacetic acid). Iron oxide nanoparticles such as superparamagnetic iron oxide particles (SPIO), ultrasmall iron oxide agents (USPIO) and micrometer-sized iron oxide particles (MPIO) have been employed as T_2* contrast agents to label cells in vitro and in vivo (Hinds et al., 2003; Shapiro et al., 2004). Clinical SPIO have been approved by the FDA to label dendritic cells that are applied as cancer vaccines in melanoma patients (de Vries et al., 2005). One drawback of MRI contrast agents such as SPIO is a general difficulty to distinguish negative contrast (voids) created by labeled cells from other void artifacts (blood clots, air bubbles etc.).

One MR technique for tracking cells in vivo that provides advantages over MR techniques that utilize applying T_2* iron-oxide nanoparticles involves the labeling of cells with fluorine (^{19}F) nanoparticles (Ahrens et al., 2005). These nanoparticles are used to label inflammatory cells which can then be imaged and quantified by ^{19}F MRI. ^{19}F nanoparticles are prepared from emulsions of ^{19}F-rich perfluorocarbons (PFC) and their size ranges from 100 nm up to 500 nm, depending on the preparation method (Janjic and Ahrens, 2009; Waiczies et al., 2011).

Fluorine (^{19}F) MRI is an underutilized method that would benefit immensely from the increase in SNR achieved with UHF MRI. Particularly in the clinic more efforts should be invested to make use of this unique and valuable tool. The absence of ^{19}F background signal makes ^{19}F a highly attractive label of fluorinated compounds that are administered in vivo. The important advantages of in vivo ^{19}F MRI over other MR techniques are (i) a biological absence of organic ^{19}F in vivo that yields background-free images and complete cell selectivity, (ii) a possibility to quantify the cell signal with ^{19}F MR methods and (iii) a biological and chemical inertness of PFC.

For several years, the main application of ^{19}F MRI was to study inflammatory pathology in experimental disease models such as the EAE (Nöth et al., 1997; Waiczies et al., 2013b; Zhong et al., 2015). ^{19}F MRI is typically performed several hours following intravenous application of ^{19}F nanoparticles to allow label immune cells in the bloodstream that are on their way to the inflamed organ. In EAE, nanoparticles are taken up by inflammatory cells during their migration into the CNS.

The ^{19}F MRI method of detecting CNS inflammation is still not applicable in MS patients, due to the necessity of administering ^{19}F nanoparticles intravenously. SPIO nanoparticles have been applied since several years in patients, including those with MS (Vellinga et al., 2008; Vellinga et al., 2009). Several SPIOs have been studied; these come in various sizes, the ultrasmall SPIOs starting at 11 nm and the larger ones at 100 nm (approaching ^{19}F nanoparticle size). Correspondingly, the half-life in blood is diverse, from 10 minutes up to more than 24 hours in case of the smaller and dextran coated ones (Daldrup-Link, 2017). Most of the SPIOs developed for clinical imaging have been taken off the market because of their limited application spectrum. However, SPIOs that are indicated for the treatment of anemia (such as the USPIO ferumoxytol) are still used off-label as contrast agents in MS (Buch et al., 2020). Concerns exist about their toxicity, especially in BBB disorders such as MS, where they have been shown to aggravate pre-existing disease in the animal model (Hsiao et al., 2019). Prior to distributing further valuable contrast agents into the clinic, additional experimental study is warranted and developments even necessary, such as paradigm shifts involving substitution of gadolinium with iron chelates (Boehm-Sturm et al., 2018).

1.6 Experimental UHF MRI to study cellular and pharmacological therapy

Despite uncertainties associated with contrast agent administration in patients, there are already clear and promising opportunities for clinical ^{19}F MRI today. The method has already been applied to follow intradermally-applied cell therapies in cancer patients (Ahrens et al., 2014). While the method of cell labelling is still experimental and needs to be treated with caution (Waiczies et al., 2017b), the expected risks are related to the cell labelling procedure itself, namely the impact of labelling on the efficacy of the cell therapy or a failed labelling thereof. There are no expected adverse effects on patients.

Using MRI to monitor therapy during pathology bears the potential to make patient management more effective (Reid and Murphy, 2008; Niendorf et al., 2016c) and ^{19}F MRI has the inherent advantage of making this possible (Ji et al., 2015). The prospect of non-invasively monitoring drugs in MS patients heralds an age when exact drug concentrations in the CNS and other disease-relevant tissue, e.g., draining lymph nodes can be determined, to inform drug therapies. The SNR achieved with ^{19}F MRI

is a major limiting factor to detect and quantify ^{19}F drugs with ^{19}F MRI or single voxel spectroscopy (SVS) MR methods. Compared to other MR-active nuclei (e.g., ^{1}H, ^{23}Na, ^{39}K), the availability of ^{19}F nuclei in a tissue of interest in vivo, following a ^{19}F drug application, is exceptionally low. Additionally, ^{19}F MR properties such as chemical shift, T_1 and T_2 relaxation times, as well as pharmacological factors, such as metabolism or protein binding, could influence SNR and ^{19}F MR signal detection. Due to sensitivity constraints, and influences of the environment (temperature, pH) and protein binding on the MR properties of ^{19}F drugs, particularly T_2 relaxation (Prinz et al., 2018; Prinz et al., 2021), which would ultimately influence the MR signal, drug detection in vivo is limited to non-localized ^{19}F MR spectroscopy (MRS). To improve SNR for ^{19}F MRI, implementation of SNR efficient acquisition method specific to each ^{19}F drug will be key (Faber and Schmid, 2016). The combination of SNR-boosting technologies will be key to achieve this goal and allow to monitor drugs in vivo with ^{19}F MRI.

The goals of the publications presented here were to develop, study, validate and combine various SNR-boosting technologies as well as UHF MRI with the ultimate purpose to:

(1) **detect and quantify anti-inflammatory and cellular therapies** non-invasively in individual patients during neuroinflammatory disease such as glioblastoma and multiple sclerosis.

(2) **study the implications of transient changes in brain ventricle volumes** as a pathological feature to detect inflammatory dynamics and as potential MR biomarker in multiple sclerosis patients.

2 Eigene Arbeiten

The research within the selected five publications was performed at the Experimental Ultrahigh Field Magnetic Resonance of the Max Delbrück Center (MDC) for Molecular Medicine in the Helmholtz Association (Director: Professor Thoralf Niendorf).

2.1 Molecular mechanisms of brain autoimmunity and tumor responses

This chapter builds on **publication 1** "ERK1 as a Therapeutic Target for Dendritic Cell Vaccination against High-Grade Gliomas" published in Molecular Cancer Therapeutics (Ku et al., 2016).

Early during my research studies in neuroimmunology at the Charité, we studied experimental therapies in MS and its animal model to modulate the T cell response (Lunemann et al., 2002; Waiczies et al., 2002; Aktas et al., 2003; Waiczies et al., 2005; Waiczies et al., 2007; Paul et al., 2008). I studied the mechanisms of these therapies to uncover new druggable targets for treating autoimmunity. Other than studying the role of Rho GTPases in T cell migration as part of a collaborative research centre project (SFB 650) at the Charité (Waiczies et al., 2007; Waiczies et al., 2008), I also identified the MAP kinase 3 ERK1 as a potential biomarker of atorvastatin (Waiczies et al., 2005) and after some years, one of the PhD students I supervised also showed that ERK1 is crucial for the pathogenesis of neuroinflammation (Bendix et al., 2010). Another PhD student showed that dendritic cells (DCs) play a key role in the immunomodulatory mechanisms of statin therapy (Leuenberger et al., 2014). These results were in part supported by a research fellowship granted by the Charité (*Rahel Hirsch Stipendium*).

During our preliminary findings on ERK1 and DCs in the pathogenesis and treatment of autoimmune encephalomyelitis, DC immunotherapies were becoming extremely popular for the treatment of autoimmune disease (Harry et al., 2010; Idoyaga et al., 2013; Creusot et al., 2014) and particularly as cancer therapies (Palucka et al., 2011; Palucka and Banchereau, 2012). I started working with the notion that ERK1-modulated DCs could emerge as better immunotherapies not only for regulating

brain autoimmunity (upon promoting ERK1 activity) but also for promoting a potent anti-tumour response in brain tumors (upon downregulating ERK1).

DFG funding was acquired to perform research at Experimental Ultrahigh Field Magnetic Resonance of the MDC to study the impact of ERK1-deficient DCs to boost glioma immunotherapy (Ku et al., 2016).

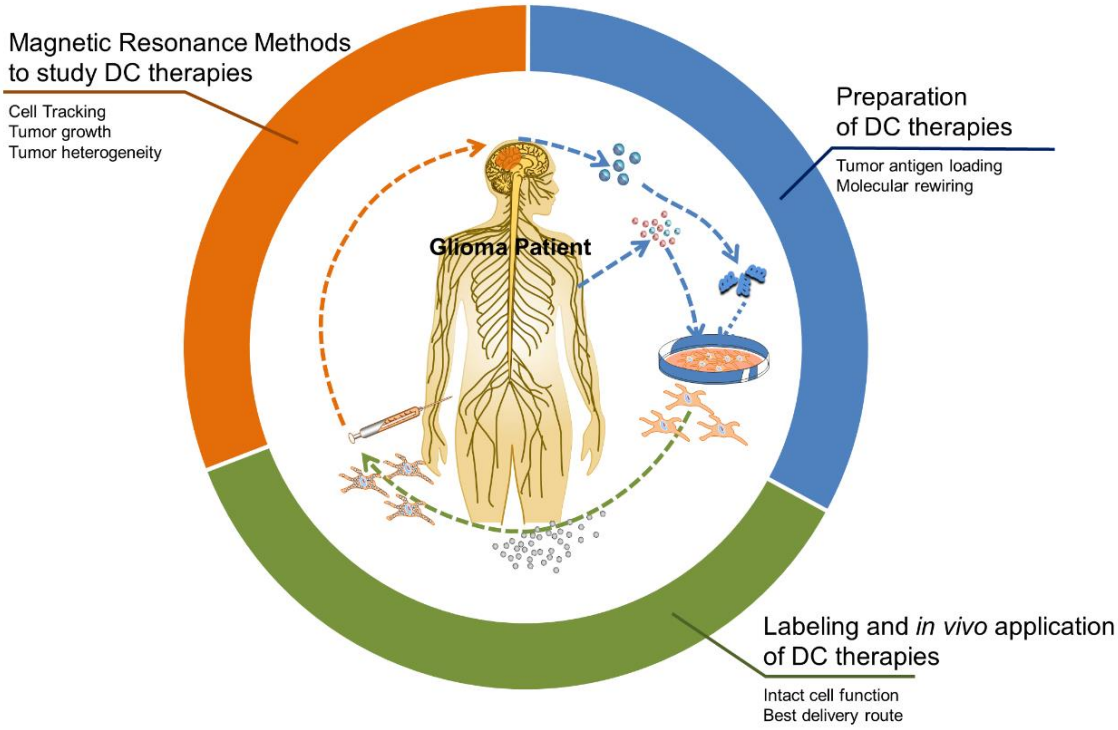

Considering the increased migration and antigenicity of ERK1-deficient DCs, we studied the role of ERK1 in glioma survival by administering GL261 glioma cells in the striatum of ERK1-deficient and control mice.

ERK1-deficient mice showed a prolonged survival compared to wild type littermates; unlike wild type mice, 40% of ERK1-deficient mice were still alive at the end of the experiment (**Figure 1** in own work 1 (Ku et al., 2016)) and showed minimal tumor growth, indicating endogenous mechanisms in ERK1-deficient recipients that regulate the expansion of glioma cells e.g. DCs with sustained Cdc42 activation and better migratory activity as a result in cytoskeletal organization (**Figure 5** in own work 1 (Ku et al., 2016)). Remarkable for DC immunotherapy, we showed that ERK1-deficient DCs were more potent vaccines and provided a higher survival rate to wild type mice harboring high grade gliomas (**Figure 7** in own work 1 (Ku et al., 2016)):

Cancer Biology and Signal Transduction

Molecular Cancer Therapeutics

ERK1 as a Therapeutic Target for Dendritic Cell Vaccination against High-Grade Gliomas

Min-Chi Ku[1], Inan Edes[2], Ivo Bendix[3], Andreas Pohlmann[1], Helmar Waiczies[4], Tim Prozorovski[5], Martin Günther[1], Conrad Martin[4], Gilles Pagès[6], Susanne A. Wolf[7], Helmut Kettenmann[7], Wolfgang Uckert[2], Thoralf Niendorf[1], and Sonia Waiczies[1]

Abstract

Glioma regression requires the recruitment of potent antitumor immune cells into the tumor microenvironment. Dendritic cells (DC) play a role in immune responses to these tumors. The fact that DC vaccines do not effectively combat high-grade gliomas, however, suggests that DCs need to be genetically modified specifically to promote their migration to tumor relevant sites. Previously, we identified extracellular signal–regulated kinase (ERK1) as a regulator of DC immunogenicity and brain autoimmunity. In the current study, we made use of modern magnetic resonance methods to study the role of ERK1 in regulating DC migration and tumor progression in a model of high-grade glioma. We found that ERK1-deficient mice are more resistant to the development of gliomas, and tumor growth in these mice is accompanied by a higher infiltration of leukocytes. ERK1-deficient DCs exhibit an increase in migration that is associated with sustained Cdc42 activation and increased expression of actin-associated cytoskeleton-organizing proteins. We also demonstrated that ERK1 deletion potentiates DC vaccination and provides a survival advantage in high-grade gliomas. Considering the therapeutic significance of these results, we propose ERK1-deleted DC vaccines as an additional means of eradicating resilient tumor cells and preventing tumor recurrence. *Mol Cancer Ther; 15(8); 1975–87. ©2016 AACR.*

Introduction

High-grade gliomas, particularly glioblastoma multiforme, remain the least curable tumors with a high rate of recurrence and low survival rates (1). Glioblastoma multiforme evade elimination in many ways, particularly by promoting complex neovascularization networks (2) and prohibiting antitumor immunologic surveillance (3). Therapeutic strategies will likely need to target these features from many possible angles to successfully eliminate tumors and prevent their recurrence. Feasible approaches include restoring, promoting, and maintaining natural antitumor immune responses through immune cell therapies such as dendritic cell (DC) vaccines (4).

DCs are potent antigen-presenting cells that have been shown to initiate adaptive immune responses. DC-based immunotherapies are being pursued as potential tools in curing glioblastoma multiforme. DCs loaded with patient-derived tumor antigens have been investigated in early clinical trials that have yielded a therapeutic proof-of-principle (5). However, multiple phase III trials have not yet demonstrated a clear superiority of DC vaccination over standard chemotherapy, even though they have prolonged the median and overall survival (OS) rate of patients (4). Taking advantage of the full therapeutic potential of DC vaccines will require a better understanding of their role in eliminating tumor tissue. A major limiting factor in DC vaccinations is the small proportion of DCs (fewer than 5%) that reach draining lymph nodes (LN) following administration (6). This might hamper their therapeutic efficacy. Noninvasive methods such as MRI are, therefore, necessary to study DC migration as measure of therapy outcome and might help identify strategies overcoming the poor DC migration observed in patients (6).

ERK MAP kinases have been shown to control cell migration by regulating cytoskeletal and focal contact dynamics (7). In myeloid DCs, persistent ERK activation leads to a reduced migration of DCs, while ERK inhibition is associated with a higher migratory phenotype (8). Notably, ERK activation prevented immune cell infiltration in the articular capsule in autoimmune arthritis (9). Most studies have validated the role of ERK1 in combination with ERK2; it is however becoming clearer that these isoforms have explicitly different functions (10). When we specifically studied ERK1 in a model of neuroinflammation using bone marrow chimeras, we observed an increased infiltration of $CD11c^+$ cells close to inflamed areas in the brain (11). ERK1 thus appears to be an important regulator of DC immunogenicity and its absence precipitates severe brain autoimmunity (11).

Taking these findings into consideration, we hypothesized that ERK1 is an important regulator of DC migration and that its deletion might increase the migratory properties and vaccination efficacy of DCs toward high-grade gliomas. We used high-

[1]Berlin Ultrahigh Field Facility (B.U.F.F.), Max Delbrueck Center for Molecular Medicine in the Helmholtz Association (MDC), Berlin, Germany. [2]Department of Molecular Cell Biology and Gene Therapy, Humboldt-University Berlin and Max Delbrueck Center for Molecular Medicine in the Helmholtz Association (MDC), Berlin, Germany. [3]Department of Pediatrics I, Neonatology, University Hospital Essen, University Duisburg-Essen, Essen, Germany. [4]MRI TOOLs GmbH, Berlin, Germany. [5]Department of Neurology, Heinrich Heine University, Düsseldorf, Germany. [6]University Nice-Sophia Antipolis, Institute for Research on Cancer and Aging of Nice (IRCAN), Nice, France. [7]Department of Cellular Neurosciences, Max Delbrueck Center for Molecular Medicine in the Helmholtz Association (MDC), Berlin, Germany.

Corresponding Author: Sonia Waiczies, Max Delbrueck Center for Molecular Medicine in the Helmholtz Association, Robert Rössle Street, 10, 13125 Berlin, Germany. Phone: 4930-9406-4542; Fax: 4930-9406-4517; E-mail: sonia.waiczies@mdc-berlin.de

doi: 10.1158/1535-7163.MCT-15-0850

resolution proton (^{1}H) and fluorine (^{19}F) MR methods to study the role of ERK1 in tumor progression as well as DC migration. ERK1-deficient mice were more resistant to the development of WT gliomas, and their tumors were highly infiltrated with Fascin^{+} and CD11c^{+} cells. We observed a marked increase in the *in vitro* and *in vivo* migration of *Erk1*$^{-/-}$ bone marrow derived DCs (BMDC). We also showed a marked reduction in tumor size and increase in survival following treatment of WT glioblastoma multiforme mice with *Erk1*$^{-/-}$ DC, which suggests ERK1 deletion in DC vaccines as additional therapeutic strategy against high-grade gliomas.

Materials and Methods

Preparation of retroviral vectors and transduction of murine cells

The production of retroviral vectors MP71-OVA-IRES-GFP and the transduction of GL261 cells and murine T cells are presented in Supplementary Methods.

Mice and glioma animal model

All mice were handled according to the Berlin State review board at the Landesamt für Gesundheit und Soziales (LAGeSo) and internal (MDC) rules and regulations. The following mice were used: *Erk1*$^{-/-}$ mice on C57BL/6 background (12), their wild-type litermates, and Rag1$^{-/-}$/OTI TCR transgenic mice recognizing the OVA-derived cognate peptide SIINFEKL on H2kb. *Erk1*$^{+/+}$ × *tdRFP* and *Erk1*$^{-/-}$ × *tdRFP* mice were generated by intercrossing *Erk1*$^{-/-}$ knockout mice (12) to *ROSA26*^{tdRFP} reporter mice (13) and the F1 generation. Following anesthesia and using stereotactic (David Kopf Instruments) coordinates referenced from bregma, glioma cells (2×10^4 cells in 1 µL) were implanted in the striatum (anteroposterior 1 mm; mediolateral ±1.5 mm; dorsoventral −4 mm).

Dendritic cells

Mouse DCs were prepared from adult C57BL/6 mice as described (11). Briefly, BMDC were generated from femurs of WT or *Erk1*$^{-/-}$ mice. Cells were grown in RPMI1640 medium supplemented with 10% FCS and 30 ng/mL GM-CSF (eBioscience). Cells were replenished with fresh GM-CSF medium every 3 days. On day 9, the fully differentiated BMDC were ready for further experiments.

In vitro migration assays

Murine CD4^{+} T cells were sorted and activated with anti-CD3/anti-CD28 antibodies for 72 hours. For both murine BMDC and T cells, 600 µL of RPMI-1640 with or without recombinant stromal-derived factor CXCL12 (125 ng/mL, R&D Systems) was added to 24-well plates (lower chamber). In some case, MEK inhibitor U0126 at 10 µmol/L was applied 30 minutes before the assay. Hundred µL of cell suspension (2×10^5) was added to an upper chamber consisting of a Transwell polycarbonate insert with 5-µm pore size (6.5 mm diameter; Costar Corning). The cells were then allowed to migrate at 37°C for 3 hours. Cells in the lower chamber were then collected and counted by flow cytometry.

Another method involved an agarose spot assay (14). Briefly, agarose spots with or without 2 µg/mL CCL19 (Peprotech) were placed onto 35-mm glass dishes (MatTek) and BMDC were added for 3 hours. The migration of BMDC under the spots were determined by acquiring and fusing the microscope images for all the fields of views (FOV). Image processing and analysis were done with Fiji (Image J v1.47p).

Flow cytometry

Tumor infiltrating leukocyte (TIL) single-cell suspensions (5×10^5) were stained for 25 minutes at 4°C with fluorescently conjugated antibodies in FACS buffer after blocking low affinity Fcγ receptor with CD16/CD32 antibody (BD Biosciences). The following antibodies were from Biolegend: APC-anti–mouse CD3 (clone: 145-2C11), PE-Cy7-anti–mouse CD11c (clone: N418), Pacific blue-anti–mouse CD8a (clone: RM4-5). For fascin1 (antibodies-online Inc.) staining, cells were fixed 10 minutes with 4% PFA then permeabilized 30 minutes with methanol. Cytometry acquisition was on an LSRFortessa cell analyzer (BD Biosciences) and analysis was done using FlowJo (Tree Star).

Cdc42 GTP loading and immunoblotting

BMDC were treated with CXCL12 (100 ng/mL) for 1 minutes and Cdc42 GTPase activity determined using a pull down and detection kit (Thermo Scientific). Total lysate (20 µg protein) was incubated with a GSTfusion protein, and then analyzed by 12% SDS-PAGE and immunoblotting according to the manufacturer's instructions. Guanosine 5′-O-[γ-thio] triphosphate (GTPγS) nucleotide was used as positive control. Membranes were incubated with secondary antibody and detected as previously described (15).

MRI methods

All *in vivo* MR measurements were performed on a 9.4 Tesla small animal MR system (Biospec 94/20, Bruker Biospin). Mice were anesthetized by inhalation narcosis using 0.5% to 1.5% isoflurane (Baxter), pressurized air and oxygen. Core body temperature was maintained at 37°C. Respiration rate and temperature were monitored using a remote monitoring system (Model 1025, SA Instruments Inc.). For further details on MR methods, please refer to Supplementary Methods.

Isolation and analysis of immune cells from glioma tissue

TILs were isolated as described previously (16). TILs obtained from 3 mice were pooled due to the limited cell number. Briefly, mice were transcardially perfused with PBS. Brain tumor tissue was extracted and mechanically dissociated using glass potter homogenizers (model TT57.1 Roth) into a crude suspension in RPMI 1640 complete media followed by filtering with 40-µm cell strainer (BD Falcon). Cell suspensions were spun on Percoll gradient, centrifuged at 800 g for 20 minutes, collected from the cell interface and washed two times with FACS buffer. For FACS analysis, please refer to Supplementary Methods.

Immunofluorescence microcopy

Mouse brains for sectioning were prepared as described previously (14). Sixteen µm thick brain sections were mounted on glass slides. After blocking, primary antibodies were added overnight at a dilution of 1:50 for CD11c or 1:25 for CD8a (BD Pharmingen) at 4°C. Alexa 488-conjugated goat anti-guanine pig IgG (Invitrogen) or Rhodamine Red-X (Jackson ImmunoResearch) was subsequently applied. All images were taken using a confocal microscope (LSM 710, Zeiss) with a ×20 objective.

For detecting f-actin in BMDC, 1.5×10^5 cells were plated on 1 mg/mL poly-D-lysine (Sigma-Aldrich) coated glass cover slips.

Cells were fixed with 4% PFA, and stained with rhodamine-coupled phalloidin (1:50; Molecular Probes, Invitrogen). Images were taken by inverse fluorescence microscope (Leica) and digitized by Leica DC Viewer 3.2. For detecting fascin1 in BMDC, 2×10^4 cells were plated on glass cover slips. Fixed cells were permeabilized with 0.01% Triton X100. The nuclei were counterstained with Hoechst 33342 (1:1,000, Sigma-Aldrich). Images were taken using a confocal microscope (LSM 710 Zeiss) with a ×40 objective.

Quantification of $CD8^+$ tumor-infiltrating T cells

Immunofluorescent staining sections from two animals of each group (PBS, WT-DC, and $Erk1^{-/-}$ DC treated) of glioma-bearing mice were used for quantification of $CD8^+$ tumor infiltrating T cells. For each section, $CD8^+$ T cells from at least five random fields within the tumor region were counted, each field measuring 1 to 2 mm^2. Cell number from each group were normalized with tumor area. Cell quantification was performed with Fiji (ImageJ v1.47p).

BMDC–T-cell coculture and ELISA

BMDC from WT and $Erk1^{-/-}$ mice (5×10^4), preloaded with either SIINFEKL (1 μg/mL, Biosynthan), full-length EndoGrade ovalbumin protein (1 μg/mL; Hyglos) or OVA-GL261 cell lysate (50 μg protein/ml), were cocultured with 5×10^4 OT1-TCR–transduced T cells (OT1-T cell). PMA (20 ng/mL) and ionomycin (1 μg/mL) were used for positive controls. IFNγ concentration in was determined 24 hours later by enzyme-linked immunosorbent assay (BD Biosciences).

DC vaccination protocol

BMDC from WT and $Erk1^{-/-}$ mice were incubated with GL261 cell lysate (50 μg protein/ml) and after 3 hours, DCs were further matured with 0.5 μg/mL LPS and incubate for 18 hours. On day 3, 7, 10, and 14 following tumor implantation, WT mice were divided into 3 groups and treated by intraperitoneal injections of either PBS or 2×10^6 BMDC (WT BMDC, $n = 10$; $Erk1^{-/-}$ BMDC, $n = 10$; PBS, $n = 10$). Survival studies were performed between different groups and the survival rate was calculated by the Kaplan–Meier method (MedCalc) using log-rank analysis.

Statistical group analysis

All data represent the average of at least triplicate samples. Error bars represent SEM. All data are presented as mean ± SEM. Data were analyzed by the Student t test when compared between 2 groups. When comparing more than 2 groups, one way ANOVA was used in Microsoft Office Excel 2010. For multiple comparisons the Bonferroni correction was applied. The Kaplan–Meier method was used for survival rate using log-rank analysis. The differences were considered statistically significant at *, $P < 0.05$; **, $P < 0.01$; and ***, $P < 0.001$.

Results

Glioma growth is diminished in ERK1-deficient mice

The role of ERK1 in the glioma tumor microenvironment or its indirect impact on tumor progression is unknown. We stereotactically implanted WT GL261 glioma cells in the striatum of either WT or ERK1-deficient ($Erk1^{-/-}$) mice. Using a previously established, high spatial resolution MRI protocol (14), we observed a marked reduction in glioma tumor growth in $Erk1^{-/-}$ compared with WT mouse brains 14 days post implantation (dpi; Fig. 1A, left). Tumor volume was significantly smaller in $Erk1^{-/-}$ mice (9.6 ± 1.1 mm^3) compared with WT mice (18.6 ± 2.1 mm^3; Fig. 1A, right, $P = 0.00172$). The survival rate in $Erk1^{-/-}$ glioma-bearing mice was also markedly improved compared with WT glioma mice (Fig. 1B, $P = 0.0002$). Notably, 2 of 11 $Erk1^{-/-}$ glioma-bearing mice exhibited complete tumor rejection. Altogether, these data indicate that the deletion of ERK1 in the stroma significantly attenuates glioma progression.

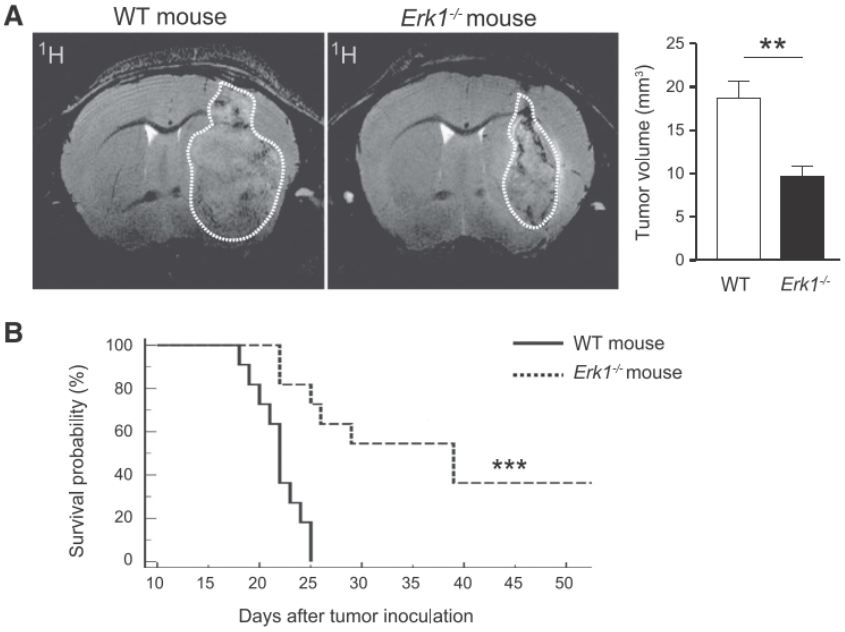

Figure 1.
$Erk1^{-/-}$ mice have a restricted glioma growth. **A,** left, MRI images of glioma-bearing WT and $Erk1^{-/-}$ mice were acquired 14 days following intracranial implantation of 2×10^4 GL261 cells using a 9.4 T animal MR system. Glioma tissue was segmented: White dashed line surrounds tumor area. Right, following segmentation, a volumetric assessment of the glioma tissue was made in WT ($n = 11$) versus $Erk1^{-/-}$ mice brains ($n = 11$). Error bars, mean ± SEM; **, $P < 0.01$. **B,** Kaplan–Meier survival rate curves for both WT ($n = 11$) and $Erk1^{-/-}$ ($n = 11$) glioma-bearing mice. Statistical significance was determined by log-rank testing; ***, $P < 0.001$.

Glioma-induced immune cell infiltration is regulated by ERK1

High-grade gliomas contain brain-infiltrating peripheral immune cells among other cell types (17). We used a ^{19}F MR method (18) to study the way leukocytes leave the circulatory system and infiltrate the tumor site in WT and *Erk1*$^{-/-}$ mice harboring WT gliomas. Before $^{19}F/^{1}H$ MRI, rhodamine-^{19}F nanoparticles (19) were intravenously injected into WT and *Erk1*$^{-/-}$ glioma-bearing mice(18 dpi) to label leukocytes traveling within the blood circulation (Fig. 2A). These cells take up nanoparticles, migrate into the brain, infiltrate glioma tissue (tumor-infiltrating

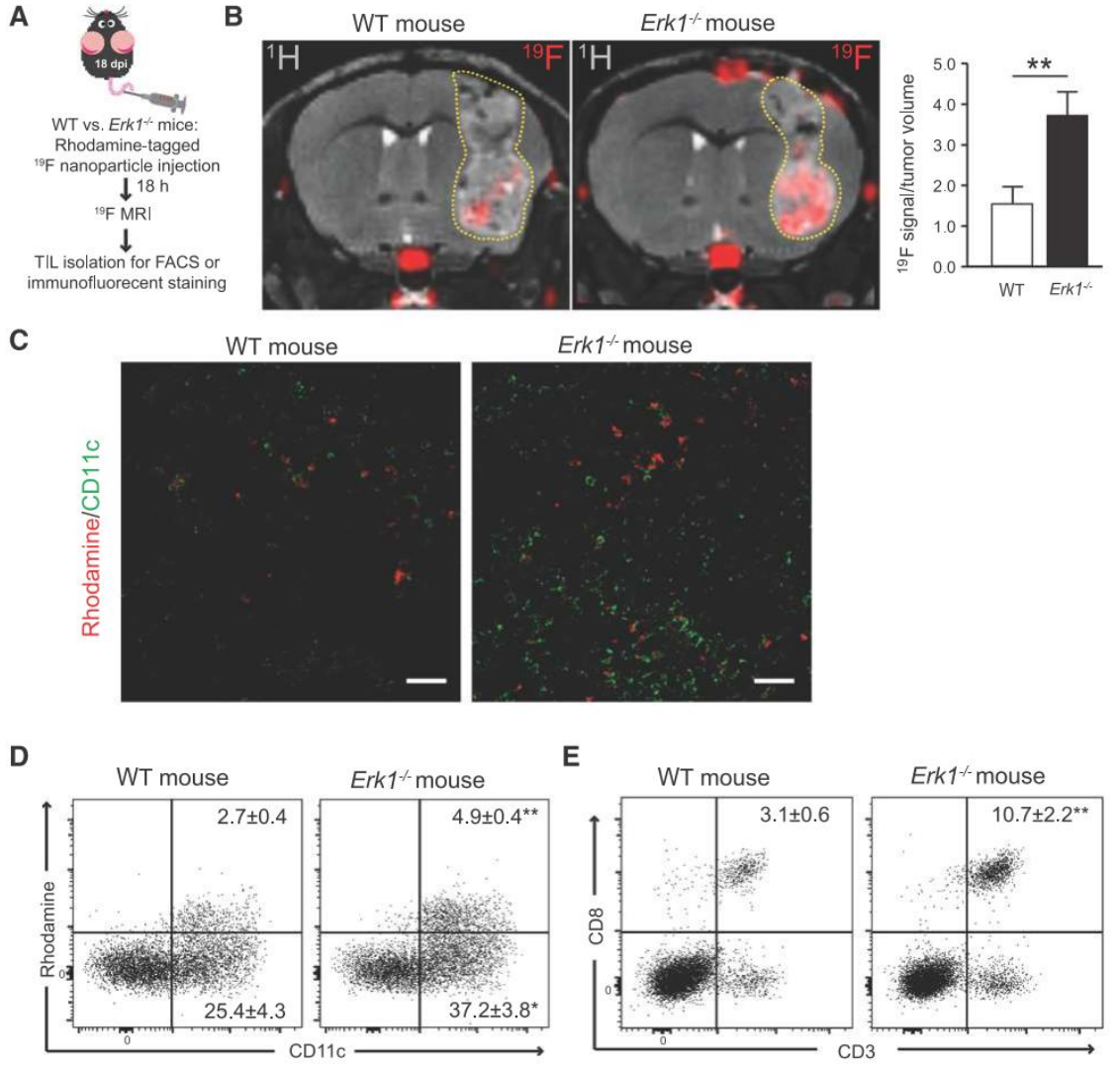

Figure 2.

Erk1$^{-/-}$ mice harbor more glioma-infiltrated leukocytes. **A,** 18 dpi, rhodamine-^{19}F nanoparticles were injected into WT and *Erk1*$^{-/-}$ glioma-bearing mice via tail vein 18 hours before $^{19}F/^{1}H$ MRI. After $^{19}F/^{1}H$ MRI, WT and *Erk1*$^{-/-}$ glioma-bearing mice were perfused to remove excess rhodamine-^{19}F nanoparticles and processed for *ex vivo* FACS or histology analysis. **B,** left, representative $^{19}F/^{1}H$ MRI of glioma-bearing WT and *Erk1*$^{-/-}$ mouse brains. Mouse brain anatomy (^{1}H grayscale image) is shown overlaid with immune cells labeled with rhodamine-^{19}F nanoparticles *in vivo* (^{19}F red pseudocolor image). Yellow dashed line surrounds tumor area. Right, intensity of ^{19}F signal from WT ($n = 8$) and *Erk1*$^{-/-}$ ($n = 8$) glioma-bearing mice was normalized to tumor volume (^{19}F intensity/mm^3); error bars, mean ± SEM; **, $P < 0.01$. **C,** representative immunofluorescent staining of CD11c (green) and rhodamine (red) signal in brain tumor sections of WT or *Erk1*$^{-/-}$ mice, which were injected with rhodamine-^{19}F nanoparticles; bars, 50 μm. **D,** 18 dpi, TILs were isolated from WT and *Erk1*$^{-/-}$ glioma-bearing mice and analyzed by FACS. Representative dot plots of glioma-infiltrating CD11c$^+$ DCs and CD11c$^+$ DCs that also took up rhodamine-^{19}F nanoparticles. The percentage represents the cells from gating of living cells. **E,** representative dot plots of CD3$^+$/CD8$^+$ T cells from infiltrating TILs. All FACS data are representative of five independent experiments with pooled 3 mice per group. Values represent mean ± SEM; **, $P < 0.01$.

leukocytes or TILs) and can then be visualized using ^{19}F MRI. Upon segmentation of the whole tumor region, we calculated a 1.7-fold increase of total ^{19}F signal within tumors in *Erk1*$^{-/-}$ mice compared with WT. Considering the significantly smaller size of these tumors in the *Erk1*$^{-/-}$ mice, we next calculated the ^{19}F signal per tumor volume, which reflects the density of ^{19}F-labeled TILs within the tumor and observed a 2.4-fold ($P = 0.0098$) increase in *Erk1*$^{-/-}$ versus WT glioma-bearing mice (Fig. 2B, right). *Ex vivo* immunofluorescence staining also revealed that higher numbers of CD11c^{+}/^{19}F rhodamine–labeled cells infiltrated the tumor region in *Erk1*$^{-/-}$ brain sections compared with WT controls (Fig. 2C). Flow cytometry of TILs extracted from dissected whole tumor tissue revealed a significant increase in the frequency of CD11c^{+} cells in *Erk1*$^{-/-}$ mice (28.1% in WT and 42.1% in *Erk1*$^{-/-}$ mice, $P = 0.0473$; Fig. 2D). More than 10% of this CD11c^{+} population took up rhodamine-^{19}F particles *in vivo*, representing cells that had infiltrated tumor tissue from the periphery. Notably, the number of CD11c^{+}/^{19}F rhodamine^{+} leukocytes was significantly higher in *Erk1*$^{-/-}$ mice (2.7 ± 0.4% from whole TIL fraction in WT and 4.9 ± 0.4% in *Erk1*$^{-/-}$ mice, $P = 0.0057$; Fig. 2D). Of note, a large proportion of CD11c^{+} cells was rhodamine negative (Fig. 2D), one reason being that CD11c is also expressed on brain resident cells such as microglia; these are abundantly present around the glioma tissue and could still be present after preparation of the tumor tissue for FACS analysis. Other than CD11c^{+}/^{19}F rhodamine^{+} cells, the CD3^{+}/CD8^{+} T cells from whole TIL fraction was also significantly higher in *Erk1*$^{-/-}$ mice compared to WT controls (3.1% ± 0.6% in WT and 10.7% ± 2.2% in *Erk1*$^{-/-}$ mice, $P = 0.0094$; Fig. 2E), although the proportion of CD3^{+}/CD8^{+} T cells that took up ^{19}F rhodamine particles *in vivo* was very low (1%–2% of whole CD3^{+}/CD8^{+} population). This can be explained by the low phagocytic properties of T cells.

Overall, we demonstrate a significantly increased infiltration of CD11c^{+} immune cells and CD3^{+}/CD8^{+} T cells from the periphery into glioma tissue in *Erk1*$^{-/-}$ mice. The recruitment of CD11c^{+} immune cells and cytotoxic T cells into glioma tissue is necessary for an efficient antitumor response (20, 21). Therefore, an increased proportion of immune cells in tumor tissue of *Erk1*$^{-/-}$ mice (Fig. 2D and E) might explain the increased resilience of these mice toward developing gliomas (Fig. 1A) and their significantly increased rate of survival (Fig. 1B).

ERK1 deficiency enhances DC migration

The previous data (Fig. 2) show that a deficiency in ERK1 increases the accumulation of TILs. This is in line with previous findings that ERK activation after pharmacologic inhibition of MEK-1 reduces DC migration toward the chemokines CCL21 (8), CCL19 and CXCL12 (22). However, MEK-1 phosphorylates both ERK1 and ERK2, and these isoforms—despite their striking homology—have explicitly different roles. Considering the role of ERKs, in general, in controlling cell migration (7), we next investigated the role of ERK1 in DC and T-cell migration through *in vitro* migration assays. CXCL12 is highly expressed in brain tumors and is a potent chemoattractant of CXCR4-expressing immune cells, including DCs and T cells (23). A modified Boyden chamber assay revealed that in comparison to WT T cells, *Erk1*$^{-/-}$ T cells exhibit a slight but not significant decrease in migration toward CXCL12 (Fig. 3A). MEK inhibition by UO126 (which inhibits both ERK1 and ERK2 activation) did not affect T-cell migration in WT or *Erk1*$^{-/-}$ T cells. In contrast, *Erk1*$^{-/-}$ BMDC revealed significantly increased migration toward CXCL12 compared with WT BMDC (Fig. 3B). With the application of UO126, BMDC migrated to a slightly but not significantly lower extent toward CXCL12 (Fig. 3B). Migration inhibition following UO126 occurred at equal levels in WT and *Erk1*$^{-/-}$ BMDC.

The chemokine CCL19 plays a key role in the trafficking of DCs into LNs (24). To confirm the role of ERK1 in DC migration, we applied another *in vitro* assay. We observed a significant increase in the numbers (>3 folds, $^{***}P < 0.001$) of *Erk1*$^{-/-}$ BMDC migrating toward CCL19-containing agarose spots 3 hours after plating (Fig. 3C). Considering the increased migration of *Erk1*$^{-/-}$ BMDC toward CCL19, we then studied expression of CCR7 on these cells to determine possible mechanisms for the increased migratory properties. However, we did not observe an increase in CCR7 expression in immature and mature *Erk1*$^{-/-}$ BMDC when compared with WT BMDC (Fig. 3D).

Given that migration is an important feature for DC homing to lymphoid organs (24), we next developed a noninvasive *in vivo* DC migration assay involving ^{19}F/^{1}H MRI and a labeling of BMDC with ^{19}F nanoparticles *in vitro* before their application *in vivo* (25, 26). In a WT mouse, one limb received 5×10^6 WT BMDC intradermally, and the other limb 5×10^6 *Erk1*$^{-/-}$ BMDC. Using this method, we observed an increased migration of ^{19}F-labeled *Erk1*$^{-/-}$ BMDC (compared with WT BMDC) toward WT popliteal LN as shown by the ^{19}F-signal in ^{19}F/^{1}H MRI (Fig. 4A). *Ex vivo* ^{19}F MR spectroscopy of the extracted popliteal LNs (Fig. 4A) revealed at least twice as many ^{19}F-labeled *Erk1*$^{-/-}$ BMDC (26.1×10^3 cells) reach the corresponding LNs compared with WT BMDC (11.8×10^3 cells; $P = 0.028$; Fig. 4B).

We attributed the increase in the *in vivo* ^{19}F signal following *Erk1*$^{-/-}$ BMDC application (Fig. 4A and B) and in *Erk1*$^{-/-}$ gliomas (Fig. 2B and C) to an increase in cell mobilization in tissue. However, an increased ^{19}F-signal could also be the result of an increased ^{19}F nanoparticle uptake by *Erk1*$^{-/-}$ DC, inspite of our previous observations showing that *Erk1*$^{-/-}$ BMDC are more mature than WT BMDC (11). We then measured phagocytosis in BMDC following overnight incubation with ^{19}F nanoparticles (same protocol as for the *in vivo* experiments) by performing ^{19}F MR spectroscopy. We did not observe any significant differences between WT and *Erk1*$^{-/-}$ BMDC to take up ^{19}F nanoparticles (Fig. 4C). We also did not observe any influence of the ^{19}F nanoparticles themselves to significantly alter the phagocytic or migratory properties of both WT and *Erk1*$^{-/-}$ BMDC (data not shown).

ERK1 controls cytoskeletal changes in DCs

The Rho GTPase Cdc42 is a master regulator of DC polarity, and is thus necessary for processes such as the reorientation of the microtubule-organizing center during endocytosis (27) and leading-edge coordination as decisive factors for DC motility *in vivo* (28). Interestingly, DCs have been shown to downregulate Cdc42 activity following activation (27). To determine ERK1's effects on Cdc42 regulation during DC migration, we performed Cdc42 activity assays in *Erk1*$^{-/-}$ and WT BMDC. Surprisingly, although Cdc42 activity was downregulated in WT BMDC, this was not the case for *Erk1*$^{-/-}$ BMDC following stimulation with CXCL12 chemokine (Fig. 5A).

Altogether our findings (Figs. 3 and 5A and B) suggest that DC polarization is increased in the absence of ERK1. We thus measured filamentous actin (f-actin) in BMDC by FACS and found larger quantities of f-actin in *Erk1*$^{-/-}$ BMDC compared with WT BMDC (Fig. 5B).

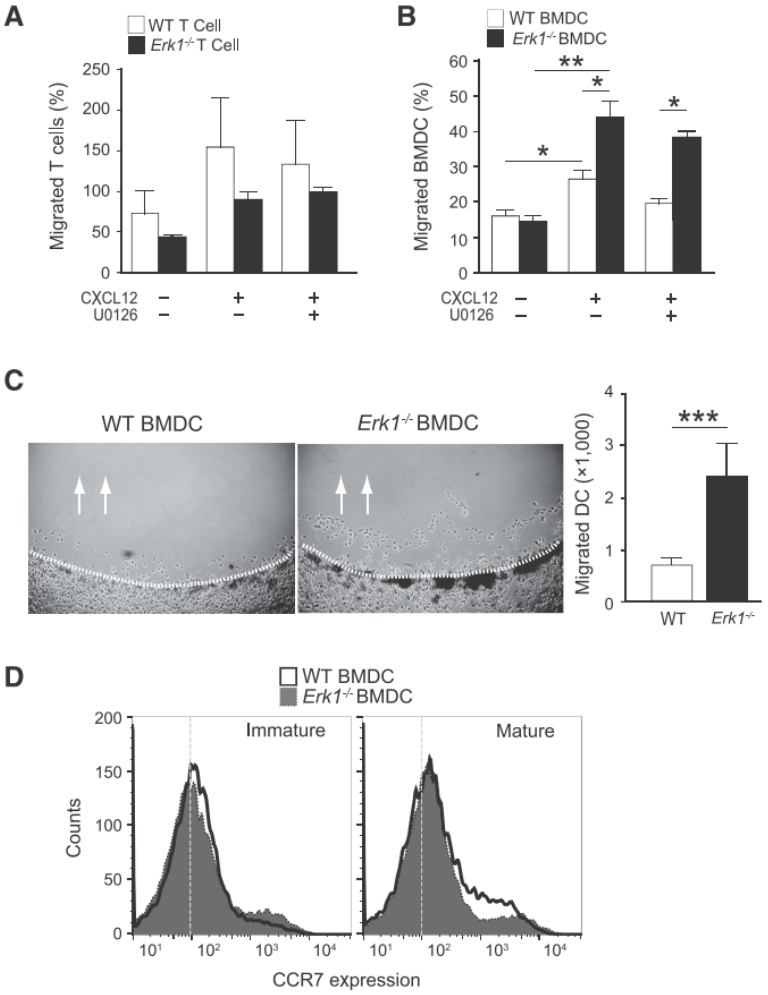

Figure 3.
ERK1 deficiency leads to increased DC migration *in vitro*. **A,** WT or *Erk1*$^{-/-}$ T-cell migration toward CXCL12 was tested using a modified Boyden chamber. **B,** WT or *Erk1*$^{-/-}$ BMDC migration was also measured using the same method; bars, mean ± SEM; *, $P < 0.05$; **, $P < 0.01$. **C,** histogram overlay of CCR7 expression in WT or *Erk1*$^{-/-}$ BMDC as measured by flow cytometry before and after maturation with LPS. **D,** representative light microscopic images of WT or *Erk1*$^{-/-}$ BMDC (1×10^6 per plate) migrating toward CCL19. White dashed-lines represent the edge of agarose spot. White arrows depict the migration direction. Right, quantified data from at least three independent experiments and at least 2 agarose spots per group; error bars, mean ± SEM; ***, $P < 0.001$.

The large cytoskeletal protein talin is an adaptor protein associated with actin filaments and is required for actin polymerization. Immunofluorescence microscopy revealed an increase in cytoskeletal protrusions and a denser expression of f-actin and talin in *Erk1*$^{-/-}$ BMDC, particularly within the intracellular compartment (Fig. 5C). This indicates a higher level of cytoskeleton organization in *Erk1*$^{-/-}$ BMDC and might explain our observations of an increase in their motility and migratory potential *in vitro* (Fig. 3) and *in vivo* (Fig. 4). Furthermore, the actin-bundling protein fascin1 is selectively expressed on DCs upon maturation (29) and is critical for the assembly of filopodia, thereby increasing cell motility (30). As shown in Fig. 5D (top row), immature BMDC expressed lower levels of fascin1 in WT and *Erk1*$^{-/-}$ BMDC. Upon LPS-induced maturation, fascin1 expression was upregulated, an effect that was more pronounced in *Erk1*$^{-/-}$ compared with WT BMDC (Fig. 5D, bottom row).

Our data indicate that in contrast with WT BMDC, *Erk1*$^{-/-}$ BMDC maintain a high level of Cdc42 activity following activation and exhibit an abundantly polymerized cytoskeleton with fully assembled filopodia. This might aid the infiltration of DCs into tumor tissue (Fig. 2C and D). We also investigated the expression of fascin1 in CD11c$^+$ cells that infiltrated glioma tissue. In glioma-bearing *Erk1*$^{-/-}$ mice, the number of fascin1-expressing CD11c$^+$ DCs in TILs isolated from dissected glioma tissue (18 dpi) was significantly higher than that from glioma tissue from WT mice (Fig. 5E, $P = 0.00334$). These data provide further evidence of increased DC migration in the absence of ERK1, which could indicate a more potent antitumor response in ERK1-deficient DCs.

ERK1 deficiency does not influence DC–T-cell interaction

A successful immune response to tumors depends on an effective crosstalk between DCs and T cells in priming tumor-specific CD8$^+$ T cells (31). Since Cdc42-associated pathways are also necessary for microtubule-organizing center reorientation in DCs during antigen presentation to T cells (32), we investigated whether *Erk1*$^{-/-}$ BMDC mount a more potent antitumor T-cell response. To explore this, we generated OVA-GL261 and transduced T cells with a T-cell receptor (TCR) that specifically recognizes OVA-derived peptide

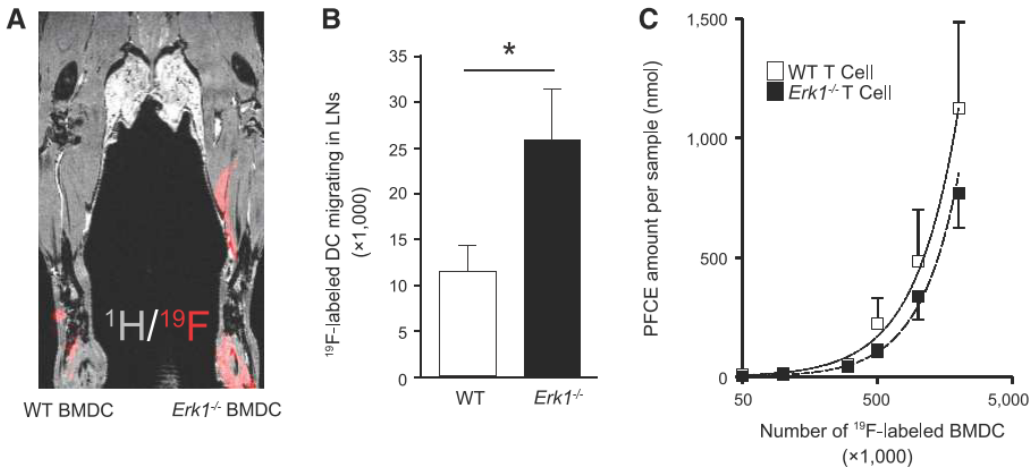

Figure 4.
ERK1 deficiency leads to increased DC migration *in vivo*. **A,** WT and *Erk1*$^{-/-}$ BMDC labeled with ^{19}F nanoparticles were injected in the left (WT BMDC) and right (*Erk1*$^{-/-}$ BMDC) footpad of WT mouse ($n = 13$) and their migration toward the popliteal LNs imaged by ^{19}F/^{1}H MRI after 4 hours. Mouse lower limb anatomy (^{1}H grayscale image) is shown overlaid with BMDC labeled with ^{19}F nanoparticles (^{19}F red pseudocolor image). **B,** after ^{19}F/^{1}H MRI, both popliteal LNs were harvested and the number of ^{19}F-labeled BMDC quantified by ^{19}F MR spectroscopy (MRS) of LNs and BMDC calibration samples. ^{19}F MR spectroscopy demonstrated significantly more ^{19}F-labeled DCs migrating in LNs for *Erk1*$^{-/-}$ BMDC versus WT BMDC; error bars, mean ± SEM; *, $P < 0.05$. **C,** the phagocytic properties of WT and *Erk1*$^{-/-}$ BMDC toward ^{19}F nanoparticles were compared by measuring the ^{19}F signal using ^{19}F MR spectroscopy for both groups in a calibration curve ranging from 5×10^4 to 5×10^6 BMDC.

in the context of MHC I (H-2Kb; please refer to Supplementary Methods). To test the specificity of the OVA-GL261 system, we stereotactically implanted OVA-GL261 cells into the striatum of WT mice and OT1 mice (CD8 T-cell TCR-transgenic recognizing OVA). Fourteen days following tumor cell inoculation, MRI revealed OVA-GL261-induced glioma formation in the WT mice (Fig. 6A, left) but no sign of tumor formation in the OT1 mice (Fig. 6A, right). This confirmed the tumorigenicity of the OVA-GL261 glioma cells and efficient antigen recognition by OT1 T cells.

We next investigated the capacity of *Erk1*$^{-/-}$ BMDC to cross-prime T cells. BMDC were isolated from WT and *Erk1*$^{-/-}$ mice and then pulsed with various antigens (LPS, OVA peptide, or OVA-GL261 lysate). After coculture with OT1-transduced T cells, we measured the secretion of IFNγ by ELISA. Secretion of IFNγ has been proven to reflect both the extent of DC-mediated T-cell cross-priming as well as cytotoxic properties of tumor antigen-specific CD8$^+$ T cells (33). We did not observe any differences between the capacity of WT and *Erk1*$^{-/-}$ BMDC to prime IFNγ secretion in tumor-specific T cells (Fig. 6B).

Antitumor activity of ERK1 deficient DC vaccines against high-grade glioma

Brain tumor regression requires the recruitment of functional DCs into the glioma microenvironment (20). Because we observed a higher migratory potential of *Erk1*$^{-/-}$ BMDC *in vivo*, we next asked whether ERK1 deficiency might have a beneficial impact on DC vaccination in glioblastoma multiforme. To examine the therapeutic efficacy of *Erk1*$^{-/-}$ BMDC, we vaccinated glioma-bearing mice twice a week with WT or *Erk1*$^{-/-}$ BMDC, which were pulsed with GL261 lysate, and performed ^{1}H MRI 18 dpi (Fig. 7A). Tumors in both WT BMDC-treated mice and *Erk1*$^{-/-}$ BMDC-treated mice were smaller than those in PBS-treated glioma-bearing mice (Fig. 7B, right), although tumors in the *Erk1*$^{-/-}$ BMDC-treatment group showed a greater difference in size (8.4 ± 2.9 mm^3, compared with 30.9 ± 2.8 mm^3 for the PBS-treated group; $P = 0.000035$) than the *Erk1*$^{-/-}$ BMDC treatment group (20 ± 5 mm^3, compared with 30.9 ± 2.8 mm^3 for the PBS-treated group; $P = 0.0803$). No significant difference in size was observed between the *Erk1*$^{-/-}$ and WT BMDC-treated mice. Consistent with previous observations made in glioma-bearing mice (34), mice receiving WT BMDC pulsed with GL261 lysate exhibited significantly enhanced survival when compared with untreated PBS controls ($P = 0.0019$; Fig. 7C). Furthermore, in line with a markedly decreased tumor size, we documented significantly improved survival probability in glioma-bearing mice receiving *Erk1*$^{-/-}$ BMDC compared with those of untreated mice ($P = 0.0005$; Fig. 7C). However, no significant difference in survival was observed between *Erk1*$^{-/-}$ and WT BMDC-treated mice.

We next wanted to study the distribution of both *Erk1*$^{-/-}$ and WT BMDC in the glioma model following intraperitoneal application (Fig. 7D). For this, we used BMDC that were derived from either (*Erk1*$^{-/-}$ × *tdRFP*) mice or [*Erk1*$^{+/+}$(WT) × *tdRFP*] littermate control mice. Although we could not detect any of the injected RFP BMDC (both WT and *Erk1*$^{-/-}$) in the brain of glioma mice 21 dpi, we observed a significant increase in CD11c$^+$ RFP$^+$ BMDC in the lymph nodes of mice treated with (*Erk1*$^{-/-}$ × *tdRFP*) BMDC when compared to mice treated with [*Erk1*$^{+/+}$(WT) × *tdRFP*] BMDC (Fig. 7D). These results in the glioma model are in line with our *in vitro* assays (Fig. 3) and *in vivo* experiments in WT healthy mice (Fig. 4A).

Although we could not detect any of the intraperitoneally administered (WT or *Erk1*$^{-/-}$) BMDC in the brain of glioma-bearing mice, we observed differences in the expression of tumor-infiltrating CD8$^+$ T cells between the different treatment groups

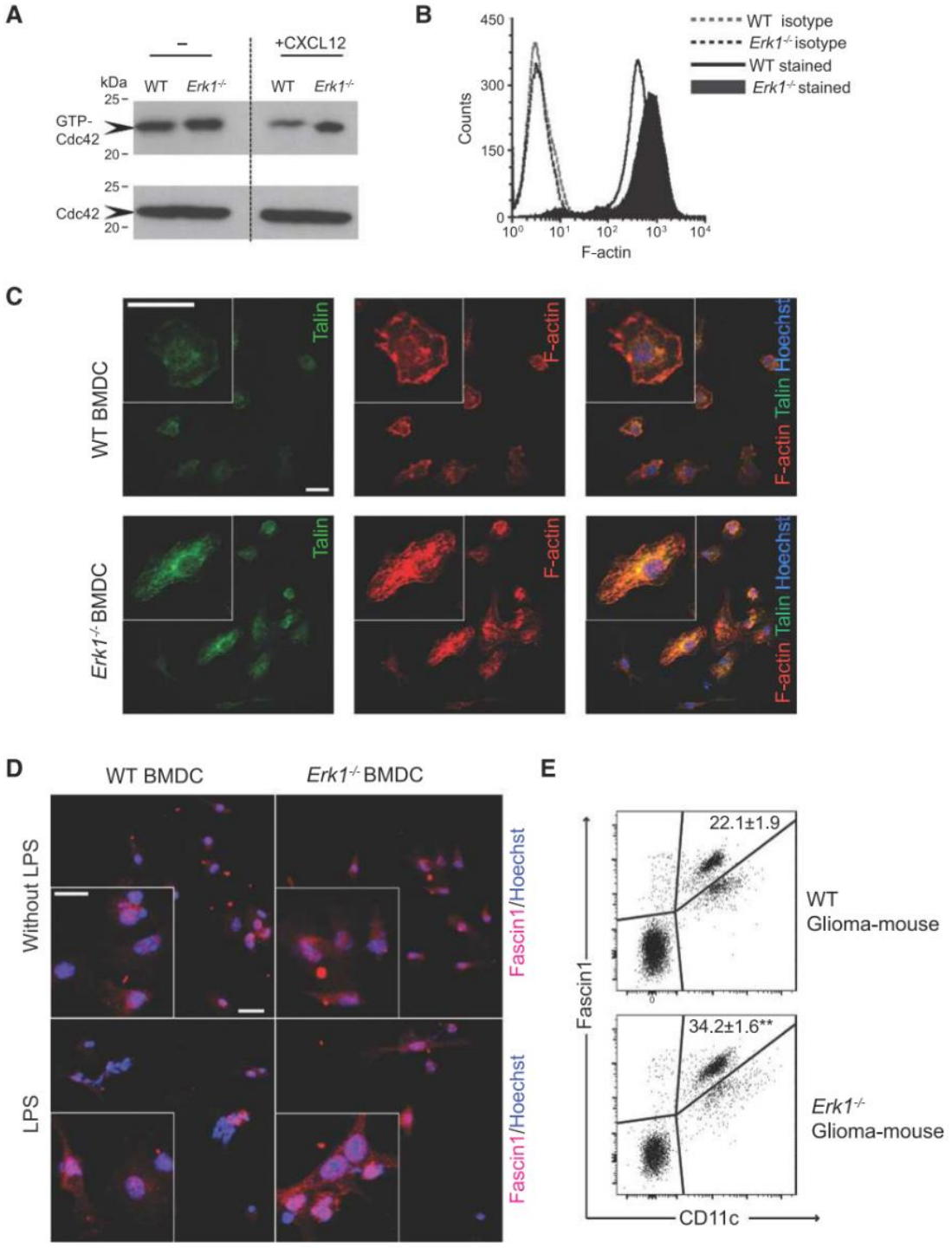
A
–
+CXCL12
kDa
WT
Erk1-/-
WT
Erk1-/-
25
GTP-Cdc42
20
25
Cdc42
20
B
450
300
150
0
Counts
10^0
10^1
10^2
10^3
10^4
F-actin
WT isotype
Erk1-/- isotype
WT stained
Erk1-/- stained
C
WT BMDC
Erk1-/- BMDC
Talin
F-actin
F-actin Talin Hoechst
D
WT BMDC
Erk1-/- BMDC
Without LPS
LPS
Fascin1/Hoechst
E
22.1±1.9
34.2±1.6**
WT
Glioma-mouse
Erk1-/-
Glioma-mouse
Fascin1
CD11c

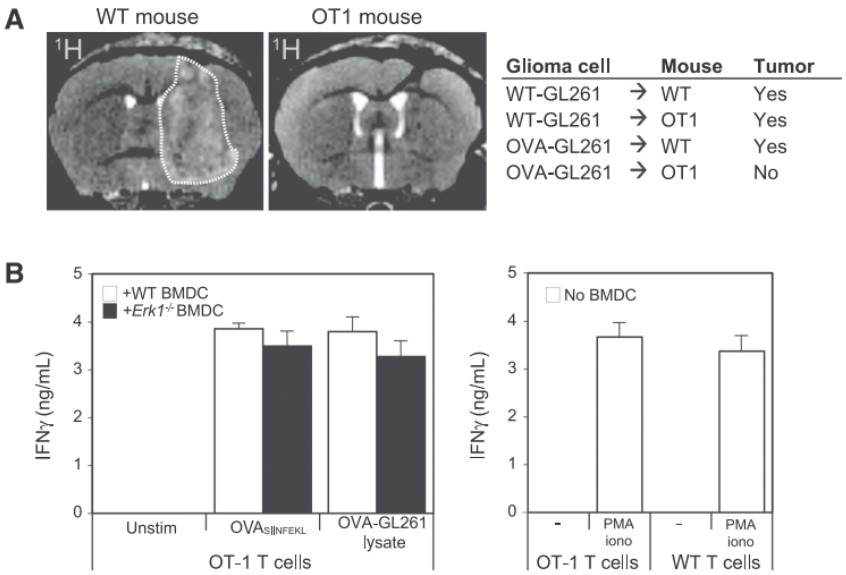

Figure 6.
Antigen-specific T-cell activation in *Erk1*$^{-/-}$ BMDC remains unaltered. **A,** MRI images show OVA specificity: OVA-GL261 cells were inoculated in WT ($n = 3$) or OT1 transgenic mice ($n = 6$) and tumor growth was monitored by ^{1}H MRI on 14 dpi. White dashed-line surrounds tumor area in WT mouse. WT-GL261 transplanted in both WT mice ($n = 3$) and OT1 transgenic mice ($n = 3$) served as control (right). **B,** WT and *Erk1*$^{-/-}$ BMDC were treated with OVA$_{SIINFEKL}$ peptide or OVA-GL261 cell lysate and then cocultured with OT1-transduced T cells. OT1-T cells and nontransduced (WT) T cells were also cultured with PMA plus ionomycin as positive control for IFNγ production (right). Serving as negative controls (but are not shown) were nontransduced WT T cells activated by WT and *Erk1*$^{-/-}$ BMDC loaded with OVA$_{SIINFEKL}$ peptide or OVA-GL261 cell lysate, as well as untreated BMDC and LPS-treated BMDC. IFNγ production was measured by ELISA. Data are representative of three independent experiments; bars, mean ± SEM.

(Fig. 7E). Although tumor sections demonstrated visibly smaller tumors when treated with BMDC, the number of CD8$^+$ T cells was significantly increased in sections derived from mice treated with WT BMDC compared with PBS-treated groups (1,359 ± 39 cells/mm^2 and 716 ± 24 cells/mm^2, respectively; $P = 0.001$). The infiltration of CD8$^+$ cells was further enhanced when treating mice with *Erk1*$^{-/-}$ BMDC (1,920 ± 49 cells/mm^2; $P = 0.02$ when compared with WT BMDC; Fig. 7E).

Discussion

In this report, we identify ERK1 as a regulator of DC migration and show that the introduction of DCs lacking ERK1 lead to a significant reduction in tumor growth as well as improved survival of glioma-bearing mice.

DCs need to actively migrate between lymphatic tissue and interstitial spaces to initiate adaptive immune responses. Here, we demonstrate that ERK1 plays a crucial role in the migratory capacity of DCs. This key ERK–MAPK intracellular signaling pathway transduces a broad range of extracellular stimuli into important biologic responses, including cell survival, proliferation, differentiation, and the regulation of DCs (9, 35) and T cells (36). The specific role of ERK1 has been studied in T cells and it was shown that ERK1 does not appear to play a direct role on the effector function of antigen-specific T cells, notwithstanding increased susceptibility toward T-cell–mediated autoimmunity (37). In DCs, ERK1 inhibits cytokine production following their stimulation by TLRs (38) and reduces surface receptors (11), which in turn affects the priming of naïve T cells toward an effector phenotype during autoimmunity (11). Most studies of tumor pathology have not distinguished ERK1 from ERK2 function, due to the assumption that they have compensatory effects (39). However, in some biologic contexts the distinction between these two kinases appears to be crucial,

Figure 5.
Erk1$^{-/-}$ BMDC display a more polarized cytoskeleton. **A,** activity of Cdc42 GTPase of WT and *Erk1*$^{-/-}$ BMDC that were untreated or pretreated with CXCL12 was determined by pull-down assay and consecutive Western blot analysis ($n = 4$). **B,** expression of intracellular f-actin on WT (solid line) or *Erk1*$^{-/-}$ (filled black histogram) BMDC as assessed by FACS. Dashed line histograms depict control staining with anti-mouse IgG. Data represent four independent experiments. **C,** immunofluorescence staining of talin (green, left column), f-actin (red, middle) and Hoechst 33342 nuclei (blue, right) on WT and *Erk1*$^{-/-}$ BMDC attached to glass coverslips; bar, 10 μm. **D,** immunofluorescence staining of fascin1 (red) on WT and *Erk1*$^{-/-}$ BMDC without (top row) and with LPS stimulation (bottom row). Data represent three independent experiments; bar, 25 μm. **E,** representative dot plots of glioma-infiltrating fascin1-expressing CD11c$^+$ DC as determined by FACS. TILs were isolated from WT and *Erk1*$^{-/-}$ glioma-bearing mice on 18 dpi. Data represent five independent experiments. Values represent mean ± SEM; **, $P < 0.01$.

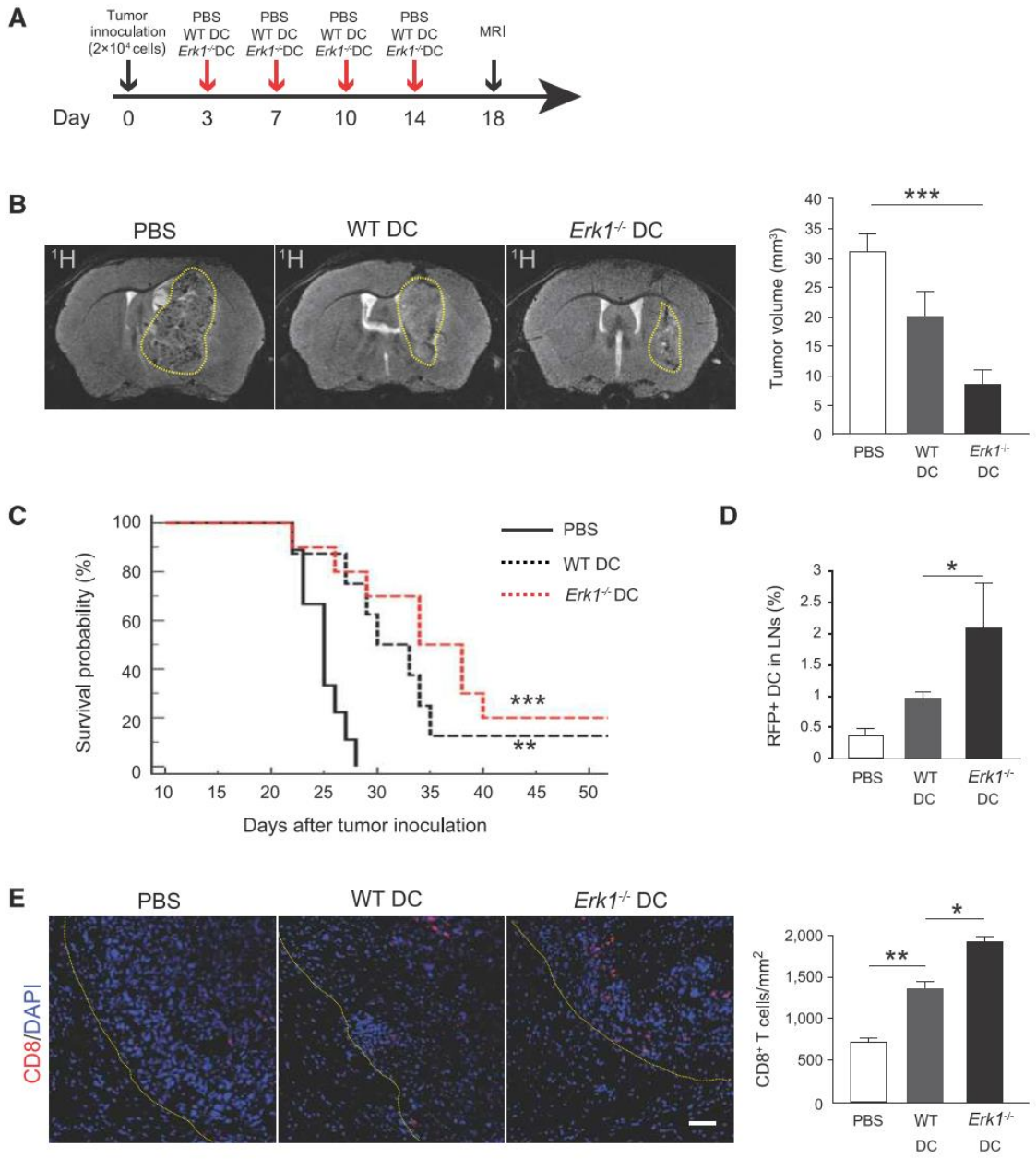

Figure 7.

Erk1$^{-/-}$ BMDC improve immunotherapy against high-grade glioma. **A,** schematic representation of DC vaccination protocol in glioma-bearing mice. **B,** WT and *Erk1*$^{-/-}$ BMDC (2×10^6) loaded with 50 μg GL261 cell lysate and activated with LPS were administered to glioma-bearing WT mice via intraperitoneal injection 3, 7, 10, and 14 dpi. Mice receiving PBS intraperitoneal injections served as negative control. Tumor growth was validated 18 dpi by MRI. Data are representative of three independent experiments with at least 3 animals per group; bars, mean ± SEM; ***, $P < 0.001$. **C,** Kaplan–Meier survival curves were plotted for PBS ($n = 10$), WT BMDC ($n = 10$), and *Erk1*$^{-/-}$ BMDC ($n = 9$)-treated glioma animal groups. Statistical significance was determined by log-rank testing (**, $P < 0.01$, WT BMDC vs. PBS; ***, $P < 0.001$, *Erk1*$^{-/-}$ BMDC vs. PBS). **D,** at 21 dpi, lymphocytes were isolated from glioma-bearing mice and analyzed for RFP$^+$ cells by FACS. All FACS data are from two independent experiments with 3 mice per group. Values represent mean ± SEM; *, $P < 0.05$. **E,** representative immunofluorescent staining of CD8a (red) and DAPI (blue) signal in brain tumor sections of WT mice, which were receiving either PBS, WT BMDC or *Erk1*$^{-/-}$ BMDC; bar, 50 μm. Yellow dashed-lines represent the edge of tumor. Right, shows quantified cell number from two independent experiments with 2 animals per group; bars, mean ± SD; *, $P < 0.05$; **, $P < 0.01$.

considering that ERK2-deficient mice are embryonically lethal (40) in contrast with ERK1-deficient mice, which are viable and fertile (12). Here we report for the first time a role for ERK1 in negatively regulating the migration specifically of DCs by showing a significant increase in migration in *Erk1*$^{-/-}$ BMDC, both in *in vitro* and *in vivo* experiments. *In vitro*, we distinguished between the impact of ERK1 on BMDC and effector T cells. Although ERK1 is expressed in both cell types, its role in migration was more pronounced in DC than in T cells. Furthermore, while ERK1 deletion promoted DC migration, application of a MEK inhibitor (U0126) inhibited DC migration. As U0126 inhibits both ERK1 and ERK2 activation, this might have masked the increase in migration we observe in the absence of ERK1 and could furthermore explain discrepancies in earlier studies using inhibitors to ascertain the signals' roles in migration-related processes (41).

Migratory phenotypes typically involve mechanisms related to cytoskeletal organization and structure, so we studied this aspect of ERK1's influence. We showed that ERK1 influences the cytoskeleton and associated adaptor and actin-bundling proteins such as talin and fascin1, another strong piece of evidence for a role of ERK1 in the regulation of DC migration. We chose fascin1 as a marker for DCs in the tumor tissue, because CD11c^{+} is not an exclusive marker for these cells in brain gliomas: CNS resident and nonresident immune cells such as peripheral macrophages (42) are also CD11c^{+}. Importantly, fascin1 is not expressed on activated microglia (43) and peripheral blood cells, including macrophages and neutrophils (44).

A role for ERK1 in DC migration is additionally supported by our finding that ERK1 deletion promotes Cdc42 activation, because Cdc42 is responsible for leading edge coordination *in vivo* (28). Notwithstanding the role of Cdc42 in DC polarity and orientation during antigen presentation to T cells (32), *Erk1*$^{-/-}$ DCs did not present OVA-GL261 (as model–tumor antigen) to T cells more effectively than WT DCs. This excludes tumor antigen presentation as an underlying mechanism for the decreased susceptibility of *Erk1*$^{-/-}$ mice to develop gliomas and for the increased infiltration of T cells in WT gliomas in these mice compared with WT mice. The observation indicates that the benefits of ERK1 deficiency in reducing the growth of gliomas likely derive from an ultimate increase in immune cell surveillance in the glioma tissue as shown by an increase in CD11c^{+} leukocytes, fascin1^{+} DCs and CD8^{+} T cells in *Erk1*$^{-/-}$ glioma-bearing mice as well as increase in CD8^{+} T cells in *Erk1*$^{-/-}$ BMDC-treated glioma-bearing mice. From our results, we believe that ERK1 deficiency is better adapted for providing a higher availability/localization of BMDC in the periphery rather than increasing tumor antigen presentation, and therefore priming of antigen-specific cytotoxic T cells. Although we did not detect the administered *Erk1*$^{-/-}$ BMDC in the tumor tissue following therapeutic application in the glioma model, we did observe a significantly increased proportion of *Erk1*$^{-/-}$ RFP^{+} cells in the LNs and an increased CD8^{+} population of T cells infiltrating the tumor tissue.

Ultimately, improved immune cell surveillance would also augment the reactivation and expansion of cytotoxic T cells within tumor-relevant sites. Our results suggest that the significant reduction in glioma growth by *Erk1*$^{-/-}$ BMDC in contrast with WT BMDC could be the result of an improvement in the delivery of *Erk1*$^{-/-}$ BMDC to the lymphatic tissue, which eventually results in a larger infiltration of CD8^{+} T cells into the tumor tissue. A recent NIH-funded clinical trial found that improving the LN homing of DCs in glioblastoma multiforme patients significantly enhances the therapeutic efficacy of tumor antigen-loaded DCs (45). Their finding and our study suggest that monitoring DC migration might deliver a predictive readout for the effectiveness of DC vaccines.

Here, we used ^{19}F MR to do this, and although still in early clinical development (46), it might offer significant advantages in the future over other methods to track DC migration such as scintigraphy combined with radioisotope ^{111}In-oxine (47). MRI in general was shown to be better at localizing DC vaccines *in vivo* (48); paramagnetic iron oxide nanoparticles were used to label and follow cells in melanoma patients (48). Even though this represented a major step forward in the tracking of DCs, lower image contrast often makes it difficult to distinguish MRI signal hypointensities originating from magnetically labeled cells from hypointensities caused by endogenous factors (e.g., deoxygenated blood). ^{19}F MR-based methods were simultaneously introduced in animal models to overcome these hurdles in cellular MR imaging (25).

The elegance of ^{19}F MR lies in the fact that it provides background-free images in mammals and permits a highly selective detection of cells *in vivo* throughout the organism's body (49). The main hurdle is signal sensitivity, which can pose a challenge when imaging ^{19}F-labeled DCs in cancer patients (46). In a recent report, we aimed to promote the signal achieved per unit cell; we enriched ^{19}F nanoparticles with the phosphatidylethanolamine DPPE and observed a stronger enhancement of ^{19}F signal (from 74 to 771 nmol) per 10^6 cells, which equates to an order of magnitude increase in ^{19}F spins from 0.89×10^{12} ^{19}F spins (control nanoparticles) to 0.93×10^{13} ^{19}F spins (in DPPE-enriched nanoparticles) per DC unit (19). In the present study, we made use of the recently developed ^{19}F marker (19) to label and track DCs *in vivo* with greater sensitivity and to determine the role of ERK1 in DC migration.

We can follow the ^{19}F signal from DCs that we had administered and showed that *Erk1*$^{-/-}$ DCs migrate more readily than WT DCs into popliteal LNs. We also quantified the ^{19}F signal and thereby the number of DCs in draining LNs by *ex vivo* ^{19}F MRS and observed a significant increase in the number of *Erk1*$^{-/-}$ DCs compared with WT DCs that appeared in the corresponding draining LNs. Although further developments in ^{19}F MR will be needed to expand its use in clinical applications (50), it is a valuable tool to monitor DC homing in cancer therapy and to effectively interpret the *in vivo* distribution of DCs as a means of assessing the effectiveness of these therapies in glioblastoma multiforme patients. The advent of cryogenically cooled MR detectors (51) will help boost ^{19}F MR sensitivity and lower detection levels of ^{19}F-labeled cells to facilitate *in vivo* cell tracking within shorter scan times.

Here, we identified ERK1 as a molecular player that negatively regulates the mobility of DCs and their capacity to eliminate malignant gliomas. The results were demonstrated in a preclinical mouse glioblastoma multiforme model and further studies will be required to predict the safety, efficacy and potential benefits of *Erk1*$^{-/-}$ DC vaccines in human high-grade or recurrent gliomas. It should be noted that *Erk1*$^{-/-}$ BMDC, although significantly reducing glioma growth in comparison with untreated controls, were not significantly different to WT BMDC ($P = 0.05196$), even though WT BMDC did not show significant differences to untreated controls. Furthermore, statistically significant treatment effects

with regard to survival were observed by both *Erk1*$^{-/-}$ BMDC ($P < 0.001$) and WT BMDC ($P < 0.01$) groups. One caveat in this study was that treatment was terminated at day 14 and not later as has been done in other glioma studies (52). Future studies, perhaps using more advanced ^{19}F MR methods, should aim at studying changes in therapeutic efficacy when using different treatment schedules that extend over more than two weeks. The present study was restricted to the role of ERK1 against glioblastoma multiforme. Effective therapies will likely need to target the tumor from many different angles, employing several approaches toward tumor cell elimination while preserving sufficient natural antitumor immune responses. Other strategies such as the preconditioning of application sites with recall antigen to promote DC vaccination in humans and mice (45), as recently reported further emphasizes the need to promote DC migration as a means of optimizing DC vaccines. As negative regulator of DC migration, ERK1 appears to be an attractive target for deletion in genetically modified vaccines. Other possible molecular targets include molecules such as IRF4 (53) and CD37 (54), which favor DC migration. It has now become practical to apply simultaneous gene silencing and retroviral transgenic insertion; such combinations have proven to be highly effective (55, 56). *Ex vivo* gene silencing in immune cell therapeutics using both viral- and nonviral-based approaches has been an area of intensive research in clinical trials during the last decade (57)

In summary, our study presents ERK1 as one target for manipulating DC vaccines to promote their migration in an animal model of glioblastoma multiforme. Furthermore, this study underscores the benefits and needs of using ^{19}F MRI to measure *in vivo* cell migration and localization, which are critical parameters in the effectiveness of such vaccines. ERK1 and other molecular targets that enhance DC migration could be important tools in developing next generation of DC vaccines (45). The OS of glioblastoma multiforme patients could well be improved by patient-specific treatment regimens that use immunotherapy based on genetically modified cells in conjunction with standard treatment protocols (surgery, radiotherapy, chemotherapy, and antiangiogenic therapy).

Disclosure of Potential Conflicts of Interest

T. Niendorf has ownership interest (including patents) in MRI TOOLS GmbH. S. Waiczies reports receiving a commercial research grant from Novartis. No potential conflicts of interest were disclosed by the other authors.

Authors' Contributions

Conception and design: M.-C. Ku, M. Günther, C. Martin, S. Waiczies
Development of methodology: M.-C. Ku, I. Edes, I. Bendix, A. Pohlmann, H. Waiczies, C. Martin, S. Waiczies
Acquisition of data (provided animals, acquired and managed patients, provided facilities, etc.): M.-C. Ku, I. Edes, T. Prozorovski, M. Günther, C. Martin, G. Pagès, S.A. Wolf, T. Niendorf, S. Waiczies
Analysis and interpretation of data (e.g., statistical analysis, biostatistics, computational analysis): M.-C. Ku, I. Edes, I. Bendix, A. Pohlmann, M. Günther, C. Martin, H. Kettenmann, T. Niendorf, S. Waiczies
Writing, review, and/or revision of the manuscript: M.-C. Ku, I. Edes, I. Bendix, G. Pagès, S.A. Wolf, H. Kettenmann, W. Uckert, T. Niendorf, S. Waiczies
Administrative, technical, or material support (i.e., reporting or organizing data, constructing databases): M.-C. Ku, I. Edes, I. Bendix, W. Uckert, S. Waiczies

Acknowledgments

The authors thank S. Kox and Y. Balke for assistance with MR measurements and cell culturing, and M. Naschke for assistance with ELISA measurements. The authors also acknowledge the support of the Animal Facilities and the technology platforms for Advanced Light Microscopy and Preparative Flow Cytometry of the Max Delbrück Center for Molecular Medicine. The authors are also grateful to Prof. K. Rajewsky for valuable discussions and scientific writer R. Hodge for support in article editing.

Grant Support

This study was funded by the Deutsche Forschungsgemeinschaft (to S. Waiczies; DFG/WA2804).

The costs of publication of this article were defrayed in part by the payment of page charges. This article must therefore be hereby marked *advertisement* in accordance with 18 U.S.C. Section 1734 solely to indicate this fact.

Received October 20, 2015; revised May 16, 2016; accepted May 23, 2016; published OnlineFirst June 2, 2016.

References

1. Weller M, Cloughesy T, Perry JR, Wick W. Standards of care for treatment of recurrent glioblastoma—are we there yet? Neuro Oncology 2013;15:4–27.
2. Hardee ME, Zagzag D. Mechanisms of glioma-associated neovascularization. Am J Pathol 2012;181:1126–41.
3. Rabinovich GA, Gabrilovich D, Sotomayor EM. Immunosuppressive strategies that are mediated by tumor cells. Annu Rev Immunol 2007;25:267–96.
4. Anguille S, Smits EL, Lion E, van Tendeloo VF, Berneman ZN. Clinical use of dendritic cells for cancer therapy. Lancet Oncol 2014;15:e257–67.
5. Palucka AK, Ueno H, Fay JW, Banchereau J. Taming cancer by inducing immunity via dendritic cells. Immunol Rev 2007;220:129–50.
6. Aarntzen EH, Srinivas M, Bonetto F, Cruz LJ, Verdijk P, Schreibelt G, et al. Targeting of 111In-labeled dendritic cell human vaccines improved by reducing number of cells. Clin Cancer Res 2013;19:1525–33.
7. Webb DJ, Donais K, Whitmore LA, Thomas SM, Turner CE, Parsons JT, et al. FAK-Src signalling through paxillin, ERK and MLCK regulates adhesion disassembly. Nat Cell Biol 2004;6:154–61.
8. Luft T, Maraskovsky E, Schnurr M, Knebel K, Kirsch M, Gorner M, et al. Tuning the volume of the immune response: strength and persistence of stimulation determine migration and cytokine secretion of dendritic cells. Blood 2004;104:1066–74.
9. Arce F, Breckpot K, Stephenson H, Karwacz K, Ehrenstein MR, Collins M, et al. Selective ERK activation differentiates mouse and human tolerogenic dendritic cells, expands antigen-specific regulatory T cells, and suppresses experimental inflammatory arthritis. Arthritis Rheum 2011;63:84–95.
10. Fischer AM, Katayama CD, Pages G, Pouyssegur J, Hedrick SM. The role of erk1 and erk2 in multiple stages of T-cell development. Immunity 2005;23:431–43.
11. Bendix I, Pfueller CF, Leuenberger T, Glezeva N, Siffrin V, Muller Y, et al. MAPK3 deficiency drives autoimmunity via DC arming. Eur J Immunol 2010;40:1486–95.
12. Pages G, Guerin S, Grall D, Bonino F, Smith A, Anjuere F, et al. Defective thymocyte maturation in p44 MAP kinase (Erk 1) knockout mice. Science 1999;286:1374–7.
13. Luche H, Weber O, Nageswara Rao T, Blum C, Fehling HJ. Faithful activation of an extra-bright red fluorescent protein in "knock-in" Cre-reporter mice ideally suited for lineage tracing studies. Eur J Immunol 2007;37:43–53.
14. Ku MC, Wolf SA, Respondek D, Matyash V, Pohlmann A, Waiczies S, et al. GDNF mediates glioblastoma-induced microglia attraction but not astrogliosis. Acta Neuropathol 2013;125:609–20.

15. Waiczies S, Bendix I, Prozorovski T, Ratner M, Nazarenko I, Pfueller CF, et al. Geranylgeranylation but not GTP loading determines rho migratory function in T cells. J Immunol 2007;179:6024–32.
16. Waiczies H, Lepore S, Drechsler S, Qadri F, Purfurst B, Sydow K, et al. Visualizing brain inflammation with a shingled-leg radio-frequency head probe for 19F/1H MRI. Sci Rep 2013;3:1280.
17. Charles NA, Holland EC, Gilbertson R, Glass R, Kettenmann H. The brain tumor microenvironment. Glia 2011;59:1169–80.
18. Flögel U, Ding Z, Hardung H, Jander S, Reichmann G, Jacoby C, et al. *In vivo* monitoring of inflammation after cardiac and cerebral ischemia by fluorine magnetic resonance imaging. Circulation 2008;118:140–8.
19. Waiczies S, Lepore S, Sydow K, Drechsler S, Ku MC, Martin C, et al. Anchoring dipalmitoyl phosphoethanolamine to nanoparticles boosts cellular uptake and fluorine-19 magnetic resonance signal. Sci Rep 2015; 5:8427.
20. Curtin JF, Liu N, Candolfi M, Xiong W, Assi H, Yagiz K, et al. HMGB1 mediates endogenous TLR2 activation and brain tumor regression. PLoS Med 2009;6:e1000010.
21. Candolfi M, King GD, Yagiz K, Curtin JF, Mineharu Y, Muhammad AK, et al. Plasmacytoid dendritic cells in the tumor microenvironment: immune targets for glioma therapeutics. Neoplasia 2012;14:757–70.
22. Li G, Basu S, Han MK, Kim YJ, Broxmeyer HE. Influence of ERK activation on decreased chemotaxis of mature human cord blood monocyte-derived dendritic cells to CCL19 and CXCL12. Blood 2007;109:3173–6.
23. Li M, Ransohoff RM. Multiple roles of chemokine CXCL12 in the central nervous system: a migration from immunology to neurobiology. Prog Neurobiol 2008;84:116–31.
24. Randolph GJ, Angeli V, Swartz MA. Dendritic-cell trafficking to lymph nodes through lymphatic vessels. Nat Rev Immunol 2005;5:617–28.
25. Ahrens ET, Flores R, Xu H, Morel PA. *In vivo* imaging platform for tracking immunotherapeutic cells. Nat Biotechnol 2005;23:983–7.
26. Waiczies H, Lepore S, Janitzek N, Hagen U, Seifert F, Ittermann B, et al. Perfluorocarbon particle size influences magnetic resonance signal and immunological properties of dendritic cells. PLoS ONE 2011;6: e21981.
27. Garrett WS, Chen LM, Kroschewski R, Ebersold M, Turley S, Trombetta S, et al. Developmental control of endocytosis in dendritic cells by Cdc42. Cell 2000;102:325–34.
28. Lammermann T, Renkawitz J, Wu X, Hirsch K, Brakebusch C, Sixt M. Cdc42-dependent leading edge coordination is essential for interstitial dendritic cell migration. Blood 2009;113:5703–10.
29. Yamashiro S. Functions of fascin in dendritic cells. Crit Rev Immunol 2012;32:11–21.
30. Yamakita Y, Matsumura F, Lipscomb MW, Chou PC, Werlen G, Burkhardt JK, et al. Fascin1 promotes cell migration of mature dendritic cells. J Immunol 2011;186:2850–9.
31. Gajewski TF, Schreiber H, Fu Y-X. Innate and adaptive immune cells in the tumor microenvironment. Nat Immunol 2013;14:1014–22.
32. Pulecio J, Petrovic J, Prete F, Chiaruttini G, Lennon-Dumenil A-M, Desdouets C, et al. Cdc42-mediated MTOC polarization in dendritic cells controls targeted delivery of cytokines at the immune synapse. J Exp Med 2010;207:2719–32.
33. Wheeler CJ, Black KL, Liu G, Mazer M, Zhang XX, Pepkowitz S, et al. Vaccination elicits correlated immune and clinical responses in glioblastoma multiforme patients. Cancer Res 2008;68:5955–64.
34. Ni HT, Spellman SR, Jean WC, Hall WA, Low WC. Immunization with dendritic cells pulsed with tumor extract increases survival of mice bearing intracranial gliomas. J Neurooncol 2001;51:1–9.
35. Escors D, Lopes L, Lin R, Hiscott J, Akira S, Davis RJ, et al. Targeting dendritic cell signaling to regulate the response to immunization. Blood 2008;111: 3050–61.
36. Waiczies S, Prozorovski T, Infante-Duarte C, Hahner A, Aktas O, Ullrich O, et al. Atorvastatin induces T-cell anergy via phosphorylation of ERK1. J Immunol 2005;174:5630–5.
37. Nekrasova T, Shive C, Gao Y, Kawamura K, Guardia R, Landreth G, et al. ERK1-deficient mice show normal T-cell effector function and are highly susceptible to experimental autoimmune encephalomyelitis. J Immunol 2005;175:2374–80.
38. Agrawal A, Dillon S, Denning TL, Pulendran B. ERK1$^{-/-}$ mice exhibit Th1 cell polarization and increased susceptibility to experimental autoimmune encephalomyelitis. J Immunol 2006;176:5788–96.
39. Blasco RB, Francoz S, Santamaria D, Canamero M, Dubus P, Charron J, et al. c-Raf, but not B-Raf, is essential for development of K-Ras oncogene-driven non-small cell lung carcinoma. Cancer Cell 2011;19:652–63.
40. Hatano N, Mori Y, Oh-hora M, Kosugi A, Fujikawa T, Nakai N, et al. Essential role for ERK2 mitogen-activated protein kinase in placental development. Genes Cells 2003;8:847–56.
41. Fincham VJ, James M, Frame MC, Winder SJ. Active ERK/MAP kinase is targeted to newly forming cell-matrix adhesions by integrin engagement and v-Src. EMBO J 2000;19:2911–23.
42. Parney IF, Waldron JS, Parsa AT. Flow cytometry and *in vitro* analysis of human glioma–associated macrophages. J Neurosurg 2009;110:572–82.
43. Gao Z, Tsirka SE. Animal models of MS reveal multiple roles of microglia in disease pathogenesis. Neurol Res Int 2011;2011:383087.
44. Mosialos G, Birkenbach M, Ayehunie S, Matsumura F, Pinkus GS, Kieff E, et al. Circulating human dendritic cells differentially express high levels of a 55-kd actin-bundling protein. Am J Pathol 1996;148:593–600.
45. Mitchell DA, Batich KA, Gunn MD, Huang MN, Sanchez-Perez L, Nair SK, et al. Tetanus toxoid and CCL3 improve dendritic cell vaccines in mice and glioblastoma patients. Nature 2015;519:366–9.
46. Ahrens ET, Helfer BM, O'Hanlon CF, Schirda C. Clinical cell therapy imaging using a perfluorocarbon tracerand fluorine19 MRI. Magn Reson Med 2014;72:1696–701.
47. De Vries IJ, Krooshoop DJ, Scharenborg NM, Lesterhuis WJ, Diepstra JH, Van Muijen GN, et al. Effective migration of antigen-pulsed dendritic cells to lymph nodes in melanoma patients is determined by their maturation state. Cancer Res 2003;63:12–7.
48. de Vries IJ, Lesterhuis WJ, Barentsz JO, Verdijk P, van Krieken JH, Boerman OC, et al. Magnetic resonance tracking of dendritic cells in melanoma patients for monitoring of cellular therapy. Nat Biotechnol 2005;23:1407–13.
49. Ahrens ET, Bulte JW. Tracking immune cells *in vivo* using magnetic resonance imaging. Nat Rev Immunol 2013;13:755–63.
50. Ji Y, Waiczies H, Winter L, Neumanova P, Hofmann D, Rieger J, et al. Eightchannel transceiver RF coilarray tailored for 1H/19F MR of the human knee and fluorinated drugs at 7.0 T. NMR Biomed 2015;28:726–37.
51. Niendorf T, Pohlmann A, Reimann HM, Waiczies H, Peper E, Huelnhagen T, et al. Advancing cardiovascular, neurovascular and renal magnetic resonance imaging in small rodents using cryogenic radiofrequency coil technology. Front Pharmacol 2015;6:255.
52. Pellegatta S, Poliani PL, Corno D, Menghi F, Ghielmetti F, Suarez-Merino B, et al. Neurospheres enriched in cancer stem–like cells are highly effective in eliciting a dendritic cell–mediated immune response against malignant gliomas. Cancer Res 2006;66:10247–52.
53. Bajaña S, Roach K, Turner S, Paul J, Kovats S. IRF4 promotes cutaneous dendritic cell migration to lymph nodes during homeostasis and inflammation. J Immunol 2012;189:3368–77.
54. Gartlan KH, Wee JL, Demaria MC, Nastovska R, Chang TM, Jones EL, et al. Tetraspanin CD37 contributes to the initiation of cellular immunity by promoting dendritic cell migration. Eur J Immunol 2013;43:1208–19.
55. Bunse M, Bendle GM, Linnemann C, Bies L, Schulz S, Schumacher TN, et al. RNAi-mediated TCR knockdown prevents autoimmunity in mice caused by mixed TCR dimers following TCR gene transfer. Mol Ther 2014;22: 1983–91.
56. Cox DBT, Platt RJ, Zhang F. Therapeutic genome editing: prospects and challenges. Nat Med 2015;21:121–31.
57. Burnett John C, Rossi John J. RNA-based therapeutics: current progress and future prospects. Chem Biol 2012;19:60–71.

2.2 Fluorine magnetic resonance imaging to monitor immune cell migration

This chapter builds on **publication 2** “Anchoring dipalmitoyl phosphoethanolamine to nanoparticles boosts cellular uptake and fluorine-19 magnetic resonance signal” published in Scientific Reports (Waiczies et al., 2015).

Motivated by the findings in **publication 1** that manipulated DCs immunotherapies have better migratory properties in brain tumors (Ku et al., 2016), we established a non-invasive method that could follow the migration of these cells in vivo, using fluorine (^{19}F) MRI. The first method developments were related to nanotechnology (Waiczies et al., 2011; Waiczies et al., 2015), DC tracking (Waiczies et al., 2013a) and designing radio frequency coils for ^{19}F brain MRI (Waiczies et al., 2013b).

Labelling cells with ^{19}F nanoparticles is a crucial first step for tracking cell therapies in vivo. We showed that ^{19}F MRI is highly suited to follow DCs in vivo (Waiczies et al., 2013a). We also reported that ^{19}F nanoparticle size affects the immunological properties of DCs (Waiczies et al., 2011). We also administered ^{19}F nanoparticles in animal models to label inflammatory cells in vivo to study their migration to the CNS during inflammation, both in the EAE animal model (Waiczies et al., 2013b; Waiczies et al., 2017a; Waiczies et al., 2018; Starke et al., 2019; Waiczies et al., 2019) as well as in the glioma model (**Figure 2** in own work 1 (Ku et al., 2016)).

Tracking transplanted ^{19}F labelled cell therapies in vivo with ^{19}F MRI demands more signal sensitivity and signal-to-noise ratio (SNR) than the detection of inflammation e.g. in the EAE. The number of ^{19}F-labeled cells clustering in inflammatory regions e.g., in the CNS during EAE, is much larger than the number of ^{19}F-labeled transplanted therapeutic cells that traffic to their target organ. Therefore we recognized the need to enhance the ^{19}F signal per transplanted cell by increasing nanoparticle uptake without altering therapeutic efficacy (Waiczies et al., 2011; Waiczies et al., 2015). We altered the nanoparticle shell composition with different phosphatidylethanolamines (PE), since these are critical components of biological membranes (**Figure 1A** in own work 2 (Waiczies et al., 2015)). Both electron microscopy and MR spectroscopy revealed a striking (at least one order of magnitude) increase in cytoplasmic uptake of ^{19}F nanoparticles in DCs, without significantly influencing migration, following enrichment with 1,2-dipalmitoyl-sn-glycero-3-phosphoethanolamine (DPPE) but not 1-palmitoyl-2-oleoyl-sn-glycero-3-phosphoethanolamine (POPE) (**Figure 1B, 2B** in own work 2 (Waiczies et al., 2015)). We observed a subsequent enhancement in ^{19}F MR signal in vivo (**Figure 6C** in own work 2 (Waiczies et al., 2015)):

SCIENTIFIC REPORTS

OPEN

SUBJECT AREAS:
TRANSLATIONAL RESEARCH
IMAGING TECHNIQUES AND AGENTS

Received
24 September 2014

Accepted
15 January 2015

Published
12 February 2015

Correspondence and requests for materials should be addressed to S.W. (sonia@waiczies.de)

* These authors contributed equally to this work.

Anchoring Dipalmitoyl Phosphoethanolamine to Nanoparticles Boosts Cellular Uptake and Fluorine-19 Magnetic Resonance Signal

Sonia Waiczies[1]*, Stefano Lepore[1]*, Karl Sydow[2]*, Susanne Drechsler[1], Min-Chi Ku[1], Conrad Martin[1], Dorothea Lorenz[2], Irene Schütz[2], Henning M. Reimann[1], Bettina Purfürst[4], Matthias A. Dieringer[1,5], Helmar Waiczies[3], Margitta Dathe[2], Andreas Pohlmann[1] & Thoralf Niendorf[1]

[1]Berlin Ultrahigh Field Facility, Max Delbrück Center for Molecular Medicine, Berlin, Germany, [2]Leibniz-Institut für Molekulare Pharmakologie, Berlin, Germany, [3]MRI TOOLs GmbH, Berlin, Germany, [4]Electron Microscopy Core Facility, Max Delbrück Center for Molecular Medicine, Berlin, Germany, [5]Experimental and Clinical Research Center, Berlin, Germany.

Magnetic resonance (MR) methods to detect and quantify fluorine (^{19}F) nuclei provide the opportunity to study the fate of cellular transplants in vivo. Cells are typically labeled with ^{19}F nanoparticles, introduced into living organisms and tracked by ^{19}F MR methods. Background-free imaging and quantification of cell numbers are amongst the strengths of ^{19}F MR-based cell tracking but challenges pertaining to signal sensitivity and cell detection exist. In this study we aimed to overcome these limitations by manipulating the aminophospholipid composition of ^{19}F nanoparticles in order to promote their uptake by dendritic cells (DCs). As critical components of biological membranes, phosphatidylethanolamines (PE) were studied. Both microscopy and MR spectroscopy methods revealed a striking (at least one order of magnitude) increase in cytoplasmic uptake of ^{19}F nanoparticles in DCs following enrichment with 1,2-dipalmitoyl-sn-glycero-3-phosphoethanolamine (DPPE). The impact of enriching ^{19}F nanoparticles with PE on DC migration was also investigated. By manipulating the nanoparticle composition and as a result the cellular uptake we provide here one way of boosting ^{19}F signal per cell in order to overcome some of the limitations related to ^{19}F MR signal sensitivity. The boost in signal is ultimately necessary to detect and track cells in vivo.

Tracking immune cells in vivo is a prerequisite for understanding the development of pathologies associated with disorders of the immune system[1]. Dendritic cells (DCs) are immune cells that play key roles in the development of immunity and immunopathology. Of note, an understanding of the distribution and fate of cells such as DCs following their therapeutic application in vivo such as in cancers is crucial to assess treatment efficacy[2]. The lack of *a priori* knowledge of the kinetics and dynamics of these cells during physiological and pathological settings makes their localization a challenging task. It is therefore a top priority to develop methods for the non-invasive spatiotemporal tracking of immune cells in vivo that can be easily transferred to the clinical scenario[3–6].

Magnetic resonance imaging (MRI) offers an ideal solution for tracking cells in vivo due to its non-invasiveness and clinical translation as well as the opportunity of repetitive measurements and longitudinal studies. Major challenges in differentiating cells from the recipient tissue and signal sensitivity constraints nevertheless exist. For instance, iron oxide nanoparticles that reduce T_2* relaxation[7] in MR have been used to label cells, however present a challenge whereby the contrast created by the labeled cells is not easily distinguishable from other intrinsic tissue contrasts[8]. This limitation of cellular MRI is surmounted by fluorine (^{19}F) MR techniques[3]. Carbon-bound fluorine is absent in living organisms. This guarantees background-free MR signals for externally-applied ^{19}F compounds. Therefore ^{19}F MR techniques are advantageous for localizing ^{19}F-containing exogenous agents in vivo since they permit complete signal selectivity and specificity[9–11]. Importantly, the ^{19}F MR signal can also be equated to measurable cell numbers within defined regions[6,12]. For in vivo tracking, cells are typically labeled with nanoparticles enriched with perfluorocompounds (PFCs) prior to their introduction into living organisms[3–6]. These compounds possess unique properties (inertness, biocompatibility and hydrophobicity) which stem from

the C–F bonds within the molecular structure[13]. Hydrophobicity becomes more significant with increasing number of ^{19}F atoms and a critical factor for increasing the ability of these compounds to cross biological membranes[14,15]. Making use of these properties, ^{19}F-rich nanoparticles are prepared via various techniques – commonly by emulsifying PFCs with phospholipids or surfactants – in order to label and track immune cells in vivo with the aid of combined ^{19}F and anatomical/proton (^{1}H) MR imaging as well as ^{19}F spectroscopy techniques[3–6]. Notwithstanding the benefits specified above, some limitations and challenges exist for ^{19}F-based MR techniques, especially those pertaining to detection limit and signal sensitivity. These limitations come at a cost in increased signal averaging and thus acquisition times to compensate for low signal-to-noise ratio (SNR). There is a need to optimize cellular ^{19}F MR methods especially since clinical trials with DC vaccines have thus far provided a proof-of-principle as cancer therapy[16] and the applicability of ^{19}F MR techniques for DC vaccines are being explored in colorectal cancer patients[17].

In the present study we explored the possibility of altering the composition of ^{19}F nanoparticles in order to maximize their uptake by DCs and therefore to promote the ^{19}F signal per cell. To meet this goal, we investigated the incorporation of phosphatidylethanolamines (PEs) into the ^{19}F nanoparticle shell. PEs are aminophospholipids that constitute an integral part of biological membranes[18,19]. These aminophospholipids are cone-shaped, they do not form bilayers but inverted hexagonal phases, are believed to exert a lateral pressure that regulates membrane curvature and, are thought to stabilize membrane proteins in their optimum conformations[20]. PE analogs have been used successfully in non-viral transfection systems[21,22] as well as in nanotube carriers for drug delivery[23]. For all these reasons we studied the influence of PE enrichment on the uptake of ^{19}F nanoparticle by DCs. Using both electron microscopy and ^{19}F MR spectroscopy we observed a dramatic increase in uptake of ^{19}F nanoparticles enriched with 1,2-dipalmitoyl-sn-glycero-3-phosphoethanolamine (DPPE) by DCs. As a result, the ^{19}F signal/cell was increased by at least one order of magnitude and the cell detection limit considerably reduced. With this advantage at hand we could reduce the PFCE concentration per nanoparticle to avoid impairment in cell function, particularly cell migration. Our findings further offset the constraints of ^{19}F MR and bring us a step closer to the crucial goal of ultimate signal sensitivity and minimal cell detection limit.

Results

Dipalmitoyl-Phosphoethanolamine promotes nanoparticle uptake by DCs. Considering the power of PE analogs to promote cellular uptake in transfection and drug delivery systems[21–23], we first set off to enrich ^{19}F-rich (PFCE) nanoparticles (NP) used in our previous studies[5,6,12] with different phospholipids of the phosphoethanolamine (PE) family (Figure 1A). The basic nanoparticles were prepared using Pluronic F-68 block copolymer. To enrich the ^{19}F nanoparticles with PE we chose two analogs differing in their two long fatty acid hydrocarbon chains; one PE contained one unsaturated bond (1-palmitoyl-2-oleoyl-sn-glycero-3-phosphoethanolamine, **POPE**) and the other PE consisted of only saturated bonds (1,2-dipalmitoyl-sn-glycero-3-phosphoethanolamine, **DPPE**). Also consisting solely of saturated bonds was the third candidate we chose: 1,2-Distearoyl-*sn*-glycero-3-phosphoethanolamine (DSPE), bound to polyethylene glycol-2000 (**DSPE-PEG2000**). PEG is widely employed as polymeric steric stabilizer and is anchored to stealth liposomal surfaces via cross-linked DSPE lipid[24,25]. PEG2000 was chosen since blocks of higher molecular weight in similarly-sized nanoparticles have been shown to reduce nanoparticle uptake in macrophages (uptake: PEG2000 > PEG5000 > PEG10000)[26]. We used DPPE and POPE to enrich Pluronic-based PFCE-containing nanoemulsions and prepared liposomal PFCE nanoparticles using DSPE-PEG2000. For all nanoparticle preparations, the molar fraction of the constituents and the physical characteristics (size, polydispersity, surface charge) are shown in Table 1.

To determine differences in uptake between the different nanoparticle groups we performed ^{19}F magnetic resonance spectroscopy (MRS) of the fixed DCs following labeling to determine the amount of ^{19}F compound (PFCE) per 10^6 cells. Pluronic-nanoparticles enriched with PE polymers appeared to be taken up more efficiently by DCs than basic Pluronic nanoparticles and DSPE–PEG2000 liposomes as determined by the increase in cellular ^{19}F signal. POPE enrichment already resulted in an increased ^{19}F signal (*POPE 1x*: 138 nmol per 10^6 cells and *POPE 10x*: 179 nmol per 10^6 cells) compared to the basic nanoparticle formulations (74 nmol per 10^6 cells) and DSPE–PEG2000 liposomes (69 nmol per 10^6 cells). When we employed DPPE to enrich the nanoparticle shell, we observed an even stronger enhancement of ^{19}F signal (771 nmol per 10^6 cells) (Figure 1B). This equates to an increase in ^{19}F spins from 0.89×10^{12} ^{19}F spins (in basic formulations) to 0.93×10^{13} ^{19}F spins (in DPPE-enriched nanoparticles) per dendritic cell unit.

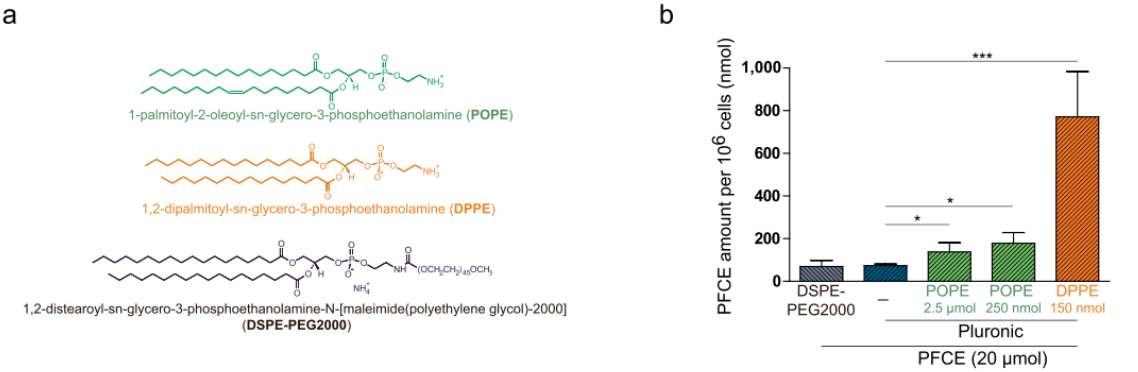

Figure 1 | Selection of phosphoethanolamines for enrichment of PFCE nanoparticles. (a) Chemical structures of DPPE (1,2-dipalmitoyl-sn-glycero-3-phosphoethanolamine), POPE (1-palmitoyl-2-oleoyl-sn-glycero-3-phosphoethanolamine used for the ^{19}F nanoemulsion and DSPE-PEG2000 (1,2-distearoyl-sn-glycero-3-phosphoethanolamine-N[methoxy(polyethylene glycol) -2000]) used for the liposomal nanoparticles. (b) DCs were labeled with different ^{19}F nanoparticle preparations (DSPE-PEG2000, Pluronic-basic, Pluronic-POPE and Pluronic-DPPE) using a PFCE concentration of 20 µmol per 10^7, fixed in 2% PFA and transferred (10^6) to NMR tubes. After positioning in a ^{19}F-tuned loop coil (see Methods), ^{19}F signal was acquired using a 90° block excitation pulse with 10 kHz bandwidth and the PFCE amount per 10^6 calculated using a 500 mM PFCE standard.

www.nature.com/scientificreports

Table 1 | Composition and characteristics of nanoparticles (NP) used

	Molar fraction of constituents			Physical characteristics		
	Pluronic	PE Lipid	PFCE	Particle size	Polydispersity	Zeta Potential
Nanoparticle	*X*	*X*	*X*	[nm] (±*S.D.*)	Index (±*S.D.*)	[mV] (±*S.D.*)
Pluronic-Basic—PFCE NP	0.01419	—	0.98581	186 (*15*)	0.06 (*0.02*)	−4.81 (*1.52*)
Pluronic-(*DPPE*)—PFCE NP	0.00582	0.00001	0.99417	246 (*16*)	0.30 (*0.02*)	−18.55 (*1.61*)
Pluronic-(*POPE 1x*)—PFCE NP	0.00580	0.00001	0.99418	200 (*6*)	0.03 (*0.01*)	−12.13 (*0.31*)
Pluronic-(*POPE 10x*)—PFCE NP	0.00580	0.00011	0.99408	200 (*1*)	0.12 (*0.08*)	−7.37 (*0.53*)
(*DSPE-PEG2000*)—PFCE NP	—	0.00006	0.99994	216 (*19*)	0.20 (*0.01*)	−28.43 (*1.33*)

Dynamic light scattering was used to measure Z-average diameter (mean diameter based on intensity of scattered light and sensitive to presence of large particles), peak diameter, peak width and polydispersity index (PdI). PFCE = perfluoro-15-crown-5-ether; *X* = mole fraction; PE = phosphoethanolamine; *DPPE* = 1,2-dipalmitoyl-sn-glycero-3-phosphoethanolamine; *POPE* = 1-palmitoyl-2-oleoyl-sn-glycero-3-phosphoethanolamine; *DSPE-PEG2000* = 1,2-distearoyl-sn-glycero-3-phosphoethanolamine-N[methoxy(polyethylene glycol)-2000.

Intracellular appearance of Dipalmitoyl-Phosphoethanolamine-enriched nanoparticles. Despite the dramatic differences in ^{19}F signal within DCs between the different nanoparticles, we did not observe any conspicuous differences in the shape of the nanoparticles employed as investigated by Cryo-TEM (Figure 2A). We next went on to investigate whether the striking increase in ^{19}F signal in the DPPE-enriched nanoparticles was the result of increased nanoparticle uptake. In ultrathin sections of DCs derived from the same culture conditions, we observed intense differences in cytoplasmic uptake between the nanoparticle formulations (Figure 2B, *EM images in upper two panels and lower left panel*). We commonly observed the nanoparticles as white globules within the cell cytoplasm but similar to our previous observations[5] the nanoparticles also often appeared compartmentalized as clusters in a lipid membrane capsule within an amorphous grey compartment. We also observed increased DC uptake of nanoparticles enriched with DPPE linked to the tracer dye Rhodamine as shown from the Rhodamine fluorescence imaged by laser scanning microscopy

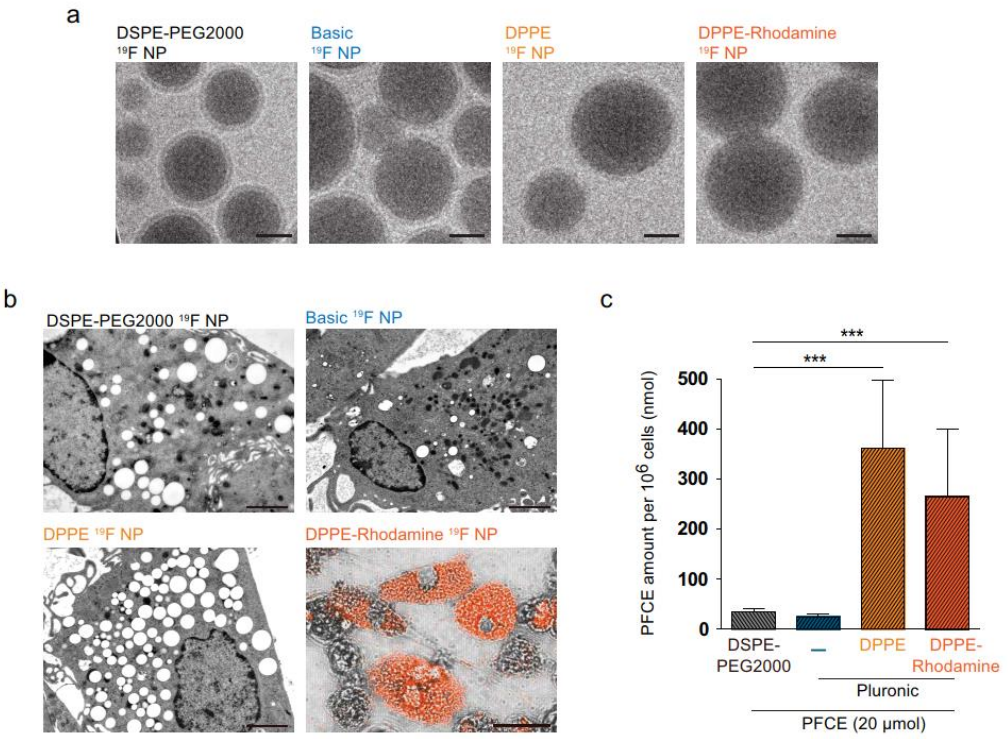

Figure 2 | Appearance of phosphoethanolamine-enriched PFCE nanoparticles. (a) Cryogenic transmission electron microscopy (TEM) images of DSPE-PEG2000, Pluronic-basic, Pluronic-DPPE and Pluronic-DPPE-Rhodamine nanoparticles encapsulating PFCE fluorine compound (size-bar for TEM images: 50 nm). (b) Upper two panels and lower left panel show ultrathin sections of DCs labeled with DSPE-PEG2000, basic and DPPE-enriched PFCE nanoparticles (size-bar for EM images: 2 µm). Lower right panel shows a laser scanning microscopy image of DCs labeled with DPPE-Rhodamine-enriched ^{19}F nanoparticles (size-bar for LSM image: 10 µm). (c) DCs were labeled with different nanoparticle preparations (DSPE-PEG2000 NP, basic NP, DPPE-NP and DPPE-Rhodamine-NP) using a PFCE concentration of 10 µmol per 10^7, fixed in 2% PFA and transferred (10^6) to NMR tubes. ^{19}F signal was acquired using a 90° block excitation pulse and the PFCE amount per 10^6 calculated using a 500 mM PFCE standard.

(Figure 2B, *LSM image in lower right panel*); these nanoparticles were also loaded into DCs similarly to the non-Rhodamine linked DPPE-enriched ^{19}F nanoparticles.

As a next step, the same groups of cells labeled with basic (-), DPPE or DPPE-Rhodamine ^{19}F nanoparticles as well as DSPE-PEG2000 liposomes were investigated by ^{19}F MRS (Figure 2C). Similarly to the results in Figure 1B, we observed a significant increase in ^{19}F signal per cell when DCs were labeled with nanoparticles enriched with DPPE (361 nmol per 10^6 cells $\equiv 0.44 \times 10^{13}$ ^{19}F spins per cell) compared to the basic formulation (25 nmol per 10^6 cells $\equiv 0.3 \times 10^{12}$ ^{19}F spins per cell) and DSPE–PEG2000 liposomes (35 nmol per 10^6 cells $\equiv 0.42 \times 10^{12}$ ^{19}F spins per cell) (Figure 2C). The ^{19}F signal per cell in DCs labeled with DPPE-Rhodamine nanoparticles was slightly lower (264 nmol per 10^6 cells $\equiv 0.32 \times 10^{13}$ ^{19}F spins per cell) than those from DCs labeled with nanoparticles enriched with DPPE containing no Rhodamine (Figure 2C).

Titrating the ^{19}F label in DPPE-enriched nanoparticles. In the next experiments we performed dose titration curves for the ^{19}F label (perfluoro-15-crown-5-ether, PFCE) in cells loaded with DPPE or basic ^{19}F nanoparticles. With these experiments we wanted to determine the lowest concentration of PFCE feasible for detecting a sufficient ^{19}F signal in MRS (Figure 3). Using the Pluronic-based nanoparticles we had previously employed up to 40 µmol PFCE per 10^7 DCs in culture[5]. Taking into account the dramatic increase in ^{19}F signal achieved following enrichment with DPPE we titrated the PFCE amount from 40 µmol to 2 µmol PFCE per 10^7 DCs. In line with the previous results (Figure 1–2), 5 µmol PFCE label within DPPE ^{19}F nanoparticles gave a larger ^{19}F signal than 40 µmol PFCE label within basic ^{19}F nanoparticles when used to label 10^7 DCs (Figure 3A, 3B). This observation can be made already from the spectral representations of the ^{19}F signal (Figure 3A) and upon quantification of the ^{19}F signal from the maximum signal intensity of the FID (Figure 3B). By extrapolating the linear fit ($[PFCE]_{label}/[PFCE]_{intracellular}$) for the basic ^{19}F nanoparticles, we estimate a requirement of 70 µmol for the basic ^{19}F nanoparticles to reach the equivalent ^{19}F signal of DCs labeled with 5 µmol DPPE-enriched nanoparticles (Δ PFCE concentration ~65 µmol) (Figure 3B).

Higher concentrations of ^{19}F label hinder DC migration. Ultimately, the ^{19}F-labeled DCs will be applied in living organisms. Therefore it was necessary to determine the influence of increasing PFCE labeling on DC migration for both DPPE-enriched as well as basic ^{19}F nanoparticles. For this, we employed an agarose assay to determine the chemotaxis of DCs towards a chemokine gradient following maturation with bacterial lipopolysaccharide (LPS). In the initial experiments comparing ^{19}F signal between basic and DPPE nanoparticles we employed 10–20 µmol of PFCE to label 10^7 cells (Figure 1–2). When we investigated the influence of 10 µmol PFCE label on DC migration, we observed differences in the number of DCs moving towards chemokine between unlabeled cells treated for 18 h with LPS and cells labeled with ^{19}F nanoparticles (Figure 4A). For DCs labeled with DPPE ^{19}F nanoparticles, quantities of PFCE higher than 10 µmol per 10^7 cells reduced the migration of DCs towards chemokine by more than 50% (Figure 4B). For lower doses of PFCE – specifically 5 µmol per 10^7 cells – the reduction in migration was less extensive and the difference between DPPE and basic ^{19}F nanoparticles less substantial; the inhibition in migration for DPPE-NP labeled cells was 35% (n = 1270) and the inhibition in migration for basic-NP labeled DCs was 22% (n = 1555) in comparison to unlabeled DCs (n = 1985) (Figure 4B). This finding and considering our previous observation that 5 µmol PFCE in DPPE nanoparticles generate an equivalent ^{19}F signal by at least one order more PFCE in basic nanoparticles (Figure 3B), led us to employ 5 µmol PFCE for all the following experiments.

Lower number of cells detected following labeling with DPPE-enriched nanoparticles. Using 5 µmol PFCE for both DPPE and basic ^{19}F nanoparticles we next measured the intracellular ^{19}F signal in increasing numbers of DCs to determine the cell detection limit. We measured the ^{19}F signal in each fixed cell sample by performing global spectroscopy of the NMR tube containing the cell pellet (see Methods). By using a ^{19}F standard (500 mM PFCE) we quantified the amount of PFCE within each sample. Both spectral representation of the ^{19}F signal (Figure 5A) as well as PFCE quantification (Figure 5B) for both DPPE-enriched and basic ^{19}F nanoparticles demonstrated that ^{19}F signal amplitude correlates with the number of labeled cells.

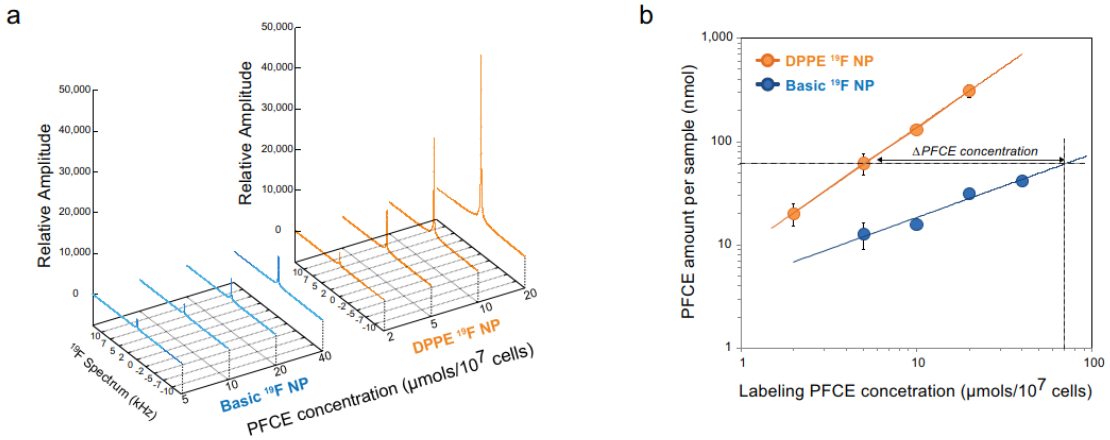

Figure 3 | Dose titration of the ^{19}F label for ^{19}F NMR signal. (a) Spectral representation of ^{19}F signal acquired from basic and DPPE-enriched label within DCs using different doses of the ^{19}F label PFCE. DCs were labeled with nanoparticle preparations using PFCE concentrations between 2 µmol and 40 µmol) per 10^7, fixed in 2% PFA and transferred (10^6) to NMR tubes. ^{19}F signal was acquired using a 90° block excitation pulse and spectral representation using a FFT of the acquired FID. (b) The ^{19}F signal was quantified from the intercept of the FID fit and the PFCE amount per 10^6 was calculated using a 500 mM PFCE standard.

www.nature.com/scientificreports

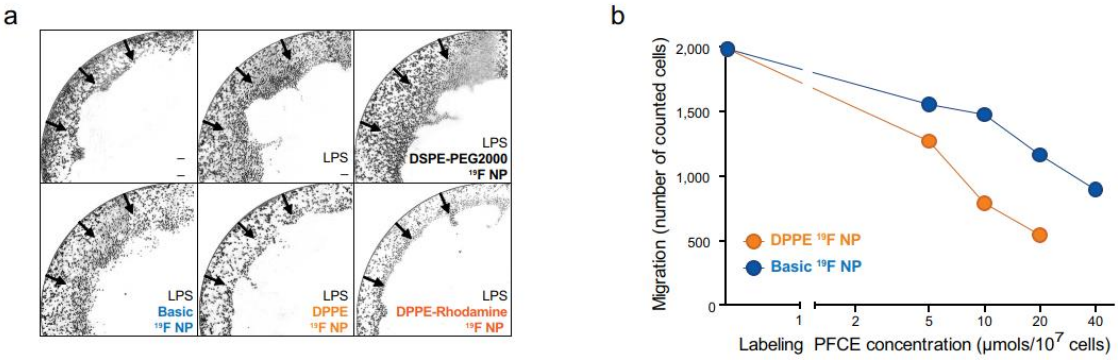

Figure 4 | Dose titration of the ^{19}F label for chemotaxis assay. (a) DCs (10^5) labeled with different nanoparticle preparations (10 μmol PFCE) were introduced to glass dishes containing CCL21-agarose spots and the number of cells entering the agarose spot was visualized by acquisition of microscope images. (b) DCs (10^5) labeled with increasing PFCE concentrations of both basic and DPPE-enriched ^{19}F nanoparticles were introduced to glass dishes containing CCL21-agarose spots and the number of cells entering the agarose spot was determined by acquiring and fusing the microscope images for all the fields of views (FOV) and counting all cells entering the corresponding spot. This experiment is representative of 3.

From the spectral representation of the cell dilution curves it was already evident that far less DPPE-NP labeled DCs could be detected than basic-NP labeled DCs (Figure 5A). It should be noted that in these experiments (in line with the chemotaxis assays above) we used low PFCE labeling doses (5 μmol per 10^7 cells) in contrast to previously published work where we commonly employed 20 μmol per 10^7 cells[5,6,12]. In the present experiments we observed that a minimum of 10^6 DCs labeled with basic nanoparticles (5 μmol) were required to achieve a detectable ^{19}F signal. However for DPPE-NP labeled DCs, 1.5×10^5 of cells could be detected (Figure 5A). Following quantification of the ^{19}F signal from the FID fit and calculation of the intracellular PFCE amount (using PFCE standard), we observed that 10^5 DPPE-NP labeled DCs give a similar ^{19}F signal and contain similar PFCE amounts (14.48 nmol) as 10^6 basic-NP labeled DCs (10.45 nmol). It can also be deduced from the spectral representations (Figure 5A) that a baseline intracellular value of approximately 10 nmol PFCE (Figure 5B) is the threshold above which DCs become detectable.

Gain in sensitivity and cellular detection following labeling with DPPE ^{19}F nanoparticles. In order to reach the goal of this study (to identify the influence of PE nanoparticle enrichment on signal sensitivity in vivo), we next wanted to identify the ^{19}F signal and detection limit within defined regions of interest. For this we selected DC numbers used in the cell dilution curves and performed combined ^{19}F/^{1}H MRI (Figure 6A) as well as voxel-based ^{19}F PRESS in order to quantify the ^{19}F signal within this defined region (Figure 6B). We used the same radio frequency volume coil used for tracking DCs in mice, in order to be able to project our findings to the in vivo experiment. For the volume used to embed cells in agarose (100 μl) within NMR tubes it was sufficient to place a ($5 \times 5 \times 5$) mm^3 PRESS voxel that covered the entire sample (Figure 6B). The ^{19}F/^{1}H MR imaging experiments showed that 2.5×10^6 was the minimum amount of cells detected in the case of basic-NP labeled DCs and 0.3×10^6 was the minimum for the DPPE-NP labeled DCs (Figure 6A). This corresponds to a cell detection limit of 1.7×10^6 DCs per mm^3 for basic-NP labeled DCs and 2×10^5 DCs

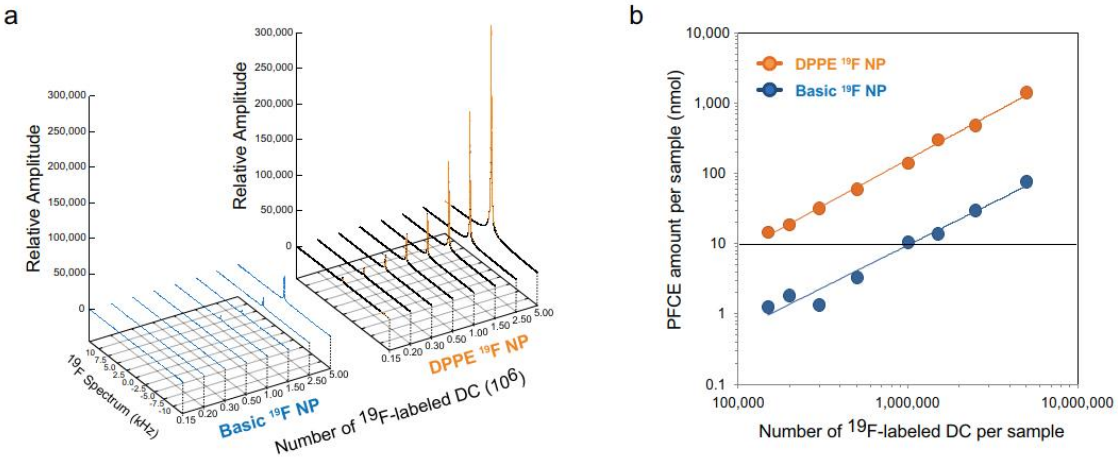

Figure 5 | Lower number of cells detected by ^{19}F MRS following labeling with DPPE-enriched nanoparticles. (a) Spectral representation of ^{19}F signal acquired from different numbers of basic and DPPE-NP labeled DCs using 5 μmol PFCE per 10^7 cells for ^{19}F labeling. ^{19}F spectra are represented from the FFT of the acquired FID. (b) The ^{19}F signal was quantified from the intercept of the FID fit and the PFCE amount per 10^6 was calculated using a 500 mM PFCE standard.

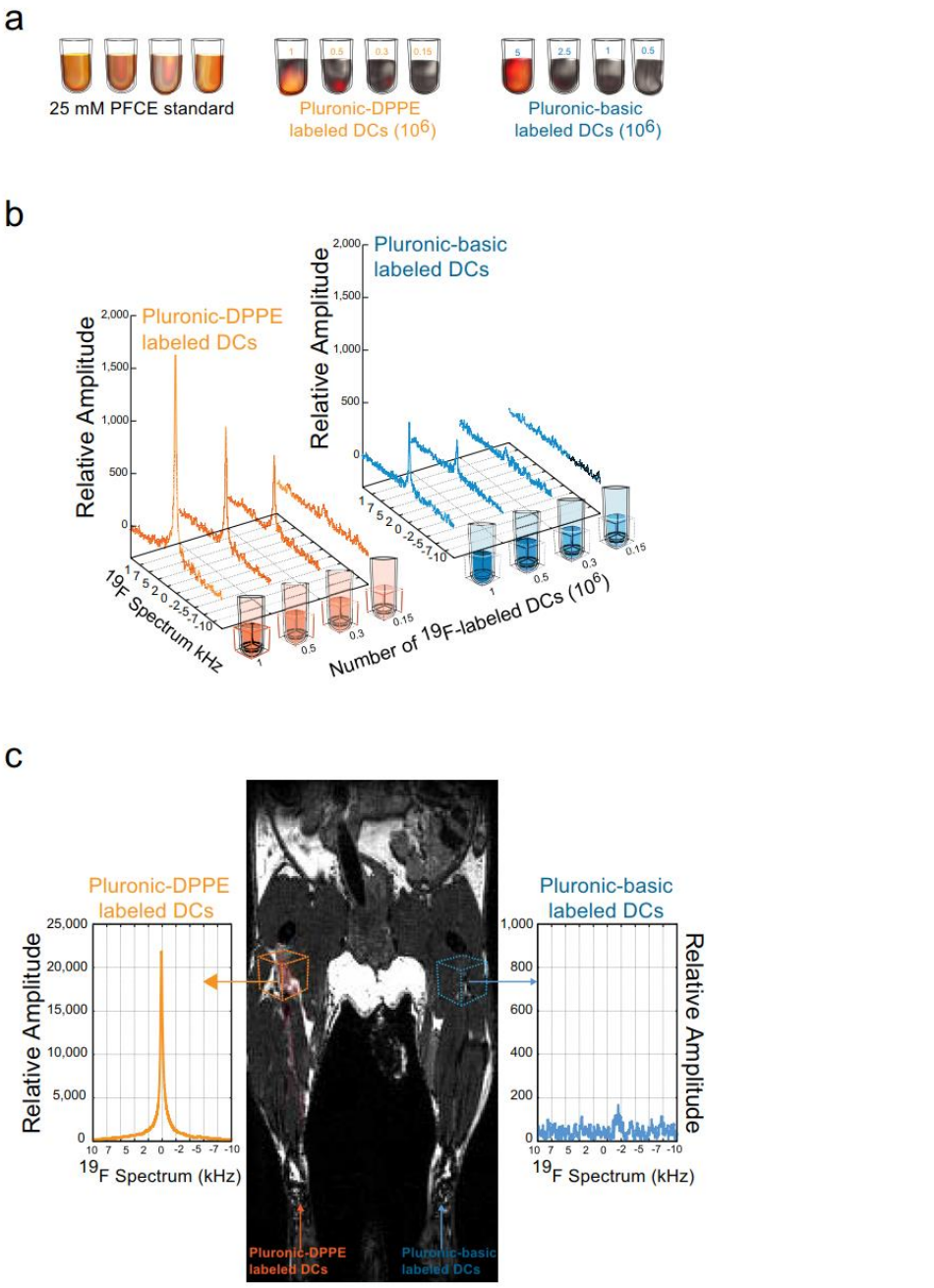

Figure 6 | **^{19}F/^{1}H MRI and Voxel-based ^{19}F MRS of DCs in vitro and in vivo.** (a) 3D rendering of images of PFCE standard (4 × 25 mM) and different number of DCs (labeled with basic or DPPE-enriched nanoparticles) suspended in agarose gel. Images for both ^{19}F and ^{1}H nuclei were acquired using the bSSFP sequence and post-processing of data using ImageJ (National Institutes of Health, USA, http://imagej.nih.gov/ij). (b) After acquisition of the bSSFP images, a (5 × 5 × 5) mm^3 voxel was placed over the whole region of cells in agarose and spectra were acquired using a PRESS-protocol for ^{19}F MRS (see Methods). (c) DCs (10^7) labeled with DPPE-enriched nanoparticles were intradermally injected in the left hind limb and DCs (10^7) labeled with basic nanoparticles in the right hind limb of C57BL/6 mice. Three hours following intradermal application a (3 × 3 × 3) mm^3 voxel was placed around left and right popliteal lymph node and the ^{19}F content measured within each lymph node using PRESS sequence as described above.

www.nature.com/scientificreports

per mm^3 for DPPE-NP labeled DCs for an ^{19}F MR scan time of 16.85 minutes (NEX = 64). The voxel-based spectroscopy method was more sensitive in detecting ^{19}F signal: 0.5×10^6 basic-NP labeled DCs and 0.15×10^6 DPPE-NP labeled DCs could be detected with this method (Figure 6B). This corresponds to a cell detection limit of 4×10^3 DCs per mm^3 for basic-NP labeled DCs and 1.2×10^3 DCs per mm^3 for DPPE-NP labeled DCs for an ^{19}F MR scan time of 13 minutes (NEX = 512).

To study the signal and migration efficiency of DPPE-NP labeled DCs in vivo, we next applied DCs (10^7) to the left hind limbs of C57BL/6 mice and compared their ^{19}F signal to those labeled with basic ^{19}F nanoparticles (right hind limb). Three hours following intradermal application we placed a $(3 \times 3 \times 3)$ mm^3 PRESS voxel around both left and right popliteal lymph node and measured the ^{19}F signal within each lymph node using PRESS sequence as described above. Both from the ^{19}F/^{1}H MR imaging as well as from the voxel-based spectra illustrating the region-specific ^{19}F signal we observed that DPPE-NP labeled DCs gave a more prominent signal in vivo than the basic-NP labeled DCs (Figure 6C). Using the cell calibration curves described above (Figure 5B) and the FID values at t = 0 for the PRESS spectra, we could translate the quantified ^{19}F signal to the number of cells within the specific lymph node regions: we calculated that after 3 hours 2.85×10^6 DPPE-NP labeled DCs were present in the left lymph node and 0.79×10^5 basic-NP labeled DCs in the right lymph nodes (Figure 6C).

Discussion

Phosphatidylethanolamines (PEs) are aminophospholipids that constitute an integral part of biological membranes. However, PE analogs have also been employed as components of non-biological systems such as non-viral transfection agents[21,22] and as coatings of poorly soluble carbon nanotubes to promote cellular uptake[23]. In the cell, PEs are mainly found in the inner leaflet of the lipid bilayer[27] and make up over one fourth of the whole membrane[28]. PEs play a role in membrane fusion and in cell division[29]. These phospholipids are translocated to intracellular surfaces via ATP-dependent mechanisms to maintain asymmetrical distribution within the membrane leaflet[30,31]. Aminophospholipid asymmetry is necessary for preserving the viability of the cell[18]. The phospholipids PE, PC (phosphatidylcholine), PS (phosphatidylserine), PI (phosphatidylinositol) and SM (sphingomyelin) are irregularly distributed throughout the cellular membrane (23 : 43 : 12 : 9 of PC : PE : PS : PI/SM) in dendritic cells[32]. The variable distribution of phospholipids is necessary for endocytosis in DCs[33,34].

In this study we investigated the influence of two PE analogs on the uptake of fluorine-rich nanoparticles into DCs. We made use of 1,2-dipalmitoyl-sn-glycero-3-phosphoethanolamine (DPPE) and 1-palmitoyl-2-oleoyl-sn-glycero-3-phosphoethanolamine (POPE) to enrich basic nanoparticles with PE. These PEs possess different phase transition temperatures (POPE: +25°C[35]; DPPE: +64°C[36]) and their assemblies have very different fluidity. One important difference between the two analogs is the presence of an unsaturated bond within one of the fatty acid hydrocarbon chains in POPE; both fatty acid chains in DPPE are made up of only saturated bonds (Figure 1A).

We found that anchoring DPPE to nanoparticle structures dramatically improved their uptake by DCs (Figures 1–3, Figures 5–6). We also observed an increase in cellular uptake when incorporating POPE into the nanoparticle structure; however the increased uptake was not as remarkable when compared to DPPE (Figure 1B). DSPE-PEG2000 was without any effect (Figures 1–2). In our study we chose PEG2000, with an intermediate molecular weight, in order to stabilize DSPE-based nanoparticles and secure their uptake by DCs. Larger PEG chains are associated with reduced phagocytosis: PEG2000 nanoparticles are taken up more efficiently by macrophages than PEG4000, PEG5000 and PEG10000 coated nanoparticles[26,37]. Earlier studies reported that covering nanoparticles with higher MW PEG (e.g. PEG5000) prolongs their circulation time in vivo[38–40], probably due to the decreased phagocytosis and thereby protection from the reticuloendothelial system[26,37]. In addition to cell uptake and circulation time, the length of the PEG block influences other biological aspects such as target recognition and uptake of delivery systems mediated by address molecules. While long PEG chains may cover the vectors, short PEG chains do not inhibit their enzymatic degradation[41]. Phospholipid-based drug delivery systems modified with PEG2000 are highly efficient and specific at drug targeting in tumor tissue, and remain longer in tumor tissue compared to other DSPE-based carriers with other PEG masses[42–44]. Molecular targeting and cellular uptake can be further enhanced by modification with vector molecules such as receptor-recognizing and cell-penetrating peptides[45,46]. In our study we did not modify the DSPE-PEG and do not observe any changes in uptake by DCs. Our finding correlates with transfection studies that showed that increasing number of methyl or methylene groups are progressively less active in transfection[47]. Furthermore, PEG-lipids were found to impair transfection efficacy[22]. In future it will be interesting to study the impact of peptide-modified DSPE-PEG nanoparticles to promote cellular uptake in DCs[46,48].

The observation that DPPE is superior to POPE with regard to cellular uptake is however surprising since liposomal transfection formulations doped with PE analogs revealed that analogs with increasing acyl chain saturation were progressively less active than unsaturated analogs[47]. In our study we enriched nanoparticles generated from emulsification of PFCE with Pluronic with DPPE. Since PE is strictly bound to the cytosolic leaflet, the observed increased efficiency of internalization of DPPE-enriched nanoparticles by DCs could be explained by an active process translocating PE to the inner membrane surface. It has been shown that multiple unsaturation of the fatty acyl chain significantly decreases the interaction with cholesterol in both bilayers and monolayers[19]. The success of conveying nanocomplexes into the intracellular compartment is dependent on several factors: hydrophobic alkyl side chains, saturation of C-C bonds in hydrophobic moieties, the head group of the phospholipids utilized to make up the nanocarrier. In a study comparing the combination of a number of phospholipids to liposomal nanoparticles used for gene delivery, combinations containing DPPE and DOPE (1,2-dioleoyl-sn-glycero-3-phosphoethanolamine) were most effective with regards to cellular transfection[49].

PE and PS aminophospholipids are present in cell-derived membrane vesicles: microparticles, microvesicles, exosomes[50]. Recently a study reported that PE is extensively found on the external surface of microparticles derived from various human cellular sources[51]. Although cell-derived membrane vesicles were first discovered as a product of platelets during blood coagulation[52] and thought to be cellular waste, it is now becoming clear that they play a crucial role in intercellular communication[53,54] that may include fusion with their target cells[55]. Therefore it is conceivable that DPPE-enriched nanoparticles would behave in a similar fashion as these cellular vesicles in order to translocate into intracellular compartments of DCs.

Two clear differences between POPE and DPPE that could explain the differences in cellular uptake are: (i) the presence of an unsaturated bond in POPE and (ii) their dissimilar phase transition temperatures from fluid to liquid crystalline of +25°C for POPE[35] and +64°C for DPPE[36]. These distinct differences between 2 otherwise very similar PEs might determine differences in the fluidity of their assemblies and rigidity of their bilayers, thereby conveying differences in the stability of the particulate structures. The character of the acyl chains in aminophospholipids such as PEs has indeed been shown to be crucial for the fluidity of a monolayer; saturated chains lead to lesser membrane fluidity than unsaturated ones[56]. It was recently proposed that aminophospholipids with unsaturated oleoyl chains such as POPE are more prominent in areas of protrusion due

to their overall conical shape and aminophospholipids consisting of solely saturated palmitoyl chains (that are considered less conical/more cylindrical in shape) do not participate in curvature formation[57]. Curvature stress is indeed antagonized by addition of more cylindrical lipids[58]. Changes in the fluidity of biological membranes is also attributed to changes in membrane-initiated signaling processes; for instance, alcohol potentiation of calcium-activated potassium channels is favored by cylindrical phospholipids and blunted by conical ones, regardless of phospholipid head group charge[59]. Differences in membrane fluidity for DPPE and POPE nanoparticles might influence their interaction with DCs and perhaps the mechanism of entry into the cells. In future, it will be interesting to study the mode of internalization for different rigid and fluidic nanostructures by performing inhibition studies of specific uptake routes (e.g. energy-dependent processes, clathrin-mediated endocytosis, caveolae-mediated endocytosis, macropinocytosis)[60] and to follow nanoparticle uptake over time using time-lapse video microscopy[61]. State-of-the-art technologies such as computational modeling[62] or four-dimensional electron microscopy[63] will shed light in the future on structure–property relationships of nanocomposites and single-nanoparticle structural dynamics.

In the present study we showed that the incorporation of DPPE in ^{19}F nanoparticles for labeling of DCs increases the intracellular ^{19}F signal in DCs by at least one order of magnitude compared to ^{19}F nanoparticles devoid of DPPE. The observation of an increased uptake of ^{19}F nanoparticles was demonstrated by ^{19}F MR spectroscopy as well as electron and laser scanning microscopy. The microscopy studies demonstrated that nanoparticles are located inside discrete cytosolic endosomes after internalization by DCs, excluding the possibility of cell surface attachment. The agarose spot chemotaxis assay showed that DCs were less capable at moving towards a chemokine concentration when increasing ^{19}F label concentration. Although the migration capability of DCs labeled with DPPE-enriched fluorine nanoparticles is diminished when compared to non-enriched nanoparticles, when given at the same PFCE labeling concentration, lower concentrations of DPPE-enriched fluorine nanoparticles still resulted in a higher ^{19}F signal per million cells and minimal decrease in migration, implying a possible threshold for aminophospholipid enriched nanoparticle labelling concentration that increases the ^{19}F MRS signal without influencing DC migration ability. The order of magnitude increase in ^{19}F signal we observed with ^{19}F spectroscopy could be translated into two advantages: (i) we could decrease the concentration of the ^{19}F label (PFCE) from 20 μmol (employed in our original studies[5,6,12]) to 5 μmol per 10^7 DCs and thus decrease the impact of the ^{19}F label on cell migration and (ii) the sensitivity gain considerably improved the cell detection limit to enable imaging and quantification of DCs within specific anatomical regions in vivo.

In conclusion, we present evidence that an enrichment of ^{19}F nanoparticles with DPPE aminophospholipids enhances their uptake by DCs, thereby promoting cellular detection by various ^{19}F MRI and MRS methods. By promoting cellular uptake of ^{19}F label in cellular transplants — such as in DC vaccines for cancer therapy — we contribute to some of the solutions required to overcome the limitations and challenges of cellular MR imaging, particularly with respect to the barriers pertaining to detection limit and signal sensitivity.

Methods

Nanoparticle preparation. Nanoparticles with high fluorine content were prepared by emulsifying Perfluoro-15-crown-5-ether (PFCE, Fluorochem, Derbyshire, UK) via direct sonication, using a ultrasonic homogenizer (Hielscher Ultrasonic GmbH, Teltow, Berlin, Germany). PFCE was emulsified in Pluronic F-68 (Sigma-Aldrich, Germany) for 10 minutes on ice (1.2 M end concentration) to generate a basic formulation: Basic ^{19}F nanoparticles (NP). To enrich the basic particles with DPPE (*1,2-dipalmitoyl-sn-glycero-3-phosphoethanolamine*, Figure 1A, Avanti Polar Lipid, Inc., Alabaster, AL) diluted Pluronic-basic nanoparticles were mixed with DPPE and further emulsified using the same conditions to obtain a final PFCE concentration of 400 mM and varying DPPE concentrations of 2.5–25 μM (DPPE ^{19}F NP). The same procedure was used to prepare the Pluronic-Rhodamine-DPPE (DPPE-Rhodamine ^{19}F NP) and nanoparticles enriched with POPE (*1-palmitoyl-2-oleoyl-sn-glycero-3-phosphoethanolamine*, Figure 1A, Avanti Polar Lipid, Inc., Alabaster, AL). DSPE-PEG2000—PFCE nanoparticles were prepared by first coating a vial with 10 mg of DSPE-PEG2000 *(1,2-distearoyl-sn-glycero-3-phosphoethanolamine-N[methoxy(polyethylene glycol) -2000])*, Avanti Polar Lipid, Inc., Alabaster, AL) and then sonicating PFCE in the vial for 10 minutes on ice, to achieve a final concentration of 120 mM PFCE and 3.75 mM DSPE-PEG2000.

Zeta potential and other physical characteristics of nanoparticles. To study the physical characteristics of the above nanoparticles, dynamic light scattering (DLS) data was obtained using a Zetasizer Nano ZS instrument (Malvern Instruments, Worcestershire, UK), backscatter detection at 173 degrees and 635 nm laser module at 25°C. DLS provides information on a number of parameters including intensity-weighted z-average diameter, peak diameter and width, zeta (ζ) potential and polydispersity index (PdI). All these physical characteristics of the different nanoparticles were documented and are shown in Table 1. The z-average diameter was used for particle size since it gives an intensity-weighted harmonic diameter and is ideal for comparing different analyses. The PdI is extrapolated from the DLS function and quantitatively describes the particle size distribution best. PdI ranges from 0.01 for monodispersed particles to 0.7 for particles that have a very broad size distribution. The generated nanoparticles have a PdI < 0.3, indicating a relatively low polydispersity and narrow size distribution. The ζ potential was also indirectly determined by measuring the electrophoretic mobility of the nanoparticles under a constant voltage of 40 mV at 25°C.

Cryotransmission Electron Microscopy (Cryo-TEM) of Nanoparticles. Nanoparticle preparations were plunge-frozen onto glow discharged holey carbon grids (Quantifoil Micro Tools, Jena, Germany) in liquid ethane using the environment-controlled Vitrobot (Vitrobot MarkIV, FEI, Eindhoven, The Netherlands). Briefly, 3 μl of the nanoparticle solution were applied onto the grid which was held by tweezers inside the climate chamber (22°C, 100% relative humidity) of the Vitrobot. The solution was automatically blotted with filter paper leaving a thin film of the nanoparticle solution over the holes. The film was allowed to relax for 10 s prior to plunge freezing the sample on the grid in liquid ethane cooled near to its freezing point. Vitrified nanoparticle samples were imaged at −170°C using a Gatan cryo-transfer holder (Gatan 626, Gatan Inc. Pleasanton, USA) and standard low-dose imaging conditions (1 $e^-/Å^2.s$)[64] at a Tecnai G2 F20 transmission electron microscope (FEI, Oregon, USA), operated at 200 kV. Images were acquired at × 25,000 magnification on a 2k × 2k CCD camera (894 Ultrascan 1000, Gatan Inc., Pleasanton, USA).

DC Preparation. DCs were prepared from bone marrow (BM) suspensions as previously described[65]. Briefly, BM from femurs of C57BL/6 mice were grown in RPMI-1640 medium containing 10% FCS (Biochrom, Germany) and supplemented with 30 ng/ml GM-CSF. After 9 days in culture, DCs were incubated overnight in the presence of different ^{19}F nanoparticle preparations (end PFCE concentration ranging from 0.1–2 mM or 2–40 μmol/10^6 cells depending on the experiment) and 1 μg/ml full-length chicken EndoGrade ovalbumin (endotoxin conc.<1 EU/mg; Hyglos, Regensburg, Germany) and 0.5 μg/ml lipopolysaccharide (LPS). Following incubation, unbound ^{19}F nanoparticles were washed thoroughly from the culture dishes by washing with warm PBS. DCs were then harvested and prepared for the ensuing experiments.

Transmission Electron Microscopy (TEM) of DCs. DCs were fixed for 24 hours in PBS containing 2% glutaraldehyde and postfixed for 2 h with 1% osmium tetroxide. Cell pellets were then dehydrated in an ascending series of ethanol and embedded in Poly/Bed 812 (Polysciences, Eppelheim, Germany). Ultrathin sections were stained with uranyl acetate and lead citrate. Sections were imaged using a FEI Morgagni electron microscope (FEI, Eindhoven, The Netherlands) and iTEM software[5].

Laser Scanning Microscopy (LSM) of DCs. Intracellular fluorescence in DCs labeled with fluorescently-labeled nanoparticles was investigated using an LSM780 laser scanning microscope (Carl Zeiss MicroImaging GmbH, Jena, Germany). DCs were harvested on day 9, washed and seeded onto 4-chamber μ-slide plates (Ibidi GmbH, München, Germany) and after 4 h labeled with ^{19}F nanoparticles. Prior to LSM, unbound nanoparticles were washed thoroughly from the μ-slide plates by washing with warm culture medium.

Chemotaxis of DCs. DC motility towards chemokine following labeling with ^{19}F nanoparticles was determined using an agarose spot assay, as previously described[66]. Briefly, a 0.5% agarose solution was prepared, cooled to 40°C and mixed with chemokine (2000 ng/ml CCL21) or PBS (as –ve control); thereafter the agarose solution was pipetted as 10 μl spots onto 35-mm glass dishes (MatTek Corporation, Ashland, MA, USA). Following harvesting, DCs labeled with ^{19}F nanoparticles were introduced, together with culture medium, to the glass dishes and incubated for 4 h at 37°C (5% CO_2). The number of cells entering the agarose spot was determined by acquiring and fusing the microscope images for all the fields of views (FOV) making up the 10 μl agarose spot and counting all cells entering the corresponding spot. Image processing (including FOV fusion) and analysis (mainly cell counting) were done with Fiji (Image JA v1.47p, Open source software, NIH, Bethesda, Maryland, USA)[67]. For fusing all images the *Stitching* plugin was used and for counting the

number of cells within the spot a semi-automatic procedure using the *3D Objects Counter* analyze tool was used.

***In vitro* ^{19}F MR Spectroscopy (MRS).** Following harvesting, DCs (10^6) labeled with ^{19}F nanoparticles were fixed in 2% PFA and transferred to NMR tubes (external diameter: 4.947 ± 0.019 mm; Wall thickness: 0.043 ± 0.02 mm; VWR International GmbH, Darmstadt, Germany) and the uptake of ^{19}F nanoparticles monitored by ^{19}F spectroscopy. For this we employed an in-house built ^{19}F-tuned loop RF coil[5] for signal transmission and reception on a 9.4 T animal MRI scanner (Biospec 94/20 USR, Bruker Biospin, Ettlingen, Germany). A 90° block pulse with 10 kHz bandwidth was used for ^{19}F signal excitation. Spectral representation was done by performing a fast Fourier transformation (FFT) of the acquired free induction decay (FID). The amount of PFCE in each sample was calculated from the amplitude of the extrapolated monoexponential decay, at t = 0 of the FID, which is proportional to the ^{19}F concentration. A standard consisting of 500 mM PFCE was used as quantitative reference in all of these experiments. To determine the cell detection limit of ^{19}F labeling, voxel-based ^{19}F spectroscopy was performed in phantom experiments using increasing numbers of ^{19}F-labeled DCs. Fixed cells were suspended in 2% agarose and transferred to NMR tubes. An NMR tube holder made of acrylonitrile butadiene styrene (ABS) material was printed in-house using a 3D rapid prototyping system (BST 1200es, Dimension Inc., Eden Prairie, MN, USA) and customized to fit within a ^{1}H/ ^{19}F dual-tunable volume RF coil (35 mm inner diameter, 50 mm length; Rapid Biomed, Würzburg, Germany). For quantification of the ^{19}F content within the fixed cells in the NMR tubes, we employed Point REsolved SpectroScopy (PRESS) single voxel spectroscopy. For this purpose we placed a (5 × 5 × 5) mm^3 voxel within the region of interest covering the whole cells in agarose (Figure 6). Then we employed the FastMap[68] method for volume specific magnetic field (B_0) shimming. After B_0 shimming, the spectra were acquired using a PRESS-protocol for ^{19}F MRS: TR = 1500 ms, TE = 11.6 ms, voxel size (5 × 5 × 5) mm^3, number of repetitions = 512, scan time = 13 min.

***In vitro* ^{19}F and ^{1}H MRI of Dendritic Cells.** To image the fluorine content within the NMR tubes holding the fixed cells labeled with ^{19}F nanoparticle we performed 3D balanced steady state free precession (bSSFP) MRI on the 9.4 T animal MRI using a custom made ^{1}H/^{19}F dual-tunable volume birdcage resonator (Rapid Biomed, Würzburg, Germany) with 35 mm inner diameter and 50 mm length. The bSSFP sequence was chosen because it was also used for the in vivo experiments (described below); it has been shown previously to provide very high SNR, allowing for high spatiotemporal resolution image acquisitions in reasonable scan times, and because it produces very good soft tissue contrast, related to their T_2/T_1 relaxation times[69]. The scan parameters for bSSFP were as follows for proton (^{1}H) scans: TR = 6.7 ms, TE = 3.3 ms, flip angle = 30°, matrix = 256 × 128 × 128, field of view (FOV) = (5.8 × 2.9 × 5.8) cm^3, (227 × 227 × 453) μm^3 spatial resolution, number of excitations (NEX) = 1, scan time = 63 sec. For fluorine (^{19}F) scans the parameters for bSSFP were: TR = 3.6 ms, TE = 1.8 ms, flip angle = 30°, matrix = 64 × 32 × 32, FOV = (5.8 × 2.9 × 5.8) cm^3, (906 × 906 × 1813) μm^3 spatial resolution, NEX = 64, scan time = 16.85 min. To reduce banding artefacts across the SSFP images for both nuclei, 4 acquisitions were made using a 0°, 90°, 180° and 270° phase cycling scheme. The four acquisitions were combined by the sum of squares method using ImageJ (National Institutes of Health, USA, http://imagej.nih.gov/ij).

***In vivo* ^{19}F ^{1}H MRI and ^{19}F MRS.** Animal experiments were carried out in accordance with the guidelines provided and approved by the Animal Welfare Department of the LAGeSo State Office of Health and Social Affairs Berlin (Permit G0070/09: *Migration v. Immunzelltherapien*). Following harvesting, ^{19}F-labeled DCs were thoroughly washed in serum-free buffer and administered intradermally (5 × 10^6) into the hind limb of C57BL/6 mice and imaged between 4–18 h following injection. Shortly before and during the MR session, mice were anesthetized using a mixture of isoflurane as inhalation narcosis (0.5–1.5%), pressurized air and oxygen. Mice were imaged on the 9.4 T animal MRI using the same ^{1}H/^{19}F dual-tunable volume birdcage resonator as above (Rapid Biomed, Würzburg, Germany) and the same 3D bSSFP pulse sequences. The temperature of the mice was regulated at 37°C. The respiration rate and temperature was monitored by a remote monitoring system (Model 1025, SA Instruments Inc., NY, USA). For quantification of the ^{19}F content within the lymph node regions, we employed the PRESS sequence as above after placing a (3 × 3 × 3) mm^3 voxel around the lymph nodes. After FastMap for volume selective B_0 shimming, ^{19}F spectra within the lymph nodes were acquired using the same PRESS-protocol for ^{19}F MRS as above.

MR Data Collection and Analysis. For both in vivo and in vitro MR-measurements a Redhat RHEL4 system and Paravision v5 (Bruker Biospin, Ettlingen, Germany) software were used. NMR data processing, analysis and spectral presentation were performed in the Matlab environment (Matlab version 7.10.0.499, R2010a, The MathWorks, Inc., Natick, Massachusetts, USA). Differences between groups were analyzed by the student t-test. A p-value of $p < 0.05$ was considered to be statistically significant.

1. Dekaban, G. A. *et al.* Tracking and evaluation of dendritic cell migration by cellular magnetic resonance imaging. *Wiley interdisciplinary reviews. Nanomedicine and nanobiotechnology* **5**, 469–483, doi:10.1002/wnan.1227 (2013).
2. Palucka, K. & Banchereau, J. Dendritic-cell-based therapeutic cancer vaccines. *Immunity* **39**, 38–48, doi:10.1016/j.immuni.2013.07.004 (2013).
3. Ahrens, E. T., Flores, R., Xu, H. & Morel, P. A. In vivo imaging platform for tracking immunotherapeutic cells. *Nat.Biotechnol.* **23**, 983–987 (2005).
4. Srinivas, M., Heerschap, A., Ahrens, E. T., Figdor, C. G. & de Vries, I. J. (19)F MRI for quantitative in vivo cell tracking. *Trends Biotechnol.* **28**, 363–370 (2010).
5. Waiczies, H. *et al.* Perfluorocarbon particle size influences magnetic resonance signal and immunological properties of dendritic cells. *PLoS One* **6**, e21981 (2011).
6. Waiczies, H. *et al.* Monitoring Dendritic Cell Migration using 19F/1H Magnetic Resonance Imaging. *J Vis Exp.* **doi: 10.3791/50251** (2013).
7. de Vries, I. J. *et al.* Magnetic resonance tracking of dendritic cells in melanoma patients for monitoring of cellular therapy. *Nat.Biotechnol.* **23**, 1407–1413 (2005).
8. Brooks, R. A., Brunetti, A., Alger, J. R. & Di Chiro, G. On the origin of paramagnetic inhomogeneity effects in blood. *Magn Reson.Med.* **12**, 241–248 (1989).
9. Lee, N., Inouye, M. & Lauterbur, P. C. 19F- and 13C-NMR studies of a specifically labelled lipoprotein in the Escherichia coli membrane. *Biochemical and biophysical research communications* **78**, 1211–1218 (1977).
10. Holland, G. N., Bottomley, P. A. & Hinshaw, W. S. F-19 Magnetic-Resonance Imaging. *Journal of Magnetic Resonance* **28**, 133–136 (1977).
11. Liu, M. S. & Long, D. M. Perfluoroctylbromide as a diagnostic contrast medium in gastroenterography. *Radiology* **122**, 71–76 (1977).
12. Waiczies, H. *et al.* Visualizing brain inflammation with a shingled-leg radio-frequency head probe for 19F/1H MRI. *Sci.Rep.* **3**, 1280 (2013).
13. Bégué, J.-P. & Bonnet-Delpon, D. *Bioorganic and medicinal chemistry of fluorine.* (John Wiley & Sons, 2008).
14. Gerebtzoff, G., Li-Blatter, X., Fischer, H., Frentzel, A. & Seelig, A. Halogenation of drugs enhances membrane binding and permeation. *Chembiochem : a European journal of chemical biology* **5**, 676–684, doi:10.1002/cbic.200400017 (2004).
15. Smart, B. E. Fluorine substituent effects (on bioactivity). *J Fluorine Chem* **109**, 3–11, doi:Doi 10.1016/S0022-1139(01)00375-X (2001).
16. Banchereau, J. & Palucka, A. K. Dendritic cells as therapeutic vaccines against cancer. *Nature Reviews Immunology* **5**, 296–306 (2005).
17. Ahrens, E. T., Helfer, B. M., O'Hanlon, C. F. & Schirda, C. Clinical cell therapy imaging using a perfluorocarbon tracer and fluorine-19 MRI. *Magnetic Resonance in Medicine*, doi:doi: 10.1002/mrm.25454 (2014).
18. Balasubramanian, K. & Schroit, A. J. Aminophospholipid asymmetry: A matter of life and death. *Annu Rev Physiol* **65**, 701–734, doi:DOI 10.1146/annurev.physiol.65.092101.142459 (2003).
19. Smaby, J. M., Brockman, H. L. & Brown, R. E. Cholesterols Interfacial Interactions with Sphingomyelins and Phosphatidylcholines - Hydrocarbon Chain Structure Determines the Magnitude of Condensation. *Biochemistry-Us* **33**, 9135–9142, doi:Doi 10.1021/Bi00197a016 (1994).
20. Sprong, H., van der Sluijs, P. & van Meer, G. How proteins move lipids and lipids move proteins. *Nat Rev Mol Cell Biol* **2**, 504–513 (2001).
21. Felgner, J. H. *et al.* Enhanced gene delivery and mechanism studies with a novel series of cationic lipid formulations. *Journal of Biological Chemistry* **269**, 2550–2561 (1994).
22. Hyvönen, Z. *et al.* Dioleoyl phosphatidylethanolamine and PEG–lipid conjugates modify DNA delivery mediated by 1, 4-dihydropyridine amphiphiles. *Journal of Controlled Release* **99**, 177–190 (2004).
23. Antonelli, A. *et al.* Improved cellular uptake of functionalized single-walled carbon nanotubes. *Nanotechnology* **21**, 425101 (2010).
24. Caliceti, P. & Veronese, F. M. Pharmacokinetic and biodistribution properties of poly(ethylene glycol)-protein conjugates. *Advanced drug delivery reviews* **55**, 1261–1277 (2003).
25. Allen, T. M., Hansen, C., Martin, F., Redemann, C. & Yau-Young, A. Liposomes containing synthetic lipid derivatives of poly(ethylene glycol) show prolonged circulation half-lives in vivo. *Biochimica et biophysica acta* **1066**, 29–36 (1991).
26. Fang, C. *et al.* In vivo tumor targeting of tumor necrosis factor-α-loaded stealth nanoparticles: Effect of MePEG molecular weight and particle size. *European Journal of Pharmaceutical Sciences* **27**, 27–36, doi:http://dx.doi.org/10.1016/j.ejps.2005.08.002 (2006).
27. Zachowski, A. Phospholipids in animal eukaryotic membranes: transverse asymmetry and movement. *The Biochemical journal* **294 (Pt1)**, 1–14 (1993).
28. Virtanen, J. A., Cheng, K. H. & Somerharju, P. Phospholipid composition of the mammalian red cell membrane can be rationalized by a superlattice model. *Proceedings of the National Academy of Sciences of the United States of America* **95**, 4964–4969 (1998).
29. Emoto, K. *et al.* Redistribution of phosphatidylethanolamine at the cleavage furrow of dividing cells during cytokinesis. *Proceedings of the National Academy of Sciences* **93**, 12867–12872 (1996).
30. Riekhof, W. R. & Voelker, D. R. Uptake and utilization of lyso-phosphatidylethanolamine by Saccharomyces cerevisiae. *Journal of Biological Chemistry* **281**, 36588–36596 (2006).
31. Muller, K., Pomorski, T., Muller, P., Zachowski, A. & Herrmann, A. Protein-dependent translocation of aminophospholipids and asymmetric transbilayer distribution of phospholipids in the plasma membrane of ram sperm cells. *Biochemistry-Us* **33**, 9968–9974 (1994).

32. Laulagnier, K. *et al.* Mast cell-and dendritic cell-derived exosomes display a specific lipid composition and an unusual membrane organization. *Biochem. J* **380**, 161–171 (2004).
33. Steinman, R. M., Mellman, I. S., Muller, W. A. & Cohn, Z. A. Endocytosis and the recycling of plasma membrane. *The Journal of cell biology* **96**, 1–27 (1983).
34. Steinman, R. M., Brodie, S. E. & Cohn, Z. A. Membrane flow during pinocytosis. A stereologic analysis. *The Journal of cell biology* **68**, 665–687 (1976).
35. Wang, X. & Quinn, P. J. Cubic phase is induced by cholesterol in the dispersion of 1-palmitoyl-2-oleoyl-phosphatidylethanolamine. *Biochimica et Biophysica Acta (BBA)-Biomembranes* **1564**, 66–72 (2002).
36. Arouri, A., Dathe, M. & Blume, A. Peptide induced demixing in PG/PE lipid mixtures: a mechanism for the specificity of antimicrobial peptides towards bacterial membranes? *Biochimica et Biophysica Acta (BBA)-Biomembranes* **1788**, 650–659 (2009).
37. Fontana, G., Licciardi, M., Mansueto, S., Schillaci, D. & Giammona, G. Amoxicillin-loaded polyethylcyanoacrylate nanoparticles: Influence of PEG coating on the particle size, drug release rate and phagocytic uptake. *Biomaterials* **22**, 2857–2865, doi:http://dx.doi.org/10.1016/S0142-9612(01)00030-8 (2001).
38. Klibanov, A. L., Maruyama, K., Torchilin, V. P. & Huang, L. Amphipathic polyethyleneglycols effectively prolong the circulation time of liposomes. *FEBS Lett* **268**, 235–237 (1990).
39. Klibanov, A. L., Maruyama, K., Beckerleg, A. M., Torchilin, V. P. & Huang, L. Activity of amphipathic poly(ethylene glycol) 5000 to prolong the circulation time of liposomes depends on the liposome size and is unfavorable for immunoliposome binding to target. *Biochimica et Biophysica Acta (BBA) - Biomembranes* **1062**, 142–148, doi:http://dx.doi.org/10.1016/0005-2736(91)90385-L (1991).
40. Mori, A., Klibanov, A. L., Torchilin, V. P. & Huang, L. Influence of the steric barrier activity of amphipathic poly(ethyleneglycol) and ganglioside GM1 on the circulation time of liposomes and on the target binding of immunoliposomes in vivo. *FEBS Lett* **284**, 263–266, doi:http://dx.doi.org/10.1016/0014-5793(91)80699-4 (1991).
41. Koren, E., Apte, A., Sawant, R. R., Grunwald, J. & Torchilin, V. P. Cell-penetrating TAT peptide in drug delivery systems: Proteolytic stability requirements. *Drug delivery* **18**, 377–384, doi:10.3109/10717544.2011.567310 (2011).
42. Lukyanov, A., Gao, Z., Mazzola, L. & Torchilin, V. Polyethylene Glycol-Diacyllipid Micelles Demonstrate Increased Accumulation in Subcutaneous Tumors in Mice. *Pharm Res* **19**, 1424–1429, doi:10.1023/a:1020488012264 (2002).
43. Torchilin, V. P. Micellar Nanocarriers: Pharmaceutical Perspectives. *Pharm Res* **24**, 1–16, doi:10.1007/s11095-006-9132-0 (2007).
44. Kale, A. A. & Torchilin, V. P. "Smart" Drug Carriers: PEGylated TATp-Modified pH-Sensitive Liposomes. *Journal of Liposome Research* **17**, 197–203, doi:10.1080/08982100701525035 (2007).
45. Sydow, K., Torchilin, V. P. & Dathe, M. Lipopeptide-modified PEG-PE-based pharmaceutical nanocarriers for enhanced uptake in blood–brain barrier cells and improved cytotoxicity against glioma cells. *European Journal of Lipid Science and Technology* **116**, 1174–1183, doi:10.1002/ejlt.201300373 (2014).
46. Sauer, I., Dunay, I. R., Weisgraber, K., Bienert, M. & Dathe, M. An apolipoprotein E-derived peptide mediates uptake of sterically stabilized liposomes into brain capillary endothelial cells. *Biochemistry-Us* **44**, 2021–2029 (2005).
47. Felgner, J. H. *et al.* Enhanced gene delivery and mechanism studies with a novel series of cationic lipid formulations. *Journal of Biological Chemistry* **269**, 2550–2561 (1994).
48. Sydow, K., Torchilin, V. P. & Dathe, M. Lipopeptide-modified PEG-PE-based pharmaceutical nanocarriers for enhanced uptake in blood-brain barrier cells and improved cytotoxicity against glioma cells. *European Journal of Lipid Science and Technology* **116**, 1174–1183, doi:10.1002/ejlt.201300373 (2014).
49. Ramezani, M., Khoshhamdam, M., Dehshahri, A. & Malaekeh-Nikouei, B. The influence of size, lipid composition and bilayer fluidity of cationic liposomes on the transfection efficiency of nanolipoplexes. *Colloid Surface B* **72**, 1–5, doi:DOI 10.1016/j.colsurfb.2009.03.018 (2009).
50. van Dommelen, S. M. *et al.* Microvesicles and exosomes: Opportunities for cell-derived membrane vesicles in drug delivery. *Journal of Controlled Release* **161**, 635–644, doi:DOI 10.1016/j.jconrel.2011.11.021 (2012).
51. Larson, M. C., Woodliff, J. E., Hillery, C. A., Kearl, T. J. & Zhao, M. Phosphatidylethanolamine is externalized at the surface of microparticles. *Biochimica et biophysica acta* **1821**, 1501–1507, doi:10.1016/j.bbalip.2012.08.017 (2012).
52. Wolf, P. The nature and significance of platelet products in human plasma. *British journal of haematology* **13**, 269–288 (1967).
53. Roseblade, A. *et al.* Cell-derived microparticles: new targets in the therapeutic management of disease. *Journal of pharmacy & pharmaceutical sciences : a publication of the Canadian Society for Pharmaceutical Sciences, Societe canadienne des sciences pharmaceutiques* **16**, 238–253 (2013).
54. Hargett, L. A. & Bauer, N. N. On the origin of microparticles: From "platelet dust" to mediators of intercellular communication. *Pulmonary circulation* **3**, 329–340, doi:10.4103/2045-8932.114760 (2013).
55. Deregibus, M. C. *et al.* Endothelial progenitor cell derived microvesicles activate an angiogenic program in endothelial cells by a horizontal transfer of mRNA. *Blood* **110**, 2440–2448, doi:10.1182/blood-2007-03-078709 (2007).
56. Saulnier, P., Foussard, F., Boury, F. & Proust, J. Structural properties of asymmetric mixed-chain phosphatidylethanolamine films. *Journal of colloid and interface science* **218**, 40–46 (1999).
57. Malcharek, S., Hinz, A., Hilterhaus, L. & Galla, H.-J. Multilayer structures in lipid monolayer films containing surfactant protein C: effects of cholesterol and POPE. *Biophysical Journal* **88**, 2638–2649 (2005).
58. Epand, R. M. & Bottega, R. Determination of the phase behaviour of phosphatidylethanolamine admixed with other lipids and the effects of calcium chloride: implications for protein kinase C regulation. *Biochimica et Biophysica Acta (BBA) - Biomembranes* **944**, 144–154, doi:http://dx.doi.org/10.1016/0005-2736(88)90427-0 (1988).
59. Crowley, J. J., Treistman, S. N. & Dopico, A. M. Distinct Structural Features of Phospholipids Differentially Determine Ethanol Sensitivity and Basal Function of BK Channels. *Mol Pharmacol* **68**, 4–10, doi:10.1124/mol.105.012971 (2005).
60. Gratton, S. E. A. *et al.* The effect of particle design on cellular internalization pathways. *Proceedings of the National Academy of Sciences* **105**, 11613–11618, doi:10.1073/pnas.0801763105 (2008).
61. Champion, J. A. & Mitragotri, S. Role of target geometry in phagocytosis. *Proceedings of the National Academy of Sciences of the United States of America* **103**, 4930–4934, doi:10.1073/pnas.0600997103 (2006).
62. Yan, L.-T. & Xie, X.-M. Computational modeling and simulation of nanoparticle self-assembly in polymeric systems: Structures, properties and external field effects. *Progress in Polymer Science* **38**, 369–405 (2013).
63. van der Veen, R. M., Kwon, O.-H., Tissot, A., Hauser, A. & Zewail, A. H. Single-nanoparticle phase transitions visualized by four-dimensional electron microscopy. *Nature chemistry* **5**, 395–402 (2013).
64. Adrian, M., Dubochet, J., Lepault, J. & McDowall, A. W. Cryo-electron microscopy of viruses. *Nature* **308**, 32–36 (1984).
65. Bendix, I. *et al.* MAPK3 deficiency drives autoimmunity via DC arming. *European journal of immunology* **40**, 1486–1495, doi:10.1002/eji.200939930 (2010).
66. Wiggins, H. & Rappoport, J. An agarose spot assay for chemotactic invasion. *BioTechniques* **48**, 121–124, doi:10.2144/000113353 (2010).
67. Schindelin, J. *et al.* Fiji: an open-source platform for biological-image analysis. *Nat Methods* **9**, 676–682, doi:Doi 10.1038/Nmeth.2019 (2012).
68. Gruetter, R. Automatic, localized in vivo adjustment of all first- and second-order shim coils. *Magnetic resonance in medicine : official journal of the Society of Magnetic Resonance in Medicine/Society of Magnetic Resonance in Medicine* **29**, 804–811 (1993).
69. Economopoulos, V., Noad, J. C., Krishnamoorthy, S., Rutt, B. K. & Foster, P. J. Comparing the MRI appearance of the lymph nodes and spleen in wild-type and immuno-deficient mouse strains. *PLoS One* **6**, e27508, doi:10.1371/journal.pone.0027508 (2011).

Acknowledgments

This study was funded by the *Deutsche Forschungsgemeinschaft* to SW (DFG WA 2804). We thank Ms. Stefanie Kox and Ms. Yvonne Balke for excellent technical support.

Author contributions

S.W., S.L. and T.N. contributed to the manuscript text; S.W., S.L., K.S., S.D., M.C.K., C.M., D.L., I.S. and B.F. performed the experiments; S.W., S.L., H.R.M., H.W., M.D. and A.P. analyzed the data. All authors reviewed the manuscript.

Additional information

Competing financial interests: S.W. received research grants and poster honoraria from Novartis. K.S. was partly financed by the DFG (DA 324/9-1). H.W. is employed by and T.N. is founder of MRI.TOOLS GmbH. T.N. received speaker honoraria from Siemens Healthcare, Erlangen, Germany. M.D. now works with Siemens Healthcare. S.L., S.D., M.C.K., C.M., D.L., I.S., H.R.M., B.F., M.D. and A.P. have nothing to disclose.

How to cite this article: Waiczies, S. *et al.* Anchoring Dipalmitoyl Phosphoethanolamine to Nanoparticles Boosts Cellular Uptake and Fluorine-19 Magnetic Resonance Signal. *Sci. Rep.* **5**, 8427; DOI:10.1038/srep08427 (2015).

2.3 Improving signal sensitivity for fluorine MR methods

This chapter builds on **publication 3** "Enhanced Fluorine-19 MRI Sensitivity using a Cryogenic Radiofrequency Probe: Technical Developments and Ex Vivo Demonstration in a Mouse Model of Neuroinflammation" published in Scientific Reports (Waiczies et al., 2017a).

Our efforts to increase signal sensitivity for ^{19}F MRI in **publication 2** (Waiczies et al., 2015) were related to the signal source itself: we increased the ^{19}F signal by increasing the cell label load with DPPE ^{19}F nanoparticles (Waiczies et al., 2015). However, SNR limitations remain a bottleneck prohibiting the detection and quantification of cellular and pharmacological therapies with ^{19}F MRI. In a further effort to increase SNR to follow therapies in vivo, here we focused on the MR method.

Physical factors such as radio frequency (RF) coil sensitivities and magnetic field strengths also dictate detection limits. A wider spectrum of method developments are necessary for ^{19}F MRI to provide its unprecedented opportunities in medical research (Waiczies et al., 2019). To boost SNR for ^{19}F MRI, I acquired further DFG funding to develop the first ^{19}F transceive quadrature cryogenically-cooled RF probe (CRP) in cooperation with Bruker Biospin (Ettlingen, Germany) (Waiczies et al., 2017a). Cryogenic cooling increases SNR by reducing thermal noise (Niendorf et al., 2015).

The ^{19}F-CRP provided a superior SNR that was over an order of magnitude beyond that of a room temperature RF coil of similar size (**Figure 4** in own work 3 (Waiczies et al., 2017a)). We reached a detection limit in the order of $10^{15.19}$F atoms per imaging voxel when using the ^{19}F-CRP, in comparison to $10^{16.19}$F atoms with the ^{19}F RT-coil. A major limitation of the ^{19}F-CRP is a strong signal loss with increasing distance from the CRP surface as a result of non-uniform B_1^+ typical of surface coils (**Figure 3** in own work 3 (Waiczies et al., 2017a)). The signal losses away from the coil hamper signal quantification. Recently we reported a method to correct B_1 variations for ^{1}H-surface coils and RARE ^{1}H-MRI by experimentally-modelling signal intensity as a function of FA and T_1 (Delgado et al., 2020) and are currently implementing this correction method for images acquired with the ^{19}F-CRP. One important utilization of the SNR gain is to acquire more spatially resolved and thereby detailed ^{19}F MR images (**Figure 5** in own work 3 (Waiczies et al., 2017a)). When using an isotropic spatial resolution of 150 µm, the majority of the ^{19}F signals obtained by the ^{19}F-CRP were not detected with the RT coil (**Figure 5** in own work 3 (Waiczies et al., 2017a)):

SCIENTIFIC REPORTS

OPEN

Received: 14 March 2017
Accepted: 19 July 2017
Published online: 29 August 2017

Enhanced Fluorine-19 MRI Sensitivity using a Cryogenic Radiofrequency Probe: Technical Developments and *Ex Vivo* Demonstration in a Mouse Model of Neuroinflammation

Sonia Waiczies[1], Jason M. Millward[1], Ludger Starke[1], Paula Ramos Delgado[1], Till Huelnhagen[1], Christian Prinz[1], Daniel Marek[2], Didier Wecker[3], Ralph Wissmann[3], Stefan P. Koch[4], Philipp Boehm-Sturm[4], Helmar Waiczies[5], Thoralf Niendorf[1,5,6] & Andreas Pohlmann[1]

Neuroinflammation can be monitored using fluorine-19 (^{19}F)-containing nanoparticles and ^{19}F MRI. Previously we studied neuroinflammation in experimental autoimmune encephalomyelitis (EAE) using room temperature (RT) ^{19}F radiofrequency (RF) coils and low spatial resolution ^{19}F MRI to overcome constraints in signal-to-noise ratio (SNR). This yielded an approximate localization of inflammatory lesions. Here we used a new ^{19}F transceive cryogenic quadrature RF probe (*^{19}F-CRP*) that provides the SNR necessary to acquire superior spatially-resolved ^{19}F MRI. First we characterized the signal-transmission profile of the *^{19}F-CRP*. The *^{19}F-CRP* was then benchmarked against a RT ^{19}F/^{1}H RF coil. For SNR comparison we used reference compounds including ^{19}F-nanoparticles and *ex vivo* brains from EAE mice administered with ^{19}F-nanoparticles. The transmit/receive profile of the *^{19}F-CRP* diminished with increasing distance from the surface. This was counterbalanced by a substantial SNR gain compared to the RT coil. Intraparenchymal inflammation in the *ex vivo* EAE brains was more sharply defined when using 150 μm isotropic resolution with the *^{19}F-CRP*, and reflected the known distribution of EAE histopathology. At this spatial resolution, most ^{19}F signals were undetectable using the RT coil. The *^{19}F-CRP* is a valuable tool that will allow us to study neuroinflammation with greater detail in future *in vivo* studies.

Central nervous system (CNS) inflammation, as occurs in multiple sclerosis (MS), involves immune cell recruitment from the periphery into the CNS, resulting in tissue destruction and neurodegeneration[1]. During active disease, a massive infiltration of immune cells is predominant, particularly around white matter lesions. T cells find their way into the white matter via a disruption of the blood brain barrier[2]. In MS, T cells may also enter the CNS grey matter such as the cerebral cortex via the meninges[3,4]. Even in the cerebellum, extensive grey matter pathology in secondary progressive MS is linked to inflammation of the subarachnoid space[5]. Studies of the animal model of MS, experimental autoimmune encephalomyelitis (EAE), have helped identify mechanisms of cell migration between the periphery, CNS and lymphatic system during neuroinflammation[6–8]. This is a topic of active interest, with divergent views regarding immune cell entry and exit in the CNS (inside-out versus

[1]Berlin Ultrahigh Field Facility (B.U.F.F.), Max Delbrück Center for Molecular Medicine in the Helmholtz Association, Berlin, Germany. [2]Bruker BioSpin AG, Fällanden, Switzerland. [3]Bruker BioSpin MRI, Ettlingen, Germany. [4]Department of Experimental Neurology, Center for Stroke Research Berlin (CSB), Charité Core Facility 7T Experimental MRIs, and NeuroCure, Charité University Medicine Berlin, Berlin, Germany. [5]MRITOOLS GmbH, Berlin, Germany. [6]Experimental and Clinical Research Center, a joint cooperation between the Charité Medical Faculty and the Max Delbrück Center for Molecular Medicine in the Helmholtz Association, Berlin, Germany. Correspondence and requests for materials should be addressed to S.W. (email: sonia@waiczies.de)

outside-in hypotheses) in MS[9,10]. Therefore there is an acute need for more precise and non-invasive methods that support longitudinal studies of inflammatory cell migration during disease progression to resolve some of the discrepancies in the literature.

Previously we studied immune cell infiltration in EAE brains using fluorine-19 (^{19}F)-loaded nanoparticles (NPs) and a room temperature (RT) dual-tuned ^{19}F/^{1}H radio frequency (RF) volume resonator[11]. Intravenously administered NPs are taken up by inflammatory cells during their migration from the systemic circulation into the inflamed organ[11–17]. Although tracking of inflammation following intravenous ^{19}F-NP administration is one application for ^{19}F MRI, several other state-of-the-art applications for ^{19}F imaging exist. These include *in vivo* tracking of cell therapies labeled in culture with ^{19}F-NPs prior to their adoptive transfer[18–20] and intracellular oximetry using ^{19}F-NP emulsions[21] to study changes in pO2 in tumor cells during therapy[22].

One major limitation of ^{19}F MRI is the low signal-to-noise ratio (SNR). The acquisition method is one aspect of ^{19}F MRI that influences SNR. SNR efficiency of the most commonly used acquisition methods — RARE (Rapid Acquisition with Relaxation Enhancement), UTE (Ultra-short Echo Time), and bSSFP (Balanced Steady-State Free Precession) — depends on the T_1 and T_2 values of the particular ^{19}F compound studied[23]. For most T_1 and T_2 combinations, especially those pertaining to intracellular ^{19}F-NPs, bSSFP and 3D RARE sequences have the highest SNR sensitivity. However, while bSSFP often has a higher SNR efficiency, it is not always the method of choice due to the high RF energy deposition associated with longer acquisition times, and pronounced banding artifacts. The SNR and the sensitivity of the radio frequency (RF) probe used are main determinants that dictate the level of spatial resolution. Factors to be kept in mind when designing a probe include the geometry, the filling factor and the homogeneity of the B_1^+ transmit field.

The SNR constraint limited spatial resolution to approximately 600 μm when detailing the dynamics of inflammation during EAE[11]. Given this limited precision, the location of inflammatory cells within the brain was not sharply defined. To overcome the sensitivity constraints in ^{19}F MR and improve detail of inflammatory cell location, we applied the concept of cryogenically-cooling RF coil hardware to improve SNR by reducing thermal noise. Until now this technology has been available only for ^{1}H, ^{13}C and ^{31}P small animal MRI. Here we made use of the first ^{19}F transceive cryogenically-cooled RF probe (*^{19}F-CRP*) to substantially boost SNR beyond that of available RT coils, thus facilitating the acquisition of better spatially-resolved images. In this study we evaluated the advantages and disadvantages of the *^{19}F-CRP* for imaging neuroinflammation.

Methods

Radio frequency coils. The performance of a novel transceive ^{19}F cryogenic quadrature RF surface probe at 9.4T (*^{19}F-CRP*, $f \sim 376$ MHz) was compared to a dual-tunable ^{19}F/^{1}H volume resonator ($\phi_{in} = 18.4$ mm, $l_{total} = 39$ mm), previously developed for imaging mouse brain inflammation[11]. The *^{19}F-CRP* has a similar geometry to the existing Bruker ^{1}H quadrature CryoProbes[24]. The rectangular transceive copper coil elements are overlapping side-by-side on a cylindrical surface ($r \sim 11$ mm, axis parallel to the main magnetic field direction). The outer dimensions (O.D.) of one coil element are: 16×20 mm^2 [arc length ($\phi \times z$)] and the total O.D. are: 27×20 mm^2 [$\phi \times z$]. The *^{19}F-CRP* operates at ~28 K with a dual cooled preamplifier at the base running at ~77 K. Constant cooling is ensured by a closed loop system connected to a remote cryo-cooler. The RF coil is thermally insulated by a vacuum separating it from the surrounding ceramic finger (Fig. 1A). The outer surface of the RF finger is equipped with a temperature sensor and kept at a temperature of choice (35 °C) using a resistive heater. The SNR gain of this CRP relative to a RT coil with similar geometry is expected to be comparable to existing 400 MHz proton CryoProbes[24,25].

Experimental setup. To evaluate the *^{19}F-CRP* performance, three different phantom-setups were prepared (Fig. 1B):

Setup 1 (high concentration ^{19}F): a 10 ml syringe (inner/outer diameter = 17.0 mm/15.5 mm) for the *^{19}F-CRP* and a 5 ml syringe (I.D./O.D. = 13.5/12.0 mm) for the *^{19}F/^{1}H RT-coil*, both containing the same ^{19}F reference compound to study $\boldsymbol{B}_1^+$ and compare spatial SNR. The reference compound was 33% v/v 2,2,2-Trifluoroethanol (TFE, Sigma-Aldrich, Germany) in water.

Setup 2 (^{19}F nanoparticles): NMR tubes (I.D./O.D. = 4.0/5.0 mm) containing different concentrations of perfluoro-15-crown-5-ether (PFCE) loaded nanoparticles to compare ^{19}F signal sensitivity as a function of the number of ^{19}F atoms. Nanoparticles were prepared by emulsifying 1200 mM PFCE (Fluorochem, UK) with Pluronic F-68 (Sigma-Aldrich, Germany) using a titanium sonotrode (Sonopuls GM70, Bandelin, Germany) as previously described[26]. The PFCE nanoparticle stock was then diluted to 25 mM, 50 mM, 100 mM, 200 mM, 400 mM and 600 mM nanoparticle suspensions. NMR tubes containing different nanoparticle concentrations were placed below the CRP using a spacer of 0.75 mm thickness to mimic the distance of the mouse brain from the CRP surface in *in vivo* applications.

Setup 3 (mouse brain): *Ex vivo* tissues from fixed EAE mice embedded in 15-ml tubes, for comparing ^{19}F signal sensitivity and anatomical detail. All experiments were conducted in accordance with procedures approved by the Animal Welfare Department of the State Office of Health and Social Affairs Berlin (LAGeSo), and conformed to national and international guidelines to minimize discomfort to animals (86/609/EEC). EAE was induced as described previously[11] in SJL/J mice (n = 6, female, 6–8 weeks old). Five days following EAE induction, mice were administered nanoparticles (10μmol PFCE) intravenously each day for 5 d as described previously[11]. EAE mice were transcardially perfused with 20 ml PBS followed by 20 ml 4% paraformaldehyde (PFA) following terminal anesthesia. Mice were cleared from external pelt, extremities, and abdominal tissues. Brain, spinal cord and neck lymphoid organs were preserved *in situ* within the skull and vertebral column. The tissues were transferred into a 15 ml tube filled with 4% PFA and stored at 4 °C.

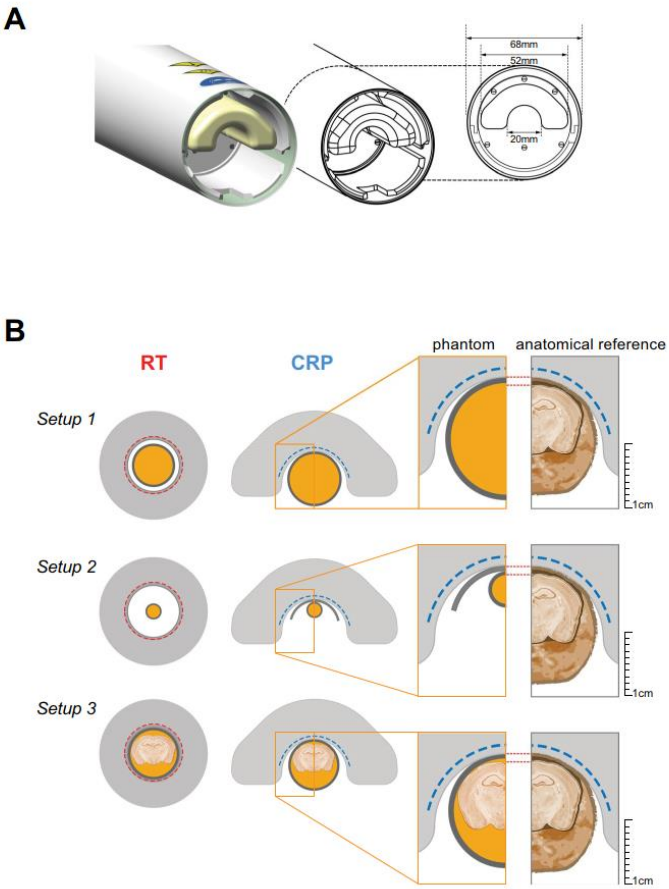

Figure 1. ^{19}F Cryogenic Radiofrequency Probe design and experimental setup. (**A**) Side view of the *^{19}F-CRP* showing its geometry including external protective cylinder and an inner ceramic probe head that encloses the loop coil elements (not shown). The inner diameter dimension for the inner ceramic structure is shown in the cross-sectional view (right). (**B**) Three different experimental setups that were used to assess the *^{19}F-CRP* quality. Shown are Setup 1 for the high concentration ^{19}F phantom (*upper panel*), Setup 2 for the ^{19}F nanoparticle phantoms (*middle panel*) and Setup 3 for the mouse brain phantom (*lower panel*). The dimension of the phantom setups are to scale with the dimensions of both *^{19}F-CRP* and RT coil and an anatomic reference is shown on the right for comparison. The nanoparticles used in this study had the following physical characteristics: Z-average diameter = 164 nm, PdI = 0.06, z-Potential = 0.19 mV.

MRI Methods and Data Analysis. All experiments were carried out on a 9.4 T small animal MR system (BioSpec 94/20, Bruker BioSpin MRI, Ettlingen, Germany) operating at 400 MHz (^{1}H) and 376 MHz (^{19}F).

Transmit Field Characteristics. Using a 15 ml tube containing 33% TFE in water (*Setup 1*), we acquired 2D-FLASH images (TR = 20 s, TE = 4.9 ms, FOV = (20 × 20) mm^2, matrix = 256 × 256, 1 slice of 4 mm thickness, averages = 1, TA = 1 h 25 min) with nominal excitation flip angles $\alpha = 60°$ and $2\alpha = 120°$ and calculated the actual flip angles (FA) using the double-angle method[27,28]:

$$FA = \arccos(SI_{2\alpha}/(2SI_{\alpha})) \quad (1)$$

with SI_{α} and $SI_{2\alpha}$ being the signal intensities obtained with α and 2α. FA maps were normalized to a nominal angle of 90° by multiplying by the factor $90°/\alpha$.

SNR assessment in phantoms. To measure the spatial distribution of SNR at increasing distances from the *^{19}F-CRP* surface, a high-concentration ^{19}F phantom (*Setup 1*) and an axial 2D-RARE scan (TR = 10 s, TE = 6.2 ms,

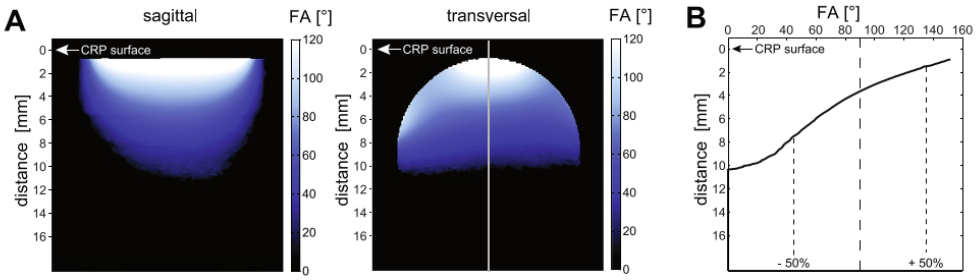

Figure 2. Transmission B_1^+ Field (B_1^+) for the *^{19}F-CRP*. (**A**) Flip angle maps acquired in vertical and transversal orientation using a high concentration ^{19}F phantom (Setup 1). (**B**) Profile plot of the FA along the vertical axis that depicts the change in FA with increasing distance to the CRP surface.

ETL = 256, FOV = (25.6 × 25.6) mm², matrix = 256 × 256, averages = 100, TA = 17 m) was used. To quantify and compare SNR in a way more relevant for brain inflammation, we measured SNR as a function of the number of ^{19}F atoms using phantoms containing different concentrations of ^{19}F nanoparticles (*Setup 2*, Fig. 1B). Measurements involved 2D-RARE scans (TR = 3000 ms, TE = 10.8 ms, ETL = 8, FOV = (10 × 10)mm², matrix = 96 × 96, averages = 1, TA = 36 s) with varying slice thicknesses: 0.4/1.0/1.2/2.0/3.6/4.7/6.0 mm to measure SNR as a function of the number of ^{19}F atoms.

SNR was calculated by dividing signal S_m from magnitude images by background standard deviation σ_m, and corrected to compensate for the non-Gaussian distribution[29]. For single channel RF coils, intensity values of MR images follow a Rician distribution[30,31]. For a two-receiver, quadrature system (*^{19}F-CRP*), they follow a non-central chi distribution[32]. We estimated the true SNR from the S_m and background σ_m using

$$SNR = \frac{S}{\sigma} = \frac{S_m}{\sigma_m} \cdot \frac{f_S(S_m, \sigma_m)}{1/c_\sigma} \quad (2)$$

where c_σ is 0.655 (Rician) and 0.687 (chi), and the correction function f_S is derived from the respective distribution's mean[30,32]. For *Setup* 2, a single SNR value was determined from the mean signal intensity over a central circular region-of-interest covering ~90% of pixels. The number of atoms per image pixel was estimated from nanoparticle concentration and voxel size.

Ex vivo mouse brain ^{19}F and ^{1}H MRI (Setup 3). ^{19}F MR images of the EAE mouse brain were acquired using 3D-RARE: TR = 800 ms, TE = 5.1 ms, ETL=33, FOV=(30 × 20 × 20) mm³, matrix = 195 × 65 × 65 zero-filled to 195 × 130 × 130, averages = 384, TA = 11 h. ^{1}H MR images were acquired using 3D-FLASH (TR = 50 ms, TE = 12.5 ms, FOV = (30 × 20 × 20) mm³, matrix = 384 × 256 × 284 zero-filled to 768 × 512 × 512, averages = 2, TA = 6 h 3 min). ^{19}F MR images from the *^{19}F-CRP* were registered with those from the *^{19}F/^{1}H RT-coil*. Since the *^{19}F-CRP* has no *^{19}F/^{1}H* dual resonant capacity, we registered the CRP ^{19}F images onto the RT ^{19}F images in order for both ^{19}F images (RT and CRP) to be spatially aligned with the RT ^{1}H images. For this, three repetitions of the RT ^{19}F scan were averaged to achieve sufficient ^{19}F signal with the RT-coil and an effective registration. Co-registration was applied using affine diffeomorphic image registration (12 degrees of freedom) by explicit B-spline regularization[33], which is part of the Advanced Normalisation Tool (ANTs)[34]. Registration of the Allen brain atlas[35] to the ^{1}H image was achieved as follows: (1) ^{1}H image and atlas template were segmented in grey matter (GM), white matter (WM) and cerebrospinal fluid (CSF) probability maps with SPMMouse (http://www.spmmouse.org/)[36], (2) two synthetic images were generated with signal intensity in each voxel I(x,y,z) = 1.0 × GM (x y, z) + 2.0 × WM + 4.0 × CSF, i.e. one registered with the ^{1}H image and one registered with the atlas, (3) both synthetic images were warped to the ^{1}H image using nonlinear B-spline registration in ELASTIX (http://elastix.isi.uu.nl/)[37]. Raw ^{1}H MRI files were converted to NIFTI-format and brains segmented with ITK-SNAP version 3.4.0[38]. For 2D representation of ^{19}F/^{1}H MRI we performed overlays of the raw ^{19}F MR data with SNR-based scaling using Matlab. For 3D representation we used ImageJ (National Institutes of Health, USA, http://imagej.nih.gov/ij).

Results

Transmit field characteristics of the *^{19}F-CRP*. Since transceive surface coils do not achieve a spatially uniform excitation like volume resonators[24], we assessed the B_1^+ characteristics of the *^{19}F-CRP* (Fig. 2A) and quantified changes in FA. A profile plot of the FA along the vertical axis (Fig. 2B) reveals a strong FA decrease with increasing distance from the CRP surface. Across a distance of 10.4 mm the measured FA varies between 152° and 0°. From the nominal FA of 90° the actual FA deviates up to 50% within a range of 6.0 mm (1.5–7.5 mm from CRP surface).

SNR assessment in phantoms. To study the SNR performance of the *^{19}F-CRP*, we first used a high ^{19}F concentration (33% TFE solution) (Fig. 3A). The transversal spin-echo ^{19}F MR images demonstrate a homogenous SNR for the RT coil and a spatially varying SNR for the CRP (Fig. 3A). We adjusted the reference pulse

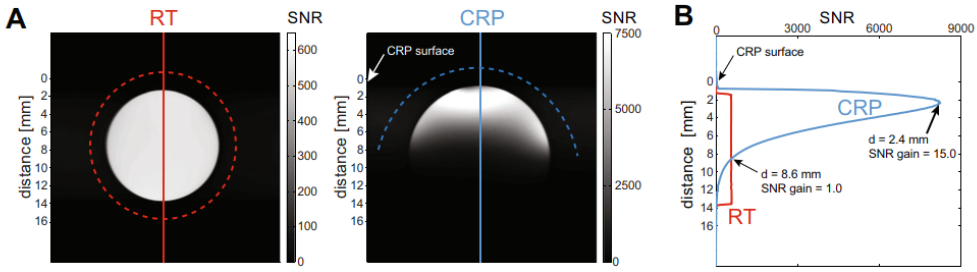

Figure 3. Comparison of SNR between the *^{19}F-CRP* and *^{19}F/^{1}H RT-coil*. (**A**) Cross-sectional spin-echo ^{19}F MR images of a TFE phantom acquired with the RT RF coil (left) and the CRP (right). The CRP showed a spatially varying sensitivity that is typical for transceive surface coils. (**B**) Plots of the SNR profile along the vertical axis at the center of the phantom. For the RT volume resonator (red curve) the SNR was very uniform within the phantom. In contrast, for the CRP the SNR drops rapidly with increasing distance to the RF coil. For this particular reference pulse power, SNR reached its maximum at 2.4 mm from the CRP surface, where it is 15-fold higher than the SNR of the RT coil. Beyond a distance of 8.1 mm the *^{19}F-CRP* did not provide any SNR gain with regard to the *^{19}F/^{1}H RT-coil*.

power in order to avoid substantial signal loss at the dorsal side of the brain. Using this reference pulse power, the SNR reached its peak at a distance of 2.4 mm, where it was ~15-fold higher than the SNR of the RT coil (Fig. 3B). The SNR of both RF coils are approximately equal at a distance of 8.6 mm from the CRP.

We next investigated the detection limits for both coils by measuring ^{19}F nanoparticles, as a biologically relevant preparation. We employed concentrations of PFCE (25 mM–200 mM) yielding a range of 10^{15}–10^{18} ^{19}F atoms per voxel (Fig. 4A). Qualitatively, we reached a detection limit in the order of 10^{15} fluorine atoms using the *^{19}F-CRP*, compared to 10^{16} fluorine atoms with the *^{19}F RT-coil*. Specifically, an SNR of 3.0 was achieved with $(0.1 \times 0.1 \times 0.4)$ mm³ voxels of a 25 mM PFCE concentration (equating to 5.2×10^{15} fluorine atoms) when using the *^{19}F-CRP*. In contrast an SNR of 2.4 was achieved with $(0.1 \times 0.1 \times 1.2)$ mm³ voxels of a 100 mM PFCE concentration (equating to 6.2×10^{16} fluorine atoms) when using the *^{19}F- RT-coil*. In both cases the measurement time was 36 s. MR images with an SNR value below 2 were not sharply defined. To estimate SNR provided by the *^{19}F-CRP* compared to the *^{19}F/^{1}H RT-coil*, we used SNR = 2 as a cutoff equating to $\sim 5 \times 10^{16}$ (RT) and $\sim 4 \times 10^{15}$ (CRP) fluorine atoms per voxel. Next we prepared higher concentrations of ^{19}F nanoparticles (200 mM to 1200 mM) to achieve SNR values well above 2, spanning a range of 10^{17}–10^{19} atoms per voxel. From these experiments we calculated an SNR gain of ~16 for the *^{19}F-CRP* when compared to the *^{19}F/^{1}H RT-coil* (Fig. 4B).

High spatially-resolved ^{19}F MRI. An important utilization of the SNR gain is to localize cell infiltrates in the brain with more detail. Previously areas of inflammation were detected using spatial resolutions greater than 600 μm[11]. Here we exploited the superior SNR of the *^{19}F-CRP*, and used an isotropic spatial resolution of 150 μm. *Ex vivo* MR images obtained with the *^{19}F-CRP* from an exemplary EAE mouse (day 10 following EAE induction, score = 1.25) show a more precise distribution of intraparenchymal inflammation. At this spatial resolution, the majority of the ^{19}F signals obtained by the *^{19}F-CRP* were not detected with the RT coil (Fig. 5A–C). In addition we show similar inflammatory patterns in a pre-symptomatic mouse, also sacrificed on day 10 following EAE induction (Supplementary Figure). Within the cerebellum, inflammatory infiltrates were mostly localized within the white matter of the arbor vitae, particularly near deep cerebellar nuclei (Fig. 5B). Clearly delineated inflammatory areas were found in grey matter regions running adjacent to white matter tracts in the cerebellum (Fig. 5A). This is consistent with the expected patterns of inflammation in the EAE model[39,40], also as observed in our own prior studies[11,41,42]. Using the *^{19}F-CRP*, we also observed strong ^{19}F signals in the cerebrum emanating from the striatum and pallidum appearing continuous with ^{19}F signals from the third ventricle (Fig. 5A). Additionally, clear extraparenchymal meningeal inflammation could be seen, consistent with recent reports[43–45]. Especially strong inflammatory signals were observed along the dorsal surface of the brain, including meningeal regions lining fissures between the cerebellar lobules. These inflammatory regions extended ventrally to the prepyramidal fissure, paraflocculus and lateral recess of the fourth ventricle. A dominant ^{19}F signal was observed around the meninges lining the ventral part of the retrosplenial area of the cerebral cortex (Fig. 5B), spreading caudally towards the cerebellum, running in parallel to the superior sagittal sinus, and eventually the retroglenoid vein (Fig. 5C). In these experiments we focused on highly resolved inflammation imaging in the EAE brain, employing long acquisition times in order to compensate for the considerably lower ^{19}F signal sensitivity of the *^{19}F/^{1}H RT-coil*. Since these acquisition times (11 h) are not applicable for *in vivo* studies, we performed further experiments in which we reduced the scan time. Upon reducing the scan time from 11 h to 0.5 h we could still detect ^{19}F signals with the *^{19}F-CRP* (Fig. 6). Despite the clear differences we were nevertheless still able to detect a considerable ^{19}F signal, even with a scan of only 2 h, which is amenable for *in vivo* MRI.

Discussion

In this study we show first ^{19}F MR images obtained with a *^{19}F-CRP* driven in quadrature mode. Compared to the *^{19}F/^{1}H RT-coil* we previously developed[11], we show that the *^{19}F-CRP* facilitates superior *ex vivo* images of brain

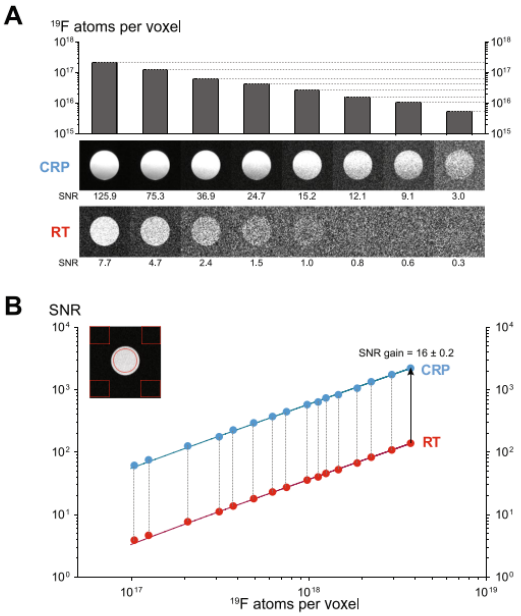

Figure 4. Comparison of ^{19}F signal sensitivity between *^{19}F-CRP* and *^{19}F/^{1}H RT-coil* as a function of the number of ^{19}F atoms. (**A**) Cross-sectional spin-echo ^{19}F MR images of ^{19}F nanoparticle phantoms acquired for both CRP (middle panel) and RT coil (lower panel). Each ^{19}F MR image indicates an MR scan with a defined number of ^{19}F atoms per voxel (upper panel) achieved with different concentrations of PFCE (ranging from 25 mM to 200 mM) and slice thicknesses varying from 0.4 to 2.0 mm. (**B**) Estimation of SNR gain provided by the *^{19}F-CRP* compared to the *^{19}F/^{1}H RT-coil* using high PFCE concentrations (200 mM to 1200 mM) and slice thicknesses varying from 1.0 to 6.0 mm. Shown is a log-log plot of SNR versus ^{19}F atoms per voxel including a linear fit for both CRP ($y = 5e^{-16}x$) and RT coil ($y = 4e^{-17}x$).

inflammation in an animal model of MS. At the current stage of development the *^{19}F-CRP* cannot yet be employed for *in vivo* imaging due to incompatibilities with conventional ^{1}H RT coils, as discussed later. Nevertheless the results are encouraging, and offer proof-of-concept demonstration of the potential for this technology.

After introducing the concept of cryogenically-cooled RF coil hardware to reduce thermal noise and thus increase SNR[46], CRP technologies were developed for small animal MRI, particularly for anatomical ^{1}H MRI of mouse brain[41,47–50]. Introducing a quadrature CRP design, enabled further SNR gains (~2.5) at 400 MHz[24,25] compared to RT coils with similar geometries. The SNR gain prediction for the *^{19}F-CRP* is expected to be equivalent due to the close Larmor frequency (376 MHz at 9.4T).

The potential applications of ^{19}F MR methods to image inflammation have long been recognized[11–17]. For several years, neuroinflammation has been studied using gadolinium-based contrast agents. However, gadolinium-enhancing lesions are diffuse, and lack spatial precision. Improvements have been realized with the use of alternative contrast agents, such iron oxide nanoparticles, although their effects on magnetic susceptibility limit their discrimination from endogenous confounding artifacts. ^{19}F MR methods abrogate this, since ^{19}F signals derive exclusively from exogenously applied ^{19}F nanoparticles. Efforts have been made to boost ^{19}F signal e.g. by promoting ^{19}F nanoparticle cellular uptake[20]. Nevertheless, major challenges of signal sensitivity constraints remain. Improving ^{19}F sensitivity with the *^{19}F-CRP* will be essential to realizing the full potential of ^{19}F MR.

Our motivation to investigate the *^{19}F-CRP* was to increase the sensitivity to detect neuroinflammation. Considering the geometrical differences between both coils, it was imperative to measure SNR at locations below the CRP that correspond to the mouse brain, using phantoms spanning the entire coronal view, as a basis for future *in vivo* studies. We performed SNR measurements for both *^{19}F-CRP* and control *^{19}F/^{1}H RT-coil* using a spin echo sequence (RARE), commonly used for ^{19}F MRI due to its high SNR per unit time compared to spoiled gradient echo sequences.

The sensitivity of the *^{19}F-CRP* is spatially dependent. Given that the CRP is a transceive quadrature surface coil array, both transmit field (B_1^+) and receive sensitivity (B_1^-) diminish with increasing distance from the RF coil – a factor that must be accounted for in quantitative imaging by measuring the actual B_1 and correcting the signal intensities using the signal equation of the employed pulse sequence. This is absolutely essential when signal quantification is necessary in order to ascertain the level of inflammation over the entire region of the brain during EAE. Nevertheless, this characteristic is shared by all transceive surface coils. This adverse effect is counterbalanced by an SNR gain, up to ~15-fold in the practical comparison made within this study. This SNR

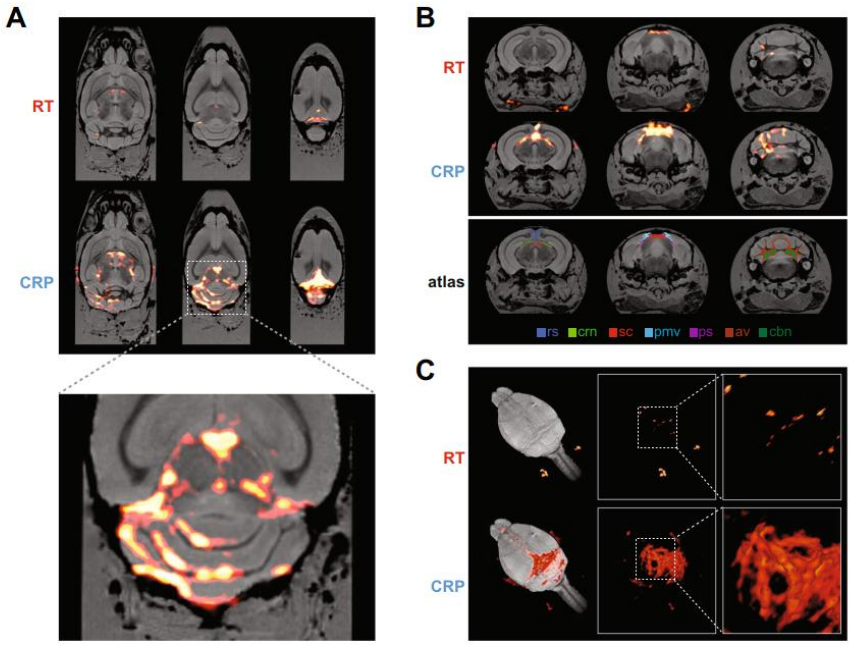

Figure 5. High spatial resolution ^{19}F MR image of an *ex vivo* brain from an EAE mouse showing clinical disease. With both *^{19}F-CRP* and *^{19}F/^{1}H RT-coil*, ^{19}F MR images were acquired using a 3D-RARE sequence. ^{19}F MR images (shown in red) were combined with ^{1}H MR images (shown in grayscale). ^{1}H MR images were acquired using a 3D-FLASH sequence and the *^{19}F/^{1}H RT-coil*. (**A**) Three exemplary slices from horizontal views of combined ^{19}F/^{1}H MR images for both *^{19}F/^{1}H RT-coil* (*upper panel*) and *^{19}F-CRP* (*middle panel*), in the *lower panel* a 300% zoom of the ^{19}F/^{1}H MR images acquired with the CRP. (**B**) Three exemplary slices from coronal views of combined ^{19}F/^{1}H MR images for both RT coil (*upper panel*) and CRP (*middle panel*). Registration of the Allen brain atlas to the ^{1}H image (*lower panel*) shows following labelled brain regions: rs: retrosplenial area; crn: cranial nerves; sc: superior colliculus (sensory related); pmv: posteromedial visual area; ps: postsubiculum; av: arbor vitae; cbn: cerebellar nuclei. (**C**) 3-D rendering of the combined ^{19}F/^{1}H MR images for both *^{19}F/^{1}H RT-coil* (*upper panel*) and *^{19}F-CRP* (*lower panel*).

gain can be attributed to factors including cooling (in the range of 2–3 for ^{1}H[24,25]), differences in RF coil design (birdcage vs. surface coil; quadrature versus linear), RF coil sample loading, and the specific RF pulse power adjustments. Here, pulse power was adjusted in order to avoid substantial signal loss at the dorsal part of the brain, which is observed when using a RARE sequence with excessive RF power. Predicting the sensitivity and detection limits of ^{19}F measurements for specific hardware setups[51] will help facilitate further *^{19}F-CRP* studies with other fluorinated compounds.

An SNR gain of 15 can be exploited in several ways — by reducing scan time by a factor 225 (e.g. from 1 h to ~15 s), or doubling 3D spatial resolution (e.g. from 600 µm to 300 µm) while still gaining SNR (~2.5). In this study we made use of the superior SNR, employing isotropic spatial resolutions of 150 µm to study neuroinflammation. Using the *^{19}F-CRP* at this resolution, we gained more precise information regarding inflammatory cell localization in the brain, compared to our previous study[11]. The ^{19}F MR images with the CRP showed excellent correspondence with the typical pattern of histopathology[39,40]. A robust accumulation of inflammatory lesions, especially in the white matter tracts of the cerebellum, is a hallmark of EAE in SJL mice, which we also observed in our prior studies using high resolution ^{1}H MR[41,42] and low resolution ^{19}F MR[11]. The pathology also extends into the cerebrum, as shown both prior to the occurrence of clinical symptoms (Supplementary Figure) and also during ongoing clinical disease (Figs 5 and 6). The *^{19}F-CRP* MR images also enabled discrimination of extraparenchymal meningeal inflammation, consistent with recent reports highlighting the relevance of inflammatory cell trafficking via the blood meningeal barrier[43,44] and extravasation via leptomeningeal microvessels into the subarachnoid space[45]. This also reflects the situation in MS[3–5]. Recent studies have argued for the presence of a lymphatic circulation in the meninges in association with these vessels, capable of draining immune cells from meningeal spaces[8] and brain parenchyma[7] into deep cervical lymph nodes. Therefore, the capacity to perform non-invasive longitudinal investigations with fidelity ^{19}F MRI to monitor the dynamics and distribution of infiltrating immune cells will be directly relevant for experimental neuroimmunologists.

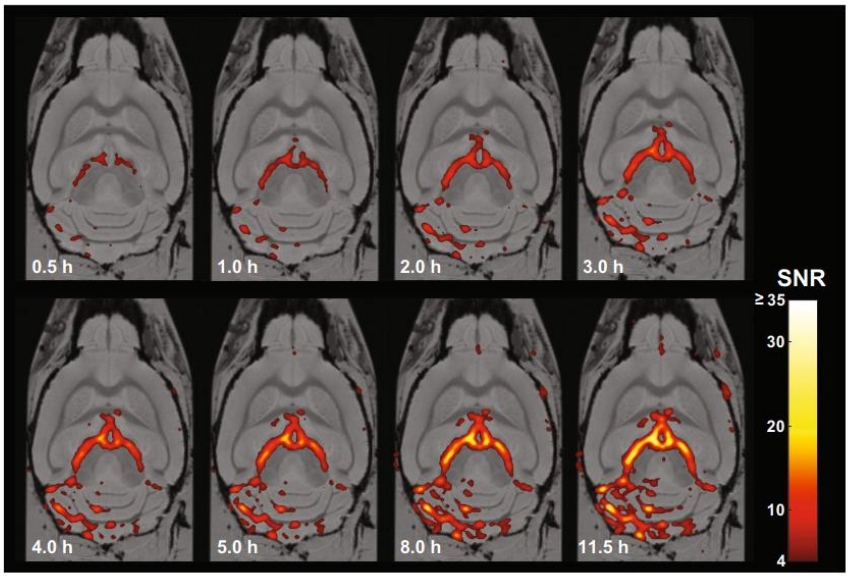

Figure 6. High spatial resolution ^{19}F MRI using acquisition times feasible for *in vivo* imaging. ^{19}F MR images were acquired with the *^{19}F-CRP* using acquisition times between 30 min and 11 h. The ^{19}F images were scaled to units of SNR, thresholded at SNR = 4, and overlayed onto the ^{1}H MR images using a pseudocolor scale.

The gradient in the B_1 field of the *^{19}F-CRP* leads to a gradual decline in ^{19}F MR signal with increasing distance from the probe head. This results in reduced signal in ventral regions. Studies of the EAE model are, in general, more focused on imaging of the CNS, and less so on imaging of the superficial lymph nodes. When imaging of the lymph nodes in the ventral regions is necessary, one could consider measuring the mouse brain in the supine and prone positions, in order to ensure coverage of the dorsal sides comprising the whole brain as well as ventral sides to include the draining lymph nodes. Other possible workarounds include adding an anterior ^{19}F RT RF coil to the mouse bed or combining ^{19}F images from RT and CRP. These approaches could help to overcome this inherent limitation of the *^{19}F-CRP*, while still utilizing its superior SNR. While the spatial dependency poses a constraint for studies investigating the involvement of the draining lymph nodes, the translational applications of the *^{19}F-CRP* are not limited to EAE. The *^{19}F-CRP* will also be useful for studying brain inflammation in animal models of tumour growth (especially those tumours implanted in the cortex or striatum), and studies on the middle cerebral artery occlusion model of stroke. Inflammation in these preclinical models could readily be imaged, since the focus of pathology in these models is located in regions where the *^{19}F-CRP* clearly outperforms the *^{19}F/^{1}H RT-coil*.

In vivo ^{19}F MRI studies require acquisition of anatomical ^{1}H MR images within a reasonable time frame. A dual-tunable RF probe would be most ideal, in order to avoid inaccurate co-registration of both signals[52]. Despite the clear improvement in SNR of the *^{19}F-CRP*, the quadrature design prohibits the presence of a dual resonant MR signal that would be needed for anatomical ^{1}H MRI. Furthermore conventional ^{1}H RF resonators cannot be used in combination with the *^{19}F-CRP* due to coupling between both RF coils. To avoid this, the *^{19}F-CRP* would need to be removed while the *in vivo* ^{1}H images are acquired. This would cause changes in the alignment of the mouse within the scanner during *in vivo* measurements that are serious enough to constitute a major hindrance. Even with the use of reference markers, any slight shift in the position of the markers with respect to the mouse during the procedure will result in an incorrect registration between ^{19}F and ^{1}H images. The current procedure of registering the ^{19}F images of the CRP with those of the RT RF coil is complicated and time consuming, requires sufficient SNR and is an impediment for *in vivo* experiments. A proposed solution to this limitation could be to construct an anterior ^{1}H RT RF coil, specifically designed to be added to the mouse bed while the *^{19}F-CRP* remains installed, in order to provide anatomical guidance. A dual-tunable ^{1}H/^{19}F RT RF coil would also take into account the above approach (implementation of a ^{19}F RF-coil below the mouse head).

This study presents the first demonstration of the performance of a quadrature *^{19}F-CRP* tailored for small rodents, showing superior SNR and ^{19}F MR image quality. The logical extension of this work will be to translate these results into *in vivo* studies, such as those studying pathological changes during neuroinflammatory disease. While the results of the current study are highly encouraging, a challenging road still lies ahead for the application of the *^{19}F-CRP* in *in vivo* studies. Previous studies using ^{19}F MR have been seriously hampered by the low SNR, and compensating for this limitation by using low spatial resolution has generally yielded images with rather poor definition, and therefore limited scientific utility. The current study aims to improve this situation, bringing ^{19}F

MR imaging a step closer to the objective of 'microscopic MRI'. Our results showed a remarkable SNR and detail of neuroinflammation, compared to conventional ^{19}F MRI, heralding a bright potential for the application of *^{19}F-CRP* for non-invasive MRI *in vivo*.

References

1. Stadelmann, C., Wegner, C. & Bruck, W. Inflammation, demyelination, and degeneration-recent insights from MS pathology. *Biochim.Biophys.Acta* **1812**, 275–282 (2011).
2. Lucchinetti, C. *et al.* Heterogeneity of multiple sclerosis lesions: implications for the pathogenesis of demyelination. *Ann.Neurol.* **47**, 707–717 (2000).
3. Gilmore, C. P. *et al.* Regional variations in the extent and pattern of grey matter demyelination in multiple sclerosis: a comparison between the cerebral cortex, cerebellar cortex, deep grey matter nuclei and the spinal cord. *J. Neurol. Neurosurg. Psychiatry* **80**, 182–187 (2009).
4. Howell, O. W. *et al.* Meningeal inflammation is widespread and linked to cortical pathology in multiple sclerosis. *Brain* **134**, 2755–2771 (2011).
5. Howell, O. W. *et al.* Extensive grey matter pathology in the cerebellum in multiple sclerosis is linked to inflammation in the subarachnoid space. *Neuropathol. Appl. Neurobiol.* **41**, 798–813 (2015).
6. Reboldi, A. *et al.* C-C chemokine receptor 6-regulated entry of TH-17 cells into the CNS through the choroid plexus is required for the initiation of EAE. *Nat. Immunol.* **10**, 514–523 (2009).
7. Aspelund, A. *et al.* A dural lymphatic vascular system that drains brain interstitial fluid and macromolecules. *J. Exp. Med.* **212**, 991 (2015).
8. Louveau, A. *et al.* Structural and functional features of central nervous system lymphatic vessels. *Nature* **523**, 337–341 (2015).
9. Kipnis, J. Multifaceted interactions between adaptive immunity and the central nervous system. *Science* **353**, 766–771 (2016).
10. Engelhardt, B. *et al.* Vascular, glial, and lymphatic immune gateways of the central nervous system. *Acta. Neuropathologica* **132**, 317–338 (2016).
11. Waiczies, H. *et al.* Visualizing brain inflammation with a shingled-leg radio-frequency head probe for 19F/1H MRI. *Sci. Rep.* **3**, 1280 (2013).
12. Flögel, U. *et al.* *In vivo* monitoring of inflammation after cardiac and cerebral ischemia by fluorine magnetic resonance imaging. *Circulation* **118**, 140–148 (2008).
13. Ahrens, E. T., Young, W. B., Xu, H. & Pusateri, L. K. Rapid quantification of inflammation in tissue samples using perfluorocarbon emulsion and fluorine-19 nuclear magnetic resonance. *Biotechniques* **50**, 229–234 (2011).
14. Flogel, U. *et al.* Selective activation of adenosine A2A receptors on immune cells by a CD73-dependent prodrug suppresses joint inflammation in experimental rheumatoid arthritis. *Sci. Transl. Med.* **4**, 146ra108 (2012).
15. Temme, S., Bonner, F., Schrader, J. & Flogel, U. ^{19}F magnetic resonance imaging of endogenous macrophages in inflammation. *Wiley Interdiscip. Rev. Nanomed. Nanobiotechnol.* **4**, 329–343 (2012).
16. Ahrens, E. T. & Zhong, J. In vivo MRI cell tracking using perfluorocarbon probes and fluorine-19 detection. *NMR Biomed.* **26**, 860–871 (2013).
17. Jacoby, C. *et al.* Probing different perfluorocarbons for *in vivo* inflammation imaging by 19F MRI: image reconstruction, biological half-lives and sensitivity. *NMR Biomed.* **27**, 261–271 (2014).
18. Ahrens, E. T., Flores, R., Xu, H. & Morel, P. A. *In vivo* imaging platform for tracking immunotherapeutic cells. *Nat. Biotechnol.* **23**, 983–987 (2005).
19. Ahrens, E. T., Helfer, B. M., O'Hanlon, C. F. & Schirda, C. Clinical cell therapy imaging using a perfluorocarbon tracer and fluorine-19 MRI. *Magn. Reson. Med.* **72**, 1696–701 (2014).
20. Waiczies, S. *et al.* Anchoring dipalmitoyl phosphoethanolamine to nanoparticles boosts cellular uptake and fluorine-19 magnetic resonance signal. *Sci. Rep.* **5**, 8427 (2015).
21. Dardzinski, B. J. & Sotak, C. H. Rapid tissue oxygen tension mapping using ^{19}F inversion-recovery echo-planar imaging of P erfluoro-15-crown-5-ether. *Magnetic resonance in medicine* 32, (88–97 (1994).
22. Kadayakkara, D. K., Janjic, J. M., Pusateri, L. K., Young, W. B. & Ahrens, E. T. *In vivo* observation of intracellular oximetry in perfluorocarbon-labeled glioma cells and chemotherapeutic response in the CNS using fluorine-19 MRI. *Magn. Reson. Med.* **64**, 1252–1259 (2010).
23. Faber, C. & Schmid, F. Pulse Sequence Considerations and Schemes in *Fluorine Magnetic Resonance Imaging* (ed. Flögel, U. and Ahrens, E.) 1–28 (Pan Stanford Publishing (2016).
24. Baltes, C., Radzwill, N., Bosshard, S., Marek, D. & Rudin, M. Micro MRI of the mouse brain using a novel 400 MHz cryogenic quadrature RF probe. *NMR Biomed.* **22**, 834–842 (2009).
25. Junge, S. Cryogenic and Superconducting Coils for MRI in *eMagRes* (ed. Wasylishen, R.) 505–514 (John Wiley & Sons, Ltd (2012).
26. Waiczies, H. *et al.* Perfluorocarbon particle size influences magnetic resonance signal and immunological properties of dendritic cells. *PLoS One* **6**, e21981 (2011).
27. Akoka, S., Franconi, F., Seguin, F. & Le Pape, A. Radiofrequency map of an NMR coil by imaging. *Magn. Reson. Imaging* **11**, 437–441 (1993).
28. Insko, E. K. & Bolinger, L. Mapping of the Radiofrequency Field. *J. Magn. Reson., Series A* **103**, 82–85 (1993).
29. NEMA. Determination of signal-to-noise ratio (SNR) in diagnostic magnetic resonance imaging. *NEMA Standards Publication MS*, 1–2008 (2008).
30. Henkelman, R. M. Measurement of signal intensities in the presence of noise in MR images. *Med. Phys.* **12**, 232–233 (1985).
31. Gudbjartsson, H. & Patz, S. The Rician Distribution of Noisy MRI Data. *Magn. Reson. Med.* **34**, 910–914 (1995).
32. Constantinides, C. D., Atalar, E. & McVeigh, E. R. Signal-to-noise measurements in magnitude images from NMR phased arrays. *Magn. Reson. Med.* **38**, 852–857 (1997).
33. Tustison, N. & Avants, B. Explicit B-spline regularization in diffeomorphic image registration. *Front. Neuroinform.* **7**, doi:10.3389/fninf.2013.00039 (2013).
34. Avants, B. B. *et al.* A reproducible evaluation of ANTs similarity metric performance in brain image registration. *Neuroimage* **54**, 2033–2044 (2011).
35. Lein, E. S. *et al.* Genome-wide atlas of gene expression in the adult mouse brain. *Nature* **445**, 168–176 (2007).
36. Sawiak, S., Wood, N., Williams, G., Morton, A. & Carpenter, T. Use of magnetic resonance imaging for anatomical phenotyping of the R6/2 mouse model of Huntington's disease. *Neurobiol. Dis.* **33**, 12–19 (2009).
37. Shamonin, D. P. *et al.* Fast parallel image registration on CPU and GPU for diagnostic classification of Alzheimer's disease. *Front. Neuroinform.* **7**, 50 (2014).
38. Yushkevich, P. A. *et al.* User-guided 3D active contour segmentation of anatomical structures: Significantly improved efficiency and reliability. *Neuroimage* **31**, 1116–1128 (2006).
39. Gold, R., Linington, C. & Lassmann, H. Understanding pathogenesis and therapy of multiple sclerosis via animal models: 70 years of merits and culprits in experimental autoimmune encephalomyelitis research. *Brain* **129**, 1953–1971 (2006).
40. Brown, D. A. & Sawchenko, P. E. Time course and distribution of inflammatory and neurodegenerative events suggest structural bases for the pathogenesis of experimental autoimmune encephalomyelitis. *J. Comp. Neurol.* **502**, 236–260 (2007).

41. Waiczies, H. *et al.* Identification of Cellular Infiltrates during Early Stages of Brain Inflammation with Magnetic Resonance Microscopy. *PLoS One* **7**, e32796 (2012).
42. Lepore, S. *et al.* Enlargement of cerebral ventricles as an early indicator of encephalomyelitis. *PLoS One* **8**, e72841 (2013).
43. Bartholomaus, I. *et al.* Effector T cell interactions with meningeal vascular structures in nascent autoimmune CNS lesions. *Nature* **462**, 94–98 (2009).
44. Mues, M. *et al.* Real-time *in vivo* analysis of T cell activation in the central nervous system using a genetically encoded calcium indicator. *Nat. Med.* **19**, 778–783 (2013).
45. Schläger, C. *et al.* Effector T-cell trafficking between the leptomeninges and the cerebrospinal fluid. *Nature* **530**, 349–353 (2016).
46. Hoult, D. I. & Richards, R. E. The signal-to-noise ratio of the nuclear magnetic resonance experiment. *J. Magn. Reson.(1969)* **24**, 71–85 (1976).
47. Ratering, D., Baltes, C., Nordmeyer-Massner, J., Marek, D. & Rudin, M. Performance of a 200-MHz cryogenic RF probe designed for MRI and MRS of the murine brain. *Magn. Reson. Med.* **59**, 1440–1447 (2008).
48. Nouls, J. C., Izenson, M. G., Greeley, H. P. & Johnson, G. A. Design of a superconducting volume coil for magnetic resonance microscopy of the mouse brain. *J. Magn. Reson.* **191**, 231–238 (2008).
49. Wagenhaus, B. *et al.* Functional and morphological cardiac magnetic resonance imaging of mice using a cryogenic quadrature radiofrequency coil. *PLoS One* **7**, e42383 (2012).
50. Niendorf, T. *et al.* Advancing Cardiovascular, Neurovascular and Renal Magnetic Resonance Imaging in Small Rodents Using Cryogenic Radiofrequency Coil Technology. . *Front. Pharmacol.* **6**, 255 (2015).
51. Taylor, A. J. *et al.* Probe-Specific Procedure to Estimate Sensitivity and Detection Limits for 19F Magnetic Resonance Imaging. *PLoS One* **11**, e0163704 (2016).
52. Tomanek, B., Volotovskyy, V., Gruwel, M. L. H., McKenzie, E. & King, S. B. Double-frequency birdcage volume coils for 4.7T and 7T. *Concepts Magn. Reson. Part B Magn. Reson. Eng.* **26B**, 16–22 (2005).

Acknowledgements
This study was funded by the Deutsche Forschungsgemeinschaft to S.W. (DFG WA2804) and A.P. (DFG PO1869). The funders had no role in study design, data collection and analysis, decision to publish, or preparation of the manuscript. We thank Stefanie Kox for preparation of nanoparticles, Marco Küng for building and optimizing the RF coil and associated circuitry, and Marco Sacher for contributions to mechanical design.

Author Contributions
S.W., T.N., and A.P. conceived the development of the *19F-C R P* and designed the study S.W., J.M.M, P.R.D., C.P., D.W., R.W. and A.P. carried out the experiments and measurements. S.W., L.S., P.R.D., T.H., S.P.K., P.B.S., H.W. and A.P. performed the analyses. D.M. developed the RF-Probe. S.W., J.M.M., T.N. and A.P. wrote the manuscript with the assistance of all other co-authors.

Additional Information
Competing Interests: The authors declare that they have no competing interests.

Publisher's note: Springer Nature remains neutral with regard to jurisdictional claims in published maps and institutional affiliations.

2.4 Detecting disease modifying treatments in vivo

This chapter builds on **publication 4** “In vivo detection of teriflunomide-derived fluorine signal during neuroinflammation using fluorine MR spectroscopy” published in Theranostics (Prinz et al., 2021).

The main motivation of **publication 3** was to improve SNR for ^{19}F MRI to detect and quantify therapies in vivo (Waiczies et al., 2017a). One clearly promising opportunity for implementing ^{19}F MRI in the clinic today is to detect and quantify therapies non-invasively in patients, particularly in organs that are difficult to access such as the brain. Although DMTs administered to MS patients act on inflammatory processes already outside the CNS to avert neurodegeneration, these therapies also exert their effect behind the BBB, within the CNS. However, it is not clear how much of these therapies are reaching the CNS. A non-invasive method that quantifies MS drugs in CNS and lymphatic tissue would be desirable.

Using the SNR-boosting ^{19}F-CRP technology developed in the previous publication (Waiczies et al., 2017a), we recently detected the dihydroorotate dehydrogenase inhibitor teriflunomide (TF) in EAE, the animal model of MS (Prinz et al., 2021). We studied the efficacy of TF in preventing EAE in two mouse strains: EAE was prevented in SJL/J mice that follow a relapsing-remitting disease form, in contrast to C57BL/6 mice that follow a more chronic disease progression and were not significantly affected by TF (**Figure 1** in own work 4 (Prinz et al., 2021)). TF was detected in the brain and CSF of both strains (**Figure 4** in own work 4 (Prinz et al., 2021)). Prior to in vivo experiments, a thorough ^{19}F MR characterization of TF was made, particularly at different temperatures, pH and during protein binding (Prinz et al., 2018; Prinz et al., 2021); this is necessary to select MRI acquisition methods best suited for detecting TF with the best SNR efficiency. In the presence of plasma proteins, the T_2 relaxation time of TF was markedly shortened from 465 ms to 5 ms. Thus, acquisition methods with short echo times (TE) are required to avoid significant signal losses during rapid relaxation. Using ^{19}F MRS we detected TF in the head area of both EAE and healthy SJL/J mice (**Figure 3** in own work 4 (Prinz et al., 2021)). Importantly, a TF quantification with HPLC/MS was important to establish the ground truth for validating in vivo ^{19}F MRS data. Although the estimation of TF concentration with ^{19}F MRS was elevated by 130% when compared to HPLC/MS, a clear correlation

between both methods was determined (**Figure 4C** in own work 4 (Prinz et al., 2021)):

Volume 11 | Number 6 | 2021

ISSN: 1838-7640

2019 IF
8.579

OPEN ACCESS

Theranostics

The Forum for Diagnostics, Imaging, and Therapy Research

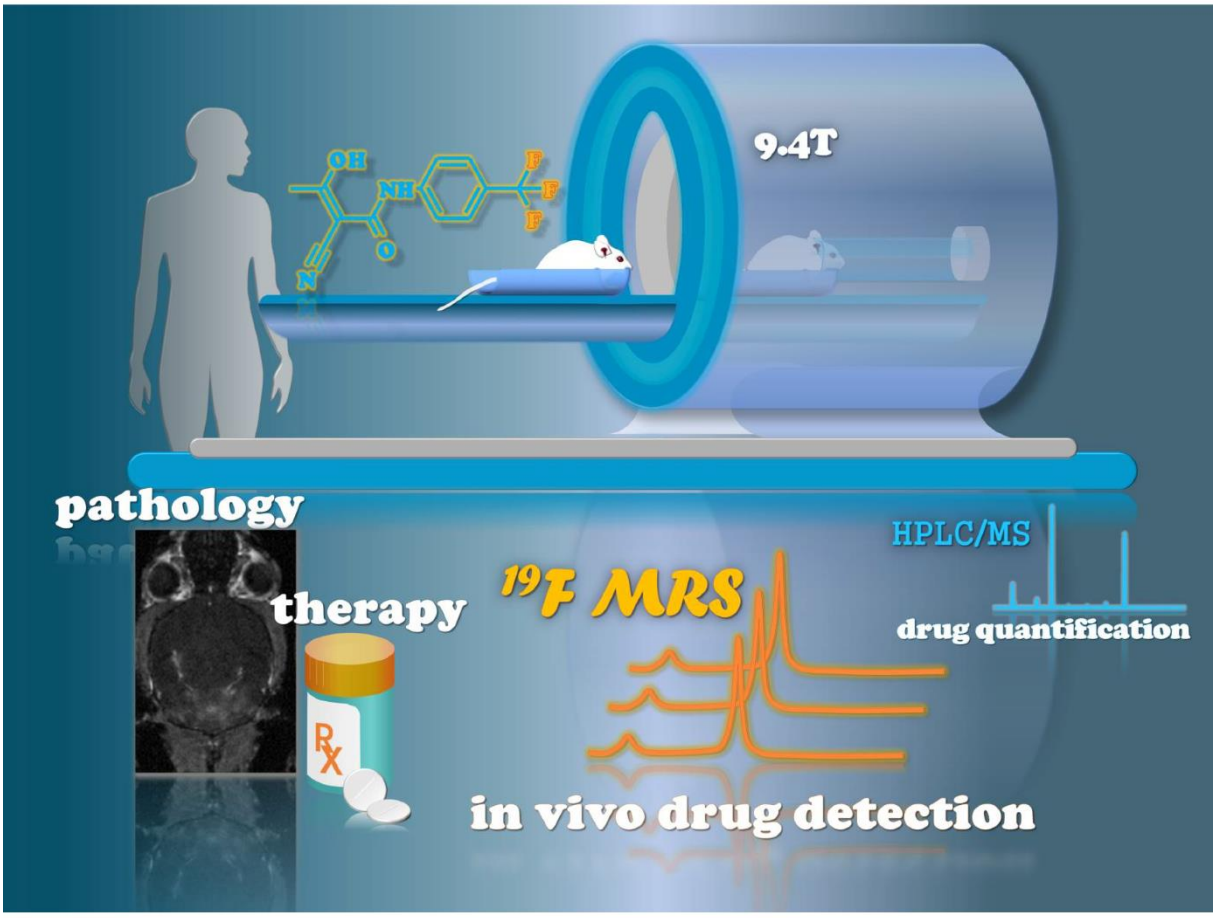

Inside Back Cover:

In vivo detection of teriflunomide-derived fluorine signal during neuroinflammation using fluorine MR spectroscopy

C. Prinz et al. pp.2490

IVYSPRING INTERNATIONAL PUBLISHER

IVYSPRING INTERNATIONAL PUBLISHER

Theranostics

2021; 11(6): 2490-2504. doi: 10.7150/thno.47130

Research Paper

In vivo detection of teriflunomide-derived fluorine signal during neuroinflammation using fluorine MR spectroscopy

Christian Prinz[1,2], Ludger Starke[1], Jason M. Millward[1,2], Ariane Fillmer[3], Paula Ramos Delgado[1,2], Helmar Waiczies[4], Andreas Pohlmann[1], Michael Rothe[5], Marc Nazaré[6], Friedemann Paul[2,7], Thoralf Niendorf[1,2] and Sonia Waiczies [1,2]✉

1. Berlin Ultrahigh Field Facility (B.U.F.F.), Max Delbrück Center for Molecular Medicine, Berlin, Germany.
2. Experimental and Clinical Research Center, a joint cooperation between the Charité - Universitätsmedizin Berlin and the Max Delbrück Center for Molecular Medicine in the Helmholtz Association, Berlin, Germany.
3. Physikalisch-Technische Bundesanstalt (PTB), Berlin, Germany.
4. MRI TOOLS GmbH, Berlin, Germany.
5. Lipidomix GmbH, Berlin, Germany.
6. Medicinal Chemistry, Leibniz-Institut für Molekulare Pharmakologie (FMP), Berlin, Germany.
7. Charité – Universitätsmedizin Berlin, corporate member of Freie Universität Berlin, Humboldt-Universität zu Berlin, and Berlin Institute of Health (BIH), Berlin, Germany.

✉ Corresponding author: Dr. Sonia Waiczies, Berlin Ultrahigh Field Facility (B.U.F.F.), Max Delbrück Center for Molecular Medicine (MDC) in the Helmholtz Association, Robert-Rössle-Str. 10 | D-13125 Berlin-Buch; E-mail: sonia.waiczies@mdc-berlin.de.

Received: 2020.04.17; Accepted: 2020.11.17; Published: 2021.01.01

Abstract

Background: Magnetic resonance imaging (MRI) is indispensable for diagnosing neurological conditions such as multiple sclerosis (MS). MRI also supports decisions regarding the choice of disease-modifying drugs (DMDs). Determining *in vivo* tissue concentrations of DMDs has the potential to become an essential clinical tool for therapeutic drug monitoring (TDM). The aim here was to examine the feasibility of fluorine-19 (^{19}F) MR methods to detect the fluorinated DMD teriflunomide (TF) during normal and pathological conditions.

Methods: We used ^{19}F MR spectroscopy to detect TF in the experimental autoimmune encephalomyelitis (EAE) mouse model of multiple sclerosis (MS) *in vivo*. Prior to the *in vivo* investigations we characterized the MR properties of TF *in vitro*. We studied the impact of pH and protein binding as well as MR contrast agents.

Results: We could detect TF *in vivo* and could follow the ^{19}F MR signal over different time points of disease. We quantified TF concentrations in different tissues using HPLC/MS and showed a significant correlation between *ex vivo* TF levels in serum and the *ex vivo* ^{19}F MR signal.

Conclusion: This study demonstrates the feasibility of ^{19}F MR methods to detect TF during neuro-inflammation *in vivo*. It also highlights the need for further technological developments in this field. The ultimate goal is to add ^{19}F MR protocols to conventional ^{1}H MRI protocols in clinical practice to guide therapy decisions.

Key words: MRI, MRS, Fluorine, Teriflunomide, Magnetic Resonance Spectroscopy, experimental autoimmune encephalomyelitis, Multiple Sclerosis

Introduction

Multiple sclerosis (MS) is a chronic inflammatory disease of the central nervous system (CNS) [1, 2]. The disease course is highly variable, involving a wide spectrum of neurological and motoric symptoms [3]. Most patients show a relapsing and remitting (RRMS) disease course, which ultimately transitions to a progressive phase [2, 4].

^{1}H Magnetic resonance imaging (^{1}H MRI) has been indispensable for diagnosing MS [5-7]. ^{1}H MRI can distinguish chronic from active lesions when using contrast agents to reveal blood brain barrier (BBB) disruptions [8-11]. Furthermore, MRI has been

vital for making safe informed decisions with respect to disease modifying drugs (DMDs) [12, 13] to ensure a better dampening of disease activity [14]. Typically, T_2 lesion load [15, 16] and brain atrophy [16] are used as outcome measures, especially during clinical studies. These MRI endpoints are commonly used as primary and secondary measures in phase II DMD trials involving large amounts of patients [17]. Despite the substantial armamentarium of DMDs available for MS [18-20], predicting treatment outcomes and tailoring DMD dosages to treatment objectives for individual patients poses a major unmet clinical need [21-23]. DMDs may need to traverse the BBB, to modify inflammatory responses within the CNS or to reduce neurodegeneration [24].

Currently there are no standard clinical methods to non-invasively monitor the distribution of drugs in patients. However, the possibility to quantify the concentration of drugs in the brain would greatly improve the assessment of individual treatment responses [22]. Drug levels are typically measured in blood, urine, saliva, and infrequently cerebrospinal fluid (CSF). However, drug levels in these fluids do not reliably reflect concentrations within the CNS. Imaging techniques such as positron emission tomography (PET) and single-photon emission computed tomography (SPECT) are used to detect drugs labeled with a radioisotope; these imaging methods are highly sensitive and are particularly useful in phase I clinical studies for small cohorts of human subjects [25-29]. However, they are not used for standard drug monitoring in patients; disadvantages include high costs, the necessity to inject radioactive compounds, restricted observation window due to short radiotracer half-life (^{18}F $t_{1/2}$ = 110 min), and a lack of distinction between drugs and their metabolites.

One third of all approved drugs are fluorinated, and are potentially detectable by fluorine-19 (^{19}F) MRI *in vivo* [30-32]. The amount of ^{19}F atoms endogenously present in the human body that can be detected with MR methods is negligible. The absence of background signal makes the ^{19}F nucleus a unique and highly attractive biomarker for detecting administered fluorinated DMDs *in vivo* using ^{19}F-MR methods. ^{19}F MR methods have been applied to detect fluorinated drugs in animal [33-38] and human studies [39-45] in the past. They have also been applied in combination with drugs encapsulated in fluorine rich nanoparticles to monitor the efficacy of these therapies in animal models [46]. ^{19}F-MR methods have also been employed in diagnostic imaging [47], for guiding tumor ablation therapies [48], and for imaging intracellular therapeutic targeting [49]. However, they remain under-utilized for the majority of drugs, especially in MS.

Teriflunomide (TF) is an anti-inflammatory DMD approved for use in MS that contains a trifluoromethyl group [50]. TF is administered orally once-daily and has a rapid, complete absorption with a long half-life (> 2 weeks) due to extensive enterohepatic recycling [51]. In RRMS patients, it reduces the annual relapse rate, slows disability progression, reduces the lesion volume [51, 52] and brain volume loss [53]. TF has a high tolerability and low discontinuation rate [50, 54]. TF was investigated in preclinical studies using the animal model of MS, experimental autoimmune encephalomyelitis (EAE) [55-57]. In rats, TF administration at EAE onset reduced disease severity and delayed progression [55, 57]. TF treatment delayed EAE onset in SJL/J mice, and suppressed disease entirely in C57BL/6 mice.

In this study we used ^{19}F MR spectroscopy to study the possibility of detecting TF during EAE *in vivo*. We characterized the MR properties of TF *in vitro*, studying the impact of pH, protein binding, and MR contrast agents. We demonstrated the feasibility of ^{19}F MR methods to detect TF non-invasively during neuroinflammation, with the ultimate goal for further development into future clinical applications.

Methods

Teriflunomide

Teriflunomide (TF) (Sanofi-Genzyme, Bridgewater, US) was formulated in 0.6% carboxymethylcellulose, sodium salt (CMC, Sigma, Schnelldorf, Germany) in the form of a suspension for *in vivo* use. CMC is an inactive ingredient used as thickening excipient, stabilizer and suspending agent. TF (20 mg) was mixed with 5 mL CMC/Tween-80 (0.6% CMC, 0.5% Tween-80 in water) using medium speed magnetic stirring (circa 24 h at RT) until a uniform milky suspension was obtained. The suspension was transferred to a clean glass vial and the original vial rinsed with a further 5 mL of CMC/Tween-80. The TF suspension (2 mg/mL) was adjusted to a pH of 7 using HCl and NaOH. For phantom experiments, TF was prepared in CMC, DMSO and human serum to study the effects of protein binding.

Animals

Dark Agouti rats (n = 2, Janvier Labs, Le Genest-Saint-Isle, France), C57BL/6N mice (n = 27, Charles River, Sulzfeld, Germany) and SJL/J (n = 33, Janvier Labs, Le Genest-Saint-Isle, France) mice (all female, age 2-4 months) were used to study the TF signal following oral application *in vivo*. The numbers of animals within each group are specified in the relevant experiments below.

Animal experiments were conducted in accordance with procedures approved by the Animal Welfare Department of the State Office of Health and Social Affairs Berlin (LAGeSo) and conformed to guidelines to minimize discomfort to animals (86/609/EEC).

EAE induction

EAE was induced by subcutaneous immunization of SJL/J mice with proteolipid protein peptide ($PLP_{139-151}$) and C57BL/6 mice with myelin oligodendrocyte glycoprotein peptide (MOG_{35-55}); for both peptides 250 µg peptide (Pepceuticals, Leicester, UK) per animal were emulsified with M. Tuberculosis H37RA (List Biological Laboratories, Campbell, US, 800 µg/animal) in 100 µL Complete Freund's Adjuvant (BD Difco, Heidelberg, Germany). Pertussis Toxin (Biotrend, Cologne, Germany, 1.25 ng/µL in SJL/J and 2 ng/µL in C57BL/6) was administered intraperitoneally in 200 µL PBS on days 0 and 2 [58].

EAE scoring was performed daily: righting reflex weakness = 0.5, tail paresis = 0.5, tail paralysis = 1, unilateral hindlimb paresis = 0.5, bilateral hindlimb paralysis = 1, unilateral forelimb paresis = 0.75, bilateral forelimb paralysis = 1.5.

Teriflunomide treatment and preparation for *in vivo* MR measurements

Rats (n = 2) were treated orally with 10 mg/kg TF and MR measurements were performed directly following administration. Animals were anesthetized by intraperitoneal (ip) injection using ketamine (40 mg/kg, WDT, Garbsen, Germany) and medetomidine (0.5 to 0.75 mg/kg, Henry Schein, Berlin, Germany) maintained by an ip catheter line. TF was administered via a catheter line to the stomach while the animal was in the scanner.

Mice were treated daily for 14 days with 30 mg/kg TF [55-57, 59] or vehicle control (CMC) administered by oral gavage. The increased dose used in mice takes into consideration guidelines on dose conversions in animals and is mostly due to differences in metabolism [56, 60]. EAE mice were treated with TF (C57BL/6 n = 12, SJL/J n = 12) or CMC (C57BL/6 n = 6, SJL/J n = 6). Healthy non-immunized C57BL/6 (n = 9) or SJL/J (n = 15) mice served as therapy controls. MR measurements in mice were performed on days 8 and 14 following EAE start, 16-24 h after the last drug administration. For *in vivo* MR measurements, mice were anesthetized by intraperitoneal injection using a mixture of xylazine (5 mg/kg, CP Pharma, Burgdorf, Germany) and ketamine (50 mg/kg, WDT, Garbsen, Germany) maintained by an ip catheter line.

Animals were transferred to a temperature-regulated bed (receiving circulated warm water from a water bath) and supplied with pressurized air (30 %) and O_2 (70 %). Pulse, respiration and body temperature (Neoptix, OmniLink version 1.15, Omniflex, Neoptix, Québec, Canada) were continuously monitored. The body temperature was kept at 37 °C throughout the experiments.

For studying the BBB disruption in SJL/J EAE mice, gadopentetate dimeglumine (0.2 mmol/kg Gd-DTPA Magnevist, Bayer Pharma, Berlin, Germany) was administered intravenously via the tail vein using an infusion pump (Harvard PHD 2000, Harvard Apparatus, Cambridge, US).

Phantom construction

For characterizing the ^{19}F MR properties (chemical shift, spectral shape and relaxation times) of TF, phantoms were prepared in 2.5 mL syringes (inner diameter, id: 9.7 mm, total length: 7.6 cm, B.Braun, Melsungen, Germany) equipped with stopper closing-cones (B.Braun, Melsungen, Germany) using dimethylsulfoxide (DMSO, Roth, Karlsruhe, Germany, 27.02 mg/mL), human serum (4.84 mg/mL) or CMC (2.70 mg/mL) as solvents/ suspending agent. Given the different pH of various compartments *in vivo*, we studied the influence of pH on the relaxation times T_1 and T_2 as well as the ^{19}F signal intensity in CMC in 1 mL syringes (id: 4.7 mm, total length: 9.6 cm, B.Braun, Melsungen, Germany). The pH for the 2.70 mg/mL TF concentration was adjusted to pH values of 5, 7.4, 10 and 13 with HCl or NaOH.

For studying the influence of contrast agent on ^{19}F MR properties, 4 phantoms containing 16.67 mg/mL TF and different concentrations of Gd-DTPA (0.5 mM, 1 mM, 2 mM, and 4 mM) in DMSO were prepared in NMR tubes (id: 4.2 mm).

For assessing the limit of detection (LOD) for ^{19}F MRS and performing calibrations, four TF concentrations were prepared in serum (400 µL) and the exact concentration for each sample was determined by mass spectrometry (11.8, 105.7, 787.4, 4208.2 µg/g). The serum samples (350 to 500 µL) were prepared in 1 mL syringes (as above).

MR methods

Hardware

MR experiments were performed on a Bruker Biospec 9.4 T MR scanner (Bruker Biospin, Ettlingen, Germany) with a horizontal bore. A room temperature (RT) dual-tunable $^{19}F/^{1}H$ head RF transceive coil (16 mm inner diameter) [61] was used to characterize TF in DMSO/serum/CMC in phantom experiments.

A RT dual-tunable $^{19}F/^{1}H$ rat body RF transceive

coil (MRI.TOOLS GmbH, Berlin, Germany, 62 mm inner diameter) was used to study *in vivo* ^{19}F MR spectroscopy (MRS) signals in the abdomen of the rat.

A cryogenically-cooled transceive ^{19}F quadrature RF surface probe (20 mm inner diameter, Cryogenic Radiofrequency Probe, CRP, Bruker, Fällanden, Switzerland) [62] was used for *in vivo* ^{19}F MRS measurements of the mouse head and abdomen as well as serum samples. With this coil we had previously shown that ^{19}F MR sensitivity is enhanced by a factor of 15 compared to RT head coils [62]. The bed of the ^{19}F CRP was adjusted with respect to the surface of the coil in order to acquire ^{19}F MRS in different regions of the mouse body. The measurement volume above the bed was adjusted with respect to the surface of the coil-head by using a position gauge. This device reproduces the geometry of the coil-head and supporting components and can be used to adjust the position of the mouse on the bed outside of the MR scanner. Anatomical ^{1}H scans ensured correct positioning and complete coverage of the regions of interest.

Phantom MR measurements

A non-selective single-pulse ^{19}F MRS FID-acquire sequence (TR = 1000 ms, nominal flip angle = 90°, blockpulse, 4096 sampling points, acquisition delay = 0.05 ms, excitation pulse bandwidth = 10000 Hz, spectral read bandwidth = 25000 Hz, averages for serum/CMC/DMSO phantoms: avg_{serum} = 8, avg_{CMC} = 16, avg_{DMSO} = 16) was used for detecting TF in phantoms and studying chemical shift and spectral shape (full-width half maximum, FWHM). This sequence (later referred to as default) was slightly modified e.g. using increased averages or bandwidth to increase signal-to-noise ratio (SNR) in *in vivo* and *ex vivo* experiments (see below).

^{19}F T_1 and T_2 relaxation times were measured using MR spectroscopy. For T_1, the default FID-acquire sequence was used but with 16 TRs ranging from 100 to 10000 ms, avg_{serum} = 40, avg_{DMSO} = 30, avg_{CMC} = 30. For T_2, a CPMG pulse sequence was used: 25 echoes, echo spacing for serum/CMC/DMSO phantoms: es_{serum} = 2.8 ms, es_{DMSO} = 40 ms, $es_{DMSO+Gd\text{-}DTPA}$ = 10.6 ms, es_{CMC} = 10.6 ms, excitation pulse = 5000 Hz, spectral read bandwidth = 25000 Hz; TR_{serum} = 2000 ms, TR_{DMSO} = 5000 ms, TR_{CMC} = 5000 ms, avg = 50 (for all phantoms).

For studying the influence of pH on the ^{19}F MR signal detection, the default FID-acquire sequence was used, but a long TR of 8000 ms was chosen to allow full relaxation.

The LOD for the ^{19}F CRP to perform ^{19}F MRS *in vivo* was assessed using the above four concentrations of TF in serum and the default ^{19}F MRS FID-acquire sequence but using avg = 1024, acquisition time = 17 min. The SNR of these spectra was measured and the LOD was determined as the concentration/number of ^{19}F atoms that corresponded to an SNR of 5 (SNR_1 estimation below) using a linear fit with y-axis intercept = 0. The SNR value of 5 was chosen as a conservative threshold for determining LOD.

In vivo ^{1}H MRI using ^{19}F/^{1}H coils

Anatomical ^{1}H MRI was performed using FLASH (Fast Low-Angle Shot) [63] and T_2 weighted TurboRARE (Rapid Acquisition with Relaxation Enhancement) [64] pulse sequences. In EAE mice, BBB disruptions were assessed using an MDEFT (Modified Driven-Equilibrium FT) [65] sequence with inversion (TR/TE/TI 2600/3.9/950 ms, FOV (30.2×12.8×9) mm^3, matrix size = 256×170×18, avg = 2, acquisition time = 3 m 7 s).

In vivo ^{19}F MRS using ^{19}F CRP

TF-derived ^{19}F MR signal was studied in healthy and EAE mice immediately following acquisition of the anatomical scans. To account for the B_1 inhomogeneity of the CRP surface coil during *in vivo* measurements, we calibrated the flip angle. Before *in vivo* measurements, a phantom reference sample of 1 mL TF in DMSO (27.02 mg/mL) was used to manually calibrate the flip angle and reference power. This sample was in a 2.5 mL syringe and was positioned at the coil surface. We acquired 10 spectra with the default ^{19}F MRS FID-acquire sequence using different reference powers (0.0001 - 0.01 W). The best reference power from these manual measurements was verified by the automatically adjusted power settings for this sample by the MR system. Prior to each *in vivo* measurement, we adjusted the reference power manually (automatic ^{19}F adjustments were not possible due to low SNR): spectra (avg = 128, 2 min 8 s each) with different reference powers (0.001, 0.002, 0.004, 0.008 W) were acquired from the head region of mice *in vivo* using the default FID-acquire method. The optimal reference power yielding the highest signal intensity was then chosen for the ^{19}F MRS data acquisitions. For these acquisitions, the default FID-acquire sequence was used with avg = 1024, acquisition time = 17 min.

In vivo ^{19}F MRS using ^{19}F/^{1}H rat body coil

To study ^{19}F MRS signal of TF in the abdominal region of rats at different time points, the default FID-acquire sequence was used with alterations in: TR = 1500 ms, avg = 256, acquisition time = 6 min.

Ex vivo measurements

Tissue processing

Animals were sacrificed after 14 days of *in vivo* experiments. Under deep anesthesia, blood was withdrawn and animals were transcardially perfused with 30 mL (> 10× the estimated total mouse blood volume) phosphate-buffered saline (PBS) solution. CSF was collected from the cisterna magna and the perfused brain was isolated. The perfused brain samples are mostly depleted of blood and CSF. Samples were frozen (-80 °C) for subsequent mass spectrometry studies.

Perfused brain tissue (50 mg), serum (50 µL) or CSF (1-3 mg) was weighed/measured and homogenized in 450 µL phosphate buffer (100 mmol/L, pH = 6.0). 1 mL ethylacetate was added. The mixture was shaken vigorously for 5 min and centrifuged at 11000 rpm for 10 min. The upper layer was transferred to a 2 mL glass vial. The extraction was repeated twice. The organic extract was evaporated to dryness with a gentle N_2 stream at 40 °C, after which the residue was dissolved in 1 mL ethanol.

High performance liquid chromatography mass spectrometry (HPLC/MS)

For assessing the LOD for HPLC/MS, 5 TF concentrations (1 ng/mL to 1000 ng/mL) were prepared in DMSO. LOD was calculated at an SNR = 9 using peak-to-peak algorithm from lowest calibrator 1 ng/mL.

HPLC-measurements were performed using an Agilent 1290 HPLC system with binary pump, autosampler and column thermostat equipped with a Phenomenex Kinetex-C18 column 2.6 µm, 2.1×150 mm column (Phenomenex, Aschaffenburg, Germany). Ammonium acetate (5 mM) and acetonitrile was used as solvent system. All solvents and buffers in HPLC-MS-grade were obtained from VWR Germany. The solvent gradient started at 5 % acetonitrile and was increased to 95 % within 5 min until 8 min with a flow rate of 0.4 mL/min and 1 µL injection volume. The HPLC was coupled with an Agilent 6470 triplequad mass spectrometer with electrospray ionization source using established parameters (gas temp = 250 °C, gas flow = 9 L/min, nebulizer pressure = 20 psi, sheath gas temp = 390 °C, sheath gas flow = 12 L/min, capillary voltage = 2700 V, nozzel voltage = 300 V) operated in negative multiple reaction monitoring mode (269.2 –160 capillary electrophoresis (CE) 28 V, – 82 CE 21, fragmentor voltage = 120 V, mass resolution wide/wide).

Ex vivo ^{19}F MRS

For correlating the TF-derived ^{19}F MR signal with HPLC/MS TF quantification, calibrations were first performed with mouse sera spiked with TF (using 3 concentrations closer to biologically expected values) in 1 mL syringes. These concentrations were measured with HPLC/MS (11.8, 105.7, 787.4 µg/g) and the default ^{19}F MRS FID-acquire method (but excitation pulse = 70000 Hz, spectral read bandwidth = 70000 Hz, avg = 4096, acquisition time = 1 h 8 min). Next we measured the *ex vivo* serum samples from EAE mice (n = 10) in 1 mL syringes using the default FID-acquire method and HPLC/MS.

For both the calibration experiment (spiked serum) as well as the between-method correlation (*ex vivo* serum) we computed a linear fit with y-axis intercept = 0 to determine the relation of signal to concentration and then used this ratio to estimate TF concentrations in *ex vivo* serum samples from the ^{19}F MRS signal intensity after accounting for slight volume differences.

MR data analysis

For *in vivo* proton image processing and analysis, the freely available software Fiji (Image J v1.47p, Open source software, NIH, MD, USA) [66] was used.

All spectral analyses and processing were performed in MATLAB (The MathWorks Inc., Natick, USA). Chemical shifts are referenced to trichloro-fluoro-methane, $CFCl_3$ (δ_F=0 ppm). Post-processing of the real spectra included zero-filling to 2^{14} points of all original FID data and a line-broadening of 70 Hz. The signal from both receive channels was averaged after zeroth and first order phase-correction.

We used two conventions to measure SNR of the main spectral peaks: SNR_1 was measured by calculating the ratio of the peak amplitude (maximal peak height minus mean background signal) and one standard deviation of the background noise (σ_1), as suggested in a recent expert's consensus paper on *in vivo* MR spectroscopy [67]. SNR_2 was measured by calculating the ratio of the peak amplitude and the noise height (peak-to-peak) divided by 2.5 (σ_2) [68]. Both SNR estimations are shown for all *in vivo* ^{19}F MR measurements in healthy and EAE mice (**Table S1**). SNR_1 was used for all data analysis. SNR_2 is only reported in Table S1.

The time domain (TD) signal intensity was measured by calculating the y-axis intercept of the magnitude free-induction decay using a 4–th degree polynomial fit (FID fit) in MATLAB. The frequency domain (FD) signal intensity was determined by computing the integral of the MRS peak at -61 ppm (peak area). For this, we used a Lorentzian fit of the real spectrum [69] including a baseline offset and a

secondary peak if the amplitude of the secondary peak exceeded $SNR_1 = 2$. Only the area of the main peak was attributed to TF.

T_1 and T_2 were determined by mono exponential fitting of data points obtained from ^{19}F MRS (T_1) and CPMG (T_2, three parameter fit).

Statistical analysis

MR-data and mass spectrometry data were pooled from all experiments. ^{19}F signal intensities from ^{19}F MR and TF concentrations in serum, perfused brain tissue and CSF samples from HPLC/MS experiments were log transformed, and the log-normal distribution confirmed using the Shapiro-Wilk normality test. EAE disease scores were presented as mean and standard error of the mean, maximum scores as median and interquartile range and were analyzed with the Mann-Whitney U test. Bodyweight was analyzed using the t-test; the logrank test was used to analyze the time-to-onset of clinical signs. ^{19}F MR signal detection over time and mass spectrometry data was analyzed using ANOVA or 2-factor ANOVA, with the Tukey post-hoc test for multiple comparisons, or with an unpaired t-test. Levene's test was used for testing for homogeneity of variance. Correlation was assessed using the Pearson correlation (R) or the non-parametric Spearman rank-order correlation (ρ), as appropriate. *p*-values < 5 % were considered significant (depicted as $*p < 0.05$; $**p < 0.01$; $***p < 0.001$). Statistical analysis was performed using the statistical computing environment R (version 3.6.1, R Foundation; https://R-project.org).

Results

Strain differences in response to teriflunomide treatment in EAE mice

We studied TF treatment response in both SJL/J (**Figure 1A-D**) and C57BL/6 (**Figure 1E-H**) EAE mice. In SJL/J mice, TF treatment prevented weight loss during the EAE disease course (**Figure 1A**, n = 12,

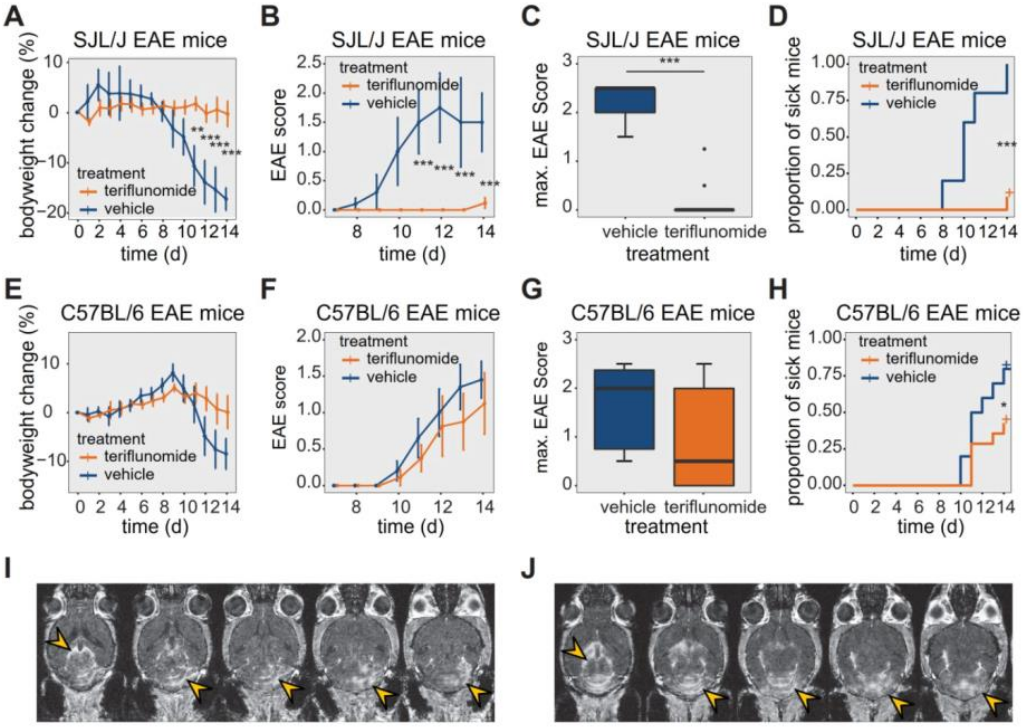

Figure 1. *Effect of teriflunomide treatment on the disease course of EAE in SJL/J and C57BL/6 mice.* **(A)** Change in bodyweight (Mean ± SE) over time in untreated (carboxymethylcellulose vehicle, n = 5) and TF treated (n = 12) SJL/J EAE mice. Changes in percent compared to the initial bodyweight are shown. **(B)** Mean EAE score ± SE of untreated (n = 5) and TF treated (n = 12) SJL/J EAE animals. The time axis is restricted to days with non-zero EAE score. **(C)** Maximum EAE score reached during the EAE disease course in untreated (n = 5) and TF treated (n = 12) SJL/J EAE animals. **(D)** Kaplan-Meier plot of untreated (n = 5) and TF treated (n = 12) SJL/J EAE animals depicting the time to disease onset (score=0.5) and the proportion of animals with clinical symptoms. **(E)** Change in bodyweight (Mean ± SE) over time in untreated (carboxymethylcellulose, n = 6) and TF treated (n = 9) C57BL/6 EAE mice. Changes in percent of the initial bodyweight is shown. **(F)** Mean EAE score ± SE of untreated (n = 6) and TF treated (n = 9) C57BL/6 EAE animals. The time axis is restricted to days with non-zero EAE score. **(G)** Maximum EAE score reached during the EAE disease course in untreated (n = 6) and treated (n = 9) C57BL/6 EAE animals. **(H)** Kaplan-Meier plot of untreated (n = 6) and treated (n = 9) C57BL/6 EAE animals depicting the time to onset (score = 0.5) of the EAE disease and the proportion of animals with clinical symptoms. **(I-J)** MR Images showing mild (I) and severe (J) blood brain barrier disruption using contrast agent (i.v.) and MDEFT on day 14 in two TF treated EAE mice. Lesions are indicated (yellow arrows) in the cerebellum and also in periventricular regions. Differences in body weight were analysed using Student's t-test; EAE scores and max scores were analysed using the Mann-Whitney U test; time to disease onset was analysed using the logrank test.

pooled from 4 EAE experiments). Control EAE mice (n = 5, pooled from 4 EAE experiments) treated with vehicle showed a substantial weight loss from day 11 post-immunization (p.i.) onward ($p = 0.002$) (**Figure 1A**). TF treatment resulted in an almost complete absence of clinical signs in SJL/J mice. TF-treated EAE mice had lower clinical scores compared to vehicle-treated EAE mice, which showed a typical disease course for SJL/J mice, reaching peak clinical score at day 12 p.i. (**Figure 1B**). In the TF-treated group, only 8% of animals showed clinical signs by day 14 p.i. compared to untreated mice (100% incidence). The maximum disease score was also different between treated (0 ± 0, median ± interquartile range, IQR) and untreated (2.5 ± 0.5, median ± IQR) EAE mice ($p < 0.001$) (**Figure 1C**). TF delayed disease onset ($p < 0.001$), which is defined as time to reach a minimum clinical score of 0.5 (**Figure 1D**).

The response of C57BL/6 EAE mice (n = 9, pooled from 3 EAE experiments) to TF treatment was less pronounced. TF-treated C57BL/6 EAE mice showed a less marked reduction in weight over time, but there was no significant difference in weight loss compared to vehicle-treated C57BL/6 EAE controls (n = 6, pooled from 3 EAE experiments) ($p > 0.1$) (**Figure 1E**). TF-treated C57BL/6 mice began to show clinical signs by day 10 p.i., and while EAE scores were generally lower than those of vehicle treated controls, there were no differences in EAE scores between the two groups ($p > 0.5$) (**Figure 1F**). Also, there was no significant decrease in maximum EAE score in TF-treated C57BL/6 EAE mice (0.5 ± 2, median ± IQR) compared to vehicle-treated (2 ± 1.625, median ± IQR) C57BL/6 EAE mice ($p > 0.05$) (**Figure 1G**). TF treatment reduced disease incidence by 65% and also delayed onset, compared to untreated mice ($p = 0.04$) (**Figure 1H**).

The extent of CNS inflammation was examined on day 14 by measuring BBB disruption using contrast-enhanced MRI (**Figure 1I-J**). We observed contrast-enhancing lesions in SJL/J EAE mice treated with TF, even in the absence of clinical signs. The extent of these lesions varied among animals, with some showing comparatively mild (**Figure 1I**) and others comparatively severe (**Figure 1J**) disruption. Contrast-enhancing lesions were particularly prominent in the cerebellum (**Figure 1I-J**) and were also present in periventricular regions (**Figure 1J**).

Environmental factors alter the magnetic resonance properties of teriflunomide

The physicochemical properties of TF in DMSO, including chemical shift, ^{19}F T_1 and ^{19}F T_2 relaxation times are shown in **Figure 2A-C**. Changes in T_1 and T_2 occur with different concentrations of gadopentetate dimeglumine (**Figure 2D**). We observed a linear correlation between the inverse T_1 (R_1) (T_1-relaxation times 1099 ms, 209 ms, 117 ms, 60 ms, 33 ms; Pearson R = 0.999, $p < 0.001$) and inverse of T_2 (R_2; T_2-relaxation times 547 ms, 76 ms, 43 ms, 24 ms; Pearson R = 0.999, $p = 0.001$) with increasing Gd-DTPA concentrations (**Figure 2D**).

TF in CMC exhibits a single narrow peak spectrum (FWHM = 116 Hz) at -61 ppm (**Figure 2E**), in comparison to a peak at -58 ppm for experiments performed in DMSO (FWHM = 117 Hz) [70].

Both T_1 (**Figure 2F**) and T_2 (**Figure 2G**) were increased with increasing pH. We also observed increased signal intensity at higher pH using global single pulse spectroscopy with full relaxation (**Figure 2H**).

Compared to spectra in DMSO (FWHM = 117 Hz) [70], we observed a broader peak for TF in serum (FWHM = 528 Hz) at -61 ppm (**Figure 2I**). In addition, we characterized T_1 (**Figure 2J**) and T_2 (**Figure 2K**) in human serum in order to optimize pulse sequences for subsequent *in vivo* measurements. T_1 of TF in serum was 1017 ms (**Figure 2J,** $R^2 = 0.999$), which was comparable to the T_1 of 1000 ms in DMSO (**Figure 2B**). Conversely, T_2 was markedly shortened to 4 ms (**Figure 2K,** $R^2 = 0.963$) in the presence of serum, which is 93-fold lower than the T_2 of 465 ms in DMSO [70].

We obtained a detection limit for the ^{19}F CRP using ^{19}F MRS, validating the concentrations with mass spectrometry. At an SNR threshold of 5, the LOD was 1.9 µg/g, which is equal to 5.04e + 15 ^{19}F atoms in a volume of 400 µL (**Figure 2L**).

In vivo detection of teriflunomide in the abdominal region of healthy animals

Similar to TF spectra in CMC phantoms, we observed a TF peak at -61 ppm in healthy Dark Agouti rats (n=2) using ^{19}F MRS (**Figure S1A**). Qualitatively, we discerned an initial increase in ^{19}F MR signal followed by gradual decrease during the observation period of 30 minutes. We also detected TF in the abdominal region of healthy C57BL/6 mice (**Figure S1B**) 24 hours after the last drug administration, using the ^{19}F CRP.

In vivo detection of teriflunomide in the head region

Similar to CMC phantoms and *in vivo* measurements in the rat abdomen, we observed a TF peak at -61 ppm in the mouse head region. We studied changes in TF levels in TF-treated healthy mice (**Figure 3A**, n = 6 on day8, n = 5 on day14, from 1 EAE experiment), and TF-treated EAE mice (**Figure 3B**, n = 7 on day8, n = 4 on day14, from 1 EAE

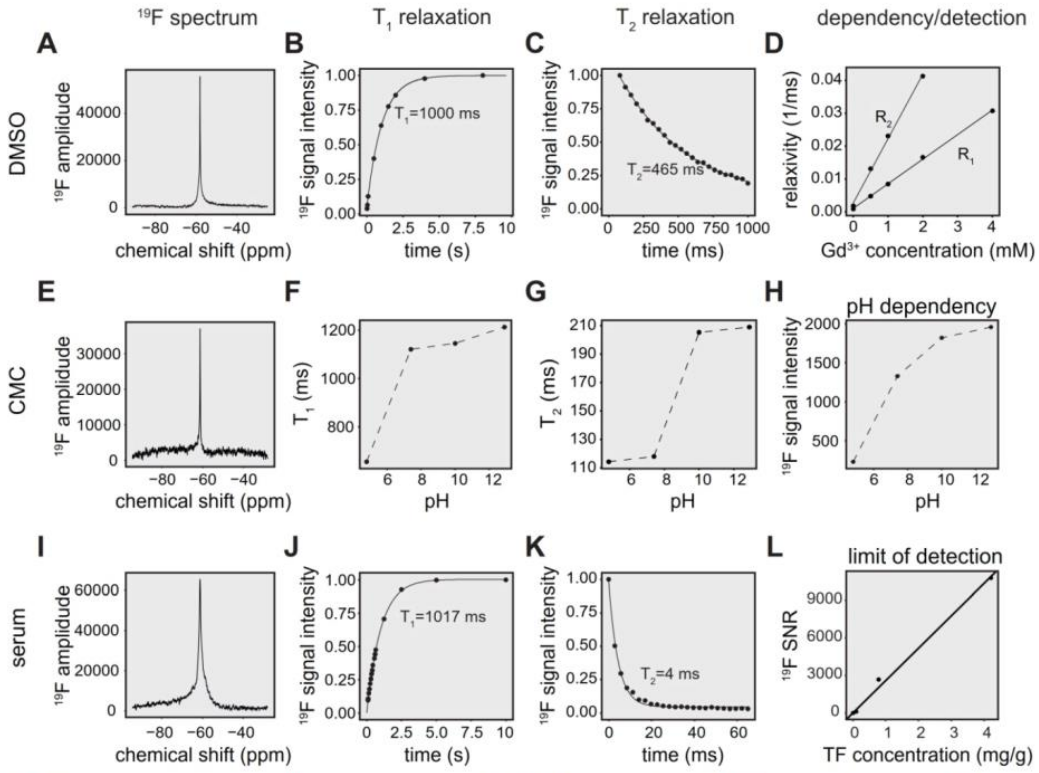

Figure 2. *^{19}F MR characterization of teriflunomide in different chemical environments.* **(A)** ^{19}F MR spectrum of TF in a DMSO phantom (global single pulse, TR=1000 ms, acquisition time = 16 s, concentration: 27.02 mg/mL in 1 mL). **(B)** Spectroscopic determination of T_1 of teriflunomide in DMSO (T_1 = 1000 ms). **(C)** Spectroscopic determination of T_2 of teriflunomide in DMSO (T_2 = 465 ms) using a CPMG sequence. **(D)** Correlation of the relaxation rates R_1 and R_2 (inverse T_1 and inverse T_2) with the concentration of the contrast agent gadopentetate dimeglumine (0.5, 1, 2, 4 mM) in DMSO ($R = 0.998$, $p = 9.17e\text{-}6$ for R_1 and $R = 0.999$, $p = 0.001$ for R_2). TF concentration = 27.02 mg/mL. **(E)** ^{19}F MR spectrum of TF in a carboxymethylcellulose (CMC) phantom (global single pulse, TR=1000 ms, acquisition time = 16 s, concentration: 2.70 mg/mL in 1 mL). **(F)** Change of the ^{19}F T_1 with pH in CMC. **(G)** Change of the ^{19}F T_2 with pH in CMC. **(H)** Change of the ^{19}F signal intensity with pH in CMC; concentration in CMC: 2.70 mg/mL in 1 mL, pH was controlled by adding HCl and NaOH. **(I)** ^{19}F MR spectrum of teriflunomide in a serum phantom (acquisition time = 8 s, concentration: 1.3 mM in 1 mL). **(J)** Spectroscopic determination of T_1 of teriflunomide in human serum (T_1 = 1017 ms). **(K)** Spectroscopic determination of T_2 of teriflunomide in human serum (T_2 = 4 ms) using a CPMG sequence. **(L)** Assessment of the spectroscopic limit of detection (SNR_1) using different TF concentrations in serum (^{19}F MRS measured with a ^{19}F CRP, global single pulse, TR = 1000 ms, acquisition time = 17 min).

experiment). Differences in animal numbers between the time points were either due to technical problems (4 cases) or due to animal welfare (mice needed to be euthanized due to disease severity, 2 cases). We observed a distinct second ^{19}F peak in healthy and EAE animals (-75 to -85 ppm). The -75 ppm peak was seen at a later stage of EAE and was also observed in the abdomen of EAE mice (data not shown).

The ^{19}F MR signal from the processed spectra of EAE and healthy mice is represented in both TD as FID fit (**Figure 3C**) and FD as peak area (integral of the main peak) at -61 ppm (**Figure 3D**) and SNR_1 of this peak (**Figure 3E**). Data from these mice are shown separately in **Table S1** (the raw data is also available as supplemental material). We did not observe any significant differences between the groups between day 8 and day 14, between EAE and healthy control mice (all $p > 0.1$) or in the pairwise comparisons (all $p > 0.1$) for all data, irrelevant whether FID fit, integral or SNR of main peak. In addition, we did not observe differences in variance of the ^{19}F signal intensities (FID fit, integral or SNR) among the animals groups on any day or any of the pairwise comparisons (all $p > 0.1$).

Ex vivo determination of teriflunomide levels in healthy and EAE animals

The TF-derived signal was also measured in the serum of SJL/J EAE mice by ^{19}F MRS (**Figure S1C**). TF concentrations in serum, CSF and perfused brain tissue were quantified by HPLC/MS for both SJL/J and C57BL/6 mice (**Table 1**). We calculated the LOD of the HPLC method to be 4.9 pg/g. In SJL/J mice there was a strong difference between biological samples (main effect $p < 0.001$), but no significant difference between healthy and EAE animals. TF concentrations in serum were an order of magnitude higher than those in perfused brain tissue or CSF, for both healthy and EAE animals (all p values < 0.001) (**Figure 4A, left panel**). In C57BL/6 mice, there was again a strong difference between biological samples

(main effect $p < 0.001$), with TF concentrations in serum greater than those in perfused brain tissue or CSF ($p < 0.001$). Upon post-hoc comparisons, we observed that TF concentrations in the CSF were greater than in the perfused brain tissue, both for C57BL/6 EAE mice ($p = 0.0025$) and for C57BL/6 healthy control mice ($p = 0.032$) (**Figure 4A, right panel**).

Table 1. Concentrations of teriflunomide in µg/g detected via HPLC/MS from *ex vivo* samples from EAE and healthy SJL/J and C57BL/6 mice (median ± interquartile range)

	SJL/J		C57BL/6	
	EAE (n = 7)	Healthy (n = 6)	EAE (n = 4)	Healthy (n = 3)
Serum	32.5 ± 13.8	33.8 ± 17.9	19.0 ± 6.8	20.6 ± 7.4
CSF	1.7 ± 2.2	1.0 ± 1.0	0.5 ± 0.5	0.9 ± 0.3
Brain	0.6 ± 0.9	0.5 ± 0.3	0.1 ± 0.0	0.3 ± 0.1

We observed significant differences in the variance of TF concentrations. In SJL/J mice, these differences were seen among perfused brain, CSF and serum samples ($p < 0.001$) but not between EAE and healthy control groups when considering all *ex vivo* samples ($p = 0.945$). When comparing EAE vs. healthy controls for each tissue separately (pairwise comparisons), the variance in TF concentration was significantly greater in the EAE group in the case of brain tissue ($p = 0.048$), but not CSF and serum samples (**Figure 4A, left panel**). In C57BL/6 mice, differences in variance were also seen among perfused brain, CSF and serum samples ($p < 0.001$). There was again no difference in TF variance between EAE and healthy controls ($p = 0.406$), even when performing the pairwise comparisons for each tissue (**Figure 4A, right panel**).

The HPLC/MS quantification of TF concentrations was important to establish the ground truth for validating *in vivo* ^{19}F MRS data. A calibration of FD ^{19}F MRS signal intensities with HPLC/MS concentration values in mouse serum (spiked with different TF dilution) is shown in **Figure 4B**. The resulting linear fit (Spearman $\rho = 1.000$, $p = 0.333$), was used to estimate the concentration from the FD ^{19}F MR signal intensity. Compared to the HPLC/MS quantification, TF concentrations estimated from ^{19}F MRS were elevated with a maximum relative deviation of 130% and a mean relative deviation of 83% (**Figure 4C**). However, TF concentrations determined by ^{19}F MRS showed a clear correlation with concentrations determined by HPLC/MS (Spearman $\rho = 0.903$, $p = 0.001$).

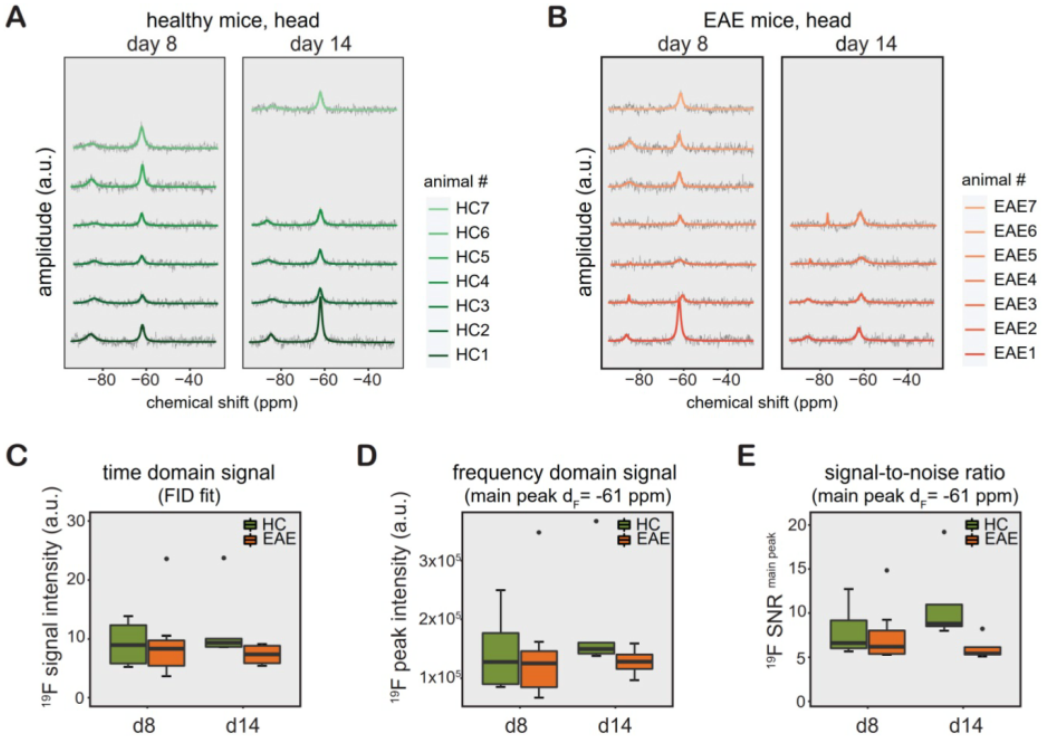

Figure 3. *^{19}F MR detection of teriflunomide (TF) in vivo.* (**A-B**) ^{19}F MR teriflunomide signal from the heads of healthy (A) and EAE (B) mice on day 8 and day 14 following the start of daily teriflunomide treatments. Measurements were performed 16-24 h after the last gavage (acquisition time = 17 min). (**C-D**) ^{19}F MR signal calculated in the time domain as signal intensity from the FID fit (C) and frequency domain as peak area, integral of the main peak (δ_F = -61ppm) using the Lorentzian fit (D) and SNR (signal per one SD of the noise) of the same peak (E) plotted as arbitrary units for all EAE and healthy SJL/J animals for days 8 and 14.

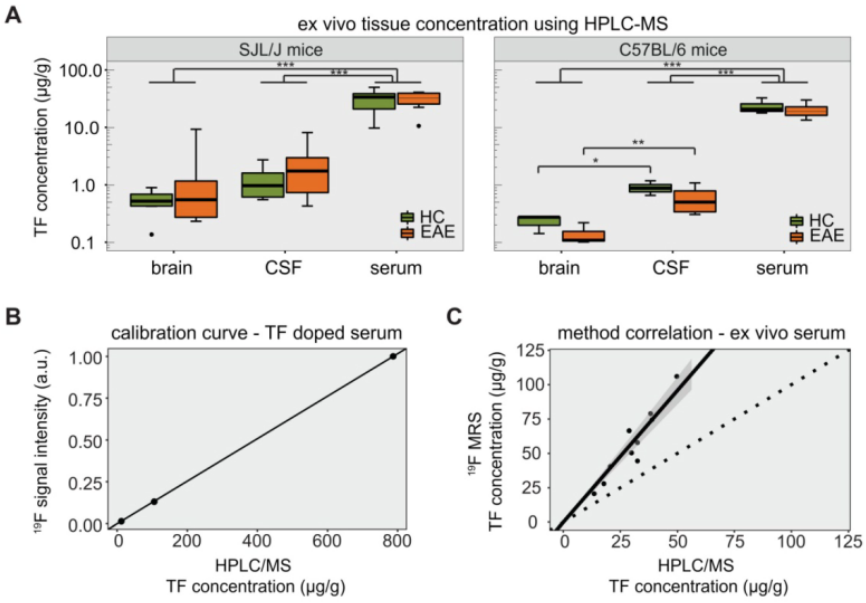

Figure 4. *Detection of teriflunomide by mass spectrometry.* **(A)** Plot showing the detection of teriflunomide by mass spectrometry in the brain, CSF and serum of EAE and healthy animals of both strains SJL/J and C57BL/6 on day 14 (EAE SJL/J n = 7, healthy SJL/J n = 6, EAE C57BL/6 n = 4, healthy C57BL/6 n = 3). **(B)** Calibration curve for ^{19}F MRS quantification using HPLC/MS concentrations of TF dissolved in serum and the corresponding ^{19}F MRS signal intensities (SNR_1; ^{19}F MRS measured with a ^{19}F CRP, global single pulse, TR = 1000 ms, acquisition time = 17 min, linear fit with Spearman ρ = 1.000, p = 0.333). **(C)** Correlation of ^{19}F MR signal quantification *ex vivo* in the serum of TF treated mice with concentrations measured by mass spectrometry in serum (^{19}F MRS measured with a ^{19}F CRP, global single pulse, TR = 1000 ms, acquisition time=1 min, Spearman ρ = 0.903, p = 0.001, dotted line with slope = 1).

Discussion

In this study, we show that non-invasive ^{19}F MR methods can be used to detect TF *in vivo*. *Ex vivo* HPLC/MS analyses confirmed the availability of TF in the CNS at pharmacologically relevant concentrations [56]. The therapeutic effect was strain-dependent, being less pronounced in C57BL/6 mice. This could be attributed to the diverging pathology that both strains present during the course of an EAE: in SJL/J mice the pathology is mainly localized to the brain, in C57BL/6 mice lesions are mostly prevalent in the spinal cord [71]. EAE in SJL/J mice presents as a relapsing-remitting disease (similar to RRMS patients). EAE in C57BL/6 mice follows a chronic disease progression without remissions and relapses (similar to progressive/secondary progressive MS). These strain differences were behind the rationale for studying different mechanism of action of DMDs for the treatment of RRMS and P/SPMS [56]. Different responses to TF treatment among species and strains could be also attributed to differences in target binding potencies [72] or immune cell susceptibilities [56].

Despite increasing concerns regarding the risks of long-term deposition in the brain, contrast-enhanced MRI remains a key tool for diagnosis and differential diagnosis [73-75]. In this study we observed contrast-enhanced brain lesions at the expected time of peak disease, even in asymptomatic TF-treated EAE mice. This underscores the critical role of MRI for early detection of pathology in MS and EAE, even prior to the occurrence of clinical signs and that clinical scoring alone is not sufficient to fully assess the disease status [58].

In addition to peripheral effects and mechanisms of action, many DMDs for MS are expected to work within the CNS. Thus a non-invasive method that studies drug distribution in the CNS would be a useful tool in MS drug development and in treatment monitoring. Hence, we are addressing an area of major interest in MS that could benefit from new studies investigating therapies and their distribution *in vivo*. Nevertheless, the *in vivo* detection of ^{19}F compounds with ^{19}F MR methods remains challenging. This is primarily due to the low drug concentrations available in the human body [70]. Additionally, technological challenges in terms of hardware sensitivity and measurement precision and accuracy limit swift transitions to clinical applications.

^{19}F MR spectroscopy techniques have been used for several years to detect fluorinated drugs in small animals [33-38] and humans [39-45]. The chemo-therapeutic agent 5-Fluorouracil (5-FU) has been studied by ^{19}F MRS in tumor-bearing rats [34] and patients with head and neck tumors [45] and more recently it was detected by ^{19}F MRI in tumor bearing mice using high drug doses and fast spin echo

sequences [38]. ^{19}F MRS imaging (MRSI) of fluvoxamine and fluoxetine was performed in patients with major depressive disorder who were on long term treatment with these drugs [42]. Alternatively, therapeutic compounds containing cytosine (e.g. the neuroprotective drug citicoline or the anticancer drug gemcitabine) can be detected via chemical exchange saturation transfer (CEST) MRI; these molecules contain exchangeable protons that can be selectively saturated and then detected indirectly through the water signal. Recently, the potential of CEST MRI to detect these therapeutic compounds *in vivo* has been shown [76, 77].

Compared to studies investigating fluorinated drugs at high doses [38, 44], in our present study we administered therapeutic doses of the fluorinated drug, which previously had shown an influence on the disease course in SJL/J EAE mice [56]. Additionally, we did not only acquire ^{19}F MR signals right after administration of the drug as has previously been done [36, 78, 79], but we also detected accumulated TF levels over time, and during pathology.

Furthermore, in this study we characterized the MR properties of TF in serum, DMSO and CMC and at varying pH, to assess alterations in the physicochemical and MR properties, which are important to consider during interpretation of data. The pH in different compartments has a known impact on the solubility, binding kinetics and hence bioavailability of drug molecules [80]. pH variations result in different protonation of molecules, changing their MR properties, such as chemical shift [81] and relaxation times [82-86]. pH changes can also effect drug solubility, e.g. at low pH only a fraction of TF is dissolved and thus detected by ^{19}F MR, the precipitated portion will not contribute to the MR signal. Furthermore, pH could also affect the properties of the CMC support matrix. The stomach environment could alter its protonation state and therefore its solubility, thereby affecting the ^{19}F MR properties of TF [87, 88].

While the T_1 of TF in serum was comparable to that in DMSO, the T_2 was substantially shortened in serum, which is also indicated by a broader TF peak [89] in serum, when compared to DMSO. Similar to micelles and nanoparticles [90], CMC could perhaps bind to serum proteins, although one would assume that the drug will be mostly bound to serum proteins in the blood stream. In any case, a shortening of T_2 if caused by drug serum binding (or CMC serum binding) makes signal detection more challenging when using standard pulse sequences.

Here, we used a three-parameter exponential fit, taking an offset of the signal decay into account until reaching the level of noise. Potentially, another fraction of TF exhibiting a different relaxation behavior might contribute to the acquired signal, which however, cannot be distinguished in the experiments performed here. Conversely, an increase in TF MR signal can be expected in short TR measurements in the presence of gadolinium-based contrast agents due to a reduction in T_1 saturation effects. This has implications for neuroinflammation since TF is likely to localize at sites of inflammatory activity in the brain or the spinal cord, and thus its proximity to gadolinium-enhanced lesions in the CNS might increase its detection.

We previously showed that temperature can influence the MR parameters of TF [70]. Here, ^{19}F MR signals increased with increasing pH. Differences in spectral widths between TF in DMSO, CMC and serum can be explained by environmental effects such as different solubility of the drug in the medium and protein-binding effects (99% of TF is plasma protein bound) [91].

As a first step towards studying drug distribution *in vivo*, we measured the ^{19}F MR signal in the abdominal region of healthy rats. The ^{19}F MR signal was acquired directly after TF administration into the stomach; we assume that most of this signal originates from the stomach during the first few minutes. Changes in ^{19}F signal in rats following oral administration can be attributed to pH and temperature changes in the stomach that may alter the solubility or binding of TF to CMC. We hypothesize that pH might play an ambivalent role in different environments e.g. in the stomach, in CMC or in DMSO with respect to solubility and consequently TF detection. The decreasing trend in ^{19}F signal after the six-minute measurement could suggest a gradual influence of the acidic pH in the stomach on signal intensity but also a gradual distribution to the intestinal compartment and absorption into the blood circulation. We expect that the ^{19}F MR signal from the abdominal region in EAE mice, measured 24 h after the last drug administration originates primarily from the liver (highest concentration of TF after blood) [92].

When studying the *in vivo* ^{19}F MR signal of TF in the head region, we observed no changes between day 8 and day 14 p.i. In patients, TF has a half-life of approximately 15 days [51, 93] administered at a dose of 14 mg per day (circa 250 µg/kg). This corresponds to a mouse dose of circa 3 mg/kg [60]. In the current study and previous ones [55, 56] mice received 3-10 times this dose, which is needed to have an effect on the disease course [56]. Leflunomide, the prodrug of TF, reaches steady state in 7 weeks when administered orally at a daily dose of 20 mg (circa 350 µg/kg). If linear pharmacokinetics are assumed

[94], the steady state of TF dose used in mice is expected to be reached earlier than day 8.

Interestingly, we observed a second peak in the range of -75 to -85 ppm alongside the main TF peak at -61 ppm in healthy and EAE mice, and in their *ex vivo* sera, but not in *in vivo* experiments carried out soon after drug administration in the rat. We assume that this peak is a TF metabolite. While we are not aware of any specific TF metabolites that resonate at this range, we are certain that this is not a contamination since it was not reproduced in our phantom experiments and our animals had not been exposed to any other ^{19}F compounds. We believe this second peak surely warrants further investigation and might be valuable to further pharmacological research.

The major metabolite of TF in human plasma is 4-trifluoro-methylaniline oxanilic acid (4-TMOA) [51, 95]. This metabolite has a chemical shift of -59.7 ppm and would overlap with the TF parent compound [96]. Other metabolites such as mono-oxidated TF sulfate, 4-trifluoromethylaniline 2-hydroxy-maionanlc malonamic acid and its sulfate were identified in urine, and mono-oxidated TF sulfate and mono-oxidated TF in feces [95].

The chemical shifts of most CF3 groups lie within the range of -60 to -80 ppm. A more negative chemical shift would indicate increased shielding of the CF3 group, which can occur as a result of branching near the CF3 group or close proximity to hydrogen bond donors [97]. In human subjects the total amount of these metabolites in plasma is lower than 1 % of the parent compound (in contrast to urine and feces) and probably not detectable *in vivo* [95, 98]. However, this might also be different in mice. Different metabolic rates and processes can be an explanation of this finding. Even the EAE pathology might have an impact due to changes in metabolic processes during inflammation [99] and warrants further investigation in future studies.

In a rat EAE model, TF distribution to the brain was shown by whole-body autoradiography [92], whereas no TF could be detected in the brains of EAE mice when using MALDI-MS [100]. The *in vivo* ^{19}F MR signal that we acquired in the head region of healthy and EAE mice with ^{19}F MRS could reflect TF signals in the blood, CSF, brain parenchyma, or perhaps even infiltrating immune cells that are causing the pathology. Since we did not observe any significant differences in TF signal between the healthy controls and EAE mice *in vivo*, there is no evidence of pathology-related alterations in the drug distribution into the head region.

The results from mass spectrometry measurements also did not show significant differences in TF concentrations in perfused brain tissue, CSF and serum between EAE mice and healthy controls. Nevertheless, TF was detectable in CSF and perfused brain tissue in both SJL/J and C57BL/6 mice, though these were significantly lower than serum concentrations. This distribution pattern could reflect the route of the drug from the systemic circulation to the brain via the CSF or the vasculature.

The observed interindividual differences in TF levels are consistent with a TF study performed in patients where steady state plasma concentrations were in the range 7.6-14.8 mg/L and 11-16.9 mg/L following at least 8 weeks daily intake [93].

One caveat of the study was that we could not perform automatic power adjustments during the *in vivo* measurements in the mouse head, due to low SNR; instead we performed short measurements with different reference power settings on the living animal to determine the optimal reference power to reach the 90 ° flip angle. Nonetheless the uncertainty in the flip angle due to potential differences in the positioning of the animal or coil filling factors could be a potential source of variability in the ^{19}F detection. We did not use a reference tube during the *in vivo* measurements for several technical (overlapping signals, potential signal losses), physical (complex *in vivo* setup and limited space) and animal welfare related (breathing obstruction) reasons.

A comparison between the ^{19}F MRS method and the HPLC/MS method in *ex vivo* serum samples showed a linear correlation. However, there were deviations between HPLC/MS and ^{19}F MRS concentration estimations; one could attribute these either to an overestimation by the ^{19}F MRS method or an underestimation by the HPLC/MS method. The proportion of metabolite to parent compound might be higher in mice than in human subjects. Therefore, one could speculate, that the ^{19}F MRS peak at -61 ppm overlaps with a significant amount of its metabolite. Potentially, metabolites detected by ^{19}F MRS are not quantified by the HPLC/MS method and thereby could explain the deviation in the concentration estimation in both methods. Alternatively, differences in the properties of TF between spiked and *ex vivo* serum samples (e.g. differences in protein composition, conductive properties) might be a source for this deviation. Still, both methods were shown to correlate with each other and indicate that TF concentrations could be measured with ^{19}F MRS in future studies, possibly even as non-invasive tool *in vivo*.

While there are still limitations in terms of technological development — in particular with regard to exact calibration of reference power due to low ^{19}F amounts — we highlight here the usefulness

and general feasibility of this approach for studying the biodistribution of fluorinated drugs. In this study, we needed to address several challenges for detecting TF *in vivo*. The quadrature, cryogenically cooled surface coil that we used in this study confers a theoretical increase in sensitivity of 40% [101] compared to a linear coil, but prohibits a dual-tunable feature that accommodates ^{1}H imaging.

To distinguish the distribution of TF in different brain regions ^{19}F MR imaging or localized ^{19}F MR spectroscopy would be highly valuable. This is possible when studying neuroinflammation with ^{19}F MRI and perfluoro-15-crown-5-ether nanoparticles; the ^{19}F MR signal in the CNS and associated lymphatic system is sufficient for single-voxel spectroscopy e.g. PRESS (Point RESolved Spectroscopy) [61] and ^{19}F MR imaging, even when using a RT coil [61]. This is not the case for small molecules such as TF that are available in much smaller quantities in the CNS. Understanding the specific ^{19}F MR properties of the drug of interest will allow the choice and tailoring of appropriate MR pulse sequences. While determining the specific origin of signals detected with non-localized MR spectroscopy is not possible, hypotheses on the origin of signals could be verified by using single voxel spectroscopy. Nevertheless, due to a low T_2 of TF in serum as well as the low TF concentrations expected *in vivo* at a therapeutic level, localized single-voxel MR spectroscopy or MRSI are not trivial techniques to be applied.

In this study we characterized the MS drug teriflunomide in phantom experiments and *in vivo* in the animal model of MS. The ^{19}F CRP significantly boosts SNR compared to other available RF coil technologies and enabled the *in vivo* detection of TF-derived ^{19}F MR signals in EAE mice within a short time [62]. However, more technological developments are needed to further boost ^{19}F MR signal sensitivity to ultimately achieve drug quantification within specific tissue compartments [102]. The combination of multiple approaches such as using cryogenically cooled RF coils [62], higher magnetic fields [103] and methods to accelerate data acquisition such as compressed sensing [104] will be key to achieve this goal and allow monitoring drugs *in vivo* with ^{19}F MRI.

Abbreviations

BBB: blood brain barrier; CFA: complete Freund's adjuvants; CMC: carboxymethylcellulose; CNS: central nervous system; CRP: cryoprobe; CSF: cerebrospinal fluid; DMD: disease modifying drug; EAE: experimental autoimmune encephalomyelitis; FWHM: full-width half maximum; HPLC/MS: high performance liquid chromatography mass spectrometry; LOD: limit of detection; MOG: myelin oligodendrocyte glycoprotein peptide; MR: magnetic resonance; MRI: magnetic resonance imaging; MRS: magnetic resonance spectroscopy; MS: Multiple Sclerosis; PLP: proteolipid protein peptide; PRESS: Point RESolved Spectroscopy; RRMS: relapse-remitting Multiple Sclerosis; SNR: signal-to-noise ratio; TF: teriflunomide.

Acknowledgments

This study was supported by Sanofi-Aventis, the European Research Council (ERC) to TN (743077, ThermalMR) and the *Deutsche Forschungsgemeinschaft* to SW (DFG WA2804). The authors would like to thank Stefanie Münchberg, Victoria Prochnov and Mariya Aravina for technical assistance.

Author Contributions

CP acquired, analyzed, interpreted the data and wrote the first draft of the manuscript; LS and JMM assisted with data acquisition, analysis and interpretation; MR acquired and analyzed the HPLC/MS data; AF, PRD, HW and AP assisted with analysis of MR data, AF, MN, FP and TN revised the manuscript critically for important intellectual content, SW conceived the experiments, analyzed and interpreted the data and wrote the manuscript with CP.

Supplementary Material

Supplementary figures and tables.
http://www.thno.org/v11p2490s1.pdf

Competing Interests

C.P. received presentation fees from Sanofi-Aventis. J.M.M. received presentation fees from Novartis. M.R. is founder and CEO of Lipidomix GmbH. T.N. is founder and CEO of MRI.TOOLS GmbH and received travel funds from Siemens Healthcare. S.W. received research grants from Novartis and Genzyme and presentation fees from Novartis.

References

1. Dendrou CA, Fugger L, Friese MA. Immunopathology of multiple sclerosis. Nat Rev Immunol. 2015; 15: 545-58.
2. Baecher-Allan C, Kaskow BJ, Weiner HL. Multiple Sclerosis: Mechanisms and Immunotherapy. Neuron. 2018; 97: 742-68.
3. Reich DS, Lucchinetti CF, Calabresi PA. Multiple Sclerosis. N Engl J Med. 2018; 378: 169-80.
4. Krieger SC, Cook K, De Nino S, Fletcher M. The topographical model of multiple sclerosis: A dynamic visualization of disease course. Neurol Neuroimmunol Neuroinflamm. 2016; 3: e279.
5. Sinnecker T, Kuchling J, Dusek P, Dörr J, Niendorf T, Paul F, et al. Ultrahigh field MRI in clinical neuroimmunology: a potential contribution to improved diagnostics and personalised disease management. EPMA J. 2015; 6: 16.
6. Wuerfel J, Sinnecker T, Ringelstein EB, Jarius S, Schwindt W, Niendorf T, et al. Lesion morphology at 7 Tesla MRI differentiates Susac syndrome from multiple sclerosis. Mult Scler. 2012; 18: 1592-9.

7. Sinnecker T, Dorr J, Pfueller CF, Harms L, Ruprecht K, Jarius S, et al. Distinct lesion morphology at 7-T MRI differentiates neuromyelitis optica from multiple sclerosis. Neurology. 2012; 79: 708-14.
8. Absinta M, Sati P, Reich DS. Advanced MRI and staging of multiple sclerosis lesions. Nat Rev Neurol. 2016; 12: 358-68.
9. Filippi M, Preziosa P, Banwell BL, Barkhof F, Ciccarelli O, De Stefano N, et al. Assessment of lesions on magnetic resonance imaging in multiple sclerosis: practical guidelines. Brain. 2019; 142: 1858-75.
10. Geraldes R, Ciccarelli O, Barkhof F, De Stefano N, Enzinger C, Filippi M, et al. The current role of MRI in differentiating multiple sclerosis from its imaging mimics. Nat Rev Neurol. 2018; 14: 199.
11. Thompson AJ, Banwell BL, Barkhof F, Carroll WM, Coetzee T, Comi G, et al. Diagnosis of multiple sclerosis: 2017 revisions of the McDonald criteria. Lancet Neurol. 2018; 17: 162-73.
12. Cohan S, Chen C, Baraban E, Stuchiner T, Grote L. MRI utility in the detection of disease activity in clinically stable patients with multiple sclerosis: a retrospective analysis of a community based cohort. BMC Neurol. 2016; 16: 184.
13. Bermel RA, Naismith RT. Using MRI to make informed clinical decisions in multiple sclerosis care. Curr Opin Neurol. 2015; 28: 244-9.
14. Naismith RT. Multiple sclerosis should be treated using a step-down strategy rather than a step-up strategy-NO. Mult Scler. 2016; 22: 1400-2.
15. Erbayat Altay E, Fisher E, Jones SE, Hara-Cleaver C, Lee J-C, Rudick RA. Reliability of classifying multiple sclerosis disease activity using magnetic resonance imaging in a multiple sclerosis clinic. JAMA Neurol. 2013; 70: 338-44.
16. Tintore M, Rovira A, Rio J, Otero-Romero S, Arrambide G, Tur C, et al. Defining high, medium and low impact prognostic factors for developing multiple sclerosis. Brain. 2015; 138: 1863-74.
17. O'Connor PW, Li D, Freedman MS, Bar-Or A, Rice GP, Confavreux C, et al. A Phase II study of the safety and efficacy of teriflunomide in multiple sclerosis with relapses. Neurology. 2006; 66: 894-900.
18. Tintore M, Vidal-Jordana A, Sastre-Garriga J. Treatment of multiple sclerosis - success from bench to bedside. Nat Rev Neurol. 2019; 15: 53-8.
19. Rommer PS, Milo R, Han MH, Satyanarayan S, Sellner J, Hauer L, et al. Immunological Aspects of Approved MS Therapeutics. Front Immunol. 2019; 10: 1564.
20. Gehr S, Kaiser T, Kreutz R, Ludwig WD, Paul F. Suggestions for improving the design of clinical trials in multiple sclerosis-results of a systematic analysis of completed phase III trials. EPMA J. 2019; 10: 425-36.
21. Tsareva E, Kulakova O, Boyko A, Favorova O. Pharmacogenetics of multiple sclerosis: personalized therapy with immunomodulatory drugs. Pharmacogenet Genomics. 2016; 26: 103-15.
22. Grossman I, Knappertz V, Laifenfeld D, Ross C, Zeskind B, Kolitz S, et al. Pharmacogenomics strategies to optimize treatments for multiple sclerosis: Insights from clinical research. Prog Neurobiol. 2017; 152: 114-30.
23. Pistono C, Osera C, Boiocchi C, Mallucci G, Cuccia M, Bergamaschi R, et al. What's new about oral treatments in Multiple Sclerosis? Immunogenetics still under question. Pharmacol Res. 2017; 120: 279-93.
24. Lassmann H. Targets of therapy in progressive MS. Mult Scler J. 2017; 23: 1593-9.
25. Gomes CM, Abrunhosa AJ, Ramos P, Pauwels EK. Molecular imaging with SPECT as a tool for drug development. Adv Drug Deliv Rev. 2011; 63: 547-54.
26. Perkins AC, Frier M. Radionuclide imaging in drug development. Curr Pharm Des. 2004; 10: 2907-21.
27. Matthews PM, Rabiner EA, Passchier J, Gunn RN. Positron emission tomography molecular imaging for drug development. Br J Clin Pharmacol. 2012; 73: 175-86.
28. Lindner JR, Link J. Molecular Imaging in Drug Discovery and Development. Circ Cardiovasc Imaging. 2018; 11: e005355.
29. Waaijer SJH, Kok IC, Eisses B, Schröder CP, Jalving M, Brouwers AH, et al. Molecular Imaging in Cancer Drug Development. J Nucl Med. 2018; 59: 726-32.
30. Niendorf T, Ji Y, Waiczies S. Fluorinated Natural Compounds and Synthetic Drugs. In: Ahrens ET, Flögel U., editor. Fluorine Magnetic Resonance Imaging. 1 ed: Pan Stanford Publishing. 2016; p: 311-44.
31. Reid DG, Murphy PS. Fluorine magnetic resonance *in vivo*: a powerful tool in the study of drug distribution and metabolism. Drug Discov Today. 2008; 13: 473-80.
32. Wolf W, Presant CA, Waluch V. 19F-MRS studies of fluorinated drugs in humans. Adv Drug Deliv Rev. 2000; 41: 55-74.
33. Stevens AN, Morris PG, Iles RA, Sheldon PW, Griffiths JR. 5-Flourouracil metabolism monitored *in vivo* by 19F NMR. Br J Cancer. 1984; 50: 113-7.
34. McSheehy P, Prior M, Griffiths J. Prediction of 5-fluorouracil cytotoxicity towards the Walker carcinosarcoma using peak integrals of fluoronucleotides measured by MRS *in vivo*. Br J Cancer. 1989; 60: 303-9.
35. Desmoulin F, Gilard V, Malet-Martino M, Martino R. Metabolism of capecitabine, an oral fluorouracil prodrug: (19)F NMR studies in animal models and human urine. Drug Metab Dispos. 2002; 30: 1221-9.
36. Morikawa S, Inubushi T, Morita M, Murakami K, Masuda C, Maki J, et al. Fluorine-19 fast recovery fast spin echo imaging for mapping 5-fluorouracil. Magn Reson Med Sci. 2007; 6: 235-40.
37. Cron GO, Beghein N, Ansiaux R, Martinive P, Feron O, Gallez B. 19F NMR *in vivo* spectroscopy reflects the effectiveness of perfusion-enhancing vascular modifiers for improving gemcitabine chemotherapy. Magn Reson Med. 2008; 59: 19-27.
38. Doi Y, Shimmura T, Kuribayashi H, Tanaka Y, Kanazawa Y. Quantitative (19)F imaging of nmol-level F-nucleotides/-sides from 5-FU with T(2) mapping in mice at 9.4T. Magn Reson Med. 2009; 62: 1129-39.
39. Karson CN, Newton JE, Livingston R, Jolly JB, Cooper TB, Sprigg J, et al. Human brain fluoxetine concentrations. J Neuropsychiatry Clin Neurosci. 1993; 5: 322-9.
40. Karson CN, Newton JE, Mohanakrishnan P, Sprigg J, Komoroski RA. Fluoxetine and trifluoperazine in human brain: a 19F-nuclear magnetic resonance spectroscopy study. Psychiatry Res. 1992; 45: 95-104.
41. Komoroski RA, Newton JE, Cardwell D, Sprigg J, Pearce J, Karson CN. *In vivo* 19F spin relaxation and localized spectroscopy of fluoxetine in human brain. Magn Reson Med. 1994; 31: 204-11.
42. Bolo NR, Hode Y, Nedelec JF, Laine E, Wagner G, Macher JP. Brain pharmacokinetics and tissue distribution *in vivo* of fluvoxamine and fluoxetine by fluorine magnetic resonance spectroscopy. Neuropsychopharmacology. 2000; 23: 428-38.
43. Ji Y, Waiczies H, Winter L, Neumanova P, Hofmann D, Rieger J, et al. Eight-channel transceiver RF coil array tailored for (1)H/(1)(9)F MR of the human knee and fluorinated drugs at 7.0 T. NMR Biomed. 2015; 28: 726-37.
44. Durst P, Schuff N, Crocq M-A, Mokrani M-C, Macher J-P. Noninvasive *in vivo* detection of a fluorinated neuroleptic in the human brain by 19F nuclear magnetic resonance spectroscopy. Psychiatry Res Neuroimaging. 1990; 35: 107-14.
45. Schlemmer H-P, Becker M, Bachert P, Dietz A, Rudat V, Vanselow B, et al. Alterations of intratumoral pharmacokinetics of 5-fluorouracil in head and neck carcinoma during simultaneous radiochemotherapy. Cancer Res. 1999; 59: 2363-9.
46. Lanza GM, Jenkins J, Schmieder AH, Moldobaeva A, Cui G, Zhang H, et al. Anti-angiogenic Nanotherapy Inhibits Airway Remodeling and Hyper-responsiveness of Dust Mite Triggered Asthma in the Brown Norway Rat. Theranostics. 2017; 7: 377-89.
47. Wu L, Wen X, Wang X, Wang C, Sun X, Wang K, et al. Local Intratracheal Delivery of Perfluorocarbon Nanoparticles to Lung Cancer Demonstrated with Magnetic Resonance Multimodal Imaging. Theranostics. 2018; 8: 563-74.
48. Shin SH, Park EJ, Min C, Choi SI, Jeon S, Kim YH, et al. Tracking Perfluorocarbon Nanoemulsion Delivery by 19F MRI for Precise High Intensity Focused Ultrasound Tumor Ablation. Theranostics. 2017; 7: 562-72.
49. Metelev V, Zhang S, Zheng S, Kumar ATN, Bogdanov A, Jr. Fluorocarbons Enhance Intracellular Delivery of Short STAT3-sensors and Enable Specific Imaging. Theranostics. 2017; 7: 3354-68.
50. Derfuss T, Mehling M, Papadopoulou A, Bar-Or A, Cohen JA, Kappos L. Advances in oral immunomodulating therapies in relapsing multiple sclerosis. Lancet Neurol. 2020; p: 336-47.
51. Wiese MD, Rowland A, Polasek TM, Sorich MJ, O'Doherty C. Pharmacokinetic evaluation of teriflunomide for the treatment of multiple sclerosis. Expert Opin Drug Metab Toxicol. 2013; 9: 1025-35.
52. Xu M, Lu X, Fang J, Zhu X, Wang J. The efficacy and safety of teriflunomide based therapy in patients with relapsing multiple sclerosis: A meta-analysis of randomized controlled trials. J Clin Neurosci. 2016; 33: 28-31.
53. Radue EW, Sprenger T, Gaetano L, Mueller-Lenke N, Cavalier S, Thangavelu K, et al. Teriflunomide slows BVL in relapsing MS: A reanalysis of the TEMSO MRI data set using SIENA. Neurol Neuroimmunol Neuroinflamm. 2017; 4: e390.
54. Bar-Or A. Teriflunomide (Aubagio®) for the treatment of multiple sclerosis. Exp Neurol. 2014; 262, Part A: 57-65.
55. Merrill J, Hanak S, Pu S-F, Liang J, Dang C, Iglesias-Bregna D, et al. Teriflunomide reduces behavioral, electrophysiological, and histopathological deficits in the Dark Agouti rat model of experimental autoimmune encephalomyelitis. J Neurol. 2009; 256: 89-103.
56. Merrill JE. *In vitro* and *in vivo* pharmacological models to assess demyelination and remyelination. Neuropsychopharmacology. 2009; 34: 55-73.
57. Ringheim GE, Lee L, Laws-Ricker L, Delohery T, Liu L, Zhang D, et al. Teriflunomide attenuates immunopathological changes in the dark agouti rat model of experimental autoimmune encephalomyelitis. Front Neurol. 2013; 4: 169.
58. Lepore S, Waiczies H, Hentschel J, Ji Y, Skodowski J, Pohlmann A, et al. Enlargement of cerebral ventricles as an early indicator of encephalomyelitis. PloS one. 2013; 8: e72841.
59. Iglesias-Bregna D, Hanak S, Ji Z, Petty M, Liu L, Zhang D, et al. Effects of Prophylactic and Therapeutic Teriflunomide in Transcranial Magnetic Stimulation–Induced Motor-Evoked Potentials in the Dark Agouti Rat Model of Experimental Autoimmune Encephalomyelitis. J Pharmacol Exp Ther. 2013; 347: 203-11.
60. Nair AB, Jacob S. A simple practice guide for dose conversion between animals and human. J Basic Clin Pharm. 2016; 7: 27-31.
61. Waiczies H, Lepore S, Drechsler S, Qadri F, Purfürst B, Sydow K, et al. Visualizing brain inflammation with a shingled-leg radio-frequency head probe for 19F/1H MRI. Sci Rep. 2013; 3: 1280.
62. Waiczies S, Millward JM, Starke L, Delgado PR, Huelnhagen T, Prinz C, et al. Enhanced Fluorine-19 MRI Sensitivity using a Cryogenic Radiofrequency Probe: Technical Developments and *Ex vivo* Demonstration in a Mouse Model of Neuroinflammation. Sci Rep. 2017; 7: 9808.

63. Haase A, Frahm J, Matthaei D, Hanicke W, Merboldt KD. FLASH imaging. Rapid NMR imaging using low flip-angle pulses. J Magn Reson. 1986; 67: 258-66.
64. Hennig J, Nauerth A, Friedburg H. RARE imaging: a fast imaging method for clinical MR. Magn Reson Med. 1986; 3: 823-33.
65. Uğurbil K, Garwood M, Ellermann J, Hendrich K, Hinke R, Hu X, et al. Imaging at high magnetic fields: initial experiences at 4 T. Magn Reson Q. 1993; 9: 259-77.
66. Schindelin J, Arganda-Carreras I, Frise E, Kaynig V, Longair M, Pietzsch T, et al. Fiji: an open-source platform for biological-image analysis. Nat Methods. 2012; 9: 676-82.
67. Kreis R, Boer V, Choi IY, Cudalbu C, de Graaf RA, Gasparovic C, et al. Terminology and concepts for the characterization of *in vivo* MR spectroscopy methods and MR spectra: Background and experts' consensus recommendations. NMR Biomed. 2020; p: e4347.
68. Günther H. NMR spectroscopy: basic principles, concepts, and applications in chemistry. 3 ed. Weinheim: Wiley-VCH. 2013.
69. Near J, Harris AD, Juchem C, Kreis R, Marjańska M, Öz G, et al. Preprocessing, analysis and quantification in single-voxel magnetic resonance spectroscopy: experts' consensus recommendations. NMR Biomed. 2020; p: e4257.
70. Prinz C, Delgado PR, Eigentler TW, Starke L, Niendorf T, Waiczies S. Toward (19)F magnetic resonance thermometry: spin-lattice and spin-spin-relaxation times and temperature dependence of fluorinated drugs at 9.4 T. Magn Reson Mater Phy. 2018; 10.1007/s10334-018-0722-8.
71. Pierson E, Simmons SB, Castelli L, Goverman JM. Mechanisms regulating regional localization of inflammation during CNS autoimmunity. Immunol Rev. 2012; 248: 205-15.
72. Fox RI, Herrmann ML, Frangou CG, Wahl GM, Morris RE, Strand V, et al. Mechanism of action for leflunomide in rheumatoid arthritis. Clin Immunol. 1999; 93: 198-208.
73. El-Khatib AH, Radbruch H, Trog S, Neumann B, Paul F, Koch A, et al. Gadolinium in human brain sections and colocalization with other elements. Neurol Neuroimmunol Neuroinflamm. 2019; 6: e515.
74. Schlemm L, Chien C, Bellmann-Strobl J, Dörr J, Wuerfel J, Brandt AU, et al. Gadopentetate but not gadobutrol accumulates in the dentate nucleus of multiple sclerosis patients. Mult Scler. 2017; 23: 963-72.
75. Boyken J, Niendorf T, Flemming B, Seeliger E. Gadolinium Deposition in the Brain after Contrast-enhanced MRI: Are the Data Valid? Radiology. 2018; 288: 630-2.
76. Li Y, Chen H, Xu J, Yadav NN, Chan KW, Luo L, et al. CEST theranostics: label-free MR imaging of anticancer drugs. Oncotarget. 2016; 7: 6369-78.
77. Liu H, Jablonska A, Li Y, Cao S, Liu D, Chen H, et al. Label-free CEST MRI Detection of Citicoline-Liposome Drug Delivery in Ischemic Stroke. Theranostics. 2016; 6: 1588-600.
78. Wolf W, Presant CA, Servis KL, el-Tahtawy A, Albright MJ, Barker PB, et al. Tumor trapping of 5-fluorouracil: *in vivo* 19F NMR spectroscopic pharmacokinetics in tumor-bearing humans and rabbits. Proc Natl Acad Sci USA. 1990; 87: 492-6.
79. Nakada T, Kwee IL, Griffey BV, Griffey RH. 19F 2-FDG NMR imaging of the brain in rat. Magn Reson Imaging. 1988; 6: 633-5.
80. Florence AT, Attwood D. Solubility of Drugs in Liquids. In: Florence AT, Attwood D, editors. Physicochemical Principles of Pharmacy. London: Macmillan Education UK. 1981; p:125-72.
81. Farrell D, Miranda E, Webb H, Georgi N, Crowley P, McIntosh L, et al. Titration_DB: Storage and analysis of NMR-monitored protein pH titration curves. Proteins. 2010; 78: 843-57.
82. Moser E, Winklmayr E, Holzmüller P, Krssak M. Temperature- and pH-dependence of proton relaxation rates in rat liver tissue. Magn Reson Imaging. 1995; 13: 429-40.
83. Meiboom S, Luz Z, Gill D. Proton Relaxation in Water. J Chem Phys. 1957; 27: 1411.
84. Schilling AM, Blankenburg FB, Bernarding J, Heidenreich JO, Wolf KJ. Intracerebral pH affects the T2 relaxation time of brain tissue. Neuroradiology. 2002; 44: 968-72.
85. Gerken JB. Measurement of pH by NMR Spectroscopy in Concentrated Aqueous Fluoride Buffers. J Fluor Chem. 2011; 132: 68-70.
86. Grant R, Condon B, Moyns S, Patterson J, Hadley D, Teasdale G. Temporal physiochemical changes during *in vitro* relaxation time measurements: the cerebrospinal fluid. Magn Reson Med. 1988; 6: 397-402.
87. Barbucci R, Magnani A, Consumi M. Swelling Behavior of Carboxymethylcellulose Hydrogels in Relation to Cross-Linking, pH, and Charge Density. Macromolecules. 2000; 33: 7475-80.
88. Koshkina O, White PB, Staal AHJ, Schweins R, Swider E, Tirotta I, et al. Nanoparticles for "two color" 19F magnetic resonance imaging: Towards combined imaging of biodistribution and degradation. J Colloid Interface Sci. 2020; 565: 278-87.
89. Jansen JF, Backes WH, Nicolay K, Kooi ME. 1H MR spectroscopy of the brain: absolute quantification of metabolites. Radiology. 2006; 240: 318-32.
90. Corbo C, Molinaro R, Tabatabaei M, Farokhzad OC, Mahmoudi M. Personalized protein corona on nanoparticles and its clinical implications. Biomater Sci. 2017; 5: 378-87.
91. Warnke C, Stuve O, Kieseier BC. Teriflunomide for the treatment of multiple sclerosis. Clin Neurol Neurosurg. 2013; 115 Suppl 1: S90-4.
92. Kaplan J, Cavalier S, Turpault S. Biodistribution of teriflunomide in naive rats vs rats with experimental autoimmune encephalomyelitis. Mult Scler J. 2015; 21: 141-.
93. Rakhila H, Rozek T, Hopkins A, Proudman S, Cleland L, James M, et al. Quantitation of total and free teriflunomide (A77 1726) in human plasma by LC-MS/MS. J Pharm Biomed Anal. 2011; 55: 325-31.
94. Haraoui B. 57 - Leflunomide. In: Hochberg MC, Silman AJ, Smolen JS, Weinblatt ME, Weisman MH, editors. Rheumatology (Sixth Edition). Philadelphia. 2015; p:451-8.
95. Yao X, Liu Y, Song L, Jiang J, Xiao F, Liu D, et al. Development of a simple HPLC-MS/MS method to simultaneously determine teriflunomide and its metabolite in human plasma and urine: Application to clinical pharmacokinetic study of teriflunomide sodium and leflunomide. Biomed Chromatogr. 2019; 33: e4420.
96. Wade KE, Troke J, Macdonald CM, Wilson ID, Nicholson JK. 19F NMR Studies of the Metabolism of Trifluoromethylaniline. In: Reid E, Robinson JD, Wilson ID, editors. Bioanalysis of Drugs and Metabolites, Especially Anti-Inflammatory and Cardiovascular. 1 ed. Boston, MA: Springer US. 1988; p:383-8.
97. Dalvit C, Vulpetti A. Intermolecular and Intramolecular Hydrogen Bonds Involving Fluorine Atoms: Implications for Recognition, Selectivity, and Chemical Properties. ChemMedChem. 2012; 7: 262-72.
98. Brunetti L, Wagner ML, Maroney M, Ryan M. Teriflunomide for the treatment of relapsing multiple sclerosis: a review of clinical data. Ann Pharmacother. 2013; 47: 1153-60.
99. Morgan ET. Impact of infectious and inflammatory disease on cytochrome P450-mediated drug metabolism and pharmacokinetics. Clin Pharmacol Ther. 2009; 85: 434-8.
100. Rzagalinski I, Hainz N, Meier C, Tschernig T, Volmer DA. Spatial and molecular changes of mouse brain metabolism in response to immunomodulatory treatment with teriflunomide as visualized by MALDI-MSI. Anal Bioanal Chem. 2018; p:353-65.
101. Glover GH, Hayes CE, Pelc NJ, Edelstein WA, Mueller OM, Hart HR, et al. Comparison of linear and circular polarization for magnetic resonance imaging. J Magn Reson. 1985; 64: 255-70.
102. Waiczies S, Srinivas M, Flögel U, Boehm-Sturm P, Niendorf T. Special issue on fluorine-19 magnetic resonance: technical solutions, research promises and frontier applications. Magn Reson Mater Phy. 2019; 32: 1-3.
103. Waiczies S, Rosenberg JT, Kuehne A, Starke L, Delgado PR, Millward JM, et al. Fluorine-19 MRI at 21.1 T: enhanced spin-lattice relaxation of perfluoro-15-crown-5-ether and sensitivity as demonstrated in *ex vivo* murine neuroinflammation. Magn Reson Mater Phy. 2018.
104. Starke L, Pohlmann A, Prinz C, Niendorf T, Waiczies S. Performance of compressed sensing for fluorine-19 magnetic resonance imaging at low signal-to-noise ratio conditions. Magn Reson Med. 2019; p:1-17.

2.5 Imaging biomarkers in MS to study inflammation

This chapter builds on **publication 5** "Transient enlargement of brain ventricles during relapsing-remitting multiple sclerosis and experimental autoimmune encephalomyelitis" published in JCI Insight (Millward et al., 2020).

While understanding the distribution of DMTs (as motivated in **publication 4**) is crucial to understand treatment response in MS patients, identifying quantitative MRI biomarkers is of equal significance to guide clinicians towards a more effective diagnosis and better treatment strategy (Filippi et al., 2019a). Contrast enhancement MRI is a diagnostic tool for MS but concerns regarding long-term gadolinium deposition underscores the need for further diagnostic tools. The application of experimental MRI methods to the EAE animal model of MS allows a direct correlation of MRI findings with histopathology as well as investigation of disease before clinical onset, which is challenging to do in patients. We could previously perform in vivo microscopic MRI in the EAE, reaching a spatial resolution of 35 µm with the help of a ^{1}H (proton)-CRP (Waiczies et al., 2012; Lepore et al., 2013). This technology facilitated detection of EAE pathology without the use of contrast agent during early stages of disease and showed excellent correspondence with conventional histology (Waiczies et al., 2012).

Apart from improving spatial resolution, the increase in SNR with the ^{1}H-CRP reduced measurement time considerably and enabled more frequent acquisitions in the same EAE mice. This opportunity uncovered a new finding in the EAE that involved pronounced changes in ventricle volume (VV) already prior to onset of disease (Lepore et al., 2013). We recently followed VV changes in the EAE for two months in the same animal and used contrast-enhanced T_1 mapping as a quantitative measure of acute inflammation (**Figure 1; Figure 2** in own work 5 (Millward et al., 2020)). Transient VV changes (particularly prior and during onset of EAE) coincided with BBB disruption.

We confirmed the clinical relevance of these findings in MS patients by performing a retrospective analysis of a clinical trial, where RRMS patients had received monthly MRI scans for one year (Paul et al., 2008). The majority of RRMS patients showed dynamic VV fluctuations, beyond normal variation, and these patients appeared to be at an earlier phase of disease **(Figure 8** in own work 5 (Millward et al., 2020). We used time-series-analysis to explore how changes in VV over time relate to changes in other MRI and clinical parameters and showed the same level of cross-correlation as that for contrast-enhanced MRI **(Figure 9** in own work 5 (Millward et al., 2020)):

JCI insight

RESEARCH ARTICLE

Transient enlargement of brain ventricles during relapsing-remitting multiple sclerosis and experimental autoimmune encephalomyelitis

Jason M. Millward,[1,2] Paula Ramos Delgado,[1] Alina Smorodchenko,[3] Laura Boehmert,[1] Joao Periquito,[1] Henning M. Reimann,[1] Christian Prinz,[1] Antje Els,[1] Michael Scheel,[4] Judith Bellmann-Strobl,[4,5] Helmar Waiczies,[6] Jens Wuerfel,[4,7] Carmen Infante-Duarte,[2] Claudia Chien,[4] Joseph Kuchling,[4] Andreas Pohlmann,[1] Frauke Zipp,[8] Friedemann Paul,[4,5] Thoralf Niendorf,[1,5] and Sonia Waiczies[1]

[1]Experimental Ultrahigh Field Magnetic Resonance, Max Delbrück Center for Molecular Medicine in the Helmholtz Association, Berlin, Germany. [2]Institute for Medical Immunology, Charité – Universitätsmedizin Berlin, Berlin, Germany. [3]Medical School Hamburg, University of Applied Sciences and Medical University, Hamburg, Germany. [4]NeuroCure Clinical Research Center, Charité – Universitätsmedizin Berlin, Berlin, Germany. [5]Experimental and Clinical Research Center, a joint venture of the Max Delbrück Center for Molecular Medicine and the Charité – Universitätsmedizin Berlin, Berlin, Germany. [6]MRI.TOOLS GmbH, Berlin, Germany. [7]Medical Image Analysis Center (MIAC AG) and Department of Biomedical Engineering, University of Basel, Basel, Switzerland. [8]Department of Neurology, University Medical Center of the Johannes Gutenberg, University of Mainz, Mainz, Germany.

The brain ventricles are part of the fluid compartments bridging the CNS with the periphery. Using MRI, we previously observed a pronounced increase in ventricle volume (VV) in the experimental autoimmune encephalomyelitis (EAE) model of multiple sclerosis (MS). Here, we examined VV changes in EAE and MS patients in longitudinal studies with frequent serial MRI scans. EAE mice underwent serial MRI for up to 2 months, with gadolinium contrast as a proxy of inflammation, confirmed by histopathology. We performed a time-series analysis of clinical and MRI data from a prior clinical trial in which RRMS patients underwent monthly MRI scans over 1 year. VV increased dramatically during preonset EAE, resolving upon clinical remission. VV changes coincided with blood-brain barrier disruption and inflammation. VV was normal at the termination of the experiment, when mice were still symptomatic. The majority of relapsing-remitting MS (RRMS) patients showed dynamic VV fluctuations. Patients with contracting VV had lower disease severity and a shorter duration. These changes demonstrate that VV does not necessarily expand irreversibly in MS but, over short time scales, can expand and contract. Frequent monitoring of VV in patients will be essential to disentangle the disease-related processes driving short-term VV oscillations from persistent expansion resulting from atrophy.

Conflict of interest: The authors have declared that no conflict of interest exists.

Submitted: May 7, 2020
Accepted: September 24, 2020
Published: November 5, 2020

Reference information: *JCI Insight*. 2020;5(21):e140040. https://doi.org/10.1172/jci.insight.140040.

Introduction

The cerebrospinal fluid (CSF) compartments are increasingly recognized for their vital role in bridging the CNS with the peripheral immune system. Immune cells, including central memory T cells, circulate throughout the CSF in the ventricles and subarachnoid spaces to surveil the CNS parenchyma, after crossing the blood-CSF barrier (BCSFB) in the choroid plexus (1). Together with the blood-brain barrier (BBB), the BCSFB tightly regulates the entry of cells and solutes into the CNS. When these barriers and other regulatory mechanisms break down, immune cells enter the CNS and may initiate neuroinflammatory diseases such as multiple sclerosis (MS) (2). In MS, pathological immune cells trigger demyelination and neurodegeneration, ultimately causing clinical disability.

MRI is an indispensable tool in diagnosing MS and monitoring disease progression (3–6). Disruptions of the BBB can be revealed by MRI using gadolinium-based contrast agents (GBCA). Contrast-enhancing lesions (CEL) indicate recent inflammatory activity, predominantly seen during the relapsing-remitting

JCI insight RESEARCH ARTICLE

(RR) disease phases. Contrast enhancement is currently the only MRI feature to assess the lesion acuity at the time of first assessment (7, 8), but increasing concerns regarding potential long-term deposition of gadolinium in the brain could potentially restrict the application of this important diagnostic tool (9–12). Improvements in MRI technology and a better understanding of key aspects of MS pathology promise to better identify changes in the CNS of MS patients and to provide clinicians with a better guide to enhance the accuracy and speed of an MS diagnosis (5).

The experimental autoimmune encephalomyelitis (EAE) animal model of neuroinflammation resembles several aspects of MS and has proven invaluable for gaining insight into its pathological processes and identification of new treatment strategies (13). Studies in the EAE model afford the possibility to directly relate MRI findings with histopathological correlates and to study the phase of disease before clinical onset — investigations that are challenging to perform in patients. We showed, using high-resolution microscopic MRI, that inflammatory lesions could be detected in the cerebellum, cortex, and periventricular regions early in disease, before the onset of clinical EAE signs (14). During this preonset phase of EAE, we observed a marked and reproducible enlargement of the brain ventricles (15). This was surprising, since profound neurodegeneration at this very early stage of disease before the emergence of clinical signs is unlikely to be the explanation for the expansion.

Cerebral ventricle enlargement is commonly linked to neurodegeneration and brain atrophy. While this occurs during the course of normal aging, shrinkage of the cortex and expansion of the ventricles proceeds more rapidly in MS patients (16–21), especially during the secondary progressive phase of MS (SPMS), in which neurodegenerative processes dominate. Nevertheless, neurodegeneration — of the deep gray matter, in particular — can also occur from the earliest stages of brain inflammatory disease (22, 23), and it is essential that aspects of disease relating to inflammation are disentangled from those relating to neurodegeneration. For this, it is crucial that noninvasive investigations are carried out at frequent time intervals in order to capture events that are likely to be overlooked in cross-sectional studies or longitudinal studies with long intervals between observations. Furthermore, correlations among multiple variables during the course of disease should be carefully considered as a time series, to elucidate possible pathological relationships.

To detail fluctuations in the ventricles, the current study examined ventricle volume (VV) changes in both EAE mice and MS patients in longitudinal studies designed with frequent serial MRI scans. We used a time-series approach to study the relationship of VV with other MRI and clinical variables relevant to the pathology. In EAE mice, we performed frequent MRI scans for up to 2 months in order to investigate how inflammatory processes may affect VV beyond the initial acute phase of disease activity. To ascertain the clinical relevance of VV fluctuations in MS, we undertook a retrospective exploratory analysis of data from a prior clinical trial, in which patients with definite RRMS underwent monthly MRI scans over the course of one year. This design afforded a higher time resolution than is typically used, while balancing the practicalities of conducting clinical studies in MS patients. We used time-series analysis to explore how changes in VV over time relate to changes in other MRI and clinical parameters. In this study, we explored the potential of brain ventricle size changes as a possible MRI biomarker that could serve as a proxy of disease activity.

Results

VV changes dynamically during the course of EAE. We performed frequent MRI of EAE mice over a period of 2 months in order to investigate changes beyond the presymptomatic phase and the first disease peak and remission, typically examined in many EAE studies. During the initial disease phase, there was a pronounced increase in VV that is clearly visible on anatomical MRIs (Figure 1A), confirming our previous observation (15). By day 8 (d8) postimmunization (p.i.), the group mean increase in VV relative to baseline values was 130.8% ± 7.74% (mean ± SEM, $P < 0.001$, 1-way ANOVA) (Figure 1B). This was well beyond the range of normal VV variation in healthy unmanipulated SJL mice, which we determined in our previous study ($n = 6$) to be plus or minus 6% (15). This increase peaked at 160.7% ± 10.25% and 157.5% ± 7.69% by d11 and d13 p.i. Four mice in the cohort showed VV increases greater than 200%.

The magnitude of expansion began tapering at d15 p.i. (139.9% ± 6.68%), and mean VV eventually returned to baseline levels by d22 (Figure 1B). For $n = 9$ SJL mice, we continued MRI examinations every 2–3 days, up to d64 p.i., in order to follow the VV changes downstream of the initial disease phase. The mice showed a typical RR disease course, with clinical signs developing around d10 p.i., peaking at d14 p.i., and remitting by d20–d22 p.i. (Figure 1C).

The expansion and contraction in VV followed a similar course as the neurological signs. In the representative case shown in Figure 1A, VV expansions can be seen at d13, d29, and d46 p.i., each followed by

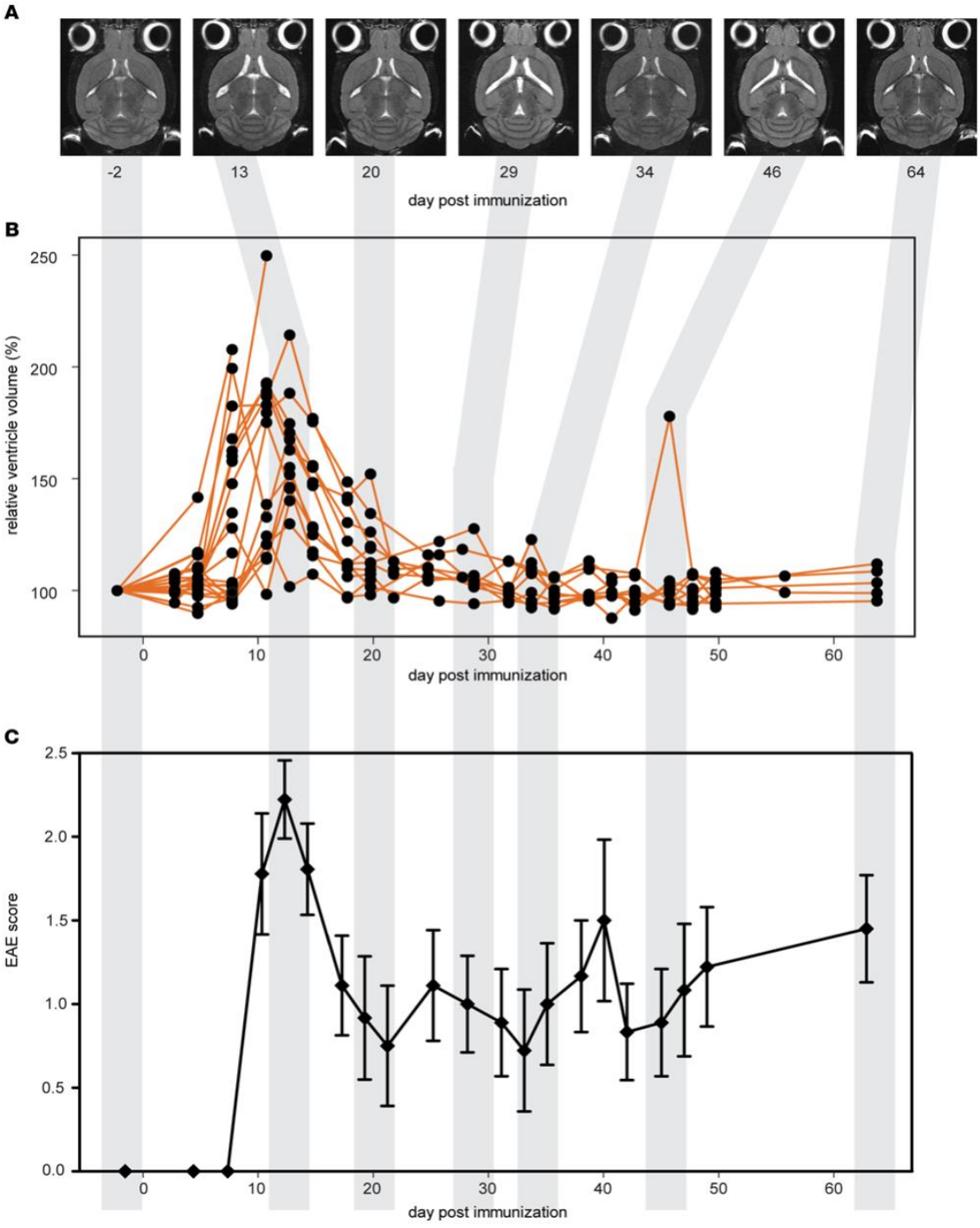

Figure 1. Ventricle volume changes dynamically during the course of EAE. (**A**) T_2-weighted horizontal MRI scans of a representative mouse brain show changes in ventricle size from baseline (day –2) to day 64 p.i. (**B**) Brain ventricle volume plotted as a percentage of baseline values (n = 35). By day 8 p.i., the mean volume was 130.8% ± 7.74% (± SEM) of the baseline volume (P < 0.001, ANOVA), well beyond the range of normal variation in healthy SJL mice of ± 6%. Ventricle volume peaked at days 11–13 p.i. and returned to baseline levels by day 22 p.i. (**C**) Emergence and remission of EAE clinical signs coincided with the peak expansion and contraction of ventricle volume (mean ± SEM).

JCI insight RESEARCH ARTICLE

VV contractions at d20, d34, and d64, respectively (Figure 1A). The timing of VV normalization coincided with remission of clinical signs, although there were differences in the kinetics among individual animals, especially at later time points. VV continued to change during the chronic stage of disease, though generally, these fluctuations were less pronounced than the prominent changes observed during the initial acute disease phase. All animals that were monitored after the initial VV expansion showed contractions back to normal volumes — i.e., no animal displayed permanently enlarged ventricles. Importantly, at the end of the experiment (d64), while most animals still exhibited a degree of neurological disease severity (EAE score 2.0 ± 1.75, median ± IQR), VVs had returned to normal baseline values.

Ventricle enlargement coincides with emergence of gadolinium-enhancing lesions and precedes onset of clinical signs of EAE. To explore the relationship between VV changes and BBB breakdown during inflammation, we administered GBCA to EAE mice during the early acute phase of disease. T_1 mapping was performed to obtain an unbiased quantitative measurement of the global changes in tissue relaxation caused by leakage of the GBCA into the brain parenchyma. In order to make the quantification robust across the longitudinal series of scans, images from each time point were registered to the baseline image (2 days before immunization [d–2]), for each individual animal.

A typical pattern of contrast enhancement — with diffuse lesions especially prominent in the cerebellum, meninges, and periventricular regions — was observed already by d5 p.i. (Figure 2A). The change in brain T_1 values after GBCA administration (ΔT_1 = precontrast minus postcontrast mean values) was calculated for n = 16 mice, at time points ranging from baseline (d–2 p.i.) to d25 p.i. (Figure 2, B and C). Compared with baseline, the ΔT_1 in the cerebellum was significantly increased at d8 and d11 p.i. (592.9 ± 103.8 ms and 551.2 ± 71.4 ms, respectively, P = 0.0030, 1-way ANOVA) (Figure 2B). The ΔT_1 in the whole brain (Figure 2C), was also significantly increased at d8 and d11 p.i. (373.1 ± 52.9 ms and 342.8 ± 43.2 ms, respectively, P = 0.0023, 1-way ANOVA).

Gadolinium enhancement was observed before the onset of clinical signs (Figure 2D), although the timing of this varied among animals. We compared the timing of changes in ΔT_1 with that of VV and clinical changes (Figure 2D). There was no significant difference in the time to show VV increases > 6% and the time to show the maximum change in ΔT_1 (P = 0.2800, log-rank test) (Figure 2D). Both VV and ΔT_1 increases occurred significantly earlier than the onset of EAE clinical signs (P = 0.0068 and P = 0.0005, respectively). The onset of EAE clinical signs is often accompanied by a substantial reduction in body weight. Maximum body weight loss also occurred significantly later than both VV and ΔT_1 changes (P = 0.008 and P < 0.0001, respectively) (Figure 2D).

Early ventricle enlargement in EAE correlates with inflammation and minimal neurodegeneration. The macroscopic VV expansion observed by MRI could also be seen by gross examination of histological sections (Figure 3). With histological staining, we could follow the emergence of inflammatory cell infiltration in EAE brains (n = 19) up to d11 p.i. (Figure 3, A–U). Representative images of H&E-stained sections show no apparent pathology before immunization (Figure 3, A–D) or at d3 p.i. (Figure 3, E–G). The first signs of pathology were detected on d5 (Figure 3, H–J), as shown by the start of meningeal infiltration of macrophage/myeloid cells (F4/80 staining) and accompanying gliosis (GFAP staining) (Figure 3I) and the appearance of cerebellar lesions (Figure 3J). By d8 p.i., the inflammation was even more evident (Figure 3, K–M). This corresponds to the time point of statistically significant increases in VV and GBCA enhancement observed by MRI. At this time point, we observed pronounced meningeal inflammation and gliosis (Figure 3L), as well as T cell infiltration in the parenchyma, as shown by CD3 stains (Figure 3M). By d11 p.i., the marked increase in volume of the lateral, third, and fourth ventricles (Figure 3N) was accompanied by extensive histopathology, especially prominent in periventricular regions (Figure 3, O–Q) and cerebellum (Figure 3, R and S), as well as brainstem and meninges (Figure 3, T and U).

Semiquantitative scoring of the severity of inflammation positively correlated with VV — i.e., mice with the largest increase of VV showed greater burden of histopathology (Spearman's r = 0.7225, P = 0.0023) (Figure 3V). The histopathology score also correlated with the ΔT_1 of the brain (Spearman's r = 0.7480, P = 0.0013) (Figure 3W).

Neurodegeneration is expected during the course of EAE. We performed Fluoro-Jade (FJ) staining on serial sections from the same tissue samples shown in Figure 3 in order to determine to what extent this related to the inflammatory pathology and VV enlargement. No FJ^+ staining was seen in unimmunized animals (Figure 4, A and C) or at d3 p.i. FJ^+ foci were seen infrequently on d5 p.i., became more readily apparent by d8 p.i., and were more frequently observed by d11, in cerebellum and the brainstem (Figure 4, B and D).

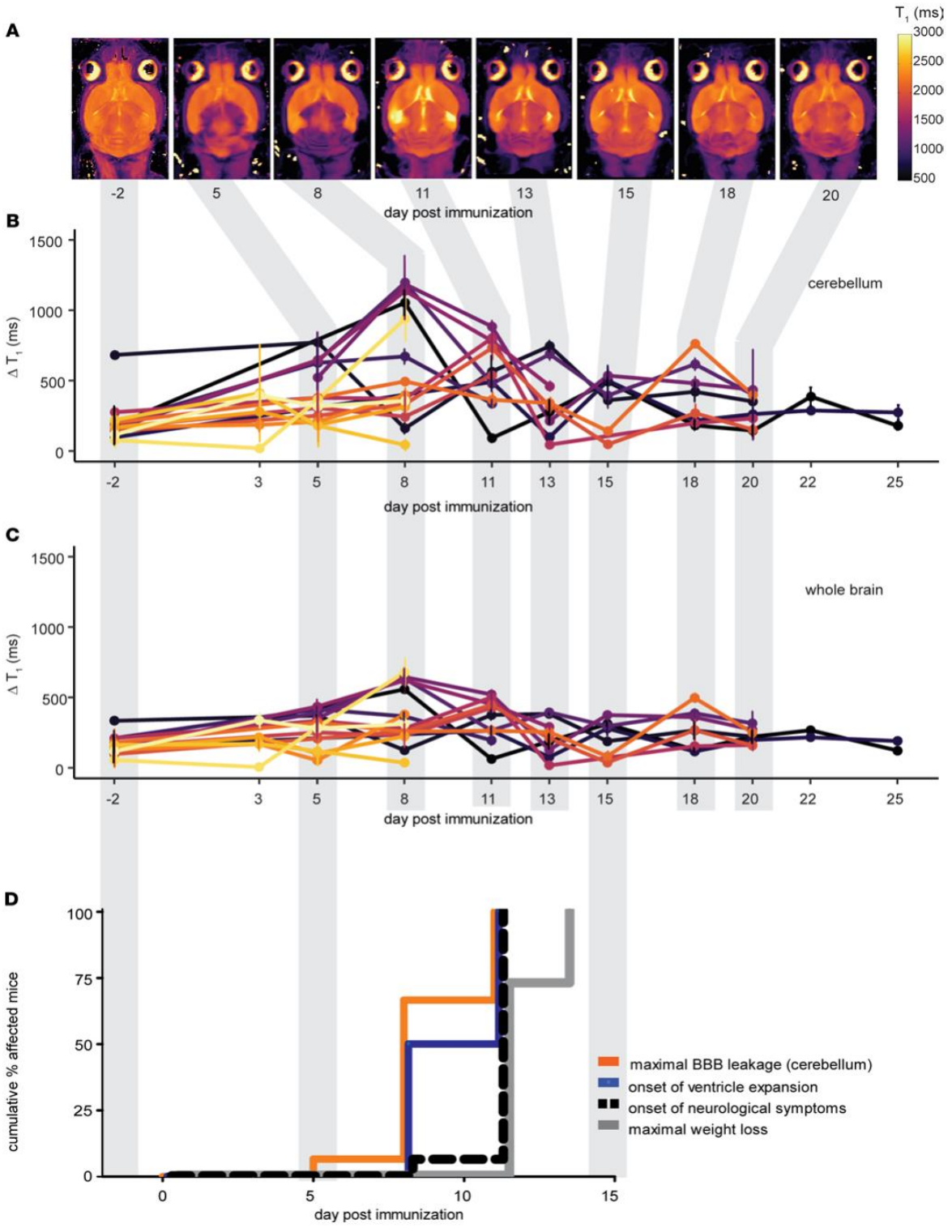
A
T1 (ms)
3000
2500
2000
1500
1000
500
-2
5
8
11
13
15
18
20
day post immunization
B
cerebellum
Δ T1 (ms)
1500
1000
500
0
-2
3
5
8
11
13
15
18
20
22
25
day post immunization
C
whole brain
Δ T1 (ms)
1500
1000
500
0
-2
3
5
8
11
13
15
18
20
22
25
day post immunization
D
cumulative % affected mice
100
75
50
25
0
0
5
10
15
day post immunization
maximal BBB leakage (cerebellum)
onset of ventricle expansion
onset of neurological symptoms
maximal weight loss

JCI insight RESEARCH ARTICLE

Figure 2. Ventricle enlargement coincides with gadolinium-enhancing lesions and precedes EAE clinical signs. (**A**) T_1 map MRIs of a representative mouse brain show altered tissue relaxation due to blood-brain barrier disruption following administration of gadolinium-based contrast agent. Reduced tissue T_1 (purple) is apparent in the meninges, cerebellum, and periventricular regions already by day 5 p.i. Note that the brain images have been registered to the baseline image for quantification; therefore, changes in ventricle volume are not apparent in these images. (**B**) Quantification of global changes in tissue T_1 following gadolinium contrast administration were especially prominent in the cerebellum (n = 16). The ΔT_1 (precontrast – postcontrast values) was significantly increased from baseline at days 8–11 p.i. (P = 0.0030, ANOVA). (**C**) The ΔT_1 of the whole-brain was also significantly increased at days 8–11 p.i. (P = 0.0023, ANOVA). (**D**) Kaplan-Meier plots show that the time of onset of ventricle expansion and the time of maximal gadolinium enhancement significantly preceded the onset of EAE clinical signs (P = 0.0068 and P = 0.0005, respectively; log-rank test) and the time of maximal body weight loss (P = 0.008, P < 0.0001, respectively).

Although FJ^+ foci always accompanied inflammatory lesions, only minimal FJ staining was observed in periventricular lesions. Quantification of FJ staining intensity from whole brain sections illustrates a modest yet increasing accumulation of neurodegeneration during this early phase of EAE (Figure 4E).

Dynamic changes in VVs in RRMS patients. The magnitude and timing of the VV changes in the EAE model were compelling. Nevertheless, the validation that these findings in the animal had any translational relevance for MS patients remained to be demonstrated. For this, we performed a time-series analysis (Figure 5) of data from our previous clinical study (NCT00616187) (24), in which RRMS patients (n = 33) underwent 13 serial MRI examinations over 1 year (Figure 5). This was a baseline-to-treatment clinical study of oral high-dose atorvastatin treatment for RRMS; all patients received atorvastatin, and 10 of 33 patients also received IFN-β throughout the study. This study included both MRI (n = 8) as well as clinical (n = 4) parameters measured at each time point.

Considering the entire cohort of 33 patients, there was a small but significant increase in the median VV between baseline and the last time point at the conclusion of the study: baseline volume = 33,500 mm^3 (27,028 – 39,468) (median ± IQR) versus 33,784 (27,953 – 41,185), resulting in an increase of 284 mm^3, equivalent to an increase of 0.08406% (P = 0.0006, Wilcoxon's signed rank test) (Figure 6A). However, plotting the VV changes over time, expressed as percent changes relative to the VV at baseline for each individual, revealed a highly heterogeneous picture. Some patients showed substantial volatility in VV over time (Figure 6B), while others showed minimal changes (Figure 6C). To distinguish among cases with varying VV volatility, we first determined the normally expected range of intraindividual variation in VV in healthy individuals by making use of data from a study that performed serial MRI of healthy subjects over 6 months (25), selecting time points to match the 1-month time intervals separating scans of the MS cohort. We calculated the median VV for each time point (Figure 6D) and changes in VV relative to baseline for each healthy control (Figure 6E). From this data, we determined that the intraindividual variation in VV fluctuated by plus or minus 6% over time in healthy subjects (Figure 6E). This result was corroborated by analysis of data from a second study that performed serial scans on healthy individuals (26).

In a large proportion of MS patients (21 of 33, 64%), changes in VV exceeding the 6% threshold were observed within 1-month intervals. A subset of patients (5 of 33, 15%) showed exclusively positive changes in VV over the duration of the study — but no contractions. When this minority was excluded from the analysis, the remaining patients showed a small overall decrease in VV (33,000 [27,560 – 39,750] versus 32798 [28,323 – 41,490], –0.00612% [baseline versus last time point, median ± IQR, P = 0.0098, Wilcoxon's]). A larger fraction of patients, 24 of 33 (73%), showed VV contractions beyond the 6% threshold, which extended consecutively over a period of at least 2 months, with no expansions in between. VV changes in this cohort were not a monotonic increase in volume throughout the study period. Based on this threshold, we segregated the patients into 2 groups, considering that a VV contraction event (beyond the level of normal variation) would necessarily follow an expansion event and that such a contraction could exclude VV changes due to brain atrophy. One group (n = 24) was labeled as MS patients with contractions > 6% (Figure 6B), and the other group (n = 9) was labeled as noncontracting MS patients (Figure 6C). The range of plus or minus 6% is depicted by a dotted line (Figure 6, B, C, and E). The whole MS patient cohort had significantly greater volatility in ventricle size, with the coefficient of variation (CV) in VV of 3.235 ± 0.234 versus that of controls 1.887 ± 0.327 (mean ± SEM, P = 0.0065, 2-tailed Student's t test) (Figure 6F).

Even within each patient group, there was a large variation in the magnitude of VV changes, as shown from the plot of relative VV changes for each individual patient during the study (Figure 7, lower panel). The maximum VV contraction for each patient (over 2 months) is depicted in the lollipop plot (Figure 7, upper panel).

Upon stratifying the patients, we investigated potential differences between the groups that could be relevant to MS. MS patients with VV contractions > 6% had significantly lower baseline expanded disability

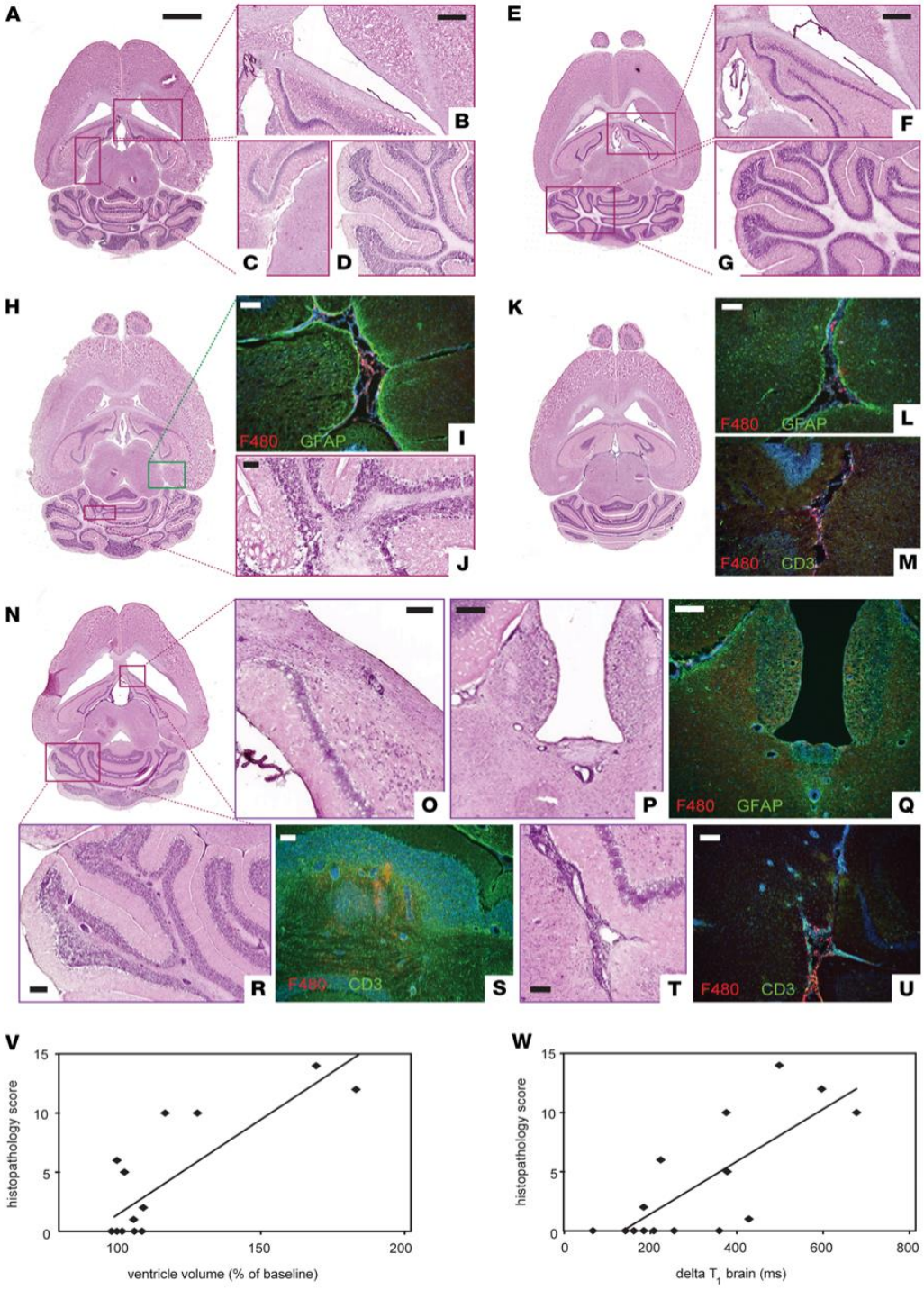

Figure 3. Early ventricle enlargement in EAE correlates with inflammation. (**A**–**G**) Representative images of H&E-stained tissue sections show absence of pathology at baseline (**A**–**D**) and day 3 p.i. (**E**–**G**). Higher magnifications views show periventricular (**B** and **F**), meningeal (**C**), and cerebellar regions (**D** and **G**). (**H**–**J**) First signs of pathology were detected on day 5 p.i., as infiltration of macrophage/myeloid cells (F4/80$^+$, red) and accompanying gliosis (GFAP, green) in meningeal areas (**I**) and inflammatory foci in cerebellar white matter (**J**). (**K**–**M**) By day 8 p.i., pronounced meningeal infiltration and gliosis was

JCI insight RESEARCH ARTICLE

present (**L**), along with T cell infiltration in the parenchyma (CD3+, green) (**M**). (**N**) At day 11 p.i., ventricular enlargement was grossly apparent from the whole brain tissue sections. (**O**–**U**) Extensive inflammation was seen throughout the brain, including periventricular regions (**O**, **P**, **Q**), cerebellum (**R**, **S**), and meningeal areas (**T**, **U**), along with gliosis (**Q**) and infiltration of F4/80 and CD3 positive cells (**Q**, **S**, **U**). (**V** and **W**) Semiquantitative scoring of histopathology (n = 19) correlated positively with ventricle volume changes (**V**) and gadolinium enhancement as ΔT1 changes in whole brain (**W**) (Spearman's r). Scale bars: **A** (whole brain images): 2 mm; **B**–**D**, **F**, and **G**: 500 μm; **P**–**R**: 200 μm; **I** and **J**, **L** and **M**, **O**, and **S**–**U**: 100 μm.

status scale (EDSS) and median EDSS throughout the study period compared with patients with no VV contractions > 6% (P = 0.0221, P = 0.0063, respectively; Mann-Whitney U test) (Figure 8, A and B). Patients with contracting VV also had a significantly lower total disease duration time (P = 0.046, 2-tailed Student's t test) (Figure 8C). There were no significant differences between contracting and noncontracting patients in the total burden of CEL, T_2, or black hole (BH) lesion volume over the course of the study (P = 0.289, P = 0.592, P = 0.598, respectively; Mann-Whitney U test) (Figure 8, D–F). Contracting and noncontracting patients did not differ in terms of age, sex, the proportion also receiving IFN-β therapy, or number of acute relapses during the study period (P = 0.26, P = 0.748, P = 0.511, P = 0.582, respectively; 2-tailed Student's t test, χ^2 test for proportion with therapy). Patients did not show any significant loss of total brain volume (BV) during the course of the study, either when considering the entire cohort (P = 0.1167) or the contracting and noncontracting patients separately (P = 0.8750, P = 0.9770, respectively; 2-way ANOVA with Tukey's post hoc test; Supplemental Figure 1; supplemental material available online with this article; https://doi.org/10.1172/jci.insight.140040DS1). Even when comparing across all time points, we did not observe significant changes in BV. There was, however, a significant negative correlation between VV and overall BV, considering the entire cohort, at selected time points (Supplemental Figure1 and Supplemental Table 2).

Time-series analysis of VV changes in MS. Given the heterogeneity of VV changes in the MS cohort, analysis of group means can potentially obscure relationships between VV changes and other parameters that are relevant to MS pathology. To address whether significant temporal relationships exist between VV changes and changes in other MRI and clinical parameters, we used time-series analysis (a schematic outline of the workflow is depicted in Figure 5). All clinical and MRI parameters (including VV measured from anatomical T_1 and T_2 images) acquired at each time point during the study were included in the analysis. Given the parametric nature of the time-series analysis, ordinal variables such as EDSS were not included. We performed the time-series analysis on the subset of 24 MS patients who showed VV contractions above the 6% threshold.

We calculated the cross-correlation function (CCF) for each individual patient using VV as the X variable and the other 8 MRI and 4 clinical parameters as Y variables. We considered only those significant cross-correlation coefficients that occurred within plus or minus 2 time lags (i.e., ±2 months) as reflecting a meaningful temporal relationship with VV changes (Figure 9A). The CCF analysis resulted in a total of 101 cross-correlation coefficients with nominal $P < 0.05$. Upon FDR correction for multiple comparisons, 25 significant coefficients were retained (Figure 9A). The significant cross-correlation coefficients were detected in 10 of 24 MS patients included in the analysis. These were distributed among all clinical parameters and most of the MRI (7 of 8) parameters. All 5 time lags considered (0, ±1, and ±2 months) appeared among the significant cross-correlations.

Detection of CEL is a major criterion for MS diagnosis. The CCF analysis was repeated using CEL volume as the X variable and the remaining 12 parameters (including VV) as Y variables (Figure 9B). This analysis yielded a total of 96 cross-correlations with nominal $P < 0.05$. This was reduced to 23 significant cross-correlations following FDR correction for multiple comparisons (Figure 9B). Of note, 9 of 23 significant cross-correlations were correlations between CEL volume and CEL count, which was to be expected, and 14 of 23 were at 0 lags (i.e., the changes occurred at the same time as CEL volume changes).

As an additional comparison, we repeated the CCF analysis using the performance in the 9-hole peg test of the dominant hand (hpt dom) as the X variable and comparing it with the other 12 parameters (including VV) as Y parameters (Figure 9C). This analysis yielded 73 cross-correlations with nominal $P < 0.05$; only 5 significant cross-correlations were retained following correction for multiple comparisons (Figure 9C).

Discussion

In this study, we demonstrate a pronounced enlargement of the mouse brain ventricles of up to 200%, before the onset of clinical signs, during the first disease peak in EAE. We show that this enlargement resolves at the time of clinical remission, strongly suggesting that it is not the result of brain atrophy due

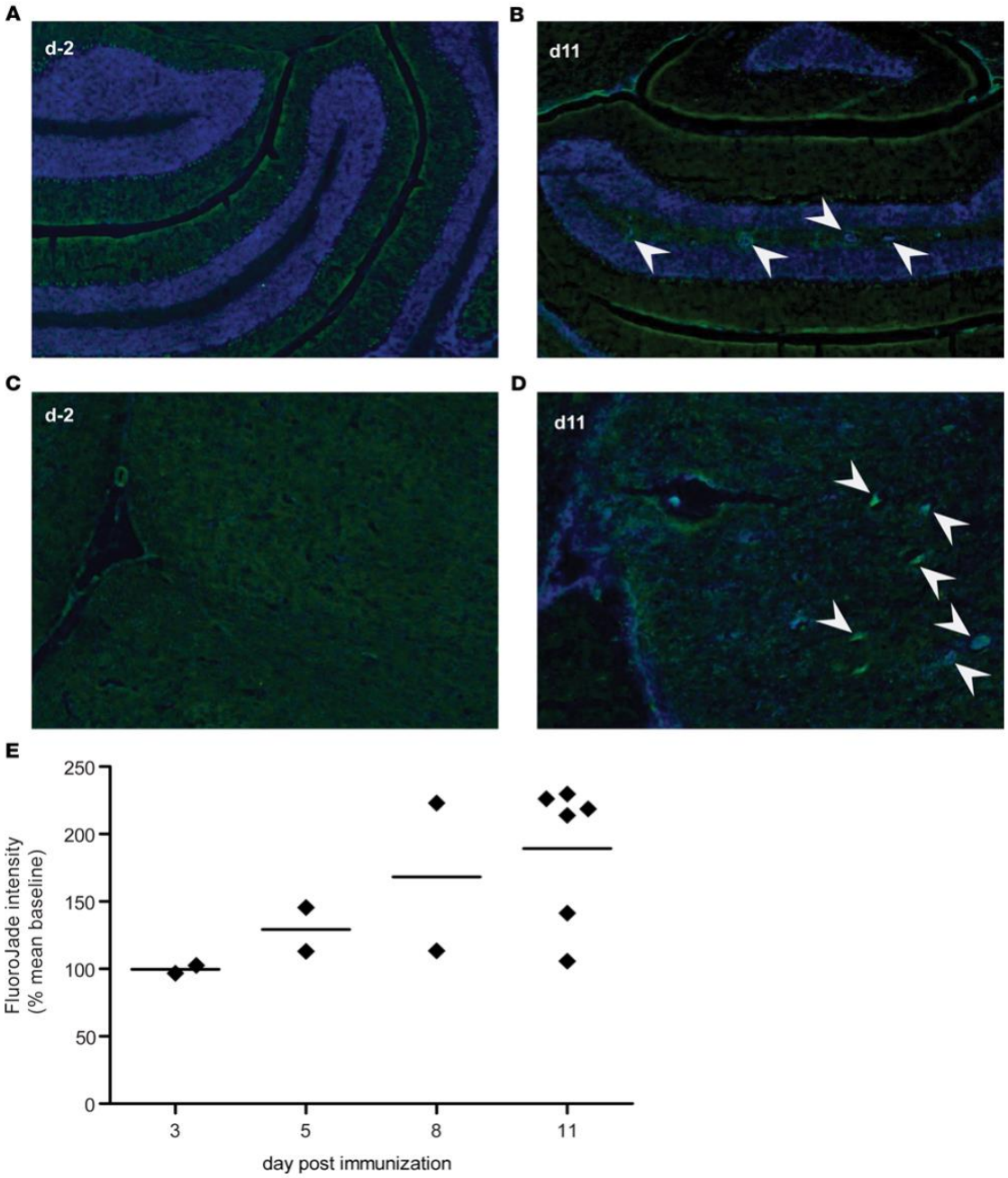

Figure 4. Modest neurodegeneration detected by Fluoro-Jade staining during early EAE. (**A** and **C**) No evidence of Fluoro-Jade$^+$ staining was seen in brain tissue sections from unimmunized control mice; representative images of cerebellum (**A**) and brainstem (**C**). (**B** and **D**) Fluoro-Jade$^+$ foci (indicated with arrows) were observed in cerebellum (**B**) and brainstem (**D**) of mice at day 11 p.i. (Fluoro-Jade, green; DAPI, blue). The Fluoro-Jade$^+$ foci consistently accompanied inflammatory foci (**B** and **D**). (**E**) Quantification of fluorescence intensity of the tissue section showed an increasing accumulation of Fluoro-Jade staining by day 11 p.i. (arbitrary units) (n = 15).

JCI insight RESEARCH ARTICLE

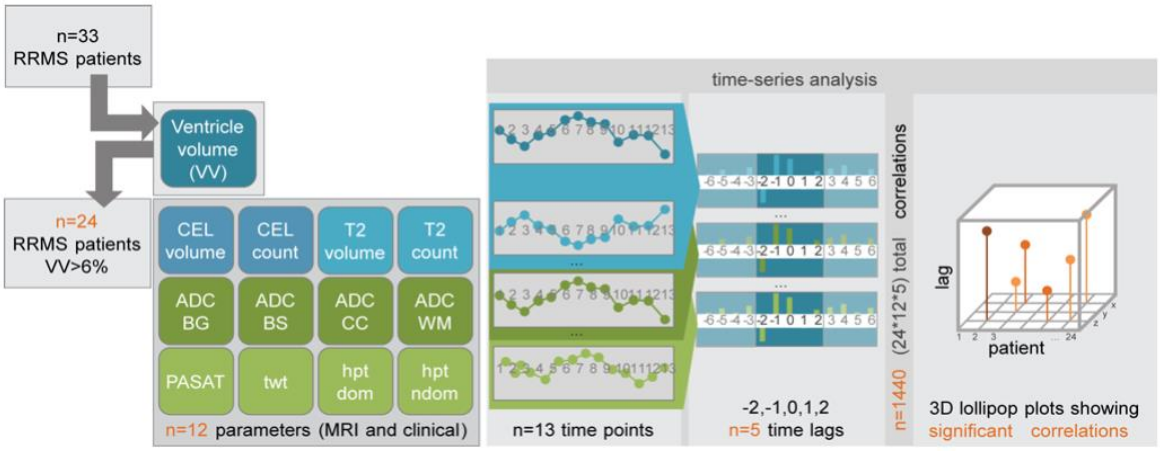

Figure 5. Schematic for time-series analysis workflow. From the cohort of *n* = 33 RRMS patients, we performed the time-series analysis on the subset of *n* = 24 patients who showed contractions in ventricle volume greater than the ± 6% range of normal variation. Ventricle volumes were measured at 13 monthly time points. At the same time points, an additional 8 MRI parameters and 4 clinical parameters were measured. This allowed each of these measures to be considered as a time series. Using the cross-correlation function, the cross-correlation coefficients between 2 time series can be calculated; significant coefficients indicate that events of one series precede (negative time lag) or follow (positive time lag) the events of another series. In the current study, we limited the consideration of significant cross-correlation coefficients to ± 2 time lags (i.e., ± 2 months). From *n* = 24 patients, *n* = 12 variables, and *n* = 5 time lags (including the 0 time lag), a total of 1440 coefficients was calculated. From the coefficients with nominal $P < 0.05$, the FDR correction for multiple comparisons was applied, to yield the corrected significant cross-correlation coefficients, which were then displayed in the 3D plots.

to neurodegeneration. The VV continues to fluctuate during the disease course. This phenomenon has clinical relevance, as the majority of RRMS patients in our cohort showed dynamic enlargement and contraction of VV, beyond the range of variation seen in healthy individuals. Those patients who showed the most volatility in VV appeared to be at an earlier stage of disease; they had significantly lower baseline and median EDSS throughout the study period, and they had a significantly shorter total disease duration compared with the patients who did not show contractions. Crucially, these results demonstrate that VV in RRMS patients does not only increase unidirectionally over time as a result of atrophy, but in the majority of cases, VV expands and contracts dynamically during the disease course. These short-term fluctuations occur at a time scale of less than 1 year and are unlikely to be the result of neurodegeneration exclusively. They suggest that other disease-related processes might be contributing factors. Close monitoring of VV changes during disease could therefore offer further valuable insights.

A distinguishing feature of this work is the relatively high time resolution of the longitudinal studies. EAE mice were scanned every 2–3 days over a period of 64 days. EAE studies typically consider fewer time points during the disease course. Long intervals between observations can limit the detection of potential changes that take place at shorter time scales, obscuring the complexities of the underlying processes. Similarly, the clinical study we investigated for time-series analysis was originally designed to evaluate the efficacy of atorvastatin in RRMS patients and included 13 monthly MRI investigations over a period of 1 year. These time intervals are shorter than those typically considered in clinical practice and offer the possibility to capture subtle changes that might otherwise remain unnoticed.

In our analysis, we considered changes at the individual patient level. When analyzing the MS patients as a group, we observed a small though significant increase in VV between the start and end of the study, which is consistent with the conventional interpretation of neurodegeneration and brain atrophy (27). However, there was no significant change in BV throughout the study, suggesting that subtle atrophy may be proceeding on a central rather than global level (28, 29). It is expected that VV will increase over time in the course of normal aging, and it is indisputable that this is accelerated in MS (19, 21, 30, 31). When studying the VV in MS patients individually, we observed an oscillating behavior in the majority of patients, with VV expansions and contractions. This suggested that, superimposed upon the long-term expansion of VV resulting from neurodegeneration, other disease-related processes drive the short-term oscillations in VV. Another confounding process is the phenomenon of pseudoatrophy (nontissue related BV reduction) that can occur following introduction of antiinflammatory therapies (32–34) as a result of accelerated water losses and

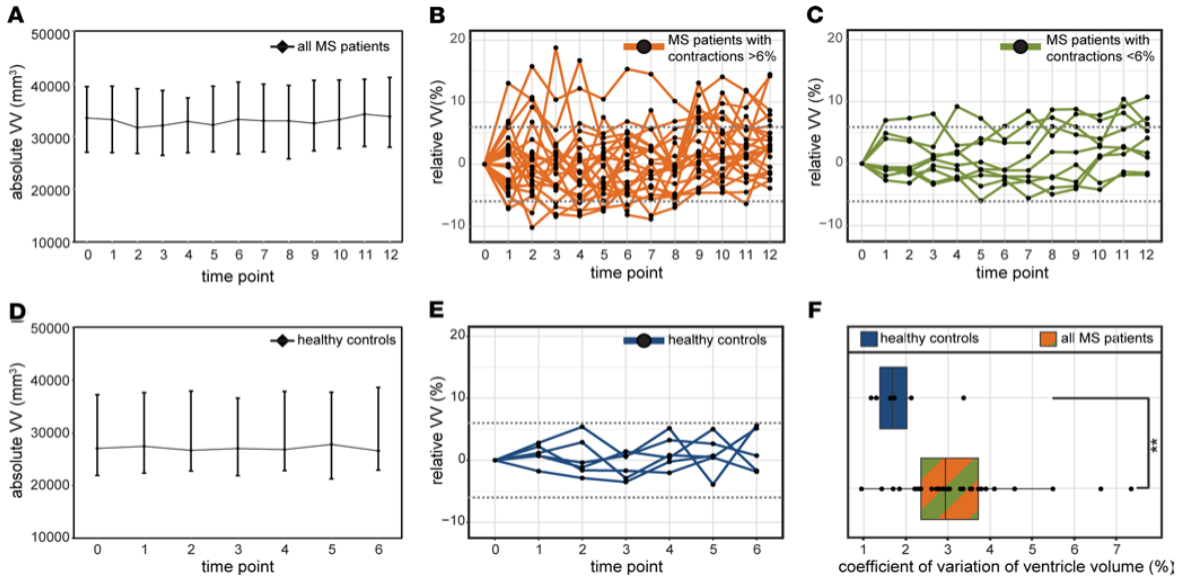

Figure 6. Relapsing-remitting MS patients show dynamic changes in ventricle volumes. (**A**) Over the course of 1 year, the cohort of MS patients showed a small but significant increase in ventricle volume of +284 mm, equivalent to +0.08406% (median ± IQR, $P = 0.0006$, Wilcoxon signed rank test, $n = 33$). (**B** and **C**) Plotting the values for individual patients showed a heterogeneous picture, with some individuals showing high variability in ventricle volume (**B**) and others showing lower variability (**C**). (**D**) A reference cohort of healthy subjects showed no significant changes over the course of a 6-month observation period ($n = 6$). (**E**) The maximum change in ventricle volume of the healthy subjects was ± 6%. (**F**) The MS patient cohort showed significantly greater variability in ventricle volumes (as indicated by the coefficient of variation) compared with healthy controls (**$P = 0.0065$, Student's t test).

fluid shifts (35), as well as resolution of immune cell infiltration. The patients in the clinical trial that we retrospectively investigated were treated with atorvastatin (and some also with IFN-β) but did not show any signs suggestive of pseudoatrophy (24). During the relatively short duration of our study (1 year), there was no significant reduction in BV in all cohorts. Aside from pseudoatrophy, some immunomodulatory agents (e.g., S1P agonists) appeared to slow down BV losses. In addition to reducing new MRI activity, 6 months of treatment with fingolimod resulted in significantly lower BV losses compared with placebo control (36), suggesting neuroprotective mechanisms were operating, beyond the expected antiinflammatory activity. In parallel to monitoring BV changes, it would be interesting to follow changes in VV in S1P agonist–treated patients as a possible surrogate marker to differentiate antiinflammatory from neuroprotective activities. In such studies, a high frequency of MRI scans, as performed in the presently investigated clinical study, would facilitate the disentanglement of immunomodulatory-induced reductions in transient VV fluctuations from neuroprotective-induced reductions in BV losses that occur at different time scales. Distinguishing short-term processes from long-term VV and BV changes is vital, especially since the rate of VV expansion was shown to predict disease progression more strongly than the rate of whole brain atrophy (20).

The dynamics of CSF flow through the brain, and how this is altered under pathological conditions, is receiving increased attention in light of the recognition of the glymphatic system within the brain (37). CSF flows from the choroid plexus through the ventricular system and enters the brain parenchyma via the perivascular spaces along arteries, where it mixes with interstitial fluid (38). The CSF exits the brain along the perivenous spaces to the cervical lymphatics, the arachnoid granulations, and the meningeal lymphatics (39, 40). Immune cell accumulation in the perivascular space could interfere with normal glymphatic processes, and meningeal inflammation could disrupt clearance of the CSF. We observed that meningeal inflammation was extensive in EAE brains by d11 p.i. and could already be detected as early as d5 p.i. This is consistent with other reports that meningeal inflammation preceded inflammation in the parenchyma (41). A recent report described GBCA enhancements in the leptomeninges in myelin oligodendrocyte glycoprotein–immunized (MOG-immunized) C57BL/6J EAE mice, and these were especially prominent during the initial disease peak (42). In proteolipid protein–immunized (PLP-immunized) SJL/J EAE mice, we also observed GBCA leakage early during disease, as shown by reduced T_1 values, particularly in leptomeningeal

JCI insight RESEARCH ARTICLE

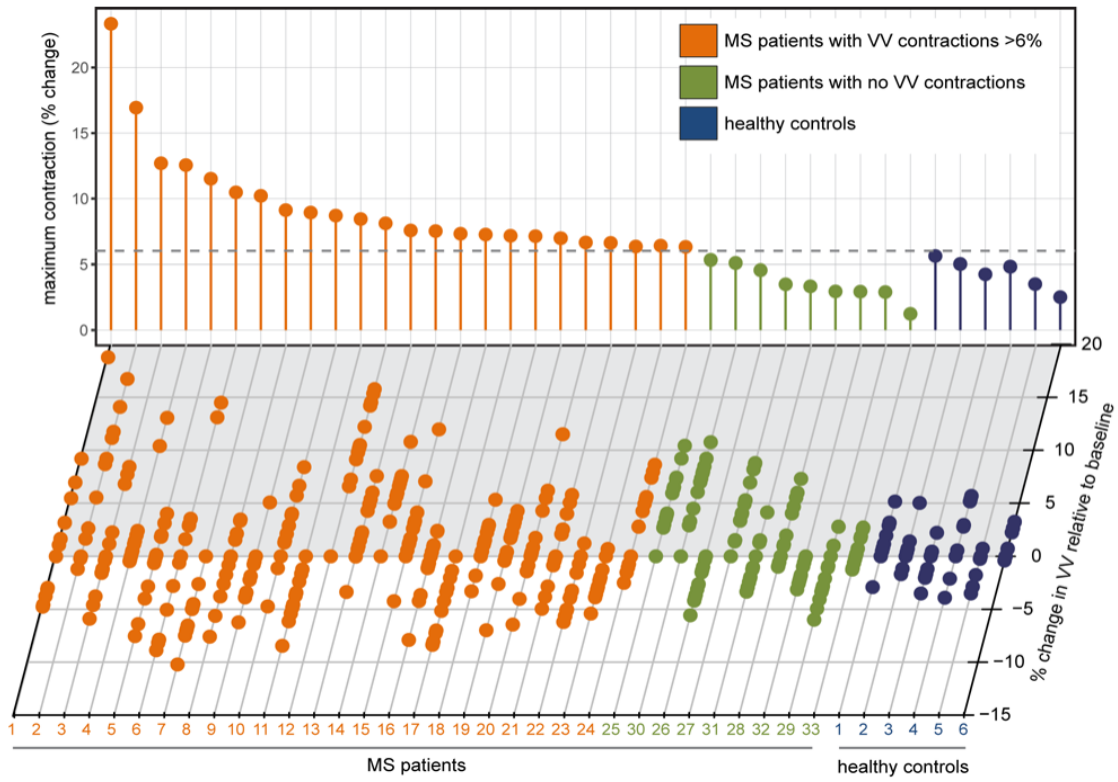

Figure 7. MS patients show variable ventricle volume (VV) changes. Individual MS patients showed considerable variability in the patterns of VV changes during the course of 13 monthly MRI examinations. Ventricle volumes from each patient and healthy subject are shown along the *x* axis; each dot represents 1 time point. Results are depicted as a percentage change from the baseline measurement. The vertical lollipop lines indicate the maximum contraction observed for each individual during the study period, in percentage change. The dotted line illustrates the maximum ventricle contraction observed in the healthy cohort: 6%. Based on this threshold, the cohort was divided into MS patients with contractions > 6% (orange) and MS patients without contractions (green). Healthy subjects are depicted in blue.

and cerebellar regions. Impaired CSF clearance was reported in EAE (43) and could impact VV changes. Leptomeningeal inflammation is frequently observed in MS and other neuroinflammatory conditions (44, 45). Impairment of CSF elimination associated with meningeal inflammation could contribute to transient VV changes in MS. Support for this notion comes from a recent study using the positron-emission tomography tracer ^{11}C-PiB, which showed reduced CSF clearance in MS patients compared with healthy controls (46).

Inflammatory processes could interfere with the normal function of the choroid plexus, leading to altered CSF composition or CSF hypersecretion. Inflammation and disruption of the choroid plexus tissue architecture is seen in MS (47, 48), and there is compelling evidence that the choroid plexus is implicated in the very early stages of neuroinflammation. The choroid plexus mediates physiological immune surveillance of the CNS by entry of immune cells into the CSF circulation (1), and it is also a site for entry of pathological Th17 cells in EAE (49). We previously detected accumulation of very small superparamagnetic iron oxide particles (VSOP) in the choroid plexus (50) by MRI, confirmed by histology. Importantly, VSOP could be detected in the choroid plexus before the onset of clinical EAE signs and before the detection of histopathology in the rest of the brain, indicating early involvement of the choroid plexus in the disease process (51). Furthermore, in our previous study first demonstrating VV changes in EAE, we showed an alteration in the T_2 relaxation of the CSF, suggesting an increase in the free water fraction (15), possibly as a result of altered composition or increased production of CSF due to choroid plexus inflammation.

Insights into the mechanisms of how inflammation can disrupt choroid plexus function have come from recent studies on experimental models of posthemorrhagic hydrocephalus (PHH) (52, 53). While PHH was previously attributed to primary impairments in CSF reabsorption, these recent studies demonstrate the

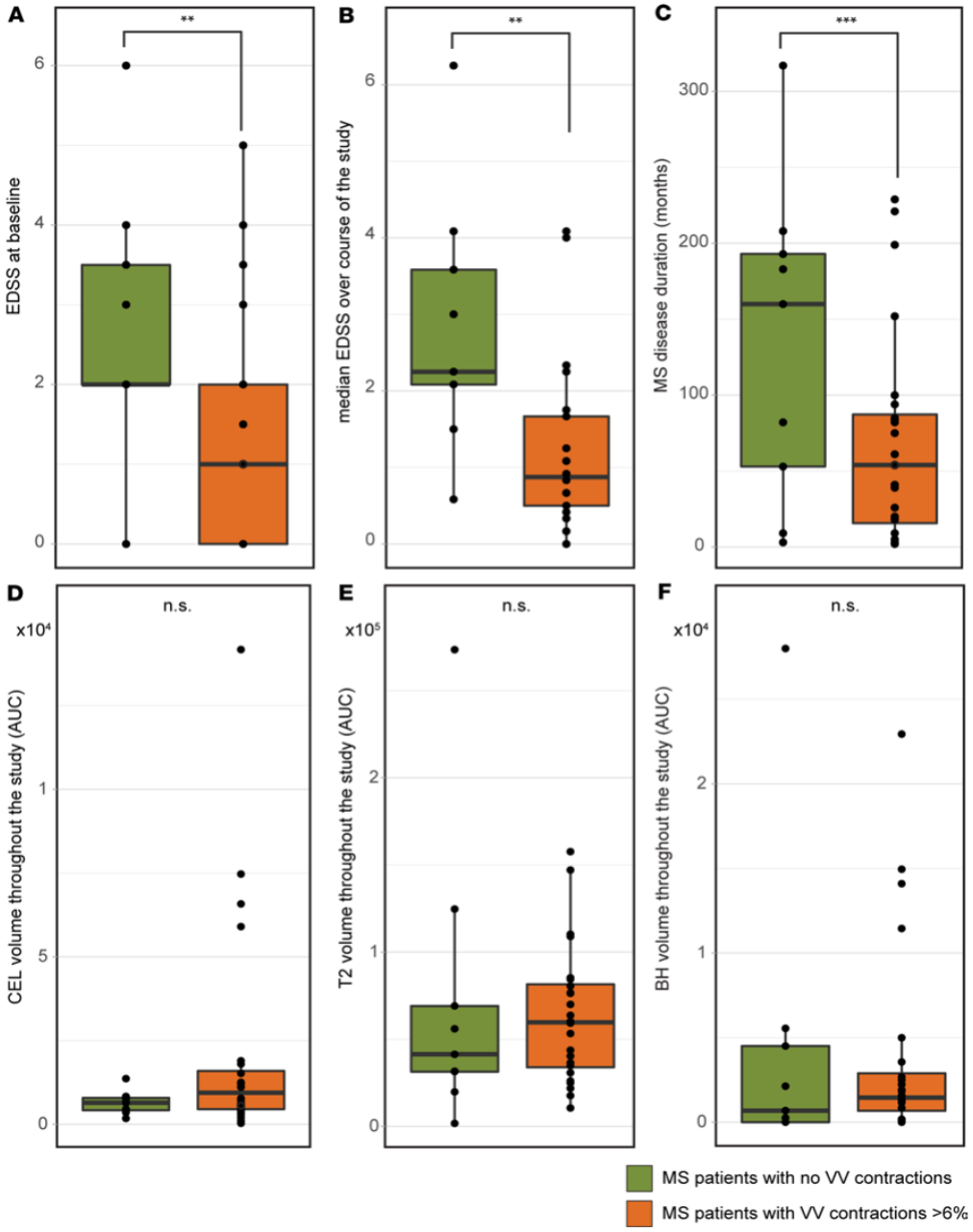

Figure 8. MS patients with contracting ventricles have lower disease severity and duration. (**A** and **B**) MS patients who showed contractions (n = 24) in ventricle volumes greater than 6% had significantly lower disease severity at the study baseline, as indicated by the Expanded Disability Status Scale, EDSS) (**P = 0.0221, Mann-Whitney test) (**A**), and significantly lower median EDSS during the study period (**P = 0.0063, Mann-Whitney test) (**B**). (**C**) The patients with ventricle contractions also had significantly shorter total disease duration (***P = 0.046, Student's t test). (**D**–**F**) There were no significant differences between contracting and noncontracting patients (n = 9) in volume of CEL (**D**), T_2 (**E**), or BH lesions (**F**) over the course of the study.

contribution of CSF hypersecretion to the pathogenesis of PHH. In a model of intraventricular hemorrhage, PHH was shown to be the result of CSF hypersecretion by the choroid plexus. This was driven by a TLR4- and NF-κB–dependent production of proinflammatory cytokines that, in turn, upregulate Ste20-type stress

JCI insight RESEARCH ARTICLE

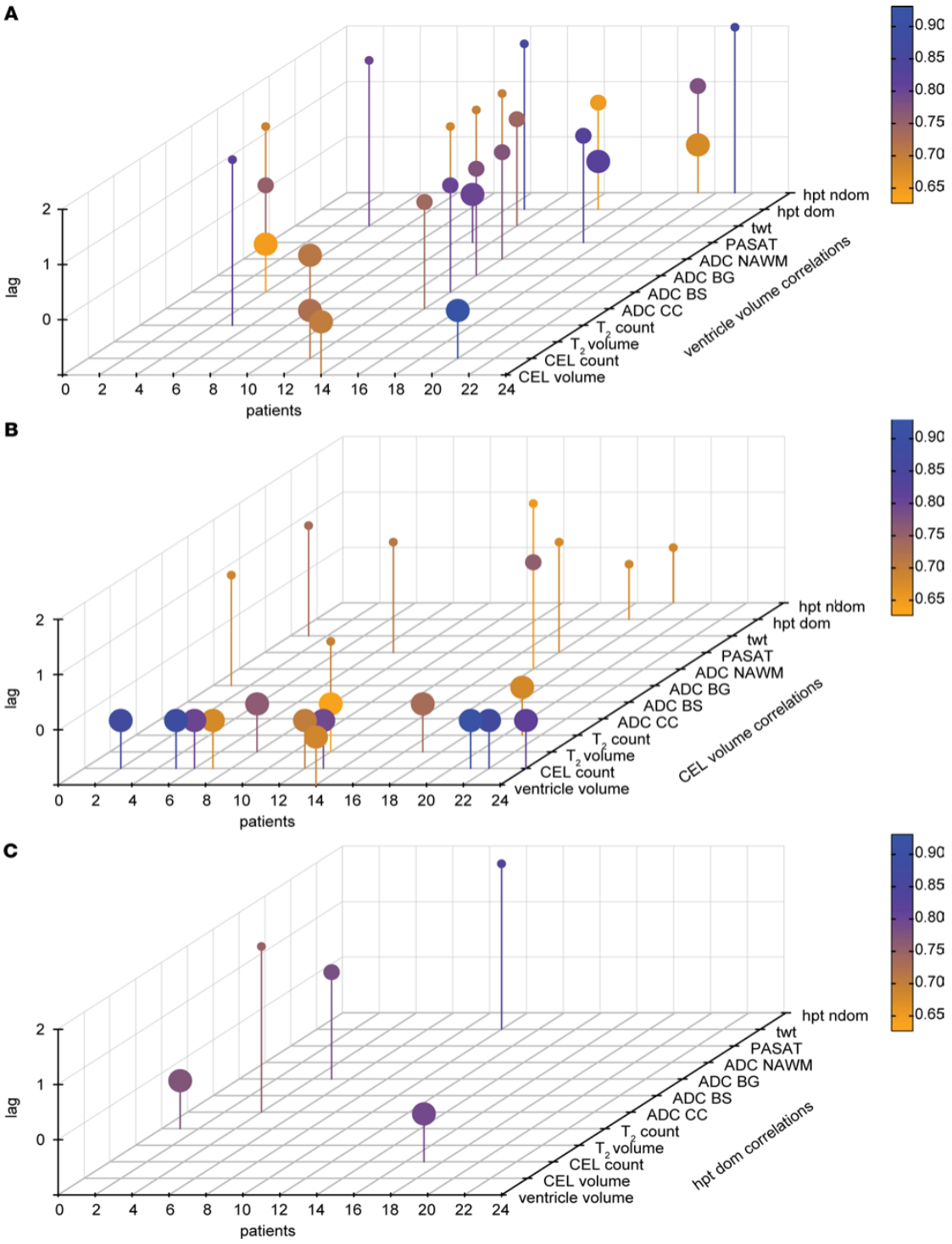

Figure 9. Time-series analysis of ventricle volume changes in MS. (**A**) For each individual patient with ventricle volume contractions > 6% (n = 24), we calculated the cross-correlation function (CCF) between the time series of ventricle volume (as the X variable) and the time series of the other 8 MRI and 4 clinical measures (as the Y variables). The CCF yielded 25 significant cross-correlation coefficients, within a time lag of ± 2 months, after FDR correction for multiple comparisons. The significant coefficients are depicted as lollipops in the 3D plot; color is scaled to the magnitude of the coefficient. Individual patients are arranged on the x axis; the MRI and clinical parameters are arranged on the y axis. The absolute values of the time lags are shown on the z axis, and size of the lollipop is scaled to the time lag (lag 0, largest). (**B**) Using the time series of CEL volume as the X variable and the other MRI and clinical parameters (including ventricle volume) as the Y variables, the CCF analysis yielded 23 significant cross-correlation coefficients after correction for multiple comparisons. Of these, 9 of 23 were correlations between CEL volume and CEL count at 0 time lags. (**C**) Repeating the analysis using the time series of performance in the 9-hole peg test as the X variable yielded 5 significant cross correlation coefficients after correction for multiple comparisons.

kinase (SPAK); this kinase activates ion transporters in the choroid epithelium to increase CSF production (52). This could be reversed with drugs targeting these signaling pathways, leading to protection from the experimentally induced ventricle enlargement (52). Another group used a small molecule inhibitor of SPAK-dependent phosphorylation of ion transporters and were able to reverse CSF hypersecretion in experimental ischemic stroke (53). These studies demonstrate how inflammatory processes at the choroid plexus can result in expansion of the cerebral ventricles due to CSF overproduction in PHH and have implications beyond hydrocephalus and stroke to other acute and chronic inflammatory diseases (54).

Variations in VV and BV are known to be dependent on circadian rhythm (55) and hydration status (56–59). Interestingly, the activity of the glymphatic system is greatly increased during sleep. In the current study, we can exclude circadian rhythm and dehydration as contributing factors, since all patients were scanned consistently early in the morning and were instructed to eat normally and drink sufficiently. Nevertheless, potential effects of other physiological processes on VV cannot be entirely excluded. All patients in the study were treated with atorvastatin, and some also with IFN-β; therefore, potential confounding drug effects on VV cannot be excluded. Patients who experienced acute relapses were also treated with corticosteroids, and while the MRI and clinical measures in those patients were postponed by 4 weeks to avoid confounding effects on GBCA enhancement, potential effects of steroids on VV, though unlikely, cannot be entirely excluded. In addition to biological variation, differences in slice position between scans and other technical sources of variation often cannot be completely controlled (26, 60). Nevertheless, no significant differences between VV contracting and noncontracting patients were observed in terms of age, sex, the proportion also receiving IFN-β therapy, and number of acute relapses during the study period.

During the initial EAE disease peak, the VV increase was pronounced — up to double the original size in some animals. Regardless of the extent of the VV changes, all VV returned to normal values upon remission of clinical signs. We detected evidence of neurodegeneration with FJ staining, which was consistently associated with inflammatory lesions, particularly in the cerebellum and brainstem. Nevertheless, the magnitude of the FJ staining at this early time point was modest, consistent with other reports showing mild FJ staining at similar time points in the C57BL/6J MOG EAE model (61). Together with the fact that the VV expansion occurred at such an early phase in the disease and was reversible, even toward the end of the study when mice still showed clinical signs of neurological disease, it is highly unlikely that the initial VV changes were a consequence of profound neurodegeneration. Rather, it is more likely that the early VV changes were the result of fluid dysregulation associated with inflammatory processes at this phase of the disease. In contrast, neurodegenerative damage in EAE accumulates progressively over time (62).

The VV changes in the MS patients were less severe than in the EAE animals. A minority of patients (5 of 33) in our cohort showed increases in VV in the study period, with no contractions; indeed, this minority was responsible for the significant increase in VV seen at the whole group level. This is in line with conventional expectations that VV of MS patients should steadily increase over time — notwithstanding normal physiological fluctuations (30). The fact that a majority of patients we analyzed showed VV contractions, as well as expansions, beyond the range of variation of healthy subjects suggests that other processes are at work, in addition to neurodegeneration. Stratifying the MS cohort based on the plus or minus 6% threshold of normal monthly variance in VV (25) revealed that the patients with contracting ventricles appeared to be at an earlier stage of their disease. If transient VV fluctuations are associated with acute inflammatory activity, then it stands to reason that these fluctuations would be more prominent in RRMS, when inflammatory processes dominate, than SPMS — when acute inflammation is less prominent and neurodegenerative processes dominate. This is in line with a previous study that reported that, while PPMS and SPMS patients had larger VV at baseline, RRMS patients showed the greatest VV changes over 6 months (63). However, that study was not designed to detect month-to-month changes in VV during the study period; therefore, it might

JCI insight RESEARCH ARTICLE

have underestimated the relevance of VV expansions and contractions. Interestingly, that study also showed that PPMS patients had the largest VV at the start of the observation period (63), which might suggest that neurodegenerative processes played a larger role in their disease, right from the onset. These speculations will require careful study of PPMS and SPMS patients, with serial MRI.

The clinical study that was the source of our MS patient data was designed as a time series with monthly MRI scans, including multiple parameters such as GBCA enhancement. This permits the use of time-series analysis in order to look for correlations between the timing of changes across multiple parameters — an approach that is under-used in MS research. The data set we examined can be considered as a short-time series (64), and given that the measurements took place over 1 year, there is no expectation of seasonality in the data, which can be a confounding feature of time series that extend over several years. Considering the short duration and the modest sample size, we adopted a conservative approach to the time-series analysis, with no attempt to draw causal interpretations or forecast outcomes. Rather, the objective was to determine whether there was any evidence indicating that changes in VV occurred at the same time (or shifted in time) as changes in the other MRI and clinical parameters measured.

The time-series analysis detected several significant cross-correlation coefficients distributed among the other MRI and clinical parameters. This revealed a complex picture, in which the timing of VV changes in some patients was significantly correlated with the timing of changes in other parameters. This suggests that VV changes may reflect disease activity, although no single parameter dominated the set of significant coefficients. We repeated the time-series analysis using CEL volume — the gold standard for MS disease activity — to see how the timing of changes in this parameter compared with the other parameters (including VV). There was a high degree of cross-correlation between CEL volume and CEL count at time lag 0, meaning that changes in CEL volume occurred at the same time as changes in CEL count, in some though not all patients. Aside from this expected cross-correlation, lesser significant coefficients were observed, and these too were distributed among all other parameters. This suggests that the degree to which the timing of changes in VV and CEL volume reflect changes in other disease-related parameters was comparable. In contrast, when the analysis was done to compare the timing of changes in performance in the HPT with other disease-related parameters, only 5 significant cross-correlation coefficients were retained after correction for multiple comparisons. This could reflect that the HPT measures motoric performance and may be related to spinal cord involvement (65, 66) or may simply be less indicative of rapid changes when compared with parameters such as VV and CEL volume.

The diagnostic value of GBCA for revealing disease activity in MS is indisputable. Nevertheless, there have recently been increasing safety concerns regarding the potential for long-term deposition of GBCA in the brain (9–12). In light of these concerns, there is a strong motivation to find contrast-free quantitative MRI parameters, which can serve as markers of disease activity. In this line, quantitative MRI measures such as T_1 mapping, especially at ultra-high magnetic field strengths, can be especially informative (67). In the current study, we used T_1 mapping of EAE brains to quantify gadolinium leakage as an indicator of BBB disruption. Crucially, we could show that the timing of VV changes coincided with the peak of BBB leakage and that both of these significantly preceded the onset of clinical signs of EAE. The T_1 maps showed a pattern of contrast enhancement typical for SJL mice, with extensive involvement of the cerebellum, meninges and periventricular regions. This corresponded to histological detection of immune infiltrates and gliosis in these locations, and the severity of the histopathology correlated with the magnitude of VV changes. Thus, VV changes may be considered as a surrogate indicator of inflammatory activity. Future studies using even more sensitive histological methods for detecting BBB disruption would add further detail, complementing the quantitative T_1-mapping approach.

In summary, close monitoring of VV changes in individual MS patients will be important to understand whether these are truly transient or persistent. Persistent changes would indicate irreversible progressive destruction, while transient events might be related to other pathological mechanisms superimposed upon the neurodegenerative process. Being able to disentangle these intermingled processes will have profound implications for determining more effective treatment strategies. Given that the RRMS patients with contracting VV in the current study appeared to be at an earlier phase of their disease, it is tempting to speculate that the cessation of VV volatility may be an indication of transition to the progressive phase of disease. This hypothesis remains to be confirmed in larger-scale data sets. Nevertheless, changes in VV could serve as a quantitative MRI biomarker of disease activity, which can be readily acquired in the course of routine clinical investigations of MS patients. However, in order for this to become part of routine clinical practice,

it will be necessary to have tools available for the clinician to quickly and seamlessly integrate the calculation of VV into the clinical workflow. Continuing advances in machine learning–based methods for analysis of MRIs will be crucial for these developments. To accompany VV monitoring, further technical developments in MRI-based methods to monitor CSF flow (68) and composition (69) — as well as inflammatory processes (70) — are becoming increasingly available, particularly at higher magnetic field strengths. Together, these tools can help drive our understanding of the dynamic changes in the CSF compartment during neuroinflammatory disease and can lead to superior diagnosis, prognosis, and monitoring of patients.

Methods

Induction of EAE. EAE was induced as previously described (15). Female SJL/J mice (8–12 weeks) were obtained from Janvier SAS. A total of n = 35 mice in 6 cohorts were used in the study. Mice were immunized s.c. with 250 μg $PLP_{139–151}$ (Pepceuticals Ltd.) and 800 μg mycobacterium tuberculosis H37Ra (Difco), and they were administered 200 ng of pertussis toxin (List Biological Laboratories) on d0 and d2. Mice were weighed and scored daily as follows: 0, no disease; 1, tail weakness and righting reflex weakness; 2, paraparesis; 3, paraplegia; 4, paraplegia with forelimb weakness or paralysis; and 5, moribund or dead.

Animal MRI. Animals were anesthetized with a mixture of 1%–1.5% isofluorane (Abbott GmbH & Co.), air, and oxygen, and they were placed on an animal holder, kept warm with circulating water. Body temperature and respiration rate were monitored continuously with a remote monitoring system (Model 1025, SA Instruments Inc.). MRI was performed (Supplemental Methods), keeping slice positioning constant through the experiment, positioned parallel to the base of the brain. Mice were imaged at baseline, 2 days before immunization, and every 2–3 days after immunization, until day 64 after EAE induction. A total of n = 9 mice underwent the full longitudinal examination. We confirmed that the signal-to-noise and contrast-to-noise ratio (between cortex and ventricles) were consistent throughout the entire study period.

Analysis of MRI data. Quantification of mouse brain VV was done as in our previous study (15), using FMRIB Software Library (FSL v5.0, www.fmrib.ox.ac.uk/fsl) (71–73), and the transformed ventricle masks were manually corrected (Supplemental Methods). Data from the T_1 maps were extracted and post-processed using MATLAB (MathWorks Inc.), MATLAB Image J software module (MIJ), and Advanced Normalization Tools Toolkit (74, 75) (Supplemental Methods).

Histology. Brain tissue was collected from n = 19 mice at various time points: baseline (unimmunized controls) and d3, d5, d8, and d11 p.i. After terminal anesthesia using ketamine/xylazine, mice were perfused transcardially with 20 mL PBS and then with 20 mL zinc fixative (0.5% zinc acetate, 0.5% zinc chloride, 0.05% calcium acetate) (Sigma-Aldrich). Following extraction, brains were postfixed, frozen in OCT, and cut into 15 μm cryosections. Sections were stained with H&E according to standard procedures. H&E-stained tissue sections were reviewed and scored for the presence of inflammation in the following regions: meninges, periventricular regions, brainstem, cerebellum, cortex, and hippocampus. Absence of inflammation was scored as 0; minor signs of inflammation as +; multiple inflammatory foci as ++; and severe inflammation as +++. These semiquantitative scores were then correlated with the VVs and ΔT_1 values. Immunostaining protocols (Supplemental Methods) were also performed.

Healthy human controls. Data from healthy control subjects were obtained from 2 publications that performed repeated serial MRI scans on healthy individuals and which had made their raw data available to the scientific community (25, 26). In one study to investigate intraindividual variability in brain structures and other measurements, subjects (n = 6) underwent multiple serial MRI scans over 6 months. From this data set, we selected scans at 1-month intervals in order to match the timing of the scans in the MS patient cohort. Demographic details of these subjects are listed in Supplemental Table 1. In a separate study to evaluate intra- and intersession reliability of brain imaging and automated segmentation software, n = 3 subjects underwent repeated MRI scans within a 31-day period (26). Given the retrospective nature of our study, it was not possible to age-match the healthy controls with the MS patient cohort. Both studies acquired T_1-weighted scans, using 3.0 Tesla clinical MR scanners; details about the scan parameters can be found in the original publications (25, 26). Absolute VVs from scans of healthy controls were obtained using FreeSurfer v5.3 (76).

MS Patient cohort. Data from RRMS patients were obtained from our previous clinical study investigating oral atorvastatin therapy (NCT00616187) (24). All patients (n = 33) in this study had clinically definite MS (77) and had at least 1 CEL on brain MRI at the time of enrolment. Clinically active disease (i.e., signs of relapse) was not required for inclusion in the study. In addition to treatment with atorvastatin, 10 of 33 patients were cotreated with IFN-β. Patients who experienced acute relapses underwent

JCI insight RESEARCH ARTICLE

corticosteroid treatment (methylprednisolone) for 3–5 days; subsequent MRI and clinical examination was postponed by 4 weeks to avoid confounding effects. Patients underwent 13 MRI examinations at 1-month intervals over the course of 1 year. T_1- and T_2-weighted MRI scans were acquired using a 1.5 Tesla clinical MR scanner (Siemens Sonata, Siemens Medical Systems). Diffusion-weighted imaging was performed, and the apparent diffusion coefficient (ADC) calculated in 4 regions of interest: corpus callosum (ADC CC), basal ganglia (ADC BG), brainstem (ADC BS), and normal-appearing white matter (ADC WM). All scans were performed between 8 and 9 a.m. in order to avoid circadian bias, and patients were advised to have regular meals and drinks to avoid dehydration. Detailed information on the scan parameters can be found in the original publication (24). Demographic and clinical details from the original publication are listed in Supplemental Table 1 (note that the current study used 33 patients who completed the full MRI scan protocol at all time points).

Analysis of MRI Data (Supplemental Methods) included VV and BV, CEL numbers and volumes, T_2-weighted lesions and BH lesions. Additional parameters included the Paced Auditory Serial Addition Test (PASAT), the 9-hole peg test of the dominant (hpt dom) and nondominant (hpt ndom) hand, and the timed walk test (twt). EDSS scores were assessed at baseline and at selected time points during the study.

Statistics. For each patient, VVs, as well as lesion volumes, lesion counts, and additional clinical measures that were gathered and quantified from the 12-month clinical study, were analyzed using time-series analysis. The CCF calculates the cross-correlation coefficient, which indicates the relationship between 2 metrics as they change over time. Significant coefficients indicate that events of 1 series precede (negative time lag) or follow (positive time lag) the events of another series. Absence of significant CCF coefficients indicates that no temporal relationship between the 2 series exists. For this 12-month clinical study, we adopted a conservative approach, considering only those coefficients that were significant at time lags between –2 to +2 months. Given that the CCF requires continuous data, noncontinuous ordinal variables such as EDSS were not included in the time-series analysis. All time series for each individual patient for each parameter were detrended by first-order differencing, in which each point is replaced by the difference between its value and the value of the preceding point. This was done to ensure that the time series were stationary — i.e., lack an overall trend — in order to avoid spurious false-positive cross-correlations. The differencing was done using the R package forecast (78). Following first-order differencing, we confirmed stationarity for all time series for all patients with the Augmented Dickey-Fuller test (79), using the R package fUnitRoots (80).

The CCF was then applied using the R package time series (81) to look for temporal relationships between the VV time series and the time series for the other parameters for each individual patient. The Benjamini-Hochberg FDR method was used to correct for multiple comparisons, with FDR-corrected $P < 0.05$ considered significant. We also verified that there was no autocorrelation (periodicity) in the time series of each parameter we studied, using the ACF function (R package, time series).

Statistical analysis (including those in Supplemental Methods) was done using the statistical computing environment R v.3.3.4 (https://www.R-project.org) and GraphPad Prism v.5.01 (GraphPad Software, Inc.). All statistical tests are specified throughout the mansucript.

Study approval. Animal experiments were carried out in accordance with the guidelines approved by the Animal Welfare Department of the LAGeSo State Office of Health and Social Affairs in Berlin and in accordance with international guidelines on the reduction of discomfort (86/609/EEC). All procedures performed in studies involving human participants were in accordance with the ethical standards of the institutional and/or national research committee (Charité, German Federal Institute for Drugs and Medical Devices, BfArM) and with the 1964 Helsinki declaration and its later amendments. Written informed consent was received from participants before inclusion in the study.

Author contributions

JMM, AS, LB, and SW acquired EAE data. JMM, PRD, JP, HMR, CP, AE, CID, HW, JBS, JW, MS, AP, and SW analyzed data. FP, SW, JW, JBS, and FZ conducted the clinical trial. JMM and SW wrote the manuscript. TN and FP critically reviewed the manuscript. SW, JMM, FP, and TN conceptualized the study.

Acknowledgments

We thank Klaus Wernecke, Sophie Piper, and Lea Waller for consultations and discussions regarding the statistical analysis of the study. We thank Andrea Hasselbach for valuable discussions on brain ventricle

segmentation in patients and Simone Kühn for providing the MRI data for healthy subjects. We also thank Stephanie Münchberg for technical assistance with the animal experiments and Juliane Anders for assistance with histology slide scanning. Funding sources include DFG Exc 257 (to FP), SFB1430 (to CID), and DFG WA2804 (to SW)

Address correspondence to: Sonia Waiczies, Berlin Ultrahigh Field Facility (B.U.F.F.), Max Delbrück Center for Molecular Medicine (MDC) in the Helmholtz Association, Robert-Rössle-Strasse 10, D-13125 Berlin-Buch, Germany. Phone: 49.0.30.9406.4542; Email: sonia.waiczies@mdc-berlin.de. Or to: Friedemann Paul, Experimental and Clinical Research Center, Max Delbrück Center for Molecular Medicine and Charité – Universitätsmedizin Berlin, Lindenberger Weg 80, D-13125 Berlin, Germany. Phone: 49.0.30.450.540.002; Email: friedemann.paul@charite.de.

1. Kivisäkk P, et al. Human cerebrospinal fluid central memory CD4+ T cells: evidence for trafficking through choroid plexus and meninges via P-selectin. *Proc Natl Acad Sci USA*. 2003;100(14):8389–8394.
2. Ghersi-Egea JF, Strazielle N, Catala M, Silva-Vargas V, Doetsch F, Engelhardt B. Molecular anatomy and functions of the choroidal blood-cerebrospinal fluid barrier in health and disease. *Acta Neuropathol*. 2018;135(3):337–361.
3. Filippi M, Preziosa P, Rocca MA. Multiple sclerosis. *Handb Clin Neurol*. 2016;135:399–423.
4. Rovira A, de Stefano N. MRI monitoring of spinal cord changes in patients with multiple sclerosis. *Curr Opin Neurol*. 2016;29(4):445–452.
5. Filippi M, et al. Assessment of lesions on magnetic resonance imaging in multiple sclerosis: practical guidelines. *Brain*. 2019;142(7):1858–1875.
6. Kuchling J, Paul F. Visualizing the Central Nervous System: Imaging Tools for Multiple Sclerosis and Neuromyelitis Optica Spectrum Disorders. *Front Neurol*. 2020; 11:450.
7. Thompson AJ, et al. Diagnosis of multiple sclerosis: 2017 revisions of the McDonald criteria. *Lancet Neurol*. 2018;17(2):162–173.
8. Thompson AJ, Baranzini SE, Geurts J, Hemmer B, Ciccarelli O. Multiple sclerosis. *Lancet*. 2018;391(10130):1622–1636.
9. El-Khatib AH, et al. Gadolinium in human brain sections and colocalization with other elements. *Neurol Neuroimmunol Neuroinflamm*. 2019;6(1):e515.
10. McDonald RJ, et al. Intracranial Gadolinium Deposition after Contrast-enhanced MR Imaging. *Radiology*. 2015;275(3):772–782.
11. McDonald RJ, et al. Gadolinium Deposition in Human Brain Tissues after Contrast-enhanced MR Imaging in Adult Patients without Intracranial Abnormalities. *Radiology*. 2017;285(2):546–554.
12. Schlemm L, et al. Gadopentetate but not gadobutrol accumulates in the dentate nucleus of multiple sclerosis patients. *Mult Scler*. 2017;23(7):963–972.
13. Glatigny S, Bettelli E. Experimental Autoimmune Encephalomyelitis (EAE) as Animal Models of Multiple Sclerosis (MS). *Cold Spring Harb Perspect Med*. 2018;8(11):a028977.
14. Waiczies H, et al. Identification of cellular infiltrates during early stages of brain inflammation with magnetic resonance microscopy. *PLoS One*. 2012;7(3):e32796.
15. Lepore S, et al. Enlargement of cerebral ventricles as an early indicator of encephalomyelitis. *PLoS One*. 2013;8(8):e72841.
16. De Stefano N, et al. Assessing brain atrophy rates in a large population of untreated multiple sclerosis subtypes. *Neurology*. 2010;74(23):1868–1876.
17. De Stefano N, et al. Establishing pathological cut-offs of brain atrophy rates in multiple sclerosis. *J Neurol Neurosurg Psychiatry*. 2016;87(1):93–99.
18. Fisher E, et al. Eight-year follow-up study of brain atrophy in patients with MS. *Neurology*. 2002;59(9):1412–1420.
19. Turner B, Lin X, Calmon G, Roberts N, Blumhardt LD. Cerebral atrophy and disability in relapsing-remitting and secondary progressive multiple sclerosis over four years. *Mult Scler*. 2003;9(1):21–27.
20. Lukas C, et al. Early central atrophy rate predicts 5 year clinical outcome in multiple sclerosis. *J Neurol Neurosurg Psychiatry*. 2010;81(12):1351–1356.
21. Azevedo CJ, Cen SY, Jaberzadeh A, Zheng L, Hauser SL, Pelletier D. Contribution of normal aging to brain atrophy in MS. *Neurol Neuroimmunol Neuroinflamm*. 2019;6(6):e616.
22. Azevedo CJ, et al. Early CNS neurodegeneration in radiologically isolated syndrome. *Neurol Neuroimmunol Neuroinflamm*. 2015;2(3):e102.
23. Solomon AJ, Watts R, Dewey BE, Reich DS. MRI evaluation of thalamic volume differentiates MS from common mimics. *Neurol Neuroimmunol Neuroinflamm*. 2017;4(5):e387.
24. Paul F, et al. Oral high-dose atorvastatin treatment in relapsing-remitting multiple sclerosis. *PLoS One*. 2008;3(4):e1928.
25. Filevich E, et al. Day2day: investigating daily variability of magnetic resonance imaging measures over half a year. *BMC Neurosci*. 2017;18(1):65.
26. Maclaren J, Han Z, Vos SB, Fischbein N, Bammer R. Reliability of brain volume measurements: a test-retest dataset. *Sci Data*. 2014;1:140037.
27. Radue EW, et al. Teriflunomide slows BVL in relapsing MS: A reanalysis of the TEMSO MRI data set using SIENA. *Neurol Neuroimmunol Neuroinflamm*. 2017;4(5):e390.
28. Zivadinov R, et al. Clinical relevance of brain atrophy assessment in multiple sclerosis. Implications for its use in a clinical routine. *Expert Rev Neurother*. 2016;16(7):777–793.
29. Eshaghi A, et al. Deep gray matter volume loss drives disability worsening in multiple sclerosis. *Ann Neurol*. 2018;83(2):210–222.
30. Dwyer MG, et al. Establishing pathological cut-offs for lateral ventricular volume expansion rates. *Neuroimage Clin*.

2018;18:494–501.
31. Fox NC, et al. Progressive cerebral atrophy in MS: a serial study using registered, volumetric MRI. *Neurology*. 2000;54(4):807–812.
32. Hardmeier M, et al. Rate of brain atrophy in relapsing MS decreases during treatment with IFNbeta-1a. *Neurology*. 2005;64(2):236–240.
33. Rao AB, et al. Methylprednisolone effect on brain volume and enhancing lesions in MS before and during IFNbeta-1b. *Neurology*. 2002;59(5):688–694.
34. Miller DH, et al. MRI outcomes in a placebo-controlled trial of natalizumab in relapsing MS. *Neurology*. 2007;68(17):1390–1401.
35. Zivadinov R, et al. Mechanisms of action of disease-modifying agents and brain volume changes in multiple sclerosis. *Neurology*. 2008;71(2):136–144.
36. Kappos L, Radue EW, Chin P, Ritter S, Tomic D, Lublin F. Onset of clinical and MRI efficacy occurs early after fingolimod treatment initiation in relapsing multiple sclerosis. *J Neurol*. 2016;263(2):354–360.
37. Iliff JJ, et al. A paravascular pathway facilitates CSF flow through the brain parenchyma and the clearance of interstitial solutes, including amyloid β. *Sci Transl Med*. 2012;4(147):147ra111.
38. Iliff JJ, et al. Brain-wide pathway for waste clearance captured by contrast-enhanced MRI. *J Clin Invest*. 2013;123(3):1299–1309.
39. Chen L, Elias G, Yostos MP, Stimec B, Fasel J, Murphy K. Pathways of cerebrospinal fluid outflow: a deeper understanding of resorption. *Neuroradiology*. 2015;57(2):139–147.
40. Louveau A, et al. Structural and functional features of central nervous system lymphatic vessels. *Nature*. 2015;523(7560):337–341.
41. Shrestha B, Jiang X, Ge S, Paul D, Chianchiano P, Pachter JS. Spatiotemporal resolution of spinal meningeal and parenchymal inflammation during experimental autoimmune encephalomyelitis. *Neurobiol Dis*. 2017;108:159–172.
42. Pol S, et al. Characterization of leptomeningeal inflammation in rodent experimental autoimmune encephalomyelitis (EAE) model of multiple sclerosis. *Exp Neurol*. 2019;314:82–90.
43. Fournier AP, Gauberti M, Quenault A, Vivien D, Macrez R, Docagne F. Reduced spinal cord parenchymal cerebrospinal fluid circulation in experimental autoimmune encephalomyelitis. *J Cereb Blood Flow Metab*. 2019;39(7):1258–1265.
44. Absinta M, et al. Gadolinium-based MRI characterization of leptomeningeal inflammation in multiple sclerosis. *Neurology*. 2015;85(1):18–28.
45. Absinta M, et al. Leptomeningeal gadolinium enhancement across the spectrum of chronic neuroinflammatory diseases. *Neurology*. 2017;88(15):1439–1444.
46. Schubert JJ, et al. Dynamic ^{11}C-PiB PET Shows Cerebrospinal Fluid Flow Alterations in Alzheimer Disease and Multiple Sclerosis. *J Nucl Med*. 2019;60(10):1452–1460.
47. Engelhardt B, Wolburg-Buchholz K, Wolburg H. Involvement of the choroid plexus in central nervous system inflammation. *Microsc Res Tech*. 2001;52(1):112–129.
48. Vercellino M, et al. Involvement of the choroid plexus in multiple sclerosis autoimmune inflammation: a neuropathological study. *J Neuroimmunol*. 2008;199(1-2):133–141.
49. Reboldi A, et al. C-C chemokine receptor 6-regulated entry of TH-17 cells into the CNS through the choroid plexus is required for the initiation of EAE. *Nat Immunol*. 2009;10(5):514–523.
50. Millward JM, et al. Application of Europium-Doped Very Small Iron Oxide Nanoparticles to Visualize Neuroinflammation with MRI and Fluorescence Microscopy. *Neuroscience*. 2019;403:136–144.
51. Millward JM, Schnorr J, Taupitz M, Wagner S, Wuerfel JT, Infante-Duarte C. Iron oxide magnetic nanoparticles highlight early involvement of the choroid plexus in central nervous system inflammation. *ASN Neuro*. 2013;5(1):e00110.
52. Karimy JK, et al. Inflammation-dependent cerebrospinal fluid hypersecretion by the choroid plexus epithelium in posthemorrhagic hydrocephalus. *Nat Med*. 2017;23(8):997–1003.
53. Zhang J, et al. Modulation of brain cation-Cl$^-$ cotransport via the SPAK kinase inhibitor ZT-1a. *Nat Commun*. 2020;11(1):78.
54. Karimy JK, et al. Inflammation in acquired hydrocephalus: pathogenic mechanisms and therapeutic targets. *Nat Rev Neurol*. 2020;16(5):285–296.
55. Trefler A, Sadeghi N, Thomas AG, Pierpaoli C, Baker CI, Thomas C. Impact of time-of-day on brain morphometric measures derived from T1-weighted magnetic resonance imaging. *Neuroimage*. 2016;133:41–52.
56. Dieleman N, Koek HL, Hendrikse J. Short-term mechanisms influencing volumetric brain dynamics. *Neuroimage Clin*. 2017;16:507–513.
57. Streitbürger DP, Möller HE, Tittgemeyer M, Hund-Georgiadis M, Schroeter ML, Mueller K. Investigating structural brain changes of dehydration using voxel-based morphometry. *PLoS One*. 2012;7(8):e44195.
58. Kempton MJ, et al. Effects of acute dehydration on brain morphology in healthy humans. *Hum Brain Mapp*. 2009;30(1):291–298.
59. Amiri H, et al. Urgent challenges in quantification and interpretation of brain grey matter atrophy in individual MS patients using MRI. *Neuroimage Clin*. 2018;19:466–475.
60. Biberacher V, et al. Intra- and interscanner variability of magnetic resonance imaging based volumetry in multiple sclerosis. *Neuroimage*. 2016;142:188–197.
61. Brown DA, Sawchenko PE. Time course and distribution of inflammatory and neurodegenerative events suggest structural bases for the pathogenesis of experimental autoimmune encephalomyelitis. *J Comp Neurol*. 2007;502(2):236–260.
62. Hamilton AM, et al. Central nervous system targeted autoimmunity causes regional atrophy: a 9.4T MRI study of the EAE mouse model of Multiple Sclerosis. *Sci Rep*. 2019;9(1):8488.
63. Redmond IT, Barbosa S, Blumhardt LD, Roberts N. Short-term ventricular volume changes on serial MRI in multiple sclerosis. *Acta Neurol Scand*. 2000;102(2):99–105.
64. Kirshners A, Borisov A. A Comparative Analysis of Short Time Series Processing Methods. *The Journal of Riga Technical University*. 2012;15(1);doi:10.2478/v10313-012-0009-4.
65. Zeydan B, et al. Cervical spinal cord atrophy: An early marker of progressive MS onset. *Neurol Neuroimmunol Neuroinflamm*. 2018;5(2):e435.
66. Alcaide-Leon P, et al. Quantitative spinal cord MRI in radiologically isolated syndrome. *Neurol Neuroimmunol Neuroinflamm*. 2018;5(2):e436.
67. Pasquier B, et al. Quantitative 7T MRI does not detect occult brain damage in neuromyelitis optica. *Neurol Neuroimmunol Neu-*

roinflamm. 2019;6(3):e541.
68. Markenroth Bloch K, Töger J, Ståhlberg F. Investigation of cerebrospinal fluid flow in the cerebral aqueduct using high-resolution phase contrast measurements at 7T MRI. *Acta Radiol*. 2018;59(8):988–996.
69. Abad N, Rosenberg JT, Hike DC, Harrington MG, Grant SC. Dynamic sodium imaging at ultra-high field reveals progression in a preclinical migraine model. *Pain*. 2018;159(10):2058–2065.
70. Waiczies S, et al. Fluorine-19 MRI at 21.1 T: enhanced spin-lattice relaxation of perfluoro-15-crown-5-ether and sensitivity as demonstrated in ex vivo murine neuroinflammation. *MAGMA*. 2019;32(1):37–49.
71. Woolrich MW, et al. Bayesian analysis of neuroimaging data in FSL. *Neuroimage*. 2009;45(1 Suppl):S173–S186.
72. Smith SM, et al. Advances in functional and structural MR image analysis and implementation as FSL. *Neuroimage*. 2004;23 Suppl 1:S208–S219.
73. Jenkinson M, Beckmann CF, Behrens TE, Woolrich MW, Smith SM. FSL. *Neuroimage*. 2012;62(2):782–790.
74. Avants BB, Tustison NJ, Song G, Cook PA, Klein A, Gee JC. A reproducible evaluation of ANTs similarity metric performance in brain image registration. *Neuroimage*. 2011;54(3):2033–2044.
75. Avants BB, et al. The optimal template effect in hippocampus studies of diseased populations. *Neuroimage*. 2010;49(3):2457–2466.
76. Fischl B. FreeSurfer. *Neuroimage*. 2012;62(2):774–781.
77. McDonald WI, et al. Recommended diagnostic criteria for multiple sclerosis: guidelines from the International Panel on the diagnosis of multiple sclerosis. *Ann Neurol*. 2001;50(1):121–127.
78. Hyndman RJ, et al. forecast: Forecasting functions for time series and linear models. University of Bath. https://researchportal.bath.ac.uk/en/publications/forecast-forecasting-functions-for-time-series-and-linear-models. Accessed October 3, 2020.
79. Dickey DA, Fuller WA. Distribution of the Estimators for Autoregressive Time-Series with a Unit Root. *J Am Stat Assoc*. 1979;74(366):427–431.
80. Wuertz D, Setz T, Chalabi Y. fUnitRoots: Rmetrics - Modelling Trends and Unit Roots. R package. https://cran.r-project.org/web/packages/fUnitRoots/fUnitRoots.pdf. Published November 16, 2017. Accessed October 3, 2020.
81. Trapletti A, Hornik K, LeBaron B. tseries: Time Series Analysis Computational Finance. R project. https://cran.r-project.org/web/packages/tseries/index.html. Published June 5, 2019. Accessed October 3, 2020.

3 Diskussion

The early detection, diagnosis and differentiation of neuroinflammatory diseases such as multiple sclerosis (MS) and glioblastoma has considerably improved in the past decade thanks to new advancements in MRI and MRS (Öz et al., 2014; Langen et al., 2017). The differential diagnosis of MS from other neuroinflammatory diseases that mimic MS such as Neuromyelitis Optica Spectrum Disorder (NMOSD) and Susac syndrome (Geraldes et al., 2018b), is often challenging but new findings, especially those uncovered by UHF MRI, have proven to be indispensable to make a definitive diagnosis (Filippi et al., 2019a). Further developments and technologies in MRI will be vital to improve the armamentarium of tools available to clinicians (Sati, 2018). An added dimension to MS patient management is the monitoring of disease modifying treatments (DMTs). The importance of MRI to assess treatment response and safety is clearly recognized and MRI has indeed become a vital tool to initiate treatment as early in the disease as possible (Tintore et al., 2018). A further opportunity that comes with the MR imaging modality is the possibility to study the distribution of DMTs noninvasively during pathology. Unfortunately, this utility is not implemented in clinical routine, mostly because of the sensitivity hurdle that needs to be overcome, a hurdle that can be surmounted with more sensitive MR methods and technologies to increase SNR. The vast benefits that can be earned out of detecting and quantifying DMTs with MRI needs to be discussed.

3.1 Quantitative MRI biomarkers for the diagnosis and monitoring of MS

Following up on our previous observation involving a pronounced ventricle volume (VV) expansion already prior to disease onset in the EAE (Lepore et al., 2013), we recently reported transient changes in ventricle size, even at later disease stages in the EAE (own work 5 (Millward et al., 2020)). Transient changes in VV were also observed in the majority of RRMS patients and those exhibiting these changes were also reported to be at an earlier stage of their disease, compared to those showing no transient VV changes (own work 5 (Millward et al., 2020)). We assume

that fluctuating VVs are an indicator of acute inflammation and disease state in MS patients.

Contrast-enhanced MRI is currently the gold standard diagnostic measure to uncover acute inflammation (Rovira et al., 2015; Filippi et al., 2016b). Contrast-enhanced MRI has also acted as important outcome measure when new MS therapies are investigated in clinical trials (Comi et al., 2017). Such trials have classically involved frequent MRI measurements in association with GBCAs to study DMTs e.g. teriflunomide (Confavreux et al., 2014), dimethyl fumarate (Gold et al., 2012), natalizumab (Polman et al., 2006), atorvastatin (Paul et al., 2008) or immunosuppressive therapies followed by hematopoietic cell transplantation (Nash et al., 2015). While previously common practice, repeated use of GBCAs in MS clinical trials has subsided in recent years due to concerns regarding contrast deposition after long-term repeated application (McDonald et al., 2015; McDonald et al., 2017; Schlemm et al., 2017; El-Khatib et al., 2019). Another added complexity in MS is the clinico-radiological paradox, in which lesion load as detected by MRI is typically weakly correlated with clinical disease status and changes in lesion appearances are not synchronous with clinical disability (Barkhof, 2002).

A deeper understanding into the mechanisms of GBCA deposition in the brain is required, as well as further studies into other contrast alternatives such as low molecular weight Fe^{3+}-chelate complexes (Boehm-Sturm et al., 2018; Janke et al., 2018) and macrocyclic GBCAs that do not appear to result in tissue deposition after long term repeated use (Kanda et al., 2015; Radbruch et al., 2015), even in MS and EAE (Eisele et al., 2016; Schlemm et al., 2017; Eisele et al., 2018; Wang et al., 2019).

Furthermore, quantitative MRI biomarkers that can objectively measure changes in neuroinflammation and neurodegeneration are needed. Ideally these should include a combination of multiple quantitative ^{1}H MRI methods such as T_1, T_2, T_2^* mapping or magnetization transfer techniques (Metere et al., 2017). As expected, this would add to the patient's time in the MR scanner. Therefore novel developments in MRI such as MR fingerprinting (Ma et al., 2013), compressed sensing (Mönch et al., 2020), or synthetic MRI (Hagiwara et al., 2017) that allow

combined, accelerated, or simultaneous acquisitions would significantly reduce scanning time.

The sensitivity of the MR hardware is also crucial to promote SNR and thereby reduce scan time. In preclinical MRI, we make use of a cryogenic coils to boost SNR in the EAE animal model of MS (Waiczies et al., 2012; Lepore et al., 2013). Apart from significantly reducing measurement time, this technology enables in vivo microscopic MRI (35 µm spatial resolution) and allows excellent depiction of brain pathology in the EAE that corresponds to conventional histology (Waiczies et al., 2012). It was however thanks to the reduced scan time and chance to perform more frequent acquisitions in the same mice over time that uncovered pronounced changes in the ventricle volume (VV) in the EAE already prior to disease onset (Lepore et al., 2013).

An increase in ventricle size is typically associated with brain atrophy, particularly in neurodegenerative diseases such as Alzheimer's (Lehéricy et al., 2007). Brain atrophy is also a feature of MS that can be measured by brain volumetric MRI and occurs already early during the disease (Azevedo et al., 2015; Solomon et al., 2017). Our observation of a pronounced VV enlargement prior to onset of EAE, was not suggestive of brain atrophy since it resolved during disease remission (Millward et al., 2020). Of clinical relevance, we also reported that the majority of RRMS patients also exhibit transient VV changes that are larger than normal variation, and that these patients appear to be at an earlier phase of disease. Our extensive longitudinal study in the EAE using a relatively low number of animals, repeatedly monitored by MRI, revealed a phenomenon relevant to the pathology in MS patients (Millward et al., 2020). The MS data that we investigated in our study originated from a clinical trial on the efficacy of atorvastatin in MS (Paul et al., 2008) due to the role of this lipid-lowering drug in modulating the T cell response (Aktas et al., 2003; Waiczies et al., 2005; Waiczies et al., 2007; Waiczies et al., 2008). Some immunomodulatory agents have been reported to cause pseudoatrophy in parallel to CEL reduction (Hardmeier et al., 2005; Miller et al., 2007), probably as a result of a resolution in immune cell infiltration, accelerated water losses and fluid shifts (Zivadinov et al., 2008). In the clinical trial that we retrospectively investigated, atorvastatin did not show any signs suggestive of pseudoatrophy

since there was no significant reduction in BV during the one-year study period (Millward et al., 2020).

Our observation that MS patients with transient VV changes are at an earlier phase of disease, indicates that fluctuating VV could be considered as surrogate marker of MS-associated neuroinflammation indicative of disease state. Distinguishing short-term from long-term VV and BV changes is vital, both volumes are informative, although the rate of VV expansion predicts disease progression more strongly than the rate of whole brain atrophy (Lukas et al., 2010). In parallel to lesions, the quantification of VV, BV and more specific brain region volumes (hippocampus, cortex, etc.) from anatomical and quantitative MRI scans will be vital to separate inflammation from neurodegeneration in individual patients, as well as to differentiate the anti-inflammatory, pseudoatrophy and/or neuroprotective effects of DMTs. Short but frequent MRI data acquisition — similar to our clinical study (Paul et al., 2008; Millward et al., 2020) — will be key to disentangle short-term VV oscillations suggestive of inflammation from persistent, unidirectional VV changes that are indicative of brain atrophy. These changes (transient versus unidirectional VV/BV changes) occur at different time scales and intensities. In line with this, automatic brain segmentation tools, especially those involving deep learning (Akkus et al., 2017), will be an essential part of the MR data analysis pipeline to quantify and interpret pathology or therapy related changes in daily clinical practice.

3.2 Improving MRI sensitivity to detect therapy in MS patients

We recently detected the fluorinated DMT teriflunomide (TF) in the animal model of MS using ^{19}F MRS (own work 4 (Prinz et al., 2021)). One third of all drugs that are approved worldwide, including some that are indicated for MS, are fluorinated and could be potentially detected in vivo with ^{19}F MR methods, including ^{19}F MRI (Wolf et al., 2000; Muller et al., 2007; Reid and Murphy, 2008; Bartusik and Aebisher, 2014; Wang et al., 2014; Niendorf et al., 2016c). Using MRI to detect DMTs non-invasively in regions of pharmacological relevance (e.g. CNS in MS patients) would significantly complement the treatment process.

TF is an anti-inflammatory DMT containing a trifluoromethyl group that is approved for use in MS (Derfuss et al., 2020). By inhibiting the mitochondrial enzyme dihydroorotate dehydrogenase (DHODH), TF inhibits the synthesis of pyrimidine nucleotide precursor orotate that are necessary for DNA replication (Rückemann et al., 1998). TF selectively inhibits the expansion of aggressive autoreactive T cells that are key players in the pathology of MS (Klotz et al., 2019). TF is administered orally and has a rapid, complete absorption with a long half-life (> 2 weeks) due to extensive enterohepatic recycling (Wiese et al., 2013). In RRMS patients, TF reduces the annual relapse rate, slows disability progression and reduces lesion volume (Wiese et al., 2013; Xu et al., 2016) as well as BV losses (Radue et al., 2017). In agreement with preclinical studies using the animal model of MS (Merrill et al., 2009; Merrill, 2009; Ringheim et al., 2013) we reported the efficacy of TF to prevent disease in the EAE (Prinz et al., 2021).

Although the mechanism of action of TF in MS is to regulate the expansion of aggressive autoreactive T cells (Klotz et al., 2019), there are indications that this drug might also act within the CNS by promoting myelination and neurogenesis (Göttle et al., 2018; Prabhakara et al., 2018). ^{19}F MRI would be essential to help us understand the distribution and therefore mechanism of action of drugs such as TF in MS.

There are however still limitations that prohibit detection of ^{19}F drugs such as TF with ^{19}F MRI or localized spectroscopy. In our recent study we detected TF with non-localized ^{19}F MRS (Prinz et al., 2021). ^{19}F MRI or localized single-voxel spectroscopy will be crucial to localize drugs within specific regions e.g. in the brain, to study their distribution in their therapeutic concentration range. One of the major limiting factors of implementing ^{19}F MRI for MS treatment is SNR, mainly due to the low availability of ^{19}F nuclei in vivo, although the sensitivity of the MR method is also an important contributor.

Apart from SNR and sensitivity barriers, the ^{19}F MR properties of fluorinated compounds mainly T_1 and T_2 will contribute to their detection. Temperature, pH as well as protein binding have been shown to be important contributors and strongly influences T_2 relaxation, as reported for TF (Prinz et al., 2018; Prinz et al., 2021). The T_2 of TF was radically shortened in the serum environment, presumably due to unspecific binding of the compounds to serum proteins (Dubois and Evers). Due

to the associated rapid loss in ^{19}F signal during T_2 relaxation, signal detection with ^{19}F MRI is expected to be more challenging. Selection of the appropriate MR acquisition method according to the MR properties of the compound within a specific environment will be essential to acquire MIR data with the best SNR efficiency. Therefore a thorough characterization of ^{19}F compounds (Prinz et al., 2018; Prinz et al., 2021) is necessary to plan SNR efficient acquisition methods for ^{19}F MRI that are adapted to their specific MR properties (Mastropietro et al., 2014; Faber and Schmid, 2016; Constantinides et al., 2018).

Ultimately, a combination of synergizing efforts that increase sensitivity will be necessary to overcome SNR restrictions that currently limit the localization of small amounts of drug at therapeutic levels by ^{19}F MRI. One of the efforts that we are following is compressed sensing (CS), a digital signal processing technique that accurately recovers unknown sparse signals from underdetermined linear measurements (Candes et al., 2006; Donoho, 2006; Ye, 2019). Recently we examined the performance of CS in reconstructing undersampled ^{19}F MR signals originating from sources with no a priori location (Starke et al., 2019). We made use of the sparse distribution of ^{19}F MR signal arising from inflammatory regions in the CNS of EAE mice. The time saved by undersampling can be reinvested into increased averaging to lower the detection threshold at equal acquisition time (Liang et al., 2017). We showed that while sensitivity was consistently improved with CS, undersampled ^{19}F MR data could be reliably reconstructed and data fidelity was preserved. Higher undersampling factors led to some false positive features resulting in slight blurring at the edges of inflammatory lesions in EAE mouse brains acquired in vivo but no random appearance of false positive features (Starke et al., 2019).

In preclinical studies, another approach that we have implemented to improve signal sensitivity makes use of cryogenically cooled RF coils (CRPs) that boost SNR as a result of thermal noise reduction (Waiczies et al., 2012; Lepore et al., 2013; Niendorf et al., 2015; Waiczies et al., 2017a). Apart from facilitating earlier detection of pathology in EAE (Waiczies et al., 2012) and glioma (Ku et al., 2016), this technology also reduces scan time and enables more frequent, resolved measurements within individual mice; making it likelier to uncover new pathological findings during disease, such as VV fluctuations in the EAE (Lepore et al., 2013).

A reduction in scan time would also be beneficial for ^{19}F MRI, especially to detect ^{19}F DMTs in the brain during MS or EAE pathology. Due to the low SNR, ^{19}F MRI requires intensive averaging (thereby increasing measurement time) to detect the intrinsically low ^{19}F signal in vivo originating e.g. from DMTs. Increased measurement times can be offset by SNR-boosting technologies such as CRPs. The first CRP application that we described for ^{19}F MRI was to detect inflammatory lesions with high spatial resolution in the EAE brain (Waiczies et al., 2017a), but the CRP method would truly be beneficial for detecting even lower ^{19}F MR signals, such as those derived from DMTs e.g. teriflunomide in the mouse brain (own work 4 (Prinz et al., 2021)). Unfortunately, cryogenic cooling to reduce thermal MR noise has mostly been implemented with very small RF coils in preclinical imaging, although application in human studies has been considered for nuclei with Larmor frequencies lower than those of ^{1}H e.g. ^{13}C (Sanchez-Heredia et al., 2017). Noise arises from the RF hardware but also substantially from the sample. In human ^{1}H MRI, the sample losses are dominant because of the relatively high Larmor frequencies and the large sample sizes. Therefore, there are limitations with respect to the implementation of cryogenically cooled RF coils for human MR methods.

One compelling approach to enhance SNR for human MR applications is to transition to higher magnetic field strengths (B_0) (Ladd, 2018). SNR is expected to grow *at least* linearly with increasing B_0 (Hoult and Richards, 1976; Pohmann et al., 2016). An experimental study investigating SNR dependency on B_0 in the human brain revealed that SNR $\propto B_0^{1.65}$ in the range of 3.0 T to 9.4 T (Pohmann et al., 2016). A recent simulation study also showed that SNR grows super-linearly with frequency, particularly in deeper regions of the sample (Guérin et al., 2017). Introduction of ultrahigh field (UHF) strengths is certainly a strategic step for future clinical MRI applications (Niendorf et al., 2016a), particularly for MS where findings such as the central vein sign and hypointense rim in lesions, identified at UHF, are now acknowledged as MS-specific MR imaging markers (Sinnecker et al., 2015; Kuchling and Paul, 2020). UHF strengths have also proven benefits for X-nuclei MRI where SNR is a major challenge. For sodium MRI, an SNR gain of ~3 was observed when moving from 9.4 T to 21.1 T, compared to a gain of ~ 2 for ^{1}H MR (Schepkin et al., 2010). In the case of ^{19}F MRI, we recently showed that this change

in magnetic field strength results in a gain in SNR efficiency (SNR/√time) of 7, when comparing the best possible conditions for both B_0 and when including T_1 relaxation effects (Waiczies et al., 2018).

Apart from increasing the sensitivity of the hardware, the source of the signal should also be considered. The design and synthesis of fluorine-rich molecular labels and imaging probes is another important domain in fluorine MRI research. One way to improve signal strength is to increase the number of fluorine atoms per molecule, e.g. to label cells efficiently in order to track them *in vivo* (Jirak et al., 2018; Liu et al., 2018). In the case of cell labelling, uptake of nanoparticles in cells is also desirable. By enriching nanoparticles with 1,2-dipalmitoyl-sn-glycero-3-phosphoethanolamine (DPPE) we reported a striking increase in cytoplasmic uptake of ^{19}F nanoparticles in dendritic cells (own work 2 (Waiczies et al., 2015)). These immune cells can be employed as cell therapies in recalcitrant cancer and autoimmune diseases, and while their labelling with ^{19}F nanoparticles is still experimental and needs further intensive research (Waiczies et al., 2017b), this approach has already been implemented in colorectal cancer (Ahrens et al., 2014).

Monitoring biological and pharmacological therapy in patients has indisputable advantages in the process of patient management and treatment. We are currently investigating the impact of modulating the fluorinated side chain of effective DMTs used to treat MS patients. We are studying bioisosteres of DMTs such as teriflunomide as fluorine MRI reporters with pharmacological activity in collaboration with experts in medicinal chemistry at the Leibniz-Institut für Molekulare Pharmakologie (FMP) who have already designed and synthesized an array of DHODH inhibitors (Prinz et al., 2019). We identified SF_5 as an excellent ^{19}F reporter group for ^{19}F MR theranostics. SF_5 is a stable bioisostere of the CF_3 congener, for which the utility as a ^{19}F reporter group has not been studied in a biological context thus far. SF_5-TF showed the best ^{19}F MR signal detection as well as best capacity to inhibit T cell proliferation, as mechanism of action in MS pathology. Further research in this area will be vital as it underlines the value of adding the ^{19}F MR reporter function as added dimension to biological and pharmacological activity when screening and identifying lead compounds during drug discovery.

3.3 Future directions to transition fluorine MRI into clinical practise

In principle it is already possible to study fluorinated drugs in the brain of MS patients at 7.0 T. The main hurdle is the sensitivity of the MR method that might require long patient examinations. Future steps to overcome this hurdle involve the design of dedicated RF hardware technologies and accelerated MR techniques on clinical MR scanners that are sensitive enough to detect and quantify the ^{19}F MR signal in patients, even in regions that might contain low concentrations of the fluorinated drug. Additionally, it will be necessary to focus on the signal source while gauging ^{19}F MRI as a method to study the distribution of drug treatments. The design and synthesis of molecular labels and imaging probes will be an important domain in future ^{19}F MRI research. Apart from investigating biological and pharmacological activity, the MR reporter function will be a necessary additional dimension that will be key in investigations on lead compounds (screening and optimization) during drug discovery. Additionally, safety and efficacy studies will be necessary next steps. Collaborations with other academic partners from medicinal chemistry, pharmacology and clinical neuroimmunology as well as with the pharmaceutical and MRI industry will be necessary to fulfil these future goals and objectives.

4 Zusammenfassung

Die Magnetresonanztomographie (MRT) ist nach wie vor eines der wichtigsten klinischen Werkzeuge für die Früherkennung, Diagnose und das therapeutische Management der Multiplen Sklerose (MS). Bisher war sie wichtig, um neuroinflammatorische Erkrankungen zu erkennen und zu beurteilen sowie das Ansprechen auf verordnete krankheitsmodifizierende Behandlungen (im Englischen disease modifying treatments, DMT) zu beurteilen.

Der Goldstandard zur Erkennung neuer Schübe und neuer entzündlicher Episoden bei MS ist der Nachweis von kontrastverstärkten Läsionen mit Gadolinium-basierten Kontrastmitteln. Bedenken hinsichtlich einer möglichen Langzeitanreicherung dieser Mittel im Gehirn und in anderen Organen sprechen für einen Paradigmenwechsel hin zu neuen kontrastmittelfreien MRT-Methoden und Biomarkern. Ultrahohe Magnetfeldstärken (UHF-MR) haben dazu beigetragen, den Detailgrad und die räumliche Auflösung in MR-Bildern des Gehirns von MS-Patienten zu erhöhen und damit neue Marker wie das Zentralvenenzeichen aufzudecken, die für die MS-Pathologie relevant sind. Eine Beobachtung, die wir sowohl bei MS-Patienten als auch im Tiermodell, der experimentellen Autoimmun-Enzephalomyelitis (EAE), machten zeigt, dass Schwankungen der Hirnventrikelgröße eine wichtige Rolle in der frühen Pathogenese der Krankheit spielen. Fluktuationen der Ventrikelgröße schienen der schubförmig-remittierenden Form des Krankheitsverlaufs zu folgen. Bei MS-Patienten beobachteten wir ein hohes Maß an Kreuzkorrelation zwischen dem Zeitpunkt der abnormalen Ventrikelfluktuationen und dem Zeitpunkt der Veränderungen anderer klinischer und MRT-Parameter. Diese Kreuzkorrelationen schienen ebenso stark zu sein wie die zwischen der kontrastverstärkten MRT und den anderen Parametern. Dieser Befund weist auf einen ähnlich hohen diagnostischen Wert zwischen der Ventrikelgröße und der kontrastverstärkten MRT bei MS hin.

Die MRT hat sich auch als hilfreich erwiesen, um die Behandlung bei MS so früh wie möglich einzuleiten und die Behandlungsabläufe entsprechend dem Fortschreiten der Erkrankung anzupassen. Darüber hinaus können MR-Methoden auch eingesetzt werden, um die Verteilung von DMTs während der Pathologie zu untersuchen. Mit Hilfe der MR-Spektroskopie (MRS) haben wir kürzlich

Teriflunomid in den Gehirnen von Mäusen im EAE Modell nachgewiesen. Teriflunomid wird bei schubförmig remittierenden MS-Patienten als DMT eingesetzt, um Schübe zu verhindern. Wir verwendeten MRS, um die Teriflunomid-Spiegel während verschiedener Krankheitsstadien der EAE zu untersuchen, verglichen MRS mit einer analytischen Methode als Referenz und zeigten eine Korrelation zwischen beiden Methoden. Unsere Ergebnisse deuten darauf hin, dass die MRS in Zukunft zur nicht-invasiven Quantifizierung von Medikamenten wie Teriflunomid bei MS-Patienten eingesetzt werden könnte.

Leider ist die Bedeutung der Fluor-(^{19}F)-MRT zum Nachweis, zur Verfolgung und zur Quantifizierung von DMTs bei Patienten noch nicht ausreichend erkannt. Dies vor allem wegen ihrer Barrieren in Bezug auf die Sensitivität. Während wir MRS verwendet haben, um Teriflunomid in der EAE in vivo nachzuweisen, verbieten die Grenzwerte der Signalempfindlichkeit derzeit den Nachweis solcher Medikamente mit MRI oder Einzel-Voxel-MRS. Neue Methoden und Technologien, die die Empfindlichkeit und das Signal-Rausch-Verhältnis (SNR) verbessern, sind notwendig, um diese Hürde zu überwinden. Zu den Methoden, die wir zur Erhöhung des SNR für die ^{19}F-MRT einsetzen, gehören kryogen gekühlte Hochfrequenzantennen (HF) als Detektoren, die das thermische Rauschen der Hardware deutlich reduzieren und damit das SNR um mehr als eine Größenordnung über das einer HF-Spule ähnlicher Größe bei Raumtemperatur erhöhen. Während es fraglich ist, ob diese Technologie zur Verbesserung des SNR in der klinischen Umgebung eingesetzt werden kann, können andere Methoden zur Erhöhung des SNR sicherlich wertvoll für die Implementierung in der Klinik sein. Dazu gehören höhere Magnetfelder und Methoden zur Beschleunigung der Datenerfassung wie *Compressed Sensing*. Diese werden alle entscheidend sein, um das essenzielle Ziel der Empfindlichkeitssteigerung zu erreichen und somit Medikamente in vivo mit MR-Methoden überwachen zu können.

Zukünftige Richtungen: Neben der Erhöhung der Empfindlichkeit der MR-Methode wird es in Zukunft notwendig sein, sich auf die Signalquelle zu konzentrieren, während man die MRT als Methode zur Untersuchung der Verteilung von Medikamentenbehandlungen betrachtet. Das Design und die Synthese molekularer Marker und bildgebenden Sonden wird ein wichtiger Bereich in der zukünftigen MRT-Forschung darstellen. Die Einbindung der MR-Reporterfunktion

in Leitverbindungen sollte eine notwendige zusätzliche Dimension bei der Untersuchung neuer Verbindungen während der Arzneimittelentwicklung sein. Kooperationen zwischen Wissenschaft und Industrie werden notwendig sein, um diesen Bereich der *Theranostik* zu erweitern.

Summary

Magnetic resonance imaging (MRI) remains one of the most essential clinical tools for the early detection, diagnosis, and therapeutic management of multiple sclerosis (MS). Until now it has been important to detect and assess neuroinflammatory disease as well as to assess the response to prescribed disease modifying treatments (DMT).

The gold standard to detect new relapses and new inflammatory episodes in MS is the detection of contrast-enhanced lesions with gadolinium-based contrast agents. Concerns regarding potential long-term deposition of these agents in the brain are advocating a paradigm shift towards new contrast-free MRI methods and biomarkers. Ultrahigh field (UHF) strengths have been instrumental to increase the level of detail and spatial resolution in brain MR images of MS patients and hence to uncover novel markers such as the central vein sign that are relevant to the MS pathology. An observation that we made in MS patients as well as in its animal model, the experimental autoimmune encephalomyelitis (EAE), is that brain ventricle size fluctuations play an important role early during the pathogenesis of the disease. Fluctuations in ventricle size appeared to follow the relapsing-remitting form of disease progression. In MS patients, we observed a high degree of cross-correlation between the timing of abnormal ventricle fluctuations and timing of changes in other clinical and MRI parameters. These cross-correlations seemed to be as strong as those achieved between contrast-enhanced MRI and the other parameters, indicating a similar level of diagnostic value between ventricle size and contrast-enhanced MRI in MS.

MRI has also been instrumental to initiate treatment as early as possible in MS and to adjust treatment routines according to disease progression. Beyond this, MR methods may also be used to study the distribution of DMTs during pathology.

Using MR spectroscopy (MRS) we recently detected teriflunomide in the brains of mice during EAE. Teriflunomide is used in relapsing-remitting MS patients as a DMT to prevent relapses. We used MRS to study teriflunomide levels during different disease stages of the EAE, compared MRS with an analytical method as reference and showed a correlation between both methods. Our results indicate that MRS could be used in the future to quantify drugs such as teriflunomide non-invasively in MS patients.

Unfortunately, the significance of fluorine (^{19}F) MRI to detect, follow and quantify DMTs in patients has not yet been sufficiently recognized nor has its need been appreciated, mostly because of its hurdles with respect to sensitivity barriers. While we used MRS to detect teriflunomide in the EAE in vivo, limits in signal sensitivity currently prohibit the detection of such drugs with MRI or single-voxel MRS. Novel methods and technologies that enhance sensitivity and signal-to-noise ratio (SNR) will be necessary to surmount this hurdle. Amongst the methods that we implement to increase SNR for ^{19}F MRI, cryogenically cooled radio frequency (RF) coils significantly reduce thermal noise by the hardware, thereby increasing SNR by over an order of magnitude beyond that of a room temperature RF coil of similar size. While it is still debatable whether this technology can be used to improve SNR in the clinical setting, other methods of increasing SNR can certainly be valuable for implementation in the clinic. These include higher magnetic fields and methods to accelerate data acquisition such as compressed sensing. These will all be key to achieve the goal necessary to increase SNR and monitor drugs in vivo with MR methods.

Future directions: Apart from increasing the sensitivity of the MR method, it will be necessary to focus on the signal source in the future while gauging MRI as a method to study the distribution of drug treatments. The design and synthesis of molecular labels and imaging probes will be an important domain in future MRI research. Incorporating MR reporter function to lead compounds should be a necessary added dimension when studying new compounds during drug discovery. Collaborations between academia and industry will be necessary to broaden this field of *theranostics*.

5 Literaturangaben

Ahrens, E.T., R. Flores, H. Xu, and P.A. Morel. 2005. In vivo imaging platform for tracking immunotherapeutic cells. *Nat.Biotechnol.* 23:983-987.

Ahrens, E.T., B.M. Helfer, C.F. O'Hanlon, and C. Schirda. 2014. Clinical cell therapy imaging using a perfluorocarbon tracer and fluorine-19 MRI. *Magnetic Resonance in Medicine*

Akkus, Z., A. Galimzianova, A. Hoogi, D.L. Rubin, and B.J. Erickson. 2017. Deep Learning for Brain MRI Segmentation: State of the Art and Future Directions. *Journal of Digital Imaging* 30:449-459.

Aktas, O., S. Waiczies, A. Smorodchenko, J. Dorr, B. Seeger, T. Prozorovski, S. Sallach, M. Endres, S. Brocke, R. Nitsch, and F. Zipp. 2003. Treatment of relapsing paralysis in experimental encephalomyelitis by targeting Th1 cells through atorvastatin. *J Exp Med.* 197:725-733.

Androdias, G., R. Reynolds, M. Chanal, C. Ritleng, C. Confavreux, and S. Nataf. 2010. Meningeal T cells associate with diffuse axonal loss in multiple sclerosis spinal cords. *Annals of neurology* 68:465-476.

Arevalo, O., R. Riascos, P. Rabiei, A. Kamali, and F. Nelson. 2019. Standardizing Magnetic Resonance Imaging Protocols, Requisitions, and Reports in Multiple Sclerosis: An Update for Radiologist Based on 2017 Magnetic Resonance Imaging in Multiple Sclerosis and 2018 Consortium of Multiple Sclerosis Centers Consensus Guidelines. *Journal of computer assisted tomography* 43:1-12.

Azevedo, C.J., E. Overton, S. Khadka, J. Buckley, S. Liu, M. Sampat, O. Kantarci, C. Lebrun Frenay, A. Siva, D.T. Okuda, and D. Pelletier. 2015. Early CNS neurodegeneration in radiologically isolated syndrome. *Neurol Neuroimmunol Neuroinflamm* 2:e102.

Baecher-Allan, C., B.J. Kaskow, and H.L. Weiner. 2018. Multiple Sclerosis: Mechanisms and Immunotherapy. *Neuron* 97:742-768.

Bagnato, F., S. Hametner, E. Boyd, V. Endmayr, Y. Shi, V. Ikonomidou, G. Chen, S. Pawate, H. Lassmann, and S. Smith. 2018. Untangling the R2* contrast in multiple sclerosis: a combined MRI-histology study at 7.0 Tesla. *Public Library of Science one* 13:

Barkhof, F. 2002. The clinico-radiological paradox in multiple sclerosis revisited. *Curr.Opin.Neurol.* 15:239-245.

Barkhof, F., P.A. Calabresi, D.H. Miller, and S.C. Reingold. 2009. Imaging outcomes for neuroprotection and repair in multiple sclerosis trials. *Nature Reviews Neurology* 5:256-266.

Barkhof, F. 2016. Brain atrophy measurements should be used to guide therapy monitoring in MS – NO. *Multiple Sclerosis Journal* 22:1524-1526.

Bartusik, D., and D. Aebisher. 2014. (19)F applications in drug development and imaging - a review. *Biomedicine & pharmacotherapy = Biomedecine & pharmacotherapie* 68:813-817.

Baxter, A.G. 2007. The origin and application of experimental autoimmune encephalomyelitis. *Nat.Rev.Immunol.* 7:904-912.

Behrens, J.R., J. Wanner, J. Kuchling, L. Ostendorf, L. Harms, K. Ruprecht, T. Niendorf, S. Jarius, B. Wildemann, R.M. Gieß, M. Scheel, J. Bellmann-Strobl, J. Wuerfel, F. Paul, and T. Sinnecker. 2018. 7 Tesla MRI of Balo's concentric sclerosis versus

multiple sclerosis lesions. *Annals of Clinical and Translational Neurology* 5:900-912.

Bell, L., A. Lenhart, A. Rosenwald, C.M. Monoranu, and F. Berberich-Siebelt. 2020. Lymphoid Aggregates in the CNS of Progressive Multiple Sclerosis Patients Lack Regulatory T Cells. *Frontiers in Immunology* 10:

Bendix, I., C.F. Pfueller, T. Leuenberger, N. Glezeva, V. Siffrin, Y. Muller, T. Prozorovski, W. Hansen, U. Schulze Topphoff, C. Loddenkemper, F. Zipp, and S. Waiczies. 2010. MAPK3 deficiency drives autoimmunity via DC arming. *Eur J Immunol* 40:1486-1495.

Bergamaschi, R., S. Quaglini, E. Tavazzi, M.P. Amato, D. Paolicelli, V. Zipoli, A. Romani, C. Tortorella, E. Portaccio, M. D'Onghia, F. Garberi, V. Bargiggia, and M. Trojano. 2016. Immunomodulatory therapies delay disease progression in multiple sclerosis. *Multiple Sclerosis Journal* 22:1732-1740.

Blaabjerg, M., K. Ruprecht, T. Sinnecker, D. Kondziella, T. Niendorf, B.M. Kerrn-Jespersen, M. Lindelof, H. Lassmann, B.W. Kristensen, F. Paul, and Z. Illes. 2016. Widespread inflammation in CLIPPERS syndrome indicated by autopsy and ultra-high-field 7T MRI. *Neurology(R) neuroimmunology & neuroinflammation* 3:e226.

Blazejewska, A.I., A.M. Al-Radaideh, S. Wharton, S.Y. Lim, R.W. Bowtell, C.S. Constantinescu, and P.A. Gowland. 2015. Increase in the iron content of the substantia nigra and red nucleus in multiple sclerosis and clinically isolated syndrome: a 7 Tesla MRI study. *Journal of Magnetic Resonance Imaging* 41:1065-1070.

Boehm-Sturm, P., A. Haeckel, R. Hauptmann, S. Mueller, C.K. Kuhl, and E.A. Schellenberger. 2018. Low-Molecular-Weight Iron Chelates May Be an Alternative to Gadolinium-based Contrast Agents for T1-weighted Contrast-enhanced MR Imaging. *Radiology* 286:537-546.

Bonnier, G., A. Roche, D. Romascano, S. Simioni, D. Meskaldji, D. Rotzinger, Y.C. Lin, G. Menegaz, M. Schluep, and R. Du Pasquier. 2014. Advanced MRI unravels the nature of tissue alterations in early multiple sclerosis. *Annals of clinical and translational neurology* 1:423-432.

Bozin, I., Y. Ge, J. Kuchling, P. Dusek, S. Chawla, L. Harms, K. Ruprecht, T. Niendorf, F. Paul, and I. Kister. 2015. Magnetic resonance phase alterations in multiple sclerosis patients with short and long disease duration. *Public Library of Science one* 10:e0128386.

Bruschi, N., G. Boffa, and M. Inglese. 2020. Ultra-high-field 7-T MRI in multiple sclerosis and other demyelinating diseases: from pathology to clinical practice. *European Radiology Experimental* 4:59.

Buch, S., K. Subramanian, P.K. Jella, Y. Chen, Z. Wu, K. Shah, E. Bernitsas, Y. Ge, and E.M. Haacke. 2020. Revealing vascular abnormalities and measuring small vessel density in multiple sclerosis lesions using USPIO. *NeuroImage. Clinical* 29:102525-102525.

Candes, E.J., J. Romberg, and T. Tao. 2006. Robust uncertainty principles: exact signal reconstruction from highly incomplete frequency information. *IEEE Transactions on Information Theory* 52:489-509.

Cencioni, M.T., M. Mattoscio, R. Magliozzi, A. Bar-Or, and P.A. Muraro. 2021. B cells in multiple sclerosis — from targeted depletion to immune reconstitution therapies. *Nature Reviews Neurology*

Charcot, M. 1868. Histologie de la scl,rose en plaques. *Gazette des H"pitaux* 141:554-555.

Comi, G., M. Radaelli, and P. Soelberg Sørensen. 2017. Evolving concepts in the treatment of relapsing multiple sclerosis. *The Lancet* 389:1347-1356.

Confavreux, C., P. O'Connor, G. Comi, M.S. Freedman, A.E. Miller, T.P. Olsson, J.S. Wolinsky, T. Bagulho, J.-L. Delhay, and D. Dukovic. 2014. Oral teriflunomide for patients with relapsing multiple sclerosis (TOWER): a randomised, double-blind, placebo-controlled, phase 3 trial. *The Lancet Neurology* 13:247-256.

Constantinides, C., M. Maguire, E. McNeill, R. Carnicer, E. Swider, M. Srinivas, C.A. Carr, and J.E. Schneider. 2018. Fast, quantitative, murine cardiac 19F MRI/MRS of PFCE-labeled progenitor stem cells and macrophages at 9.4T. *PloS one* 13:e0190558.

Creusot, R.J., N. Giannoukakis, M. Trucco, M.J. Clare-Salzler, and C.G. Fathman. 2014. It's Time to Bring Dendritic Cell Therapy to Type 1 Diabetes. *Diabetes* 63:20-30.

Daldrup-Link, H.E. 2017. Ten Things You Might Not Know about Iron Oxide Nanoparticles. *Radiology* 284:616-629.

De Stefano, N., M.L. Stromillo, A. Giorgio, M.L. Bartolozzi, M. Battaglini, M. Baldini, E. Portaccio, M.P. Amato, and M.P. Sormani. 2016. Establishing pathological cut-offs of brain atrophy rates in multiple sclerosis. *Journal of neurology, neurosurgery, and psychiatry* 87:93-99.

de Vries, I.J., W.J. Lesterhuis, J.O. Barentsz, P. Verdijk, J.H. van Krieken, O.C. Boerman, W.J. Oyen, J.J. Bonenkamp, J.B. Boezeman, G.J. Adema, J.W. Bulte, T.W. Scheenen, C.J. Punt, A. Heerschap, and C.G. Figdor. 2005. Magnetic resonance tracking of dendritic cells in melanoma patients for monitoring of cellular therapy. *Nat.Biotechnol.* 23:1407-1413.

Deisenhammer, F., H. Zetterberg, B. Fitzner, and U.K. Zettl. 2019. The Cerebrospinal Fluid in Multiple Sclerosis. *Frontiers in Immunology* 10:

Delgado, P.R., A. Kuehne, J.S. Periquito, J.M. Millward, A. Pohlmann, S. Waiczies, and T. Niendorf. 2020. B1 inhomogeneity correction of RARE MRI with transceive surface radiofrequency probes. *Magn Reson Med* 84:2684-2701.

Dendrou, C.A., L. Fugger, and M.A. Friese. 2015. Immunopathology of multiple sclerosis. *Nature reviews. Immunology* 15:545-558.

Derfuss, T., M. Mehling, A. Papadopoulou, A. Bar-Or, J.A. Cohen, and L. Kappos. 2020. Advances in oral immunomodulating therapies in relapsing multiple sclerosis. *The Lancet. Neurology* 336-347.

Dieleman, N., H.L. Koek, and J. Hendrikse. 2017. Short-term mechanisms influencing volumetric brain dynamics. *NeuroImage. Clinical* 16:507-513.

Donoho, D.L. 2006. Compressed sensing. *IEEE Transactions on Information Theory* 52:1289-1306.

Dubois, B.W., and A.S. Evers. 1992. Fluorine-19 NMR spin-spin relaxation (T2) method for characterizing volatile anesthetic binding to proteins. Analysis of isoflurane binding to serum albumin. *Biochemistry* 31:7069-7076.

Dumoulin, S.O., A. Fracasso, W. van der Zwaag, J.C.W. Siero, and N. Petridou. 2018. Ultra-high field MRI: Advancing systems neuroscience towards mesoscopic human brain function. *NeuroImage* 168:345-357.

Duning, T., S. Kloska, O. Steinsträter, H. Kugel, W. Heindel, and S. Knecht. 2005. Dehydration confounds the assessment of brain atrophy. *Neurology* 64:548-550.

Eisele, P., A. Alonso, K. Szabo, A. Ebert, M. Ong, S.O. Schoenberg, and A. Gass. 2016. Lack of increased signal intensity in the dentate nucleus after repeated

administration of a macrocyclic contrast agent in multiple sclerosis: An observational study. *Medicine (Baltimore)* 95:e4624.

Eisele, P., K. Szabo, A. Alonso, M. Ong, M. Platten, S.O. Schoenberg, and A. Gass. 2018. Lack of T1 hyperintensity in the dentate nucleus after 15 administrations of a macrocyclic contrast agent in multiple sclerosis. *Journal of Neurology, Neurosurgery & Psychiatry* 89:324-326.

El-Khatib, A.H., H. Radbruch, S. Trog, B. Neumann, F. Paul, A. Koch, M.W. Linscheid, N. Jakubowski, and E. Schellenberger. 2019. Gadolinium in human brain sections and colocalization with other elements. *Neurology(R) neuroimmunology & neuroinflammation* 6:e515.

Faber, C., and F. Schmid. 2016. Chapter 1 Pulse Sequence Considerations and Schemes. In Fluorine Magnetic Resonance Imaging. Pan Stanford Publishing, 1-28.

Faissner, S., J.R. Plemel, R. Gold, and V.W. Yong. 2019. Progressive multiple sclerosis: from pathophysiology to therapeutic strategies. *Nature Reviews Drug Discovery* 18:905-922.

Filippi, M., P. Preziosa, and M.A. Rocca. 2016a. Multiple sclerosis. *Handbook of clinical neurology* 135:399-423.

Filippi, M., M.A. Rocca, O. Ciccarelli, N. De Stefano, N. Evangelou, L. Kappos, A. Rovira, J. Sastre-Garriga, M. Tintorè, J.L. Frederiksen, C. Gasperini, J. Palace, D.S. Reich, B. Banwell, X. Montalban, and F. Barkhof. 2016b. MRI criteria for the diagnosis of multiple sclerosis: MAGNIMS consensus guidelines. *The Lancet Neurology* 15:292-303.

Filippi, M., A. Bar-Or, F. Piehl, P. Preziosa, A. Solari, S. Vukusic, and M.A. Rocca. 2018. Multiple sclerosis. *Nature Reviews Disease Primers* 4:43.

Filippi, M., P. Preziosa, B.L. Banwell, F. Barkhof, O. Ciccarelli, N. De Stefano, J.J.G. Geurts, F. Paul, D.S. Reich, A.T. Toosy, A. Traboulsee, M.P. Wattjes, T.A. Yousry, A. Gass, C. Lubetzki, B.G. Weinshenker, and M.A. Rocca. 2019a. Assessment of lesions on magnetic resonance imaging in multiple sclerosis: practical guidelines. *Brain* 142:1858-1875.

Filippi, M., P. Preziosa, B.L. Banwell, F. Barkhof, O. Ciccarelli, N. De Stefano, J.J.G. Geurts, F. Paul, D.S. Reich, A.T. Toosy, A. Traboulsee, M.P. Wattjes, T.A. Yousry, A. Gass, C. Lubetzki, B.G. Weinshenker, and M.A. Rocca. 2019b. Assessment of lesions on magnetic resonance imaging in multiple sclerosis: practical guidelines. *Brain*

Frischer, J.M., S.D. Weigand, Y. Guo, N. Kale, J.E. Parisi, I. Pirko, J. Mandrekar, S. Bramow, I. Metz, W. Brück, H. Lassmann, and C.F. Lucchinetti. 2015. Clinical and pathological insights into the dynamic nature of the white matter multiple sclerosis plaque. *Annals of neurology* 78:710-721.

Gentile, A., A. Musella, S. Bullitta, D. Fresegna, F. De Vito, R. Fantozzi, E. Piras, F. Gargano, G. Borsellino, L. Battistini, A. Schubart, G. Mandolesi, and D. Centonze. 2016. Siponimod (BAF312) prevents synaptic neurodegeneration in experimental multiple sclerosis. *J Neuroinflammation* 13:016-0686.

Geraldes, R., O. Ciccarelli, F. Barkhof, N. De Stefano, C. Enzinger, M. Filippi, M. Hofer, F. Paul, P. Preziosa, and A. Rovira. 2018a. The current role of MRI in differentiating multiple sclerosis from its imaging mimics. *Nature Reviews Neurology* 14:199.

Geraldes, R., O. Ciccarelli, F. Barkhof, N. De Stefano, C. Enzinger, M. Filippi, M. Hofer, F. Paul, P. Preziosa, A. Rovira, G.C. DeLuca, L. Kappos, T. Yousry, F. Fazekas, J. Frederiksen, C. Gasperini, J. Sastre-Garriga, N. Evangelou, J. Palace, and M.s.g.

on behalf of the. 2018b. The current role of MRI in differentiating multiple sclerosis from its imaging mimics. *Nature Reviews Neurology* 14:199.

Giovannoni, G., L. Airas, R. Bove, A. Boyko, G. Cutter, J. Hobart, J. Kuhle, J. Oh, C. Tur, M. Garas, F. Model, M. Manfrini, and J.S. Wolinsky. 2019. Ocrelizumab Treatment Effect on Upper Limb Function in PPMS Patients with Disability: Subgroup Results of the ORATORIO Study to Inform the ORATORIO-HAND Study Design (P3.2-091). *Neurology* 92:P3.2-091.

Glatigny, S., and E. Bettelli. 2018. Experimental Autoimmune Encephalomyelitis (EAE) as Animal Models of Multiple Sclerosis (MS). *Cold Spring Harbor Perspectives in Medicine* 8:

Gold, R., L. Kappos, D.L. Arnold, A. Bar-Or, G. Giovannoni, K. Selmaj, C. Tornatore, M.T. Sweetser, M. Yang, S.I. Sheikh, and K.T. Dawson. 2012. Placebo-controlled phase 3 study of oral BG-12 for relapsing multiple sclerosis. *N Engl J Med* 367:1098-1107.

Göttle, P., A. Manousi, D. Kremer, L. Reiche, H.-P. Hartung, and P. Küry. 2018. Teriflunomide promotes oligodendroglial differentiation and myelination. *J Neuroinflammation* 15:76-76.

Guérin, B., J.F. Villena, A.G. Polimeridis, E. Adalsteinsson, L. Daniel, J.K. White, and L.L. Wald. 2017. The Ultimate Signal-to-Noise Ratio in Realistic Body Models. *Magnetic Resonance in Medicine* 78:1969-1980.

Hagiwara, A., M. Warntjes, M. Hori, C. Andica, M. Nakazawa, K.K. Kumamaru, O. Abe, and S. Aoki. 2017. SyMRI of the Brain: Rapid Quantification of Relaxation Rates and Proton Density, With Synthetic MRI, Automatic Brain Segmentation, and Myelin Measurement. *Investigative radiology* 52:647-657.

Harbo, H.F., R. Gold, and M. Tintoré. 2013. Sex and gender issues in multiple sclerosis. *Ther Adv Neurol Disord* 6:237-248.

Hardmeier, M., S. Wagenpfeil, P. Freitag, E. Fisher, R.A. Rudick, M. Kooijmans, M. Clanet, E.W. Radue, and L. Kappos. 2005. Rate of brain atrophy in relapsing MS decreases during treatment with IFNβ-1a. *Neurology* 64:236-240.

Harry, R.A., A.E. Anderson, J.D. Isaacs, and C.M.U. Hilkens. 2010. Generation and characterisation of therapeutic tolerogenic dendritic cells for rheumatoid arthritis. *Annals of the rheumatic diseases* 69:2042-2050.

Hemond, C.C., and R. Bakshi. 2018. Magnetic resonance imaging in multiple sclerosis. *Cold Spring Harbor Perspectives in Medicine* 8:a028969.

Herrmann, C.J.J., A. Els, L. Boehmert, J. Periquito, T.W. Eigentler, J.M. Millward, S. Waiczies, J. Kuchling, F. Paul, and T. Niendorf. 2021. Simultaneous T2 and mapping of multiple sclerosis lesions with radial RARE-EPI. *Magnetic Resonance in Medicine* 86:1383-1402.

Hinds, K.A., J.M. Hill, E.M. Shapiro, M.O. Laukkanen, A.C. Silva, C.A. Combs, T.R. Varney, R.S. Balaban, A.P. Koretsky, and C.E. Dunbar. 2003. Highly efficient endosomal labeling of progenitor and stem cells with large magnetic particles allows magnetic resonance imaging of single cells. *Blood* 102:867-872.

Hochmeister, S., R. Grundtner, J. Bauer, B. Engelhardt, R. Lyck, G. Gordon, T. Korosec, A. Kutzelnigg, J.J. Berger, M. Bradl, R.E. Bittner, and H. Lassmann. 2006. Dysferlin Is a New Marker for Leaky Brain Blood Vessels in Multiple Sclerosis. *Journal of Neuropathology & Experimental Neurology* 65:855-865.

Hoult, D.I., and R.E. Richards. 1976. The signal-to-noise ratio of the nuclear magnetic resonance experiment. *J.Magn Reson.(1969)* 24:71-85.

Hsiao, Y.-P., C.-H. Huang, Y.-C. Lin, and T.-R. Jan. 2019. Systemic exposure to a single dose of ferucarbotran aggravates neuroinflammation in a murine model of experimental autoimmune encephalomyelitis. *Int J Nanomedicine* 14:1229-1240.

Idoyaga, J., C. Fiorese, L. Zbytnuik, A. Lubkin, J. Miller, B. Malissen, D. Mucida, M. Merad, and R.M. Steinman. 2013. Specialized role of migratory dendritic cells in peripheral tolerance induction. *J Clin Invest* 123:844-854.

Jager, A., V. Dardalhon, R.A. Sobel, E. Bettelli, and V.K. Kuchroo. 2009. Th1, Th17, and Th9 effector cells induce experimental autoimmune encephalomyelitis with different pathological phenotypes. *J Immunol* 183:7169-7177.

Janjic, J.M., and E.T. Ahrens. 2009. Fluorine-containing nanoemulsions for MRI cell tracking. *Wiley Interdiscip Rev Nanomed Nanobiotechnol* 1:492-501.

Janke, H.P., N. Güvener, W. Dou, D.M. Tiemessen, A. YantiSetiasti, J.G.O. Cremers, P.J.A. Borm, W.F.J. Feitz, A. Heerschap, F. Kiessling, and E. Oosterwijk. 2018. Labeling of Collagen Type I Templates with a Naturally Derived Contrast Agent for Noninvasive MR Imaging in Soft Tissue Engineering. *Advanced Healthcare Materials* 7:1800605.

Ji, Y., H. Waiczies, L. Winter, P. Neumanova, D. Hofmann, J. Rieger, R. Mekle, S. Waiczies, and T. Niendorf. 2015. Eight-channel transceiver RF coil array tailored for 1H/19F MR of the human knee and fluorinated drugs at 7.0 T. *NMR in Biomedicine* 28:726-737.

Jirak, D., A. Galisova, K. Kolouchova, D. Babuka, and M. Hruby. 2018. Fluorine polymer probes for magnetic resonance imaging: quo vadis? *Magnetic Resonance Materials in Physics, Biology and Medicine*

Kanda, T., M. Osawa, H. Oba, K. Toyoda, J.i. Kotoku, T. Haruyama, K. Takeshita, and S. Furui. 2015. High Signal Intensity in Dentate Nucleus on Unenhanced T1-weighted MR Images: Association with Linear versus Macrocyclic Gadolinium Chelate Administration. *Radiology* 275:803-809.

Kappos, L., A. Bar-Or, B.A.C. Cree, R.J. Fox, G. Giovannoni, R. Gold, P. Vermersch, D.L. Arnold, S. Arnould, T. Scherz, C. Wolf, E. Wallström, F. Dahlke, A. Achiron, L. Achtnichts, K. Agan, G. Akman-Demir, A.B. Allen, J.P. Antel, A.R. Antiguedad, M. Apperson, A.M. Applebee, G.I. Ayuso, M. Baba, O. Bajenaru, R. Balasa, B.P. Balci, M. Barnett, A. Bass, V.U. Becker, M. Bejinariu, F.T. Bergh, A. Bergmann, E. Bernitsas, A. Berthele, V. Bhan, F. Bischof, R.J. Bjork, G. Blevins, M. Boehringer, T. Boerner, R. Bonek, J.D. Bowen, A. Bowling, A.N. Boyko, C. Boz, V. Bracknies, S. Braune, V. Brescia Morra, B. Brochet, W. Brola, P.K. Brownstone, M. Brozman, D. Brunet, I. Buraga, M. Burnett, M. Buttmann, H. Butzkueven, J. Cahill, J.C. Calkwood, W. Camu, M. Cascione, G. Castelnovo, D. Centonze, J. Cerqueira, A. Chan, A. Cimprichova, S. Cohan, G. Comi, J. Conway, J.A. Cooper, J. Corboy, J. Correale, B. Costell, D.A. Cottrell, P.K. Coyle, M. Craner, L. Cui, L. Cunha, A. Czlonkowska, A.M. da Silva, J. de Sa, J. de Seze, M. Debouverie, J. Debruyne, D. Decoo, G. Defer, T. Derfuss, N.H. Deri, B. Dihenia, P. Dioszeghy, V. Donath, B. Dubois, M. Duddy, P. Duquette, G. Edan, H. Efendi, S. Elias, P.J. Emrich, B.C. Estruch, E.P. Evdoshenko, J. Faiss, A.S. Fedyanin, W. Feneberg, J. Fermont, O.F. Fernandez, F.C. Ferrer, K. Fink, H. Ford, C. Ford, A. Francia, M. Freedman, B. Frishberg, S. Galgani, G.P. Garmany, K. Gehring, J. Gitt, C. Gobbi, L.P. Goldstick, R.A. Gonzalez, F. Grandmaison, N. Grigoriadis, O. Grigorova, L.M.E. Grimaldi, J. Gross, K. Gross-Paju, M. Gudesblatt, D. Guillaume, J. Haas, V. Hancinova, A. Hancu, O. Hardiman, A. Harmjanz, F.R. Heidenreich, G.J.D. Hengstman, J. Herbert, M. Herring, S. Hodgkinson, O.M. Hoffmann, W.E. Hofmann, W.D. Honeycutt, L.H. Hua, D. Huang, Y. Huang, D. Huang, R. Hupperts, P. Imre, A.K. Jacobs, G. Jakab, E. Jasinska, K. Kaida, J. Kalnina, A. Kaprelyan, G. Karelis, D.

Karussis, A. Katz, F.A. Khabirov, B. Khatri, T. Kimura, I. Kister, R. Kizlaitiene, E. Klimova, J. Koehler, A. Komatineni, A. Kornhuber, K. Kovacs, A. Koves, W. Kozubski, G. Krastev, L.B. Krupp, E. Kurca, C. Lassek, G. Laureys, L. Lee, E. Lensch, F. Leutmezer, H. Li, R.A. Linker, M. Linnebank, P. Liskova, C. Llanera, J. Lu, A. Lutterotti, J. Lycke, R. Macdonell, M. Maciejowski, M. Maeurer, R.V. Magzhanov, E.-M. Maida, L. Malciene, Y. Mao-Draayer, G.A. Marfia, C. Markowitz, V. Mastorodimos, K. Matyas, J. Meca-Lallana, J.A.G. Merino, I.G. Mihetiu, I. Milanov, A.E. Miller, A. Millers, M. Mirabella, M. Mizuno, X. Montalban, L. Montoya, M. Mori, S. Mueller, J. Nakahara, Y. Nakatsuji, S. Newsome, R. Nicholas, A.S. Nielsen, E. Nikfekr, U. Nocentini, C. Nohara, K. Nomura, M.M. Odinak, T. Olsson, B.W. van Oosten, C. Oreja-Guevara, P. Oschmann, J. Overell, A. Pachner, G. Panczel, M. Pandolfo, C. Papeix, L. Patrucco, J. Pelletier, R. Piedrabuena, M. Pless, U. Polzer, K. Pozsegovits, D. Rastenyte, S. Rauer, G. Reifschneider, R. Rey, S.A. Rizvi, D. Robertson, J.M. Rodriguez, D. Rog, H. Roshanisefat, V. Rowe, C. Rozsa, S. Rubin, S. Rusek, F. Saccà, T. Saida, A.V. Salgado, V.E.F. Sanchez, K. Sanders, M. Satori, D.V. Sazonov, E.A. Scarpini, E. Schlegel, M. Schluep, S. Schmidt, E. Scholz, H.M. Schrijver, M. Schwab, R. Schwartz, J. Scott, K. Selmaj, S. Shafer, B. Sharrack, I.A. Shchukin, Y. Shimizu, P. Shotekov, A. Siever, K.-O. Sigel, S. Silliman, M. Simo, M. Simu, V. Sinay, A.E. Siquier, A. Siva, O. Skoda, A. Solomon, M. Stangel, D. Stefoski, B. Steingo, I.D. Stolyarov, P. Stourac, K. Strassburger-Krogias, E. Strauss, O. Stuve, I. Tarnev, A. Tavernarakis, C.R. Tello, M. Terzi, V. Ticha, M. Ticmeanu, K. Tiel-Wilck, T. Toomsoo, N. Tubridy, M.J. Tullman, H. Tumani, P. Turcani, B. Turner, A. Uccelli, F.J.O. Urtaza, M. Vachova, A. Valikovics, S. Walter, B. Van Wijmeersch, L. Vanopdenbosch, J.R. Weber, S. Weiss, R. Weissert, P. Vermersch, T. West, H. Wiendl, S. Wiertlewski, B. Wildemann, B. Willekens, L.H. Visser, G. Vorobeychik, X. Xu, T. Yamamura, Y.N. Yang, S.M. Yelamos, M. Yeung, A. Zacharias, M. Zelkowitz, U. Zettl, M. Zhang, H. Zhou, U. Zieman, and T. Ziemssen. 2018. Siponimod versus placebo in secondary progressive multiple sclerosis (EXPAND): a double-blind, randomised, phase 3 study. *The Lancet* 391:1263-1273.

Kaskow, B.J., and C. Baecher-Allan. 2018. Effector T Cells in Multiple Sclerosis. *Cold Spring Harbor Perspectives in Medicine* 8:

Klotz, L., M. Eschborn, M. Lindner, M. Liebmann, M. Herold, C. Janoschka, B. Torres Garrido, A. Schulte-Mecklenbeck, C.C. Gross, J. Breuer, P. Hundehege, V. Posevitz, B. Pignolet, G. Nebel, S. Glander, N. Freise, J. Austermann, T. Wirth, G.R. Campbell, T. Schneider-Hohendorf, M. Eveslage, D. Brassat, N. Schwab, K. Loser, J. Roth, K.B. Busch, M. Stoll, D.J. Mahad, S.G. Meuth, T. Turner, A. Bar-Or, and H. Wiendl. 2019. Teriflunomide treatment for multiple sclerosis modulates T cell mitochondrial respiration with affinity-dependent effects. *Science translational medicine* 11:eaao5563.

Kober, T., C. Granziera, D. Ribes, P. Browaeys, M. Schluep, R. Meuli, R. Frackowiak, R. Gruetter, and G. Krueger. 2012. MP2RAGE Multiple Sclerosis Magnetic Resonance Imaging at 3 T. *Investigative Radiology* 47:346-352.

Krieger, S.C., K. Cook, S. De Nino, and M. Fletcher. 2016. The topographical model of multiple sclerosis: A dynamic visualization of disease course. *Neurology(R) neuroimmunology & neuroinflammation* 3:e279.

Ku, M.-C., I. Edes, I. Bendix, A. Pohlmann, H. Waiczies, T. Prozorovski, M. Günther, C. Martin, G. Pagès, S.A. Wolf, H. Kettenmann, W. Uckert, T. Niendorf, and S. Waiczies. 2016. ERK1 as a Therapeutic Target for Dendritic Cell Vaccination against High-Grade Gliomas. *Mol Cancer Ther* 15:1975-1987.

Kuchling, J., C. Ramien, I. Bozin, J. Dorr, L. Harms, B. Rosche, T. Niendorf, F. Paul, T. Sinnecker, and J. Wuerfel. 2014. Identical lesion morphology in primary

progressive and relapsing-remitting MS--an ultrahigh field MRI study. *Mult Scler* 20:1866-1871.

Kuchling, J., and F. Paul. 2020. Visualizing the Central Nervous System: Imaging Tools for Multiple Sclerosis and Neuromyelitis Optica Spectrum Disorders. *Frontiers in neurology* 11:450-450.

Ladd, M.E. 2018. The quest for higher sensitivity in MRI through higher magnetic fields. *Zeitschrift für Medizinische Physik* 28:1-3.

Langen, K.-J., N. Galldiks, E. Hattingen, and N.J. Shah. 2017. Advances in neuro-oncology imaging. *Nature Reviews Neurology* 13:279-289.

Lassmann, H., J. van Horssen, and D. Mahad. 2012. Progressive multiple sclerosis: pathology and pathogenesis. *Nature Reviews Neurology* 8:647-656.

Lassmann, H. 2018. Multiple Sclerosis Pathology. *Cold Spring Harbor Perspectives in Medicine* 8:

Lassmann, H. 2019. Pathogenic Mechanisms Associated With Different Clinical Courses of Multiple Sclerosis. *Frontiers in Immunology* 9:

Lee, D.S.W., O.L. Rojas, and J.L. Gommerman. 2021. B cell depletion therapies in autoimmune disease: advances and mechanistic insights. *Nature Reviews Drug Discovery* 20:179-199.

Lehéricy, S., M. Marjanska, L. Mesrob, M. Sarazin, and S. Kinkingnehun. 2007. Magnetic resonance imaging of Alzheimer's disease. *Eur Radiol* 17:347-362.

Lepore, S., H. Waiczies, J. Hentschel, Y. Ji, J. Skodowski, A. Pohlmann, J.M. Millward, F. Paul, J. Wuerfel, T. Niendorf, and S. Waiczies. 2013. Enlargement of cerebral ventricles as an early indicator of encephalomyelitis. *PloS one* 8:e72841.

Leuenberger, T., C.F. Pfueller, F. Luessi, I. Bendix, M. Paterka, T. Prozorovski, D. Treue, S. Luenstedt, J. Herz, V. Siffrin, C. Infante-Duarte, F. Zipp, and S. Waiczies. 2014. Modulation of Dendritic Cell Immunobiology via Inhibition of 3-Hydroxy-3-Methylglutaryl-CoA (HMG-CoA) Reductase. *PloS one* 9:e100871.

Liang, S., T. Dresselaers, K. Louchami, C. Zhu, Y. Liu, and U. Himmelreich. 2017. Comparison of different compressed sensing algorithms for low SNR (19) F MRI applications-Imaging of transplanted pancreatic islets and cells labeled with perfluorocarbons. *NMR Biomed* 30:

Liu, X., Z.-X. Jiang, B.Y. Yu, and E.-K. Jeong. 2018. Study of kinetics of 19F-MRI using a fluorinated imaging agent (19FIT) on a 3T clinical MRI system. *Magnetic Resonance Materials in Physics, Biology and Medicine*

Lukas, C., A. Minneboo, V. de Groot, B. Moraal, D.L. Knol, C.H. Polman, F. Barkhof, and H. Vrenken. 2010. Early central atrophy rate predicts 5 year clinical outcome in multiple sclerosis. *Journal of neurology, neurosurgery, and psychiatry* 81:1351-1356.

Lunemann, J.D., S. Waiczies, S. Ehrlich, U. Wendling, B. Seeger, T. Kamradt, and F. Zipp. 2002. Death ligand TRAIL induces no apoptosis but inhibits activation of human (auto)antigen-specific T cells. *J.Immunol.* 168:4881-4888.

Ma, D., V. Gulani, N. Seiberlich, K. Liu, J.L. Sunshine, J.L. Duerk, and M.A. Griswold. 2013. Magnetic resonance fingerprinting. *Nature* 495:187-192.

Maggi, P., S.M.C. Macri, M.I. Gaitán, E. Leibovitch, J.E. Wholer, H.L. Knight, M. Ellis, T. Wu, A.C. Silva, L. Massacesi, S. Jacobson, S. Westmoreland, and D.S. Reich. 2014. The formation of inflammatory demyelinated lesions in cerebral white matter. *Annals of neurology* 76:594-608.

Magliozzi, R., O. Howell, A. Vora, B. Serafini, R. Nicholas, M. Puopolo, R. Reynolds, and F. Aloisi. 2007. Meningeal B-cell follicles in secondary progressive multiple sclerosis associate with early onset of disease and severe cortical pathology. *Brain* 130:1089-1104.

Magliozzi, R., B. Serafini, B. Rosicarelli, G. Chiappetta, C. Veroni, R. Reynolds, and F. Aloisi. 2013. B-Cell Enrichment and Epstein-Barr Virus Infection in Inflammatory Cortical Lesions in Secondary Progressive Multiple Sclerosis. *Journal of Neuropathology & Experimental Neurology* 72:29-41.

Mahad, D.H., B.D. Trapp, and H. Lassmann. 2015. Pathological mechanisms in progressive multiple sclerosis. *The Lancet Neurology* 14:183-193.

Maranzano, J., M. Dadar, D. Rudko, D. De Nigris, C. Elliott, J. Gati, S. Morrow, R. Menon, D. Collins, and D. Arnold. 2019. Comparison of multiple sclerosis cortical lesion types detected by multicontrast 3T and 7T MRI. *American Journal of Neuroradiology* 40:1162-1169.

Mastropietro, A., E. De Bernardi, G.L. Breschi, I. Zucca, M. Cametti, C.D. Soffientini, M. de Curtis, G. Terraneo, P. Metrangolo, R. Spreafico, G. Resnati, and G. Baselli. 2014. Optimization of rapid acquisition with relaxation enhancement (RARE) pulse sequence parameters for (1)(9)F-MRI studies. *J Magn Reson Imaging* 40:162-170.

McDonald, R.J., J.S. McDonald, D.F. Kallmes, M.E. Jentoft, D.L. Murray, K.R. Thielen, E.E. Williamson, and L.J. Eckel. 2015. Intracranial Gadolinium Deposition after Contrast-enhanced MR Imaging. *Radiology* 275:772-782.

McDonald, R.J., J.S. McDonald, D.F. Kallmes, M.E. Jentoft, M.A. Paolini, D.L. Murray, E.E. Williamson, and L.J. Eckel. 2017. Gadolinium Deposition in Human Brain Tissues after Contrast-enhanced MR Imaging in Adult Patients without Intracranial Abnormalities. *Radiology* 285:546-554.

Merrill, J., S. Hanak, S.-F. Pu, J. Liang, C. Dang, D. Iglesias-Bregna, B. Harvey, B. Zhu, and K. McMonagle-Strucko. 2009. Teriflunomide reduces behavioral, electrophysiological, and histopathological deficits in the Dark Agouti rat model of experimental autoimmune encephalomyelitis. *J Neurol* 256:89-103.

Merrill, J.E. 2009. In vitro and in vivo pharmacological models to assess demyelination and remyelination. *Neuropsychopharmacology* 34:55-73.

Metere, R., T. Kober, H.E. Möller, and A. Schäfer. 2017. Simultaneous Quantitative MRI Mapping of T1, T2* and Magnetic Susceptibility with Multi-Echo MP2RAGE. *PloS one* 12:e0169265.

Miller, D.H., D. Soon, K.T. Fernando, D.G. MacManus, G.J. Barker, T.A. Yousry, E. Fisher, P.W. O'Connor, J.T. Phillips, C.H. Polman, L. Kappos, M. Hutchinson, E. Havrdova, F.D. Lublin, G. Giovannoni, A. Wajgt, R. Rudick, F. Lynn, M.A. Panzara, and A.W. Sandrock. 2007. MRI outcomes in a placebo-controlled trial of natalizumab in relapsing MS. *Neurology* 68:1390-1401.

Millward, J.M., P. Ramos Delgado, A. Smorodchenko, L. Boehmert, J. Periquito, H.M. Reimann, C. Prinz, A. Els, M. Scheel, J. Bellmann-Strobl, H. Waiczies, J. Wuerfel, C. Infante-Duarte, C. Chien, J. Kuchling, A. Pohlmann, F. Zipp, F. Paul, T. Niendorf, and S. Waiczies. 2020. Transient enlargement of brain ventricles during relapsing-remitting multiple sclerosis and experimental autoimmune encephalomyelitis. *JCI Insight* 5:10.1172/jci.insight.140040.

Mishra, M.K., and V.W. Yong. 2016. Myeloid cells — targets of medication in multiple sclerosis. *Nature Reviews Neurology* 12:539-551.

Mönch, S., N. Sollmann, A. Hock, C. Zimmer, J.S. Kirschke, and D.M. Hedderich. 2020. Magnetic Resonance Imaging of the Brain Using Compressed Sensing – Quality Assessment in Daily Clinical Routine. *Clinical Neuroradiology* 30:279-286.

Mullard, A. 2015. Roche hits multiple sclerosis landmarks. *Nature Reviews Drug Discovery* 14:739-739.

Muller, K., C. Faeh, and F. Diederich. 2007. Fluorine in pharmaceuticals: looking beyond intuition. *Science* 317:1881-1886.

Muller, K., J. Kuchling, J. Dorr, L. Harms, K. Ruprecht, T. Niendorf, J. Wuerfel, F. Paul, and T. Sinnecker. 2014. Detailing intra-lesional venous lumen shrinking in multiple sclerosis investigated by sFLAIR MRI at 7-T. *J Neurol*

Nash, R.A., G.J. Hutton, M.K. Racke, U. Popat, S.M. Devine, L.M. Griffith, P.A. Muraro, H. Openshaw, P.H. Sayre, O. Stüve, D.L. Arnold, M.E. Spychala, K.C. McConville, K.M. Harris, D. Phippard, G.E. Georges, A. Wundes, G.H. Kraft, and J.D. Bowen. 2015. High-Dose Immunosuppressive Therapy and Autologous Hematopoietic Cell Transplantation for Relapsing-Remitting Multiple Sclerosis (HALT-MS): A 3-Year Interim ReportHematopoietic Cell Transplantation for MSHematopoietic Cell Transplantation for MS. *JAMA Neurol* 72:159-169.

Neema, M., J. Stankiewicz, A. Arora, V.S. Dandamudi, C.E. Batt, Z.D. Guss, A. Al-Sabbagh, and R. Bakshi. 2007. T1-and T2-based MRI measures of diffuse gray matter and white matter damage in patients with multiple sclerosis. *Journal of Neuroimaging* 17:16S-21S.

Negron, A., O. Stüve, and T.G. Forsthuber. 2020. Ectopic Lymphoid Follicles in Multiple Sclerosis: Centers for Disease Control? *Frontiers in neurology* 11:607766-607766.

Niendorf, T., A. Pohlmann, H.M. Reimann, H. Waiczies, E. Peper, T. Huelnhagen, E. Seeliger, A. Schreiber, R. Kettritz, K. Strobel, M.C. Ku, and S. Waiczies. 2015. Advancing Cardiovascular, Neurovascular, and Renal Magnetic Resonance Imaging in Small Rodents Using Cryogenic Radiofrequency Coil Technology. *Front Pharmacol* 6:255.

Niendorf, T., M. Barth, F. Kober, and S. Trattnig. 2016a. From ultrahigh to extreme field magnetic resonance: where physics, biology and medicine meet. *Magnetic Resonance Materials in Physics, Biology and Medicine* 29:309-311.

Niendorf, T., M. Barth, F. Kober, and S. Trattnig. 2016b. From ultrahigh to extreme field magnetic resonance: where physics, biology and medicine meet. *MAGMA* 29:309-311.

Niendorf, T., Y. Ji, and S. Waiczies. 2016c. Fluorinated Natural Compounds and Synthetic Drugs. In Fluorine Magnetic Resonance Imaging. Pan Stanford Publishing Singapore 311-342.

Niendorf, T., K. Paul, C. Oezerdem, A. Graessl, S. Klix, T. Huelnhagen, F. Hezel, J. Rieger, H. Waiczies, J. Frahm, A.M. Nagel, E. Oberacker, and L. Winter. 2016d. W(h)ither human cardiac and body magnetic resonance at ultrahigh fields? technical advances, practical considerations, applications, and clinical opportunities. *NMR Biomed* 29:1173-1197.

Nöth, U., S.P. Morrissey, R. Deichmann, S. Jung, H. Adolf, A. Haase, and J. Lutz. 1997. Perfluoro-15-Crown-5-Ether Labelled Macrophages in Adoptive Transfer Experimental Allergic Encephalomyelitis. *Artificial Cells, Blood Substitutes, and Biotechnology* 25:243-254.

Nourshargh, S., and R. Alon. 2014. Leukocyte Migration into Inflamed Tissues. *Immunity* 41:694-707.

Öz, G., J.R. Alger, P.B. Barker, R. Bartha, A. Bizzi, C. Boesch, P.J. Bolan, K.M. Brindle, C. Cudalbu, A. Dinçer, U. Dydak, U.E. Emir, J. Frahm, R.G. González, S. Gruber, R. Gruetter, R.K. Gupta, A. Heerschap, A. Henning, H.P. Hetherington, F.A. Howe, P.S. Hüppi, R.E. Hurd, K. Kantarci, D.W.J. Klomp, R. Kreis, M.J. Kruiskamp, M.O. Leach, A.P. Lin, P.R. Luijten, M. Marjańska, A.A. Maudsley, D.J. Meyerhoff, C.E. Mountford, S.J. Nelson, M.N. Pamir, J.W. Pan, A.C. Peet, H. Poptani, S. Posse, P.J.W. Pouwels, E.-M. Ratai, B.D. Ross, T.W.J. Scheenen, C. Schuster, I.C.P. Smith, B.J. Soher, I. Tkáč, D.B. Vigneron, R.A. Kauppinen, and F.t.M.C. Group. 2014. Clinical Proton MR Spectroscopy in Central Nervous System Disorders. *Radiology* 270:658-679.

Padormo, F., A. Beqiri, J.V. Hajnal, and S.J. Malik. 2016. Parallel transmission for ultrahigh-field imaging. *NMR in biomedicine* 29:1145-1161.

Palucka, K., H. Ueno, J. Fay, and J. Banchereau. 2011. Dendritic cells and immunity against cancer. *J Intern Med* 269:64-73.

Palucka, K., and J. Banchereau. 2012. Cancer immunotherapy via dendritic cells. *Nat.Rev.Cancer* 12:265-277.

Paul, F., S. Waiczies, J. Wuerfel, J. Bellmann-Strobl, J. Dorr, H. Waiczies, M. Haertle, K.D. Wernecke, H.D. Volk, O. Aktas, and F. Zipp. 2008. Oral high-dose atorvastatin treatment in relapsing-remitting multiple sclerosis. *PloS one* 3:e1928-e1928.

Pereira, D.J., P. Abreu, A.M. Reis, D. Seixas, I. Carreiro, I. Cravo, J. Graça, P.M. Freitas, O. Brito, and S. Silva. 2020. Consensus Recommendations of the Multiple Sclerosis Study Group and the Portuguese Neuroradiological Society for the Use of Magnetic Resonance Imaging in Multiple Sclerosis in Clinical Practice: Part 2. *Acta Médica Portuguesa* 33:66-75.

Pohmann, R., O. Speck, and K. Scheffler. 2016. Signal-to-noise ratio and MR tissue parameters in human brain imaging at 3, 7, and 9.4 tesla using current receive coil arrays. *Magnetic Resonance in Medicine* 75:801-809.

Polman, C.H., P.W. O'Connor, E. Havrdova, M. Hutchinson, L. Kappos, D.H. Miller, J.T. Phillips, F.D. Lublin, G. Giovannoni, A. Wajgt, M. Toal, F. Lynn, M.A. Panzara, and A.W. Sandrock. 2006. A randomized, placebo-controlled trial of natalizumab for relapsing multiple sclerosis. *N Engl J Med* 354:899-910.

Prabhakara, K.S., D.J. Kota, G.H. Jones, A.K. Srivastava, C.S. Cox, and S.D. Olson. 2018. Teriflunomide Modulates Vascular Permeability and Microglial Activation after Experimental Traumatic Brain Injury. *Molecular Therapy* 26:2152-2162.

Prinz, C., P.R. Delgado, T.W. Eigentler, L. Starke, T. Niendorf, and S. Waiczies. 2018. Toward (19)F magnetic resonance thermometry: spin-lattice and spin-spin-relaxation times and temperature dependence of fluorinated drugs at 9.4 T. *Magma (New York, N.Y.)* 10.1007/s10334-10018-10722-10338.

Prinz, C., V. Martos Riaño, T.-F. Ramspoth, L. Starke, M. Neuenschwander, J.-P. von Kries, A. Pohlmann, M. Nazaré, T. Niendorf, and S. Waiczies. 2019. Enhancing Fluorine-19 Magnetic Resonance Drug Imaging: Chemical Variations in the Fluorine Side-Groups of the Immunomodulatory Drug Teriflunomide. In Proc Intl Soc Mag Reson Med. https://onlinelibrary.ectrims-congress.eu/ectrims/2018/ectrims-2018/229099/christian.prinz.fluorine-229019.magnetic.resonance.imaging.as.a.method.for.the.html?f=menu%229093D229096%229092Abrowseby%229093D229098%229092Asortby%229093D229092%229092Amedia%229093D229093%229092Ace_id%229093D221428%229092Aot_id%229093D220027

Prinz, C., L. Starke, J.M. Millward, A. Fillmer, P.R. Delgado, H. Waiczies, A. Pohlmann, M. Rothe, M. Nazare, F. Paul, T. Niendorf, and S. Waiczies. 2021. In vivo detection of teriflunomide-derived fluorine signal during neuroinflammation using fluorine MR spectroscopy. *Theranostics* 11:2490-2504.

Radbruch, A., L.D. Weberling, P.J. Kieslich, O. Eidel, S. Burth, P. Kickingereder, S. Heiland, W. Wick, H.-P. Schlemmer, and M. Bendszus. 2015. Gadolinium Retention in the Dentate Nucleus and Globus Pallidus Is Dependent on the Class of Contrast Agent. *Radiology* 275:783-791.

Radue, E.W., T. Sprenger, L. Gaetano, N. Mueller-Lenke, S. Cavalier, K. Thangavelu, M.A. Panzara, J.E. Donaldson, F.M. Woodward, J. Wuerfel, J.S. Wolinsky, and L. Kappos. 2017. Teriflunomide slows BVL in relapsing MS: A reanalysis of the TEMSO MRI data set using SIENA. *Neurology(R) neuroimmunology & neuroinflammation* 4:e390.

Reich, D.S., C.F. Lucchinetti, and P.A. Calabresi. 2018. Multiple Sclerosis. *New England Journal of Medicine* 378:169-180.

Reid, D.G., and P.S. Murphy. 2008. Fluorine magnetic resonance in vivo: a powerful tool in the study of drug distribution and metabolism. *Drug discovery today* 13:473-480.

Ringheim, G.E., L. Lee, L. Laws-Ricker, T. Delohery, L. Liu, D. Zhang, N. Colletti, T.J. Soos, K. Schroeder, B. Fanelli, N. Tian, C.W. Arendt, D. Iglesias-Bregna, M. Petty, Z. Ji, G. Qian, R. Gaur, D. Weinstock, J. Cavallo, J. Telsinskas, and K. McMonagle-Strucko. 2013. Teriflunomide Attenuates Immunopathological Changes in the Dark Agouti Rat Model of Experimental Autoimmune Encephalomyelitis. *Front Neurol* 4:169.

Rommer, P.S., R. Milo, M.H. Han, S. Satyanarayan, J. Sellner, L. Hauer, Z. Illes, C. Warnke, S. Laurent, M.S. Weber, Y. Zhang, and O. Stuve. 2019. Immunological Aspects of Approved MS Therapeutics. *Frontiers in Immunology* 10:

Ropele, S., I.D. Kilsdonk, M.P. Wattjes, C. Langkammer, W.L. De Graaf, J.L. Frederiksen, H.B. Larsson, M. Yiannakas, C.A. Wheeler-Kingshott, and C. Enzinger. 2014. Determinants of iron accumulation in deep grey matter of multiple sclerosis patients. *Multiple Sclerosis Journal* 20:1692-1698.

Rovira, A., and N. de Stefano. 2016. MRI monitoring of spinal cord changes in patients with multiple sclerosis. *Current opinion in neurology* 29:445-452.

Rovira, À., M.P. Wattjes, M. Tintoré, C. Tur, T.A. Yousry, M.P. Sormani, N. De Stefano, M. Filippi, C. Auger, M.A. Rocca, F. Barkhof, F. Fazekas, L. Kappos, C. Polman, D. Miller, X. Montalban, and M.s.g. on behalf of the. 2015. MAGNIMS consensus guidelines on the use of MRI in multiple sclerosis—clinical implementation in the diagnostic process. *Nature Reviews Neurology* 11:471.

Rückemann, K., L.D. Fairbanks, E.A. Carrey, C.M. Hawrylowicz, D.F. Richards, B. Kirschbaum, and H.A. Simmonds. 1998. Leflunomide inhibits pyrimidine de novo synthesis in mitogen-stimulated T-lymphocytes from healthy humans. *J Biol Chem* 273:21682-21691.

Sabatino, J.J., A.-K. Pröbstel, and S.S. Zamvil. 2019. B cells in autoimmune and neurodegenerative central nervous system diseases. *Nature Reviews Neuroscience* 20:728-745.

Sanchez-Heredia, J.D., E.S. Szocska Hansen, C. Laustsen, V. Zhurbenko, and J.H. Ardenkjær-Larsen. 2017. Low-Noise Active Decoupling Circuit and its Application to (13)C Cryogenic RF Coils at 3 T. *Tomography* 3:60-66.

Sati, P., J. Oh, R.T. Constable, N. Evangelou, C.R.G. Guttmann, R.G. Henry, E.C. Klawiter, C. Mainero, L. Massacesi, H. McFarland, F. Nelson, D. Ontaneda, A. Rauscher,

W.D. Rooney, A.P.R. Samaraweera, R.T. Shinohara, R.A. Sobel, A.J. Solomon, C.A. Treaba, J. Wuerfel, R. Zivadinov, N.L. Sicotte, D. Pelletier, D.S. Reich, and N.C. on behalf of the. 2016. The central vein sign and its clinical evaluation for the diagnosis of multiple sclerosis: a consensus statement from the North American Imaging in Multiple Sclerosis Cooperative. *Nature Reviews Neurology* 12:714-722.

Sati, P. 2018. Diagnosis of multiple sclerosis through the lens of ultra-high-field MRI. *J Magn Reson* 291:101-109.

Schepkin, V.D., W.W. Brey, P.L. Gor'kov, and S.C. Grant. 2010. Initial in vivo Rodent Sodium and Proton MR Imaging at 21.1 T. *Magnetic resonance imaging* 28:400-407.

Schlemm, L., C. Chien, J. Bellmann-Strobl, J. Dorr, J. Wuerfel, A.U. Brandt, F. Paul, and M. Scheel. 2017. Gadopentetate but not gadobutrol accumulates in the dentate nucleus of multiple sclerosis patients. *Mult Scler* 23:963-972.

Schmierer, K., T. Campion, A. Sinclair, W. van Hecke, P.M. Matthews, and M.P. Wattjes. 2019. Towards a standard MRI protocol for multiple sclerosis across the UK. *The British journal of radiology* 92:20180926.

Shapiro, E.M., S. Skrtic, K. Sharer, J.M. Hill, C.E. Dunbar, and A.P. Koretsky. 2004. MRI detection of single particles for cellular imaging. *Proc.Natl.Acad.Sci.U.S.A* 101:10901-10906.

Shepherd, T.M., I.I. Kirov, E. Charlson, M. Bruno, J. Babb, D.K. Sodickson, and N. Ben-Eliezer. 2017. New rapid, accurate T(2) quantification detects pathology in normal-appearing brain regions of relapsing-remitting MS patients. *NeuroImage. Clinical* 14:363-370.

Sinnecker, T., J. Dorr, C.F. Pfueller, L. Harms, K. Ruprecht, S. Jarius, W. Bruck, T. Niendorf, J. Wuerfel, and F. Paul. 2012a. Distinct lesion morphology at 7-T MRI differentiates neuromyelitis optica from multiple sclerosis. *Neurology* 79:708-714.

Sinnecker, T., P. Mittelstaedt, J. Dörr, C.F. Pfueller, L. Harms, T. Niendorf, F. Paul, and J. Wuerfel. 2012b. Multiple sclerosis lesions and irreversible brain tissue damage: a comparative ultrahigh-field strength magnetic resonance imaging study. *Arch Neurol* 69:739-745.

Sinnecker, T., I. Bozin, J. Dorr, C.F. Pfueller, L. Harms, T. Niendorf, A.U. Brandt, F. Paul, and J. Wuerfel. 2013. Periventricular venous density in multiple sclerosis is inversely associated with T2 lesion count: a 7 Tesla MRI study. *Mult Scler* 19:316-325.

Sinnecker, T., J. Kuchling, P. Dusek, J. Dörr, T. Niendorf, F. Paul, and J. Wuerfel. 2015. Ultrahigh field MRI in clinical neuroimmunology: a potential contribution to improved diagnostics and personalised disease management. *The EPMA journal* 6:16.

Sinnecker, T., M.A. Clarke, D. Meier, C. Enzinger, M. Calabrese, N. De Stefano, A. Pitiot, A. Giorgio, M.M. Schoonheim, F. Paul, M.A. Pawlak, R. Schmidt, L. Kappos, X. Montalban, À. Rovira, N. Evangelou, and J. Wuerfel. 2019. Evaluation of the Central Vein Sign as a Diagnostic Imaging Biomarker in Multiple Sclerosis. *JAMA Neurol* 76:1446-1456.

Solomon, A.J., R. Watts, B.E. Dewey, and D.S. Reich. 2017. MRI evaluation of thalamic volume differentiates MS from common mimics. *Neurology(R) neuroimmunology & neuroinflammation* 4:e387.

Sormani, M.P., D.L. Arnold, and N. De Stefano. 2014. Treatment effect on brain atrophy correlates with treatment effect on disability in multiple sclerosis. *Annals of neurology* 75:43-49.

Starke, L., A. Pohlmann, C. Prinz, T. Niendorf, and S. Waiczies. 2019. Performance of compressed sensing for fluorine-19 magnetic resonance imaging at low signal-to-noise ratio conditions. *Magn Reson Med* 1-17.

Stephenson, J., E. Nutma, P. van der Valk, and S. Amor. 2018. Inflammation in CNS neurodegenerative diseases. *Immunology* 154:204-219.

Tallantyre, E.C., P.S. Morgan, J.E. Dixon, A. Al-Radaideh, M.J. Brookes, N. Evangelou, and P.G. Morris. 2009a. A comparison of 3T and 7T in the detection of small parenchymal veins within MS lesions. *Investigative Radiology* 44:491-494.

Tallantyre, E.C., P.S. Morgan, J.E. Dixon, A. Al Radaideh, M.J. Brookes, N. Evangelou, and P.G. Morris. 2009b. A comparison of 3T and 7T in the detection of small parenchymal veins within MS lesions. *Invest Radiol* 44:491-494.

Tan, I.L., R.A. van Schijndel, P.J. Pouwels, M.A. van Walderveen, J.R. Reichenbach, R.A. Manoliu, and F. Barkhof. 2000. MR venography of multiple sclerosis. *AJNR. American journal of neuroradiology* 21:1039-1042.

Thompson, A.J., B.L. Banwell, F. Barkhof, W.M. Carroll, T. Coetzee, G. Comi, J. Correale, F. Fazekas, M. Filippi, and M.S. Freedman. 2018a. Diagnosis of multiple sclerosis: 2017 revisions of the McDonald criteria. *The Lancet Neurology* 17:162-173.

Thompson, A.J., B.L. Banwell, F. Barkhof, W.M. Carroll, T. Coetzee, G. Comi, J. Correale, F. Fazekas, M. Filippi, M.S. Freedman, K. Fujihara, S.L. Galetta, H.P. Hartung, L. Kappos, F.D. Lublin, R.A. Marrie, A.E. Miller, D.H. Miller, X. Montalban, E.M. Mowry, P.S. Sorensen, M. Tintoré, A.L. Traboulsee, M. Trojano, B.M.J. Uitdehaag, S. Vukusic, E. Waubant, B.G. Weinshenker, S.C. Reingold, and J.A. Cohen. 2018b. Diagnosis of multiple sclerosis: 2017 revisions of the McDonald criteria. *The Lancet Neurology* 17:162-173.

Thompson, A.J., S.E. Baranzini, J. Geurts, B. Hemmer, and O. Ciccarelli. 2018c. Multiple sclerosis. *The Lancet* 391:1622-1636.

Tintore, M., A. Vidal-Jordana, and J. Sastre-Garriga. 2018. Treatment of multiple sclerosis — success from bench to bedside. *Nature Reviews Neurology*

Traboulsee, A., J.H. Simon, L. Stone, E. Fisher, D.E. Jones, A. Malhotra, S.D. Newsome, J. Oh, D.S. Reich, N. Richert, K. Rammohan, O. Khan, E.W. Radue, C. Ford, J. Halper, and D. Li. 2016. Revised Recommendations of the Consortium of MS Centers Task Force for a Standardized MRI Protocol and Clinical Guidelines for the Diagnosis and Follow-Up of Multiple Sclerosis. *AJNR. American journal of neuroradiology* 37:394-401.

Trapp, B.D., J. Peterson, R.M. Ransohoff, R. Rudick, S. Mork, and L. Bo. 1998. Axonal transection in the lesions of multiple sclerosis. *N Engl J Med* 338:278-285.

Trefler, A., N. Sadeghi, A.G. Thomas, C. Pierpaoli, C.I. Baker, and C. Thomas. 2016. Impact of time-of-day on brain morphometric measures derived from T1-weighted magnetic resonance imaging. *NeuroImage* 133:41-52.

Turner, B., X. Lin, G. Calmon, N. Roberts, and L.D. Blumhardt. 2003. Cerebral atrophy and disability in relapsing-remitting and secondary progressive multiple sclerosis over four years. *Mult Scler* 9:21-27.

Uludağ, K., and P. Blinder. 2018. Linking brain vascular physiology to hemodynamic response in ultra-high field MRI. *NeuroImage* 168:279-295.

Vaughan, J.T., M. Garwood, C.M. Collins, W. Liu, L. DelaBarre, G. Adriany, P. Andersen, H. Merkle, R. Goebel, M.B. Smith, and K. Ugurbil. 2001. 7T vs. 4T: RF power, homogeneity, and signal-to-noise comparison in head images. *Magnetic Resonance in Medicine* 46:24-30.

Vellinga, M.M., R.D. Oude Engberink, A. Seewann, P.J.W. Pouwels, M.P. Wattjes, S.M.A. van der Pol, C. Pering, C.H. Polman, H.E. de Vries, J.J.G. Geurts, and F. Barkhof. 2008. Pluriformity of inflammation in multiple sclerosis shown by ultra-small iron oxide particle enhancement. *Brain* 131:800-807.

Vellinga, M.M., H. Vrenken, H.E. Hulst, C.H. Polman, B.M.J. Uitdehaag, P.J.W. Pouwels, F. Barkhof, and J.J.G. Geurts. 2009. Use of ultrasmall superparamagnetic particles of iron oxide (USPIO)-enhanced MRI to demonstrate diffuse inflammation in the normal-appearing white matter (NAWM) of multiple sclerosis (MS) patients: an exploratory study. *J Magn Reson Imaging* 29:774-779.

Waiczies, H., S. Lepore, N. Janitzek, U. Hagen, F. Seifert, B. Ittermann, B. Purfurst, A. Pezzutto, F. Paul, T. Niendorf, and S. Waiczies. 2011. Perfluorocarbon particle size influences magnetic resonance signal and immunological properties of dendritic cells. *PloS one* 6:e21981.

Waiczies, H., J.M. Millward, S. Lepore, C. Infante-Duarte, A. Pohlmann, T. Niendorf, and S. Waiczies. 2012. Identification of Cellular Infiltrates during Early Stages of Brain Inflammation with Magnetic Resonance Microscopy. *PloS one* 7:e32796.

Waiczies, H., M. Guenther, J. Skodowski, S. Lepore, A. Pohlmann, T. Niendorf, and S. Waiczies. 2013a. Monitoring dendritic cell migration using 19F / 1H magnetic resonance imaging. *J Vis Exp* e50251.

Waiczies, H., S. Lepore, S. Drechsler, F. Qadri, B. Purfurst, K. Sydow, M. Dathe, A. Kuhne, T. Lindel, W. Hoffmann, A. Pohlmann, T. Niendorf, and S. Waiczies. 2013b. Visualizing brain inflammation with a shingled-leg radio-frequency head probe for 19F/1H MRI. *Sci Rep* 3:1280.

Waiczies, S., A. Weber, J.D. Lunemann, O. Aktas, R. Zschenderlein, and F. Zipp. 2002. Elevated Bcl-X(L) levels correlate with T cell survival in multiple sclerosis. *J.Neuroimmunol.* 126:213-220.

Waiczies, S., T. Prozorovski, C. Infante-Duarte, A. Hahner, O. Aktas, O. Ullrich, and F. Zipp. 2005. Atorvastatin Induces T Cell Anergy via Phosphorylation of ERK1. *J.Immunol.* 174:5630-5635.

Waiczies, S., I. Bendix, T. Prozorovski, M. Ratner, I. Nazarenko, C.F. Pfueller, A.U. Brandt, J. Herz, S. Brocke, O. Ullrich, and F. Zipp. 2007. Geranylgeranylation but not GTP loading determines rho migratory function in T cells. *J.Immunol.* 179:6024-6032.

Waiczies, S., I. Bendix, and F. Zipp. 2008. Geranylgeranylation but not GTP-loading of Rho GTPases determines T cell function. *Sci Signal* 1:pt3.

Waiczies, S., S. Lepore, K. Sydow, S. Drechsler, M.C. Ku, C. Martin, D. Lorenz, I. Schutz, H.M. Reimann, B. Purfurst, M.A. Dieringer, H. Waiczies, M. Dathe, A. Pohlmann, and T. Niendorf. 2015. Anchoring dipalmitoyl phosphoethanolamine to nanoparticles boosts cellular uptake and fluorine-19 magnetic resonance signal. *Sci Rep* 5:8427.

Waiczies, S., J.M. Millward, L. Starke, P.R. Delgado, T. Huelnhagen, C. Prinz, D. Marek, D. Wecker, R. Wissmann, S.P. Koch, P. Boehm-Sturm, H. Waiczies, T. Niendorf, and A. Pohlmann. 2017a. Enhanced Fluorine-19 MRI Sensitivity using a Cryogenic Radiofrequency Probe: Technical Developments and Ex Vivo Demonstration in a Mouse Model of Neuroinflammation. *Sci Rep* 7:9808.

Waiczies, S., T. Niendorf, and G. Lombardi. 2017b. Labeling of cell therapies: How can we get it right? *Oncoimmunology* e1345403.

Waiczies, S., J.T. Rosenberg, A. Kuehne, L. Starke, P.R. Delgado, J.M. Millward, C. Prinz, J. Dos Santos Periquito, A. Pohlmann, H. Waiczies, and T. Niendorf. 2018. Fluorine-19 MRI at 21.1 T: enhanced spin-lattice relaxation of perfluoro-15-crown-

5-ether and sensitivity as demonstrated in ex vivo murine neuroinflammation. *Magma (New York, N.Y.)* 10.1007/s10334-10018-10710-z.

Waiczies, S., M. Srinivas, U. Flögel, P. Boehm-Sturm, and T. Niendorf. 2019. Special issue on fluorine-19 magnetic resonance: technical solutions, research promises and frontier applications. *Magma (New York, N.Y.)* 32:1-3.

Walsh, A.J., R.M. Lebel, A. Eissa, G. Blevins, I. Catz, J.-Q. Lu, L. Resch, E.S. Johnson, D.J. Emery, and K.G. Warren. 2013. Multiple sclerosis: validation of MR imaging for quantification and detection of iron. *Radiology* 267:531-542.

Walsh, A.J., G. Blevins, R.M. Lebel, P. Seres, D.J. Emery, and A.H. Wilman. 2014. Longitudinal MR imaging of iron in multiple sclerosis: an imaging marker of disease. *Radiology* 270:186-196.

Wang, C., H.N. Beadnall, S.N. Hatton, G. Bader, D. Tomic, D.G. Silva, and M.H. Barnett. 2016. Automated brain volumetrics in multiple sclerosis: a step closer to clinical application. *Journal of Neurology, Neurosurgery & Psychiatry* 87:754-757.

Wang, J., M. Sanchez-Rosello, J.L. Acena, C. del Pozo, A.E. Sorochinsky, S. Fustero, V.A. Soloshonok, and H. Liu. 2014. Fluorine in pharmaceutical industry: fluorine-containing drugs introduced to the market in the last decade (2001-2011). *Chemical reviews* 114:2432-2506.

Wang, S., B. Hesse, M. Roman, D. Stier, H. Castillo-Michel, M. Cotte, J.P. Suuronen, A. Lagrange, H. Radbruch, F. Paul, M. Taupitz, E. Schellenberger, I. Sack, and C. Infante-Duarte. 2019. Increased Retention of Gadolinium in the Inflamed Brain After Repeated Administration of Gadopentetate Dimeglumine: A Proof-of-Concept Study in Mice Combining ICP-MS and Micro- and Nano-SR-XRF. *Invest Radiol*

Wattjes, M.P., À. Rovira, D. Miller, T.A. Yousry, M.P. Sormani, N. de Stefano, M. Tintoré, C. Auger, C. Tur, M. Filippi, M.A. Rocca, F. Fazekas, L. Kappos, C. Polman, F. Barkhof, X. Montalban, and M.s.g. on behalf of the. 2015. MAGNIMS consensus guidelines on the use of MRI in multiple sclerosis—establishing disease prognosis and monitoring patients. *Nature Reviews Neurology* 11:597-606.

Wiese, M.D., A. Rowland, T.M. Polasek, M.J. Sorich, and C. O'Doherty. 2013. Pharmacokinetic evaluation of teriflunomide for the treatment of multiple sclerosis. *Expert Opin Drug Metab Toxicol* 9:1025-1035.

Wolf, W., C.A. Presant, and V. Waluch. 2000. 19F-MRS studies of fluorinated drugs in humans. *Adv Drug Deliv Rev* 41:55-74.

Wuerfel, J., T. Sinnecker, E.B. Ringelstein, S. Jarius, W. Schwindt, T. Niendorf, F. Paul, I. Kleffner, and J. Dorr. 2012. Lesion morphology at 7 Tesla MRI differentiates Susac syndrome from multiple sclerosis. *Mult Scler* 18:1592-1599.

Xu, M., X. Lu, J. Fang, X. Zhu, and J. Wang. 2016. The efficacy and safety of teriflunomide based therapy in patients with relapsing multiple sclerosis: A meta-analysis of randomized controlled trials. *Journal of clinical neuroscience : official journal of the Neurosurgical Society of Australasia* 33:28-31.

Yahr, M.D., S.S. Goldensohn, and E.A. Kabat. 1954. FURTHER STUDIES ON THE GAMMA GLOBULIN CONTENT OF CEREBROSPINAL FLUID IN MULTIPLE SCLEROSIS AND OTHER NEUROLOGICAL DISEASES. *Annals of the New York Academy of Sciences* 58:613-624.

Ye, J.C. 2019. Compressed sensing MRI: a review from signal processing perspective. *BMC Biomedical Engineering* 1:8.

Zhong, J., K. Narsinh, P.A. Morel, H. Xu, and E.T. Ahrens. 2015. In Vivo Quantification of Inflammation in Experimental Autoimmune Encephalomyelitis Rats Using Fluorine-

19 Magnetic Resonance Imaging Reveals Immune Cell Recruitment outside the Nervous System. *PloS one* 10:e0140238.

Zivadinov, R., and R. Bakshi. 2004. Role of MRI in multiple sclerosis I: inflammation and lesions. *Front Biosci* 9:C28.

Zivadinov, R., A.T. Reder, M. Filippi, A. Minagar, O. Stüve, H. Lassmann, M.K. Racke, M.G. Dwyer, E.M. Frohman, and O. Khan. 2008. Mechanisms of action of disease-modifying agents and brain volume changes in multiple sclerosis. *Neurology* 71:136-144.

Danksagung

Mein Dank gilt allen Kollegen und Co-Autoren, die an der hier vorgestellten Arbeit beteiligt waren. Insbesondere danke ich allen Kolleginnen und Kollegen des Max-Delbrück-Centrums für Molekulare Medizin und der Charité-Universitätsmedizin Berlin, die unsere Forschungsprojekte mit ihrem hohen Engagement möglich gemacht haben. Auch bei allen gegenwärtigen und ehemaligen Doktoranden und Masterstudenten bedanke ich mich für die freundliche und produktive Zusammenarbeit.

Ich bedanke mich bei Prof. Friedemann Paul, der über viele Jahre ein entscheidender Austauschpartner war und meinen Horizont in Richtung klinischer Perspektiven erweitert hat, für seinen Enthusiasmus und für die produktive Zusammenarbeit.

Ein besonderer Dank geht an Prof. Thoralf Niendorf, der mir während meiner Forschungsjahre am Experimental and Clinical Research Center (ECRC) und am Max-Delbrück-Centrums für Molekulare Medizin ein unschätzbarer Mentor gewesen ist. Ich danke ihm aufrichtig für sein Vertrauen, die überaus fruchtbare Zusammenarbeit und die stetige Unterstützung.

Meiner Familie danke ich für ihre Liebe, besonders meiner Familie in Deutschland, meinem Ehemann und meinem Sohn, besonderen Dank für ihre endlose Geduld und ihren Rückhalt. Ihre Unterstützung war ausschlaggebend für mich, um in diesem neuen Streben voranzukommen.

Eidesstattliche Erklärung

§ 4 Abs. 3 (k) der HabOMed der Charité

Hiermit erkläre ich, dass

- weder früher noch gleichzeitig ein Habilitationsverfahren durchgeführt oder angemeldet wurde,
- die vorgelegte Habilitationsschrift ohne fremde Hilfe verfasst, die beschriebenen Ergebnisse selbst gewonnen sowie die verwendeten Hilfsmittel, die Zusammenarbeit mit anderen Wissenschaftlern/Wissenschaftlerinnen und mit technischen Hilfskräften sowie die verwendete Literatur vollständig in der Habilitationsschrift angegeben wurden,
- mir die geltende Habilitationsordnung bekannt ist.

Ich erkläre ferner, dass mir die Satzung der Charité – Universitätsmedizin Berlin zur Sicherung Guter Wissenschaftlicher Praxis bekannt ist und ich mich zur Einhaltung dieser Satzung verpflichte.

Berlin, den 14. August 2021